

Femtosecond Laser Plasma Fabrication of Chalcogenide-Silicon Photonic Materials

Kheir Saad Albarkaty

Submitted in accordance with the requirements for
the degree of Doctor of Philosophy

The University of Leeds

School of Chemical and Process Engineering

December, 2019

*This thesis is dedicated to my incredible deceased mum,
Saidah Ali Albarkaty*

The following publications of a conference paper and a journal article are related to the results of chapter 5.

List of publications:

1. K. S. Albarkaty, J. Chandrappan, C. Craig, E. Kumi-Barimah, G. S. Murugan, D. Hewak, and G. Jose. Structure and optical properties of Er³⁺-doped gallium lanthanum sulfide (GLS) thin films prepared by femtosecond pulsed laser deposition. In: *PHOTON18, 2-6 September 2018, Birmingham*. Institute of Physics (IOP).
2. K. S. Albarkaty, E. Kumi-Barimah, C. Craig, D. Hewak, G. Jose, and J. Chandrappan. Erbium-doped chalcogenide glass thin film on silicon using femtosecond pulsed laser with different deposition temperatures. *Applied Physics A*. 2019, **125**(1), pp.1.

The candidate confirms that the work submitted is her own and that appropriate credit has been given where reference has been made to the work of others.

This copy has been supplied on the understanding that it is copyright material and that no quotation from the thesis may be published without proper acknowledgement.

© 2019 The University of Leeds and Kheir Saad Albarkaty

Acknowledgements

First of all, my uncommon gratitude goes to my main supervisor Prof. Gin Jose and Co-supervisor Dr Eric Kumi for providing requisite information concerning my PhD research and also for their assistance in directing me all through the period of my project from the time I started up to now. I would also to extend my gratitude to Dr Jayakrishnan Chandrappan for his support and directions in my first two years of my studies.

Furthermore, I would like to take this opportunity to say my thanks to technical staff for their considerable technical guidance. I also express my sincere thanks to all my friends, mainly; Emaan, Aishah, Amirah, and Fatimah. Thanks for offering countless words of motivation and giving me beautiful memories in Leeds that I am going to cherish for a lifetime.

Additionally, I am indebted to my parents, who have been of great help. They have fully supported to see me prosper in education. Exceptional thanks and specific regards, go to my mum, who passed away when I was just sixteen years. I miss you, mum, and I always wish you were there to celebrate the entirety of successes. I will always be grateful to mum for giving me life and for the affection that remained interminable. More so, for being a considerable and incredible mother that I ever know in the entire world, making me so fortunate to have such a superb mum in my life. Thanks go to my father, who has been the most adorable tutor there could ever be to me. He has persistently kept me reasonable and at per with my studies all the time. Thank you for your persistent believe in me in all situations, even when my self-esteem was low, and I did not have faith. Both of you made me what I am today. Also, I am indebted to express my most profound and most heartfelt gratitude to my beloved siblings, who have consistently kept in contact to support and encourage me.

Of course, no acknowledgement would be complete without thanking my sweet family, who has played a significant role and wellspring of many things in my study at the university. They have always showed supported, loved, and inspired me towards the journey of education. To my husband,

who had taken care of our children when I was busy doing researches. Also, giving me ample time for my studies. To my two kind little children (Rawasin and Nawaf), who never complained despite the limited time that I had with them. Their backing and understanding have motivated me to keep working harder and have more time to concentrate on finishing this work. Much gratitude to you all for all things considered moved me through the tough times of my study, until the most recent hour.

Lastly, gratitude is extended to the Ministry of Higher Education in Saudi Arabia, and I would like to express my sincere gratitude to my employer, Umm Al-Qura University for giving me the chance to pursue PhD at the University of Leeds.

Abstract

The research presented in this thesis covers the modification of the crystalline silicon or thin film deposition on silicon with chalcogenide glasses (ChGs) that are un-doped or doped with rare-earth ions to obtain the spectral emission in the near-infrared (NIR) region through a femtosecond pulsed laser deposition (fs-PLD) route. Four chalcogenide glass materials; gallium lanthanum sulphide (Ga-La-S), Er³⁺-doped gallium lanthanum sulphide (Er-Ga-La-S), germanium selenide (GeSe₄), and germanium antimony selenide (Ge₂₀Sb₁₅Se₆₅) were used. The properties of the chalcogenide films were studied as a function of process parameters such as; substrate temperature, laser pulse energy, deposition time, and background gas pressure. For each glass material, thin films have been deposited, implanted or diffused directly onto/into silicon substrate using fs-PLD. The structure and various physical properties of the chalcogenide thin films prepared from these chalcogenide glasses have also been systematically investigated.

Results showed that the structural characteristics of the target chalcogenide glass changed from amorphous to crystalline on increasing substrate temperatures; no intermixing and interdiffusion behaviour were observed between the silicon substrate and the deposited Ga-La-S and Er-doped Ga-La-S layers while ion-implanted Ge-Se and diffused Ge-Sb-Se layers were detected sub-surface of the silicon substrate. Furthermore, increasing the substrate temperature resulted in an increase in the thickness of the deposited layer, while the ion-implanted and diffused layer thickness decreased. Room temperature photoluminescence and lifetimes of the $^4I_{13/2} \rightarrow ^4I_{15/2}$ transition of Er³⁺ thin films are also reported in this thesis.

The results showed ChGs thin films with high homogeneity and smooth surfaces, with several droplets, were obtained in all the different configurations. It was also found that the optical properties of the thin films were strongly dependent on the preparation conditions, especially the substrate temperature.

Table of Contents

Acknowledgements	iii
Abstract	v
Table of Contents	vi
List of Tables	xi
List of Figures	xiii
List of Abbreviations	xix
Chapter 1: Introduction	1
1.1 Overview	1
1.2 Research aim and objectives	4
1.3 Thesis structure.....	4
Chapter 2: Literature review	6
2.1 Silicon as a platform optoelectronic material	6
2.1.1 Applications.....	9
2.2 Chalcogenide glasses (ChGs).....	9
2.2.1 Physical properties of ChGs.....	11
2.2.1.1 Thermal properties.....	11
2.2.1.2 Structural properties.....	12
2.2.1.3 Optical properties (absorption coefficient (α))	12
2.2.1 Applications of ChGs	14
2.2.3 Review of types ChGs used in this thesis.....	16
2.2.3.1 Gallium lanthanum sulphide (Ga-La-S) glass	16
2.2.3.2 Erbium-doped gallium lanthanum sulphide (Er ³⁺ -doped Ga-La-S) glass.....	18
2.2.3.3 Germanium selenide (GeSe ₄) glass.....	20
2.2.3.4 Germanium antimony selenide (Ge ₂₀ Sb ₁₅ Se ₆₅) glass	24
2.3 Chalcogenide thin film fabrication methods	28
2.3.1 Chemical vapour deposition technique (CVD)	29
2.3.2 Spin coating technique	29
2.3.3 Thermal evaporation technique (TVD).....	29
2.3.4 Sputter deposition.....	30
2.3.5 Pulsed laser deposition (PLD)	31

2.4 Ion implantation and diffusion processes	34
Chapter 3: Instrumentation and Methodology	41
3.1 Sample fabrication	41
3.1.1 Target materials.....	41
3.1.2 Femtosecond pulsed laser deposition (fs-PLD)	42
3.2 Thin film characterisations.....	44
3.2.1 Structural characterisations	44
3.2.1.1 X-ray diffraction (XRD).....	44
3.2.1.2 Raman spectroscopy	49
3.2.1.3 Transmission electron microscopy (TEM)	52
3.2.1.3.1 Selected area electron diffraction (SAED)	55
3.2.1.3.2 Focused ion beam (FIB) lithography for the preparation of cross-sections for TEM analysis	56
3.2.1.3.3 Energy dispersive X-ray (EDX) analysis through TEM	58
3.2.1.4 Scanning electron microscope (SEM).....	59
3.2.2 Optical characterisation	60
3.2.2.1 Photoluminescence (PL) spectroscopy.....	60
3.2.2.1.1 Time-resolved photoluminescence (TRPL).....	62
3.2.2.2 Ultraviolet–visible (UV-Vis-NIR) spectroscopy	63
Chapter 4: Gallium lanthanum sulphide (Ga-La-S) deposition on silicon	66
4.1 introduction.....	66
4.2 Deposition of gallium lanthanum sulphide (Ga-La-S) glass.....	66
4.3 Effect of substrate temperatures on the Ga-La-S thin film deposit on Si (100) substrate.....	67
4.3.1 TEM analysis of the Ga-La-S thin films.....	68
4.3.2 STEM-EDX analysis of the Ga-La-S thin film deposited at 600°C	69
4.3.3 XRD patterns of the Ga-La-S thin film prepared at different substrate temperatures.....	71
4.3.4 Raman spectroscopy of Ga-La-S thin film fabricated at different substrate temperatures.....	73
4.4 Effect of fs-laser energy and deposition time of Ga-La-S thin film on Si (100) substrate.....	74

4.4.1 TEM cross-section of Ga-La-S thin film samples fabricated at different deposition times and laser energies	75
4.4.2 STEM-EDX of samples deposited at different length of time and laser energies	76
4.4.3 Influence of deposition time and laser energy on the deposited Ga-La-S thin film (XRD).....	79
4.4.4 Influence of laser energies and deposition time on the deposition of Ga-La-S thin film (Raman spectroscopy).....	80
4.5 Conclusions	81
Chapter 5: Erbium-doped gallium lanthanum sulphide (Er³⁺-doped Ga-La-S) deposition on silicon.....	83
5.1 Introduction	83
5.2 Target material: Er-doped gallium lanthanum sulphide (Er ³⁺ -doped Ga-La-S) glass.....	83
5.3 Influence of substrate temperatures on Ga-La-S 65:34 +1 mol % Er ₂ O ₃ bulk glass deposit on Si (100) substrate	84
5.3.1 STEM-EDX cross-sectional analysis the Er ³⁺ -doped Ga-La-S thin film at different temperatures	85
5.3.2 Influence of substrate temperature on Er ³⁺ -doped Ga-La-S thin film (XRD)	86
5.3.3 Influence of substrate temperature on Er ³⁺ -doped Ga-La-S thin films (Raman Spectroscopy)	88
5.3.4 Influence of substrate temperature on Er ³⁺ -doped Ga-La-S thin film (PL spectroscopy).....	89
5.3.5 Influence of substrate temperature on Er ³⁺ -doped Ga-La-S thin film (UV-Vis spectroscopy)	91
5.4 Effect of deposition pressure on the of Er ³⁺ doped Ga-La-S thin films on Si (100) substrate at 660°C.....	93
5.4.1 Influence of pressure on the deposition Er ³⁺ -doped Ga-La-S thin film (SEM and TEM)	94
5.4.2 Influence of pressure on the deposition Er ³⁺ -doped Ga-La-S thin film (STEM-EDX)	97
5.4.3 Influence of pressure on Er ³⁺ -doped Ga-La-S thin film (XRD)	102
5.4.4 Influence of pressure on the deposition Er ³⁺ -doped Ga-La-S thin film (Raman spectroscopy).....	104

5.4.5 Influence of pressure on the deposition Er ³⁺ -doped Ga–La–S thin film (PL spectroscopy)	105
5.5 Conclusions.....	106
Chapter 6: Germanium selenide (GeSe₄) deposition and doping on silicon	108
6.1 Introduction	108
6.2 Target material: germanium selenide glass (GeSe ₄) synthesis.....	108
6.3 Influence of laser energies on the deposition of GeSe ₄ on Si (100) substrate	109
6.4 Influence of substrate temperature on GeSe ₄ bulk glass doping into Si (100) substrate.....	114
6.4.1 Influence of substrate temperature on Ge-Se thin film (SEM)	115
6.4.2 Influence of substrate temperature on Ge-Se thin film (EDX spectroscopy)	118
6.4.3 Influence of different substrate temperatures on Ge-Se thin film (XRD spectroscopy)	124
6.4.4 Influence of various substrate temperatures on the Ge-Se thin film (Raman spectroscopy)	125
6.4.5 Influence of substrate temperatures on the Ge-Se thin film (UV-Vis spectroscopy)	126
6.5 Conclusion	128
Chapter 7: Germanium antimony selenide (Ge₂₀Sb₁₅Se₆₅) deposition and diffusion on silicon	129
7.1 Introduction	129
7.2 Target material: germanium antimony selenide (Ge ₂₀ Sb ₁₅ Se ₆₅) glass	129
7.3 Influence of laser energies on deposition of Ge ₂₀ Sb ₁₅ Se ₆₅ on Si (100) substrate	130
7.4 Influence of substrate temperature on Ge ₂₀ Sb ₁₅ Se ₆₅ bulk glass doping into Si (100) substrate	136
7.4.1 Surface morphology and EDX-mapping of Ge-Sb-Se thin films deposited at various substrate temperatures.....	137
7.4.2 TEM-cross-sectional analysis of the Ge-Sb-Se thin film deposited at various substrate temperatures	143
7.4.3 XRD characterisation of the Ge-Sb-Se thin film deposited at different substrate temperatures.....	151

7.4.4 Influence of substrate temperature on the Ge-Sb-Se thin film (Raman spectroscopy)	153
7.4.5 Determining optical band gap of the Ge-Sb-Se thin film (UV-Vis spectroscopy)	155
7.5 Conclusion	157
Chapter 8: Conclusions and Future Work	159
8.1 Conclusions	159
8.2 Suggestions for future work	160
References	163
Appendices	188

List of Tables

Table 2.1: Comparison of key properties between sulphide, fluoride and silica-based devices *approximated by value for glass [88].....	11
Table 3.1: Comparison of the SAED in TEM with XRD	56
Table 4.1: Properties of 65Ga ₂ S ₃ :35La ₂ S ₃ glass [144, 158].....	66
Table 4.2: The deposition parameters for G1, G2, G3, and G4 employed in investigating the effect change in substrate temperature of Ga-La-S onto Si substrate	67
Table 4.3: Experimental variables used for fabricating Ga-La-S samples described in this section.....	75
Table 4.4: Constant parameters utilised in fabricating Ga-La-S thin film samples at different laser energies and duration.....	75
Table 4.5: The elemental concentration of different Ga-La-S specimens at measured areas #1 shown in TEM-HAADF images obtained in Fig. 4.10.	78
Table 5.1: Properties of Er ³⁺ -doped Ga-La-S glass [144, 158].....	84
Table 5.2: List of parameters employed to deposit Er ³⁺ -doped Ga-La-S on Si substrate by using various substrate temperatures	84
Table 5.3: Fluorescence lifetimes of Er ³⁺ -doped Ga-La-S samples at different substrate temperatures.....	91
Table 5.4: Optical energy band gap of Er ³⁺ -doped Ga-La-S prepared at various substrate temperatures	92
Table 5.5: List of parameters employed to deposit Er ³⁺ -doped Ga-La-S on Si substrate by using different pressures.....	94
Table 5.6: Fluorescence lifetimes of Er ³⁺ -doped Ga-La-S samples at various chamber pressures	106
Table 6.1: Some properties of GeSe ₄ bulk glass [330, 331]	109
Table 6.2: Deposition parameters employed to deposit GeSe ₄ onto silicon substrate.....	109
Table 6.3: List of parameters employed to deposit GeSe ₄ on Si substrate by using different substrate temperatures.....	115
Table 6.4: Optical energy band gap of Ge-Se films prepared at various substrate temperatures	128
Table 7.1: Some properties of Ge ₂₀ Sb ₁₅ Se ₆₅ bulk glass [341, 342].....	129

Table 7.2: Fs-PLD parameters employed in deposition of $\text{Ge}_{20}\text{Sb}_{15}\text{Se}_{65}$ thin film on Si substrate by using various fs-laser energies.....130

Table 7.3: List of parameters employed to fabricate $\text{Ge}_{20}\text{Sb}_{15}\text{Se}_{65}$ bulk glass into Si substrate by using different substrate temperatures137

List of Figures

Fig. 2.1: Silicon's transmission spectrum [74].	9
Fig. 2.2: Typical transmittance spectra of silica, fluorides, sulphide, selenide, and telluride bulk glasses [103].	13
Fig. 2.3: Energy transfer sketch of Er^{3+} when pumped at 980 nm.	20
Fig. 2.4: Schematic diagram of ds diode sputtering system (adapted from [229]).	31
Fig. 2.4: The interaction of long-pulse and short-pulse laser with target material [236].	32
Fig. 2.5: Laser material processing of a glass target by ablation of nanosecond laser (left) and femtosecond laser (right) [239].	33
Fig. 2.7: The comparison of (a) conventional ion implantation technique with (b) plasma source ion implantation (PSII) [246].	35
Fig. 3.1: Schematic setup of the fs-PLD system.	44
Fig. 3.2: Basic features of an X-ray diffractometer [271].	45
Fig. 3.3: Diagram of Bragg's law.	46
Fig. 3.4: Information content of an idealised diffraction pattern [270].	46
Fig. 3.5: XRD spectra corresponds to (a) an amorphous, (b) polycrystalline silicon colloids, and (c) a single crystal silicon sample [275].	48
Fig. 3.6: Grazing incidence XRD.	49
Fig. 3.7: Energy level diagram of Rayleigh and Raman scattering [278].	51
Fig. 3.8: Schematic structure of a Raman spectroscopy system [285].	52
Fig. 3.9: (a) General layout of a TEM describing the path of electron beam in a TEM and (b) a ray diagram for the diffraction mechanism in TEM [292].	55
Fig. 3.10: SAED pattern showing; (a) an amorphous sample pattern, (b) a polycrystalline sample pattern, and (c) a single crystal sample pattern [293].	56
Fig. 3.11: Schematic diagram showing coating FIB-TEM layers.	57
Fig. 3.12: Principle of EDX [297].	59
Fig. 3.13: Principle of photoluminescence spectroscopy (PL) [300].	62
Fig. 3.14: Block diagram of fluorescence spectrometer [301].	62
Fig. 3.15: Schematic diagram of UV-Vis-NIR spectrophotometer [302].	65

Fig. 4.1: (a) Pure Ga-La-S target glass and (b) target glass holder used to fabricate thin film in the fs-PLD.....67

Fig. 4.2: TEM cross-section images of Ga-La-S thin film on silicon glass substrates by fs-PLD at different substrate temperatures; (a) 450°C (G1), (b) 500°C (G2), (c) 550°C (G3), and (d) 600°C (G4).....68

Fig. 4.3: HAADF-STEM image and STEM-EDX elemental mapping image of Ga-La-S thin film deposited on silicon at a substrate temperature of 600°C (sample G4).....69

Fig. 4.4: STEM-EDX spectrum of the Area#1 labelled in Fig. 4.3.69

Fig. 4.5: (a) A HAADF-STEM image and (b) a line scan obtained from STEM-EDX showing that no silicon was detected in the Ga-La-S thin film prepared on silicon at a higher substrate temperature (600°C).70

Fig. 4.6: XRD patterns of pure silicon substrate (thickness = 675µm), Ga-La-S bulk glass, and ICDD reference patterns for silicon and silica.71

Fig. 4.7: XRD patterns of Ga-La-S thin film deposited on silicon at various substrate temperatures; 450, 500, 550, and 600°C along with ICDD reference patterns for Ga-La-S bulk glass.....72

Fig. 4.8: Raman spectra of a pure Si substrate (thickness = 675µm), Ga-La-S bulk glass, and thin films deposited on Si at various substrate temperatures; 450, 500, 550, and 600°C.....73

Fig. 4.9: TEM cross-section images of the Ga-La-S thin film deposited on a silicon substrate at different laser energies and depositions times: (a) G1 sample prepared with 30 µJ for 2 h, (b) G1B sample prepared with 50 µJ for 2 h, and (c) G1C sample prepared with 50 µJ for 4 h.....75

Fig. 4.10: HAADF-STEM images and STEM-EDX elemental mapping obtained during the cross-sectional TEM analysis of; (a) G1 sample prepared with 30 µJ for 2 h, (b) G1B sample prepared with 50 µJ for 2 h, and (c) G1C sample prepared with 50 µJ for 4 h.....77

Fig. 4.11: (a) Cross-sectional bright-field BF-TEM image of Ga-La-S film of G1C sample prepared with 50 µJ for 4 hours at 450°C, (b) SAED pattern captured from Ga-La-S layer, and (c) SAED pattern captured from the silicon substrate region.78

Fig. 4.12: XRD patterns of the Ga-La-S thin films deposited on silicon glass substrates by fs-PLD at various deposition times and laser energies.....79

Fig. 4.13: Raman spectra of the Ga-La-S thin films deposited on silicon glass substrates at different time depositions and laser energies.....81

Fig. 5.1: Er³⁺-doped Ga-La-S bulk glass (left) and Er³⁺-doped Ga-La-S bulk glass holder (right) which is used for fs-PLD.83

Fig. 5.2: TEM cross-section images of Er³⁺-doped Ga-La-S thin films deposited on Si substrate at different substrate temperatures; **(a)** 25°C (GE1), **(b)** 450°C (GE2), **(c)** 660°C (GE3). 85

Fig. 5.3: HAADF-STEM image and STEM-EDX elemental mapping obtained during cross-sectional TEM analysis of a GE3 sample prepared at 660°C..... 86

Fig. 5.4: XRD patterns for a pure silicon substrate (thickness = 675 μm), Er³⁺-doped Ga-La-S bulk glass, and thin films deposited on silicon at various substrate temperature. 87

Fig. 5.5: Raman spectra of a pure silicon substrate (thickness = 675μm), Er³⁺-doped Ga-La-S bulk glass, and thin films on silicon at various substrate temperatures..... 89

Fig. 5.6: **(a)** PL spectra of 1 mol% Er³⁺ -doped Ga-La-S glass and Er³⁺-doped Ga-La-S thin films deposited at various substrate temperatures, and **(b)** Energy transfer sketch of Er³⁺-doped glass when pumped at 980 nm. 90

Fig. 5.7: **(a)** Tauc plot as a function of photon energy, and **(b)** Optical band gap verses deposition temperature of Er³⁺-doped Ga-La-S glass thin films on a Si substrate..... 93

Fig. 5.8: SEM images of the top surface of Er³⁺-doped Ga-La-S thin films deposited on Si substrate with different pressures; **(a)** GP1 (under vacuum), **(b)** GP2 (40 mTorr), and **(c)** GP3 (200 mTorr)..... 95

Fig. 5.9: TEM cross-sections of Er³⁺-doped Ga-La-S layer formed on Si substrates by fs-PLD with different pressures; **(a)** under vacuum (GP1), **(b)** 40 mTorr (GP2), and **(c)** 200 mTorr (GP3). 96

Fig. 5.10: HAADF-STEM images and STEM-EDX elemental maps images of Er³⁺-doped Ga-La-S thin films prepared on Si with different pressures; **(a)** sample prepared under vacuum (GP1), **(b)** sample prepared at 40 mTorr (GP2), and **(c)** sample prepared at 200 mTorr (GP3). 98

Fig. 5.11: TEM-EDX spectrum of the yellow region labelled (Area≠1) in HAADF-STEM Fig. 5.10 of the doped layer on silicon for samples; **(a)** GP1 prepared under vacuum, **(b)** GP2 sample prepared at 40 mTorr, and **(c)** GP3 sample prepared at 200 mTorr. 99

Fig. 5.12: TEM images of Er³⁺-doped Ga-La-S thin film on silicon from sample GP1 prepared under vacuum; **(a)** cross-sectional BF-TEM image of the Er³⁺-doped Ga-La-S layer, **(b)** SAED pattern captured from a silicon substrate region, and **(c)** SAED pattern captured from the Er³⁺-doped Ga-La-S layer region.100

Fig. 5.13: TEM images of the Er³⁺-doped Ga-La-S thin film on silicon from sample GP1 prepared at 40 mTorr; **(a)** cross-sectional BF-TEM image of Er³⁺-doped Ga-La-S layer, **(b)** SAED pattern captured from a silicon substrate region, and **(c)** SAED pattern captured from the Er³⁺-doped Ga-La-S layer region. 101

Fig. 5.14: XRD patterns of a pure silicon substrate (thickness = 675 μm), Er³⁺-doped Ga-La-S bulk glass, and thin films deposited on silicon at various working pressure; a vacuum (GP1), 40 mTorr (GP2), and 200 mTorr (GP3). 102

Fig. 5.15: Raman spectra of a pure silicon substrate (thickness = 675 μm), Er³⁺-doped Ga-La-S bulk glass, and thin films on silicon at different pressures. 104

Fig. 5.16: PL spectra of 1 mol% Er³⁺-doped Ga-La-S glass and Er³⁺-doped Ga-La-S thin films deposited at different chamber pressures. 105

Fig. 6.1: GeSe₄ bulk glass **(left)** and GeSe₄ bulk glass holder **(right)** which are used for fs-PLD. 109

Fig. 6.2: SEM images of Ge-Se thin films deposited on silicon substrates at different laser energies; **(a)** 20 μJ, **(b)** 30 μJ, **(c)** 40 μJ, and **(d)** 50 μJ. ... 110

Fig. 6.3: XRD patterns of **(a)** pure silicon substrate (thickness = 675 μm), **(b)** GeSe₄ bulk glass, and **(c-f)** Ge-Se thin films fabricated on silicon glass by fs-PLD at laser energies of; 20 μJ, 30 μJ, 40 μJ, and 50 μJ, respectively. 111

Fig. 6.4: Raman spectra of **(a)** pure silicon substrate (thickness = 675 μm) and GeSe₄ bulk glass, **(b)** Ge-Se thin films deposited on silicon substrate at different laser energies; 20 μJ, 30 μJ, 40 μJ, and 50 μJ. 113

Fig. 6.5: FIB-SEM images of Ge-Se thin films deposited on silicon substrate at various temperatures; **(a)** 25°C, **(b)** 200°C, **(c)** 400°C, and **(d)** 600°C. 115

Fig. 6.6: TEM cross-section images of Ge-Se layer formed on silicon substrates by fs-PLD at various substrate temperatures; **(a)** 25°C (S25), **(b)** 200°C (S200), **(c)** 400°C (S400), and **(d)** 600°C (S600). 117

Fig. 6.7: Images of Ge-Se layer on silicon from sample S25 prepared at room temperature (25°C); **(a)** FIB-SEM image of the Ge-Se layer cross-section, **(b)** cross-sectional BF-TEM image of Ge-Se layer, and **(c)** SAED pattern captured from the Ge-Se layer region confirming the amorphous state. 118

Fig. 6.8: HAADF-STEM images and STEM-EDX elemental mapping images of Ge-Se thin film prepared on silicon at different temperatures; **(a)** 25°C, **(b)** 200°C, **(c)** 400°C, and **(d)** 600°C. 120

Fig. 6.9: (a) A HAADF-STEM image, and (b) a line scan obtained from STEM-EDX showing that no silicon was detected at the Ge-Se film prepared on silicon at a lower substrate temperature (25°C).....121

Fig. 6.10: (a) A HAADF-STEM image, and (b) a line scan gained from STEM-EDX showing that silicon was detected at the Ge-Se film prepared on silicon at a higher substrate temperature (600°C).122

Fig. 6.11: TEM-EDX spectrum of the yellow region labelled in Fig. 6.9 (a) and 6.10 (a) of the doped layer on silicon for samples; (a) S25 prepared at room temperature (25°C) and (b) S600 prepared at 600°C.....123

Fig. 6.12: XRD patterns of thin films fabricated on Si substrate by fs-PLD at various substrate temperatures; 25, 200, 400, and 600°C along with ICDD reference patterns for Ge-Se bulk glass.124

Fig. 6.13: Raman spectra of Ge-Se thin films fabricated on Si substrate by fs-PLD at various substrate temperatures; 25, 200, 400, and 600°C.....126

Fig. 6.14: Absorption coefficient as a function of photon energy for different Ge-Se thin films.127

Fig. 7.1: Ge₂₀Sb₁₅Se₆₅ bulk glass (left) and Ge₂₀Sb₁₅Se₆₅ target glass holder (right) used to fabricate Ge-Sb-Se thin film.....130

Fig. 7.2: SEM images of Ge-Sb-Se thin films deposited on silicon substrate at different laser energies; (a) 20 μJ, (b) 30 μJ, (c) 40 μJ, and (d) 50 μJ.131

Fig. 7.3: XRD patterns of a pure silicon substrate (thickness = 675 μm) and Ge₂₀Sb₁₅Se₆₅ bulk glass.132

Fig. 7.4: XRD patterns of Ge-Sb-Se thin films fabricated on Si glass substrates by fs-PLD at various laser pulse energies; (a) 20 μJ, (b) 30 μJ, (c) 40 μJ, and (d) 50 μJ along with ICDD reference patterns for Ge-Sb-Se bulk glass.....133

Fig. 7.5: (a) Raman spectra of a pure Si substrate (thickness = 675 μm), Ge₂₀Sb₁₅Se₆₅ bulk glass, and Ge-Sb-Se thin films deposited on Si substrate at different laser pulse energies; 20 μJ, 30 μJ, 40 μJ, and 50 μJ, (b) The Gaussian decomposition of the vibration Raman spectra of Ge₂₀Sb₁₅Se₆₅ bulk glass.....135

Fig. 7.6: FIB-SEM images showing the surface morphology of Ge-Sb-Se thin film grown at different substrate temperatures; (a) 25°C, (b) 200°C, (c) 400°C, and (d) 600°C.138

Fig. 7.7: SEM-EDX spectrum and the elemental quantitative data of the Ge-Sb-Se surface prepared at; (a) 400°C (sample Sb400) and (b) 600°C (sample Sb600).139

Fig. 7.8: TEM cross-section images of the Ge-Sb-Se thin film fabricated on Si substrate by fs-PLD at various substrate temperatures; **(a)** 25°C (Sb25), **(b)** 200°C (Sb200), **(c)** 400°C (Sb400), and **(d)** 600°C (Sb600). 140

Fig. 7.9: **(a)** Cross-sectional BF-TEM image of the Ge-Sb-Se layer on silicon from sample Sb25 prepared at 25°C, **(b)** SAED pattern captured from silicon substrate region, **(c and d)** SAED pattern captured from different areas of Ge-Sb-Se layer.141

Fig. 7.10: **(a)** Cross-sectional BF-TEM image of the Ge-Sb-Se layer on silicon from sample Sb200 prepared at 200°C, **(b)** SAED pattern captured from silicon substrate region, **(c-e)** SAED pattern captured from different areas of Ge-Sb-Se layer.142

Fig. 7.11: HAADF-STEM images and STEM-EDX elemental mapping images of Ge-Sb-Se thin films prepared on silicon at **(a)** 25°C, **(b)** 200°C, **(c)** 400°C, and **(d)** 600°C..... 144

Fig. 7.12: HAADF-STEM images and STEM-EDX line scans were detected Ge-Sb-Se thin film prepared on silicon at different substrate temperatures; **(a)** 25°C, **(b)** 200°C, **(c)** 400°C, and **(d)** 600°C..... 147

Fig. 7.13: TEM-EDX spectrum of the yellow regions labelled in Fig. 7.11 (a-d) of HAADF-STEM images for the doped layer prepared on silicon at different temperatures; **(a)** 25°C (sample Sb25), **(b)** 200°C (sample Sb200), **(c)** 400°C (sample Sb400), and **(d)** 600°C (sample Sb600). 150

Fig. 7.14: XRD patterns of thin films fabricated on Si glass substrates by fs-PLD at various substrate temperatures; 25, 100, 200, 300, 400, and 600°C.151

Fig. 7.15: Raman spectra of **(a)** Ge-Sb-Se thin films prepared on silicon at different substrate temperatures, and **(b)** comparison of the main peaks for all samples..... 153

Fig. 7.16: α^2 vs. $h\nu$ plots for Ge-Sb-Se thin films prepared at various substrate temperatures..... 157

List of Abbreviations

Si	Silicon
ChG	Chalcogenide Glass
IC	Integrated Circuit
PICs	Photonic Integrated Circuits
OEIC	Optoelectronic Integrated Circuit
fs	Femtosecond
ns	Nanosecond
ms	Microsecond
PLD	Pulsed Laser Deposition
FWHM	Full-width at half-maximum
IR	Infra-Red
Vis	Visible
MIR	Mid-Infrared
NIR	Near-Infrared
PL	Photoluminescence
TRPL	Time-Resolved Photoluminescence
RE	Rare-Earth
TEM	Transmission Electron Microscopy
SAED	Selected Area Electron Diffraction
SEM	Scanning Electron Microscopy
EDX	Energy Dispersive X-ray
XRD	X-Ray Diffraction
GIXRD	Grazing Incidence X-Ray Diffraction

ICDD	International Centre for Diffraction Data
FIB	Focused Ion Beam
HAADF	High-Angle Annular Dark-Field
BF-TEM	Bright Field-Transmission Electron Microscopy
PL	Photoluminescence
CVD	Chemical Vapour Deposition
REEs	Rare Earth Elements
HREEs	Heavy Rare Earth Elements
LREEs	Light Rare Earth Elements
DVD	Digital Video Disc
CMOS	Complementary Metal-Oxide-Semiconductor

Chapter 1: Introduction

1.1 Overview

The last decade has seen silicon photonics (SiP) promoted as a platform for potentially revolutionary advances in the fields of telecommunications, data communications, medical technology, security, and sensing [1-3]. The main driving force behind SiP is the potential to realise small, highly integrated, photonic sub-systems that leverage off the decades of fabrication experience, technology, and scalability already developed for complementary-metal-oxide-semiconductor (CMOS) electronics [4]. The ultimate goal is to create low-cost high-volume photonic integrated circuits (PICs) on integrating electronics. This would enable the realisation of the full potential of the silicon platform applications such as high-speed communication and sensing, CMOS-electronics for subsequent logical operations and computations [5]. The use of the effect of free-carrier plasma dispersion, in addition to integration with other integrated semiconductor materials grown selectively or heterogeneously, has allowed a wide functionalities area include electro-optic modulation [6], photodetection [7], and light generation [8].

Si has a large refractive index $n=3.45$ and band gap of (1.1 eV) and is transparent in the near-infrared O- band (1260 – 1360 nm) and C-communication band (1530 nm to 1565 nm). Furthermore, it owns a high optical damage threshold beside high third-order nonlinearity, which are very important features for all-optical signal processing and wavelength conversion [9]. However, because of large Si two-photon absorption (TPA), these applications are limited [10]. There is one way to solve this issue by the integration of ChGs into a silicon-on-insulator (SOI) platform. ChGs consists of one or more of the chalcogen elements, which include sulfur (S), selenium (Se), and tellurium (Te) mixed with other additive elements such as germanium (Ge), arsenic (As), antimony (Sb) [11].

Chalcogenide glasses are very attractive materials for developing active and passive devices due to their remarkable optical and electrical properties such as low-energy phonons [12, 13], photo-induced phenomena [14, 15],

wide transparency window [14, 16], as well as nonlinear and linear refractive indices [17, 18]. These excellent characteristics of the chalcogenide glasses make them ideal candidates for developing next generation of on-chip photonic platform for ultrafast all-optical signal processing or optical switching (memory and selector units), single-mode planar waveguide for optical communication, generating broad-band super-continuum in mid-IR for spectroscopy and sensing [19-21]. However, their structures are difficult to fabricate because they require complicated epitaxial growth (deposition of crystalline layer upon crystalline substrate), but the femtosecond pulsed laser deposition (fs-PLD) technique could readily produce them.

Chalcogenide glass systems based on Arsenic (As) for example, have been widely investigated and studied [22-25] and successfully utilised in manufacturing optical fibres and planar waveguides [26-30]. However, these binary glasses suffer from considerable issues like toxicity and are relatively difficult to work mechanically due to their low devitrification temperature. It has been found, however, that more desirable materials such as chalcogenide glasses based with better thermal and optical properties are required for future photonic devices. These chalcogenide glasses have huge potential for ultrafast optical switches, frequency converters, optical amplifiers, optical recording devices, integrated optics, infrared lasers, and infrared transmitting optical fibres [14, 31, 32]. Chalcogenide semiconducting alloys have been found in several applications not only due to their electrical and thermal properties but also own to their optical properties.

For instance, Ga-La-S glass has been known and studied extensively for many years as an alternative glass to toxic arsenic sulphides, As_2S_3 . Glasses based on arsenic sulphide have been developed into a low loss single-mode fibre. They have a slightly shifted transmission window range from 0.6 μm to 8 μm , reflecting a lower phonon or vibrational energy for the glass matrix. Moreover, it is difficult to dope arsenic-based fibres with rare-earth ions to make active devices [33]. Replacing arsenic with gallium in chalcogenide glass matrix leads to the formation of a highly stable and non-toxic chalcogenide glass [34-36] called gallium lanthanum sulphide (Ga-La-

S). Ga-La-S has become a widely studied glass due to its favourable compromise between nonlinearity and transparency [37-42]. An inherent low phonon energy (450 cm^{-1}) makes them attractive for rare-earth doping, which reduces non-radiative recombination and enhancing the radiative efficiency of the rare-earth ions emissions [43]. These glasses also support high doping concentration of the rare-earth ions, leading to high refractive index ($n = 2.4\text{--}3.0$) and low-loss transmission glasses for photonic device engineering.

Ge–Se system is another chalcogenide with enormous potential as a host material. Among various chalcogenide systems, chalcogenide glasses based on germanium are suitable materials for both passive and active infrared applications, such as optical fibres, waveguides and sensors [44], or rare-earth-doped fibre lasers and amplifiers [45]. So, germanium could be considered as an alternative to arsenic-based selenium glasses owing to its various properties like greater hardness, higher sensitivity, higher crystallisation temperature, higher conductivity, higher stability, environmental sustainability, glass-forming ability, and the sizeable optical transmission range extending in the mid-infrared. As a consequence of these exciting properties, $\text{Ge}_x\text{Se}_{1-x}$ glasses have been investigated extensively for their glass-forming region, structure, physical properties, the kinetics of the glass transition, thermoelectric properties, etc. [46-51]. Ge-based chalcogenides are suitable candidates for applications in switching and memory devices [20, 21, 52-55].

The formation of bonds by Ge atoms with Se chains in Ge–Se system can lead to an increase in the system's average bond strength. For changes to be effected in the new complex glass properties, the addition of more than one element into the selenium matrix to have these problems eliminated is worth it. Various methods have been utilised to synthesis binary alloys with selenium, which, in turn, provide high sensitivity and crystallisation temperature, as well as reduced ageing effects. Defects are observed in the Ge–Se glass system through the addition of a third element such as Sb. The bonds present in the system are modified by the presence of a third element, resulting in the rearrangement of the structure, thereby increasing

the system's randomness. Thus, it is expected that Sb in Ge–Se system addition will improve the Ge–Se system's glass-forming ability. Germanium based chalcogenide comprises of heavy elements like Sb has improved optical properties which is suitable for non-linear applications [56]. We have also selected the Ge–Sb–Se system in this work. The selection of popularly-known glass-forming system Ge–Sb–Se was made as a result of the relatively lower vapour pressure, in contrast to the Ge–As–Se [57] system.

1.2 Research aim and objectives

This research aims to dope or implant the host of chalcogenide glass materials (Ga–La–S, Er³⁺-doped Ga–La–S, GeSe₄, and Ge–Sb–Se) on/into silicon substrate networks via fs-PLD technique. The objectives of this research work include:

- Employ fs-PLD technique to deposit un-doped/doped chalcogenide glasses onto a silicon substrate.
- Evaluate the surface morphology, structural, and optical properties of the thin films for possible optical waveguide applications in the near-infrared.

1.3 Thesis structure

The structure of the thesis includes the following chapters:

After a brief introduction to the motivation and objectives behind this work in **Chapter 1**, **Chapter 2** offers a detailed literature review associated with this thesis. This chapter discusses the fundamental principle and the thin films' growth using fs- PLD mechanism, as well as comparing fs-PLD with numerous thin film fabrication techniques. Furthermore, it discusses the properties of chalcogenide glasses and rare-earth ion (Erbium) employed in this study.

Chapter 3 offers an outline of the numerous experimental techniques employed in the fabrication and the materials characterisation produce in this thesis. This chapter also makes a brief presentation of the fundamental principles and theories related to the instruments' operation.

Chapter 4, 5, 6, and 7 provide the results and discussions of the fs-PLD. This comprises of detail discussions of various processing parameters (such as substrate temperatures, laser energy, deposition time, and pressures) of the fs-PLD used to fabricate the Ga-La-S, Er³⁺-doped Ga-La-S, Ge-Se, and Ge-Sb-Se thin films on/into Si substrate (100). This is followed by the description of the results and discourse of their morphological, structural, and optical properties relative to the process limitations utilised.

Lastly, **Chapter 8** presents a short conclusion and certain recommendations made for future work.

Chapter 2: Literature review

2.1 Silicon as a platform optoelectronic material

In the world of electronics, silicon (Si) has earned the reputation of being perhaps the most ubiquitous material due to its semiconducting properties, abundance, ease to work with as well as low cost. Porous silicon was found to possess efficient photoluminescence (PL) at room temperature by Canham et al. [58] at energies above the silicon band gap of 1.12 eV [58-60]. Since then, researchers have been interested in using silicon to develop nanomaterial-based light emission sources. Several techniques and systems have been employed in studying the luminescence exhibited by silicon nanostructures ranging from silicon nanocrystals to multi-layered structures [61-63]. To fabricate Si nanostructures with photoluminescent characteristics, various physical and chemical techniques can be used; each technique has its advantages and disadvantages. However, uniqueness of the production processes is demonstrated in the solution phase reduction that facilitates the production of free-standing nanocrystals. This unique feature is related to the ability to functionalise the surface through the use of both hydrophobic and hydrophilic molecules that are responsible for making the material suitable for various biological applications.

As a semiconductor, silicon nanoparticles (NPs) also demonstrates very high electronic stability due to its bio-inertness. It is different from II-VI nanoparticle types because of its low inherent toxicity [64]. A direct band-gap transition is exhibited by a majority of II-VI quantum dots which contrasts with the indirect band gap semiconductor behaviour of bulk Si. In this case, there is a movement to the top of the valance band from the bottom of the conduction band, and this is considered a violation of the conservation of momentum and therefore barred in electronics [64]. This movement is made possible with photon assistance. This implies that an extra change in the vibration mode of the lattices is needed for photon absorption and emission. This process is indirect and therefore has a low probability. As such, bulk silicon has fewer application in optics compared

to its widespread use in electronics. On this basis, it is expected that silicon NPs would have a long PL lifetime and low PL efficiencies in comparison to direct band-gap semiconductors [64].

As noted in the previous paragraph, the abundance of silicon has seen it being widely applied in making electronics which have revolutionised the way we live our lives [65]. Silicon is still attracting the attention of many because of its numerous potential applications that include biological imaging, photonics, drug delivery, and storage of energy [66-72]. Naturally, pure silicon is difficult to find, but it can be found in the form of silica and silicate compounds. The preference given to the use of silicon as a platform for optoelectronics and integrated photonics is due to its compatibility with the already established silicon integrated circuit (IC) manufacturing processes. Additionally, in terms of cost per unit area, silicon wafers are less costly but have higher quality in comparison to other semiconductor materials. Moreover, it is behind the ability of electronic factories to manufacture thumb-size chips and microprocessors with millions of components and still sell at a low price. The production of silicon is one of the areas that has benefited from the integration of high-tech processes and economies of scale.

Researchers working on silicon photonics are motivated by the opportunity of exploiting the vast and well-developed IC industry with the intention of making photonics for various applications because of the low cost of materials and processes. Additionally, the researchers also get their motivation from the availability of high-quality silicon-on-insulator (SOI) wafers that provides the best platform for developing planar waveguide circuits. Photonic devices can also be scaled to hundreds of nanometres due to the high index contrast that exists between silicon ($n = 3.45$) and SiO_2 ($n = 1.45$) that causes a high optical intensity. This can facilitate non-linear optical interactions such as Kerr and Raman effects in chip-scale devices. This outcome has made it possible to perform wavelength conversion, optical amplification, and lasing functions which were traditionally considered to be out of the capabilities of silicon. Photonic

devices require excellent material properties which are readily available in silicon. These properties include high optical damage threshold ($\sim 10\times$ higher than GaAs), high thermal conductivity ($\sim 10\times$ higher than GaAs), and high third-order optical nonlinearities. The arguments presented above are the motivation behind the use of silicon in photonics.

Additionally, the Raman Effect and Kerr effect for silicon are 1000 and 100 times respectively stronger than those in silica fibre. Silicon's transmission spectrum is demonstrated in Figure 2.1, with the low-loss wavelength window starting at $1.1\ \mu\text{m}$ and extending to $7\ \mu\text{m}$ [73]. In the mid-infrared (MIR) spectrum, silicon displays excellent material properties, but limited in the near-infrared data communication band of $1.3\text{--}1.55\ \mu\text{m}$. At $1\ \mu\text{m}$ silicon has high loss, which is due to the indirect band gap absorption that corresponds to an energy of $1.12\ \text{eV}$. Between 1 and $6.5\ \mu\text{m}$ range, there is a low loss window that peaks the following absorption. This property is very attractive when it comes to the building of optical devices in the near IR region and mid-IR wavelengths. The losses increase past $7\ \mu\text{m}$, and this is related to the multiphoton absorption processes. However, peaking of the resonance of a single phonon occurs only at $20\ \mu\text{m}$ (or $521\ \text{cm}^{-1}$) [73].

The explosion of Si photonics witnessed recently is attributed to two main reasons. First, the development of high volume optoelectronic integrated circuit (OEIC) chips. Second, the practical development of photonic ICs on SOI. In one OEIC, all photonics, as well as electronic components required to establish a fast and bidirectional optical communication link with another OEIC chip or within one chip, can be achieved. Hence, silicon OEIC provides the best platform for optical interconnects. In the development of optical interconnects, hierarchical ranges are observed, and this includes intra-chip, chip-to-chip, board-to-board, and rack-to-rack. New generation computers would be interconnected using photonic interconnects, and this is considered an essential application of silicon photonics. However, other applications of OEIC exist, and this is attributed to their cost-effective nature and ability to intimately integrate complex photonics with electronics, which provides solutions to problems that could not be addressed by conventional

photonics or microelectronics solutions. New functionalities, as well as higher levels of performance, are offered by on-chip OE [2].

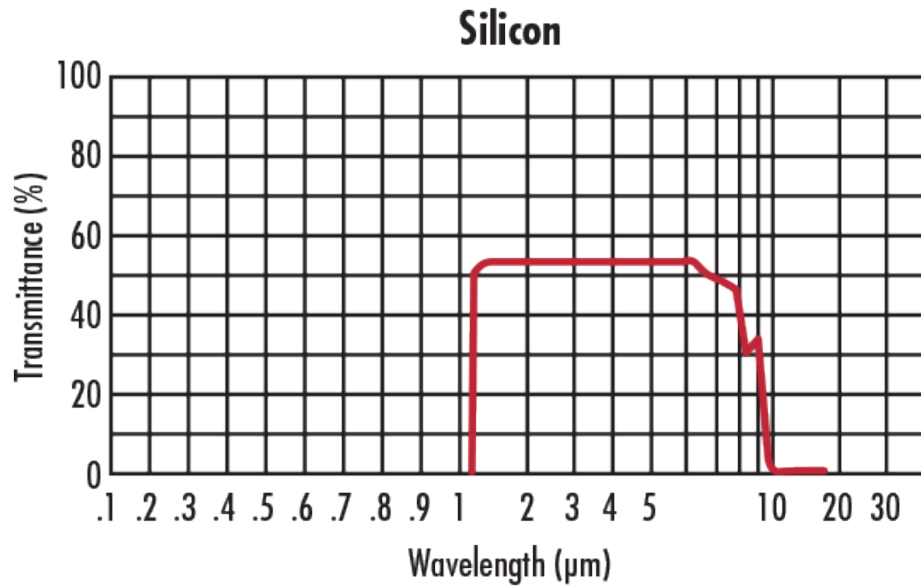


Fig. 2.1: Silicon's transmission spectrum [74].

2.1.1 Applications

At present silicon photonics finds application in many areas, which include the following: signal processing, imaging, data communication, telecommunication, switched networks, photonic interconnects, photonics for millimetre-wave/microwave/radio-frequency systems, displays, sensor fusion, radio-frequency/wireless photonics, complementary metal-oxide-semiconductor (CMOS) circuits testing, neural networks, optical storage, bionics, medical diagnosis, optical logic, spectrometer on-a-chip, laboratory-on-a-chip, photonic sensing of physical/chemical/biological variables, analogue-to-digital conversion, and electro-optical logic. On the testing of the CMOS, the defectiveness of some transistors on the IC can be determined by probing them with 1064 nm laser light or from their emission of visible light [2, 75].

2.2 Chalcogenide glasses (ChGs)

Chalcos and *gen* are Greek words. *Chalcos* means *ore* while *gen* stands for the process of *forming* something. Chalcogenides are compounds that are made from chalcogen elements of group sixteen on the periodic table.

These elements consist of; selenium (Se), sulphur (S), tellurium (Te) or polonium (Po) [76]. So far, one of the most significant innovation in chalcogenides is ChGs. Examples of stable glasses, include As_2Se_3 [22], As_2S_3 [22], $\text{Ge}_{20}\text{S}_{40}\text{Br}_{40}$ [77], and $\text{Ge}_{30}\text{As}_{10}\text{Se}_{30}\text{Te}_{30}$ [78]. These elements display very different properties from those of silica glass. The utilisation of semiconductor material in comparison to silica and fluoride glasses highly benefits from the wider IR transparent band. The chemical constituents of a chalcogenide dictate its colour which ranges from partially transparent to completely opaque. ChGs were first investigated six decades ago [79, 80]. ChGs have a red-shifted to visible or near IR band gap because their inter-atomic bonds are weak as compared to those in oxides. Red shifting of the band gap of chalcogenide glasses occurs when the visible or near IR (NIR) section of the spectrum is used. In other words, chalcogenide glasses are transparent for the mid-infrared. Covalently bonded heavy elements make up chalcogenide glasses. ChGs bonds have low vibrational energies due to their heavy atoms. This implies that in the mid-IR region, ChGs are transparent, and as a result, they are good hosts for rare-earth dopants [81, 82].

Nonlinear and waveguide optics making use of these type of glasses due to their unique optical properties can also be adopted in sensors, phase-change memories, solar cells, and photonics [83]. Transmission at IR wavelengths is typically increased when tellurium is added to glass (beyond 20 μm). Also, the addition of sulphur increases transmission at visible wavelengths of up to $\sim 11 \mu\text{m}$ and selenium up to $\sim 15 \mu\text{m}$, as demonstrated in Figure 2.2 [84].

Oxide glasses have a wide band gap as well as optical and electrical properties from those of chalcogenides [85-87]. ChGs are used to transmit and focus light. Further modifications can be done by polishing and shaping lenses and bulk optics. These are mainly fabricated as optical fibres, but in this case, they can be fabricated into thin films. As compared to conventional glasses, ChGs have a closer affinity with semi-conductors. Chalcogenides can interact with electrons and photons.

Table 2.1: Comparison of key properties between sulphide, fluoride and silica-based devices *approximated by value for glass [88]

	Silica	Fluoride	Sulphide
Composition	SiO₂	ZBLAN	Ga:La:S
Optical			
Refractive index at 0.589 μm	1.458	1.499	2.4833
Abbe number	68	76	13.7
Zero material dispersion wavelength (μm)	1.3	1.6	2.5-3
Nonlinear index (esu x10 ⁻¹³)	1	0.85	300
Approximate transmission range (μm)	0.16-2.0	0.22-4.0	0.53-5.0
Thermal			
Glass transition (°C)	1175	260	560
Melting temperature (°C)	>2200	450	842
Specific heat (cal/g-°C)	0.179	0.151	0.109*

2.2.1 Physical properties of ChGs

2.2.1.1 Thermal properties

In the science of glasses, thermal properties can help in understanding the structure of glasses and play a significant role in determining how practical the composition of ChG is for a given application. Additionally, this property covers a wide range of specification that includes devitrification stability as well as glass transition.

For amorphous materials, the glass transition is probably considered the most common and important thermal property. Glass transition is generally accepted as a relaxation phenomenon as opposed to a phase transition. Despite this, some ambiguity still clouds the nature of glass transition [89-92]. As such, there is still a considerable amount of research ongoing to improve the understanding and measurement of glass transition temperature [93]. Glass transition temperature is defined as the state of transformation in which the state of a materials changes (supercooled liquid ↔ glassy solid). During the transition, other properties of the material, including physical properties such as the hardness and volume of the material also change.

Amorphous solids normally crystallise when heated. The fabrication of fibres largely benefits from glass composition that displays a low tendency to crystallise because the formation of crystalline phases in an amorphous

matrix would likely lead to large scattering losses. In contrast, crystallisation is applied in the glass-ceramics creation and optical storage devices. Atomic mobility in a glassy solid is improved when an increase in temperature causes a decrease in viscosity. Meanwhile, chemical bonds that exist between atoms may start rearranging themselves and then result in glass crystallisation at a characteristic crystallisation temperature (T_c). Crystallisation is similar to glass transition in that it is a kind of structural relaxation but occurs exothermically.

2.2.1.2 Structural properties

Particles in solids have strong interactions that give solids their condensed state of matter. When particles are ordered, the solid is said to be crystalline, but when disordered, it is said to be non-crystalline [94]. Non-crystalline solids also lack atomic periodicity and are therefore also known as vitreous, amorphous or glassy solids. A crystalline material is different from amorphous materials in that they have a long-range order (LRO) while the latter has a short-range order (SRO) [95]. A continuous random network may be taken to be an ideal non-crystalline network for covalent solids [96, 97]. The structure of ChGs has isotropic three dimensions and cannot be described as a continuous random network; its structure shares similarity with that of amorphous silicon, As_2Se_3 , As_2S_3 , $GeSe_2$, and GeS_2 , which are local layers while pure S and Se are a chain-like [98, 99]. The characterisation of chalcogenide is split into two; short-range order (SRO) and intermediate-range order (IRO) [98]. Crystals and glasses having the same composition may have different SRO [100-102]. For chalcogenide glass, its classification may be done by making an assumption that puts it between an organic polymer (has a 1D network) and oxide glass (has 3D networks). This also implies that ChGs have an atomic bond rigidity between oxide glasses and organic polymers [95].

2.2.1.3 Optical properties (absorption coefficient (α))

The optical properties of ChG have attracted much interest from researchers due to their transparency in both the NIR and MIR range. When

a beam of light passes through a medium, there is partly a transmission, reflection as well as absorption. In ChG, the IR transmission is limited by impurity. The absorption bands can be moved from ChG to allow the extension of transmission for sulphide glasses whose transmission is about 0.6µm and 11.5µm. For the telluride glasses, the transmission is between 2µm and 20µm, while for selenide glasses, the transmission is between 1µm and 15µm [103]. Figure 2.2 demonstrates the interaction of light with a film deposited substrate. The material and the wavelength of the incident light determine the absorption coefficient.

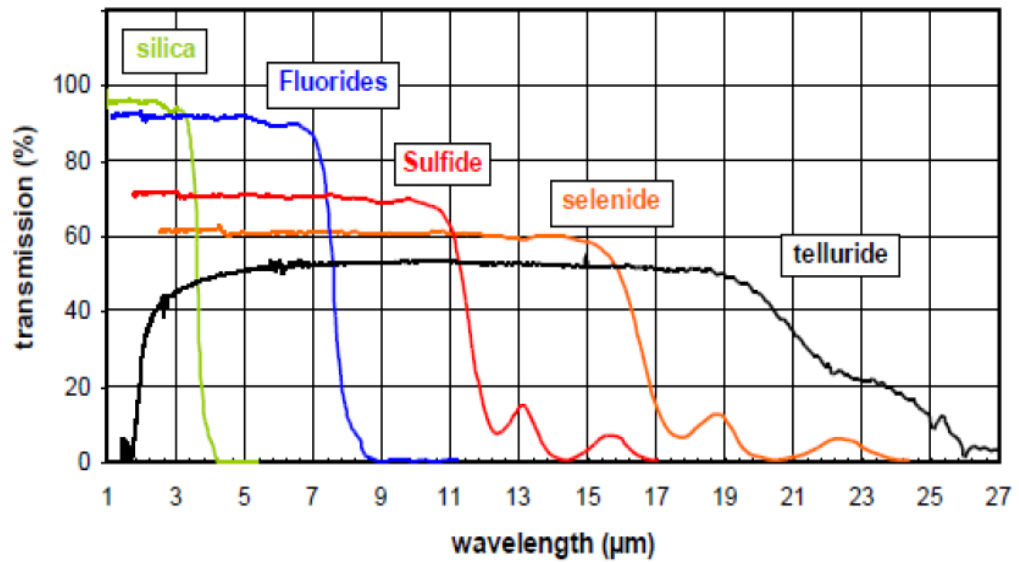


Fig. 2.2: Typical transmittance spectra of silica, fluorides, sulphide, selenide, and telluride bulk glasses [103].

The optical absorption coefficient of chalcogenide glass or its thin film can be determined from transmittance measurements. The transmission spectrum of the bulk sample or thin film is employed to calculate the absorption coefficient by using the following equation [104, 105]:

$$\alpha = \frac{1}{d} \ln \left(\frac{1}{T} \right) \quad (2.1)$$

where;

d – bulk sample or thin film thickness

T - transmission

Using the absorption coefficient obtained from the equation (2.1), the optical band gap of a bulk or thin film material can be calculated from the Tauc model or law, as shown below [104-106]:

$$\alpha h\nu = B(h\nu - E_g^{opt})^n \quad (2.2)$$

where;

B - proportional constant

$h\nu$ - incident photon energy

E_g^{opt} - optical band gap

n - take values 1/2, 2, 3/2, or 3 for direct allowed, indirect allowed, direct forbidden, and indirect forbidden transitions depending on the electronic transitions responsible for the absorption

Based on Tauc law, a plot of $(\alpha h\nu)^{1/n}$ as a function $h\nu$ can be used to obtain the optical band gap. Typically, the optical band gap for these ChGs glasses ranges from 0.7 eV to 3 eV [107].

2.2.1 Applications of ChGs

Recognition has also been given to chalcogenide glasses as one of the materials that hold the most significant promise for information transfer [108] and infrared optical elements [109]. Additionally, these materials have recently been employed in the making of switching and memory devices [110], fabrication of inexpensive solar cells [111], in sin xerography [112] as well as in reversible phase change optical records [113]. Due to the usefulness of chalcogenide glasses, it is essential that their electronic properties are well understood.

For over 50 years, optical systems in the MIR range have been manufactured using ChGs. Recently, ChGs are used in making a commercial range of lenses and bulk optical components. The exposure of ChGs to electromagnetic or optical irradiation source can lead to change in their structure and physical properties. This is known as photo-induced effects and can be either be reversed or not [114]. For instance, in xerography, amorphous selenium thin films or arsenic triselenide (As_2Se_3)

act as a photoreceptor based on their photoconductivity [115]. The photo-dissolution effect demonstrated by chalcogenides is also highly beneficial for high-resolution photoresists as well as optical storage [116].

Recently, chalcogenides have been used for the development of infrared optical fibres and waveguides. Regarding optical fibre applications, two main categories exist, namely active and passive device. The active devices are often employed in the mid-infrared wavelength region for active optical devices (e.g. IR fibre-optic amplifiers operating in the 2–10 μm range, and a wide range of spectroscopy (e.g. diffuse reflectance and absorption) and sensing (e.g. fibre-optic chemical sensor systems) of applications. On the other hand, the passive applications of ChGs in fibres are used as a conduit for passing of light from one location to others without affecting the optical properties of the materials. This makes ChGs in fibre suitable candidates for chemical and biochemical sensing (e.g. monitoring of pollution), biomolecules identification, and chemical detection [117]. The passive technique can also be applied in the delivery of laser power for surgeries with a high level of precision for ablation or tissue cutting.

ChGs are oxygen-free inorganic glasses, and the majority of them are transparent in the infrared (IR). However, a majority of chalcogenide glasses are As-based alloys, which include As–Se–S, As–Si–Te, and As–Se–Te glasses. The As-based alloys are highly toxic in nature, henceforth, preparation of bulk glass and thin film required much safety measure in place. As a result, lots of attention have been given to ChGs glasses that are free from toxic arsenic with good IR transmittance. Therefore, this thesis comprises of investigations into the fabrication of ChGs glass thin films such as gallium lanthanum sulphide (Ga-La-S), Er³⁺-doped gallium lanthanum sulphide (Ga-La-S), germanium selenide (GeSe₄), and Ge₂₈Sb₁₂Se₆₀ and the optimisation of the deposition process via fs-PLD.

2.2.3 Review of types ChGs used in this thesis

2.2.3.1 Gallium lanthanum sulphide (Ga-La-S) glass

The simplest glass forms such as arsenic selenides (As_2Se_3) [118] and arsenic sulphides As_2S_3 [119-122] had been the basis of a majority of work on femtosecond laser deposition (fs-PLD) of chalcogenides. In terms of the order of magnitude, arsenic sulphide (As_2S_3) glasses have the lowest nonlinearity properties among the ChGs. As mentioned earlier, in the event of the degradation or burning of the fibres, arsenic is released into the environment, which is very toxic. Moreover, it is also difficult to design an active device with As_2S_3 because of the challenge involved in doping arsenic-based fibres with rare-earth ions [33]. Nevertheless, a non-toxic and highly stable ChG can be synthesised by replacing arsenic with gallium to produce gallium lanthanum sulphide (Ga-La-S) [34-36, 43]. Very recently, a great deal of consideration has been given to Ga-La-S glass because of its high transparency and nonlinearity properties in the NIR and MIR regions [37-42, 123-126].

Fabrication of a bulk Ga-La-S glass as an alternative to ChGs has been reported in various studies. Early studies include that of Loireau-Lozac'h, Guittard, and Flahut in 1974, which showed that lanthanum sulphide and gallium sulphide could be used in forming glasses. These group of glasses are usually labelled as the Ga-La-S glasses. Usually, these class of glasses have a composition ratios 7:3 of Ga_2S_3 to La_2S_3 . The structure of these glasses can easily be modified to adjusted optical and physical features. For example, the thermal stability of Ga-La-S can be enhanced by adding halides such as La_2F_6 . This can increase the visible transmission as well as also reducing the level of impurities in the glass. Ga-La-S glass also has other superior qualities including; a wider transmission window ranging from 0.5 μm to 10 μm (visible to IR wavelength), low maximum phonon energy (450 cm^{-1}) and a higher optical refractive index ($n = \sim 2.2767$). Ga-La-S has thermal stability up to 550°C , which is much higher compared to 47°C for $\text{As}_5\text{Se}_{95}$ and 153°C for As_2S_3 . Being a new radical chalcogenide, Ga-La-S

offers innovative option instead of the toxic-arsenic glasses in addition to its wide commercial availability [36, 127-131].

Given the numerous advantages that Ga-La-S offers, it can be utilised to develop or design platforms for optical devices, ranging from imaging and detection environmental gases, compact optical waveguide. For instance, waveguide structures related to Ga-La-S ChGs had already been demonstrated via proton implantation and femtosecond laser inscription [127-130].

For deposition of Ga-La-S thin film, various techniques can be utilised. These include spin coating [132] or radio-frequency (RF) sputtering [133, 134]. Much promise is demonstrated by PLD, and this is attributed to the flexibility that allows it to be used with a wide range of deposition parameters that facilitates the synthesis of a large variety of thin films of complex chemical composition. There are a few studies on PLD deposition of amorphous thin films of pure Ga-La-S [128, 129, 135, 136] or related gallium lanthanum oxysulphide (Ga-La-SO) that makes use of femtosecond (Ti: sapphire 800 nm [137]) lasers, nanosecond UV and visible (KrF 248 nm [128, 135, 136] or Nd:YAG 266 nm [137], 532 nm [129]). These works aimed at building the understanding of how the properties of chalcogenide thin films can be modified by adjusting the deposition conditions that, include the duration of the pulse, pressure of the buffer gas, laser fluence, wavelength, and the distance of the target-substrate (d_{st}).

Previously, Ga-La-S thin films fabrication, as well as the optical properties of the prepared layers, were investigated by using PLD with 248 nm KrF laser line [128, 135, 136]. The structure of thin amorphous Ga-La-S films was also studied using Raman spectroscopy by N̄emec et al. [138]. Thin films were prepared using the PLD method at 532 nm laser line. It was found that the structure of the bulk glass, as well as the corresponding thin films, were created by GaS₄ tetrahedra and LaS₈ structural units [138].

In addition to the previous Ga-La-S advantages, rare-earth ion can easily be doped with Ga-La-S glass [131], which can be used to develop active

devices. Thus, Ga-La-S glasses have a high level of rare-earth solubility. The combination of these properties with the low phonon energy and high transmission in the infrared make rare-earth-doped Ga-La-S glass ideal candidate for infrared sources and lasers. Laser research is currently being pursued by researchers from various institutions and national labs in the 3 to 5 μm wavelength range [139, 140].

This glass provides new possibilities as well as increasing the pump efficiencies when doped with rare-earth with this ability attributed to their low phonon energy and high refractive index. This will be discussed in detailed in a following the ChGs material.

2.2.3.2 Erbium-doped gallium lanthanum sulphide (Er^{3+} -doped Ga-La-S) glass

The rare earth elements (REE) are also referred to as rare earth metals (REMs). The REEs are mainly divided into two groups, which are lanthanides and actinides. The lanthanides group begin from cerium (Ce) to lutetium (Lu) with atomic numbers range from $Z=58$ to $Z=71$ on the periodic table. Whereas the actinides have atomic numbers between 89 (thorium) and 102 (lawrencium). These elements are usually impurity embedded in the host material in small amount and act as the optically active centre in the host for photoluminescence emission measurements when excited with excitation source. The chemical and physical properties of the REE ions are very similar to each other because they have got analogous outer most electronic 4f shells. The coordination environment of the 4f orbitals is shielded by the filled 5s and 5p orbitals. The 4f energy levels have the following features; small induced splitting, insensitivity to the host, possession of little or no vibronic structure, weakly mixed with higher energy states, and have a weak non-radiative relaxation of excited states [141]. The REEs have been utilised to develop many devices such as REMs or their alloys, digital versatile disc (DVD), rechargeable batteries, computer memory, mobile phones, fluorescent lighting and catalytic converters.

As mentioned in the “2.2 Chalcogenide glasses” section, the composition of ChGs brings together elements, such as Se, S, and Te from the group VI of the periodic table, which are then combined with additive elements, such as arsenic (As), gallium (Ga), germanium (Ge), and antimony (Sb) [116, 142]. In the NIR and MIR wavelength region, from 1 μm to 10 μm , these glasses have many applications for passive optical devices, where the transparency window is high making [26, 88, 143, 144]. They can also be used in long-wavelength range for light-emitting and amplification devices when doped with REE ions such as erbium (Er), thulium (Tm), holmium (Ho), ytterbium (Yb), neodymium (Nd), Dysprosium (Dy), and praseodymium (Pr) [26, 116, 144]. Additionally, ChGs glasses doped with these REE ions can be used to develop active optical devices as already mentioned above.

Doping of REE ions with amorphous ChGs could also be employed in various applications, including sensing and detection [145-147], optical fibre amplifiers [148], laser devices [149, 150], optical waveguides [151], and trichromatic (RGB) display devices [152]. Various studies have also shown that high-speed telecommunication optical signal processing can benefit significantly from chalcogenide-based optical waveguides [11, 153-155]. However, chalcogenide optical waveguides have relatively huge propagation losses [156]. Thus, it is essential to develop a new material that would be capable of minimising the losses in chalcogenide to enhance the efficiency of all-optical processing. One way in which these optical losses can be decreasing is through the use of REE ions doped ChG by optical signal amplifier [156]. There have been some demonstrations of the net optical gain in waveguide amplifier by using REE ions-doped ChGs [133, 157-159]. For instance, Nd-doped Ga-La-S glass has shown to support laser action at 1080 nm in bulk [159] and fibre form [157]. The Er^{3+} ions doped host glasses are important for designing optical waveguide amplifiers and lasers as tools have revolutionised the optical telecommunication network. Besides, the net waveguide gain of optical amplifier devices can be achieved by utilising ${}^4\text{I}_{13/2} \rightarrow {}^4\text{I}_{15/2}$ (1530 nm) and ${}^4\text{I}_{11/2} \rightarrow {}^4\text{I}_{13/2}$ (2800 nm) transitions of the trivalent states of Er^{3+} ions as shown in Figure 2.3. For example, Frantz et al. [133] deposited Er-doped Ga–La–S glass thin film on

a silica substrate by RF magnetron sputtering (under argon atmosphere and at the substrate temperature of 100°C) and then demonstrated an optical gain of 2.8 dB/cm at 1.5 μm wavelength.

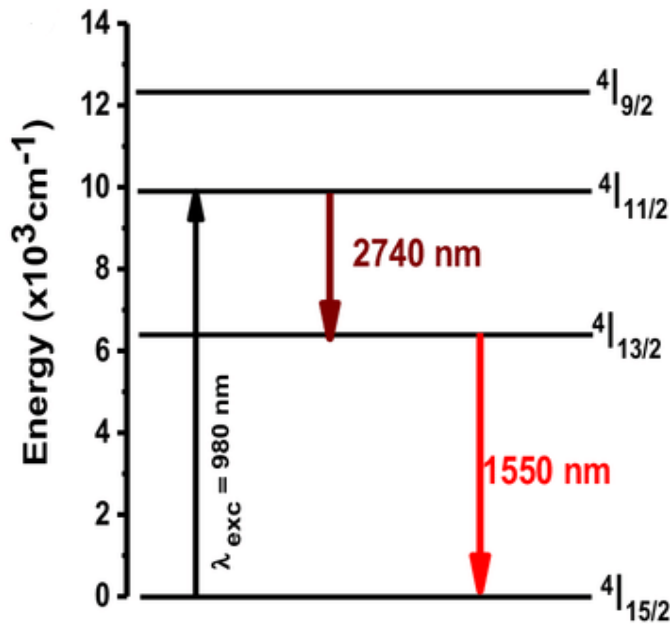


Fig. 2.3: Energy transfer sketch of Er³⁺ when pumped at 980 nm.

In this work, Er³⁺ ion was considered as an active material for the host Ga–La–S glass. The main aim of this work was to improve the understanding of how the surface morphology and optical properties of Er-doped ChG thin films change through fs-PLD ablation techniques by varying the deposition parameters such as; substrate temperature and buffer gas pressure.

2.2.3.3 Germanium selenide (GeSe₄) glass

Semiconductors made from germanium and selenide (Ge-Se) are members of ChGs and can be found in Group IV and VI elements in the periodic table. Recently, crystalline glasses and amorphous Ge-Se have gained much importance in engineering and material science due to their excellent applications in IR optics [19, 160]. This category of ChG is based on S, Se, and Te. This type of glass offers an attractive solution due to their high optical transparency density up to ~14 μm in the IR region. Some of the properties of these glasses are; high photosensitivity, good chemical durability, low phonon energy, and they are relative easiness to fabricate.

Because of these properties, these types of glasses are used in frequency converters, ultrafast optical switches, integrated optics, infrared transmitting optical fibres, optical amplifiers, and optical recording device [14, 31, 32]. The use of these chalcogenide semiconducting alloys is not only due to their attractive electrical and thermal properties, but also due to their optical properties. A majority of semiconducting glasses, particularly selenium, possess reversible phase transformation property [161]. It is used in various devices, like photocells, switching and memory, rectifiers, and xerography. However, it has several disadvantages, such as low photosensitivity and a short lifetime. Selenium has a high glass-forming ability and therefore represents a suitable host matrix for ChG investigation in both bulk and thin-film forms [162-165]. To overcome the problems facing Se, alloying using impurity atoms, such as bismuth (Bi), tellurium (Te), germanium (Ge), gallium (Ga), and arsenic (As) is recommended to improve crystallisation temperature, enhance photosensitivity, and reduce the ageing effects [166-168]. However, classical chalcogenides have arsenic, which is toxic in their elemental form (as mentioned in the sections above). Therefore, for some applications, arsenic-based nanocrystalline chalcogenides are not appropriate.

Among the various types of ChGs, germanium based chalcogenides have been found to be suitable for both passive and active IR applications such as sensors, waveguides, optical fibres [44] or RE-doped fibre lasers as well as amplifiers [45]. With these properties, germanium based ChGs can be good alternatives to arsenic-based selenium glasses. Some of the desirable properties of germanium based ChGs include higher sensitivity, higher conductivity, environmental sustainability, sizeable optical transmission range, greater hardness, higher crystallisation temperature, higher stability, and glass-forming ability [52-55, 169]. The optical transmission range extends in the MIR, which is applied in switching and memory devices [20, 21, 52, 53, 160, 170]. Because of these excellent characteristics, $\text{Ge}_x\text{Se}_{1-x}$ glasses have received much attention from researchers and scholars and have investigated for various properties, such as physical behaviours,

glass-forming region, structure, the kinetics of glass transition, and thermoelectric properties among others [47-51, 171-175].

Several fabrication methods have been used to deposit Ge-Se thin films these methods, include thermal vacuum evaporation (TVE), pulsed laser deposition (PLD), and chemical vapour deposition (CVD), among others [176-182].

It is important to establish an understanding of the properties of these interesting materials in both bulk and thin film form to facilitate the establishment of a relationship between electronic properties and the possible applications of these materials. Ge-Se materials have an ovonic memory switching behaviour that is depended on the phase transformations from amorphous to crystalline forms, but they can also retain an amorphous form without undergoing a phase transition. For example, a study by Sulitanu et al. [19] examined amorphous thin film which was made using vacuum thermal evaporation (VTE) process to evaluate their switching potential. They found that switching could be done using Ge-Se thin films and therefore concluded that they hold a promise for being used in optoelectronic devices [19]. Amorphous Ge-Se thin films can also be applied in the production of filters, antireflection coatings, and other optical devices with the ability to transmit in the IR region [21, 183, 184].

Additionally, upon exposure to photo-induction, majority of chalcogenide semiconductor thin films demonstrated photosensitivity and tend to change their phase from amorphous to crystalline. Photo induction of bulk glass would cause it to change its physical properties, such as the refractive index and the band gap energy. Studies have reported different types of chalcogenides that include amorphous selenium and stoichiometric IV-VI mixtures GeSe_2 , GeS_2 , and SiSe_2 [185, 186].

Raman spectroscopy has been utilised by many researchers in studying the photo-induced crystallisation in germanium based chalcogenide thin films [49, 176-178, 180, 186-192]. Leading bands for the GeSe_2 films were found at 200 and 217 cm^{-1} (GeSe_4 bonds), with Ge-Ge bonds observed at the low-

frequency shoulder of about $\sim 180 \text{ cm}^{-1}$ while weaker bands were obtained at ~ 270 ~ 310 and $\sim 398 \text{ cm}^{-1}$ for the Se-Se bonds. The structure of GeSe_2 , GeSe_4 , and GeSe_6 films that were ns-PLD prepared were investigated by Pan et al. [176]. They found that the thickness of prepared films at room temperature increased with increasing the ablation time. Also, they concluded their study by noting that the glassy matrix of $\text{GeSe}_{4/2}$ tetrahedra is corner-sharing (CS). GeSe_2 film has more edge-shared (ES) $\text{Ge}_2\text{Se}_{8/2}$ bi-tetrahedrons with Ge-Ge bonds. In [187] annealing the films below their glass transition temperature were noted to decrease their relative intensities significantly. Additionally, the amplitude at Raman bands near 175 cm^{-1} was observed to decrease after thermal annealing was done. Also, after annealing, Frumar et al. [188] found that the amplitudes of the Raman bands that correspond to vibrations of Se-Se bonds and $\text{Ge}_2(\text{Se}_{1/2})_6$ units reduced and attributed this to film homogenisation as well as the creation of Ge-Se bonds of $\text{GeSe}_{4/2}$ tetrahedra.

Amorphous Ge-Se thin films that were prepared using different laser energy densities were studied by Neřmec et al. [177] using Raman spectra and found that the Raman spectra of the bulk and ns-PLD thin films were very similar. From the same shapes of the Raman spectra, Neřmec et al. [177] concluded that PLD structure is not dependent on the laser beam energy density; in all the cases, surface and plume temperature are high with small differences in films.

The extensive use of amorphous Ge-Se thin films in optical devices has seen them investigated by several researchers [176-179, 181, 186-190]. The preparation of GeSe_2 and GeSe_4 films using PLD on the glass substrate was done by Pan et al. [176]. After annealing, they found that the thickness of as-deposited films reduced. This reduction in thickness is attributed to the elimination of droplet's porous structure that contains some free spaces in the as-deposited films. GeSe and GeSe_2 grown using thermal evaporation in a vacuum on the substrate of silicon as well as silica at room temperature were investigated by Almeida et al. [193] and Santos et al. [191]. The surface morphology of the films was observed to have considerable

topographic contrast that resembled a granular structure but with grain sizes of ~30 - 50 nm.

In amorphous, crystalline, and glassy materials, the optical band gap (E_g) is considered to be one of the critical physical parameters. This is because the optical band gap relates to other variables of the materials, such as preparation conditions, chemical composition, disorder degree, and the thickness of the sample. To better understand the mechanism of disorder and the formation of defect of chalcogenide films, a study on how the optical gap is affected by thickness is needed. In several studies, the optical band gap and the thickness of GeSe_2 were found to be correlated. For as-deposited films, [186] found that GeSe_2 optical band gap increased from 1.482 eV to 2.475 eV ($d = 511$ to 1022 nm) and for annealed films it increased from 1.725 eV to 2.668 eV ($d = 511$ to 1022 nm). The increase in the optical gap occurs with the assumption that defect is minimised with the increase in thickness. This assumption is supported by researchers given the changes in both the Tauc and Urbach edges. A study by [194] reported the band gap for GeSe as falling between 1.1–1.2 eV. The density of Se–Se homopolar bonds was observed to decrease when PLD prepared GeSe_2 and GeSe_4 films were annealed, and this resulted in an increase in the optical band gap [176].

Additionally, amorphous $\text{Ge}_{20}\text{Se}_{80}$ film was also thermally evaporated by Thakur [195] to examine its optical band gap. Furthermore, several studies have also reported the impact that concentration has on the optical properties of GeSe , GeSe_2 , and GeSe_4 films. The optical band gap of the as-deposited films was observed to increase from 1.92 to 1.94 eV, and this was related to the reduction of the density of Se-Se homopolar bonds due to the increase in the content of germanium as demonstrated by Raman spectral evolution.

2.2.3.4 Germanium antimony selenide ($\text{Ge}_{20}\text{Sb}_{15}\text{Se}_{65}$) glass

The Ge-Se system has also been included in this work. With the addition of a third element to the Ge-Se, the compositional and configurational disorder

will be created. Additionally, the comparison of four-fold coordinated Ge atoms with As based amorphous chalcogenides has shown that Ge atoms in a glass network possess higher glass transition temperature (T_g), increased rigidity, and improved mechanical properties, such as strength, stiffness, and hardness [196]. Another system of glasses that is increasingly gaining the attention of researchers is the covalent glasses of ternary Ge-As-Se and Ge-Sb-Se systems. This is because these glasses have some attractive properties, such as good physical and mechanical properties as well as sizeable glass-forming domain as compared to chalcogenide compounds with classical binary properties. Despite these properties of Ge-As-Se system compared to Ge-Sb-Se system, a higher polarisability increasing (non)linear refractive index and reduced photosensitivity [197] is obtained through the introduction of antimony (Sb) in the Ge-Se glass network, and this provides desirable options for applications in non-linear optics [198-200]. Additionally, Ge-Sb-Se glasses have an enhanced shaping ability that facilitates thin films or fibres to be fabricated, and this is highly important where the development of sensors is concerned. This is the reason behind the attention given to thin films of ternary Ge-Sb-Se system.

The Ge-Se system can be strengthened by the addition of Sb, which leads to the creation of cross-linkages between the structural units of Ge-Se and Sb-Se as well as the creation of stable Sb-Se bonds [201]. In the last decade, the properties of Ge-Sb-Se glasses including optical, electronic, and microstructure have been studied widely, and this is attributed to the structural arrangement of the physical properties of these glasses related to a strong influence of the Ge/Sb ratio [191, 197, 202-209].

It has already been shown that Ge-Sb-Se thin films can be prepared through various deposition methods like thermal evaporation [207], RF sputtering [210-213], and PLD [212, 214]. The PLD method appears to be favourable among these in the fabrication of ChGs films as a result of its simplicity, ease of process control, and the material transfer from the target to the thin film is often stoichiometric [188].

In addition, the films of Ge–Sb–Se having different compositions were prepared by Chen et al. [207] by employing RF sputtering on glass slide substrate at a temperature of 25°C and a normal working pressure. The impact of different Ge-Sb-Se films compositions on the physical and optical properties was studied. Energy dispersive X-ray spectroscopy (EDS) measurements demonstrated homogenous film chemical composition with properties that were close to those of the targets. The amorphous structure of the as-deposited Ge–Sb–Se films was confirmed by X-ray diffraction (XRD) patterns. Additionally, band gap values were also calculated establishing the presence of homopolar metal bonds (Ge–Ge and Sb–Sb) that was associated with several defect gap states reduced.

Using conventional RF (13.56 MHz) magnetron co-sputtering and Ge₂₈Sb₁₂Se₆₀ as a target, Halenkovi et al. [215] fabricated amorphous Ge–Sb–Se thin films in Argon (Ar) plasma onto two different substrates- single crystalline silicon (100) and crown glass (Schott BK7). The authors studied how optical properties were affected by the composition of the film. It was found that the sputtered films had a chemical composition close to that of targets. Additionally, the surface image showed the excellent quality of co-sputtered Ge-Sb-Se films. Nevertheless, the films tended to have a grainier surface. Also, they determined the optical band gap energy for the sputter films and found it to be in the value of 1.74 ±0.02 eV.

In [212] PLD technique and RF magnetron sputtering were considered in conducting the deposition of Ge₂₅Sb₁₀Se₆₅ and Ge₂₅Sb₁₀S₆₅ amorphous chalcogenide thin films, using silicon, SiO₂/Si substrates or a chemically cleansed microscope glass at room temperature. In the two compositions, high-quality thin films (considering surface roughness, devoid of any pores or defects) were found. Both surface cracks and cross-section's column-like structure were not observed regardless of the technique considered. Raman spectroscopy has been studied in investigating the structure and composition of thin films. The content decrement in chalcogen component was highly apparent for PLD. The key trends observed include antimony excess for PLD and some germanium over stoichiometry for sputtering.

Moreover, using ns-PLD ($\lambda=248$ nm, output pulse energy= 300 ± 3 μJ , pulses duration=30 ns, repetition rate= 20 Hz, and laser fluency = 2.6 $\text{J}\cdot\text{cm}^{-2}$) for 2h in the vacuum chamber at a temperature of 30K, below the glass transition temperature of Ge-Sb-Se thin films, were obtained with varying compositions on a silica/microscope glass substrate [214]. They studied the photosensitivity of ns-PLD Ge-Sb-Se films. They discovered that the irradiation at energy near to the deposited Ge-Sb-Se thin films band gap causes photobleaching (PB) effect. Also, they mentioned that this phenomenon appears to reduce when antimony content increase. The morphology study observations showed homogenous thin layers of as-deposited $(\text{GeSe}_2)_{100-x}(\text{Sb}_2\text{Se}_3)_x$. Additionally, a smooth surface as well the absence of cracks or breaks indicating good planarity were observed. A few samples were observed to have sub-micrometres size droplets. In terms of the chemical composition, thin films chemical composition showed a slight loss of Se in comparison with the real targets; with a loss of below 4%, the study associated this with higher volatility in comparison to Sb and/or Ge.

The Raman spectra of Ge-Sb-Se films and Ge-Sb-Se target have been reported in several studies. Two regions with several bands have been presented, and this includes the $50 - 120$ cm^{-1} and $150 - 250$ cm^{-1} area are considered a rich set of bands that identified Se-Se and Ge-Ge homopolar bonds and Ge-Se and Sb-Se chemical bonds are heteropolar. In Sb-Se pyramidal units, the small peaks around 64, 75, 95, and 110 cm^{-1} are associated with Sb atom vibrations [202, 205]. Decreasing the concentration of Sb in the films decreases the intensity. The vibrational modes of Sb-Se and Ge-Se heteropolar bonds are closely positioned at the 190 cm^{-1} and 200 cm^{-1} , respectively [204, 208]. The two peaks overlap to form a broad peak at around 205 cm^{-1} with the position of the shoulder located at 170 cm^{-1} . At Ge content higher than 25 %, this shoulder turns into a peak. The formation of a peak at about 170 cm^{-1} is an indication of Ge-Ge bonds formed by the cross-linking of Ge atoms in the $\text{Ge}_2\text{Se}_{6/2}$ chains ($\text{Se}_3\text{Ge}-\text{GeSe}_3$ units) [204, 207, 210]. Addition of Ge causes other low-intensity bands that are located in the region of $250-350$ cm^{-1} to appear and this is

due to the vibration of the Se-Se and Ge-Ge homopolar bonds as well as Ge-Sb heteropolar bonds in modified GeSe₄ structural units [202, 207, 208].

2.3 Chalcogenide thin film fabrication methods

A thin film refers to a layer of material whose thickness ranges from fractions of a nanometre to about some of the micrometres. The synthesis of films is highly controlled and is referred to as deposition. Thin film deposition technique is employed in various industries, such as packaging, optics, and electronics, among others. The chemical and physical properties of ChG thin films, which strongly depends on the deposition method, determine the structure of thin films, their surface quality as well as the impurity content. These days many methods are used to prepare ChG thin films.

The deposition is categorised into three; chemical vapour deposition (CVD), chemical reaction, and physical vapour deposition (PVD). CVD involves the vaporisation of chemical compounds followed by the decomposition or the response of the vapour with gases or other vapours to generate non-volatile products [216]. Sol-gel thin film deposition is considered a chemical reaction. On the other hand, PVD entails thermal evaporation that makes use of fabrication methods, such as pulsed laser deposition (PLD), molecular beam epitaxy (MBE), and sputtering.

The deposition method mostly relies on the composition of glass to be deposited. While several ways could be used, the application is the main influencing factor and includes the uniformity influence and the rate of deposition of the film thickness. The device may also influence the choice of method. For example, the rapid deposition and conformal coating of thick and precise thin film to a few nanometres are required for phase change memory devices [217-220]. In contrast, a different deposition method would be needed for integrated optical circuits which are usually a few μm thick and therefore require high levels of optical quality to ensure waveguide propagation loss is minimised [220]. This section will present a discussion of the techniques for chalcogenide glasses thin film preparation.

2.3.1 Chemical vapour deposition technique (CVD)

CVD method is mainly used in the preparation of thin films of ChGs. It makes use of thermal energy to decompose vapours. It can also make use of RF field for heating the substrate on which vapour decomposition occurs [221-224]. CVD allows high coating hardness as well as uniformity of coating which is required in the production of chalcogenide thin film with high throwing power. However, CVD is disadvantaging in that it uses high-temperatures that makes it challenging to attain sharp edge coating. It also coats only a specific range of materials.

2.3.2 Spin coating technique

Spin coating involves two stages to fabricate amorphous thin films. The first stage entails the deposition of the fluid on the substrate. In the second step, the coated substrate is withdrawn. The viscosity of the glass can be altered by modifying composition [225]. Spin coating is advantageous in that it is easier to control due to the absence of coupled process variables. Also, as the deposited film continues to thin, its uniformity increases. However, spin coating is limited in that it lacks material efficiency and with the increase in the size of the substrate, its photoresist cost increases.

2.3.3 Thermal evaporation technique (TVD)

TVD is considered the easiest method in ChG preparation. Both the substrate and the material to be deposited are vacuumed in direct line of sight and only separated by a few centimetres (cms). Heating the material to be deposited is then done until it evaporates with the vapour of this material condensing as a thin film on the substrate [226]. TVD has the following advantages in that it has excellent process control and uses a low deposition temperature. The method also allows alloying and compound coating.

2.3.4 Sputter deposition

Sputtering is a physical vapour deposition technique that works by eroding the target using ionised gas species, particularly Ar⁺. An electric field is used to accelerate the ions onto the material to be deposited, as shown in Fig 2.4. To control the growth of oxides and nitrides reactive gases, such as nitrogen and oxygen, are introduced into a vacuum chamber. This makes the sputtered material to grow on the surface of the substrate through chemical and physical deposition means when a reactive gas is used. Evaporation in a sputtering deposition is performed top-down, allowing the growth of thin films of a variety of materials that are not limited by their melting point. For metals, direct current (DC) sputtering is employed while for insulators radio frequency (RF) sputtering is applied to avoid target charging [227].

As Freund [228] mentioned one significant advantage of the sputtering process is the control it has in stoichiometric preservation, and it has better film thickness regularity compared to evaporation processes, and the fundamental deposition of crystalline and amorphous materials is flexible. Additionally, for polycrystalline films, sputter deposition generates thin film grain structures, which have typically numerous crystallographic orientations that lack preferred texture. Nevertheless, sputtered atoms' kinetic energy within sputter deposition surpasses that for atoms within the evaporative deposition due to the presence of argon gas within the sputtering system. In view of this, the deposition surface within the sputtering process shows extensive defect nucleation and damage as opposed to thermal evaporation. Besides, thermal-deposited films are lesser than impurity atom concentrations of sputtered-deposited films. Moreover, the sputtered films' grain size is usually smaller compared to that for evaporation-deposited films.

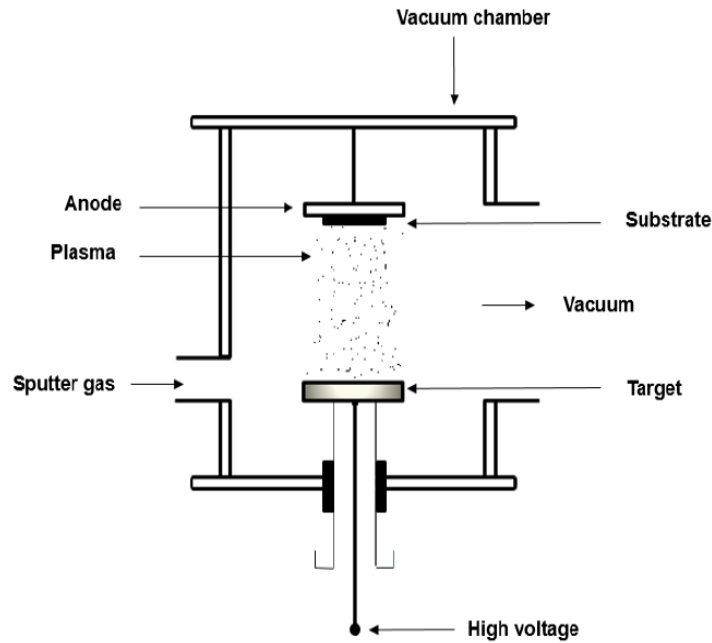


Fig. 2.4: Schematic diagram of ds diode sputtering system (adapted from [229]).

2.3.5 Pulsed laser deposition (PLD)

Pulsed-laser deposition (PLD) refers to a relatively new technique of PVD to the thin film-coating system [230]. In the process of thin film deposition, laser beams are used for ablating the material for depositing thin films within vacuum chambers. Various forms of laser sources are being utilised for target ablation. XeCl (308 nm), KrF (248 nm), and Nd-YAG laser are the familiar sources [231].

PLD involves use of laser sources (from KrF (excimer) to ultraviolet to Titanium-Sapphire (Ti: Sapphire) to Nd-YAG) at different pulse rates (from near-continuous till femtosecond) as well as pulse energies for ablating materials from targets onto substrates. Just as other PVD methods, it is mainly line-of-sight and might or might not require a controlled environment or a vacuum based on the reactive nature of the species earmarked for deposition [232].

This method shares many similarities with the sputtering method. It is the most promising method with the ability to produce uniform thin films as well as multilayer structures without altering their stoichiometric composition.

PLD is advantageous due to its flexibility, and therefore it is used in a wide range of parameters and thus employed in the synthesis of many thin films with complex chemical composition. Additionally, it can provide higher doping concentrations without significant fluorescence and lifetime quenching. Picosecond (ps) to femtosecond (fs) regimes (short and ultrashort pulse durations) PLD has been used recently for the fabrication of thin films and then processing of materials because the strengths that they have over traditional PLD nanosecond (ns) and microsecond (μ s) pulsed lasers (long pulse durations) [233, 234]. PLD at picosecond (ps) to femtosecond (fs) pulse duration levels is mainly used for short and ultrashort pulse durations. For example, ablation mechanism of short and ultrashort pulse PLD have ablation rate of about 30 to 40 times higher as compared to those of ns and ms PLDs, and therefore they are different from long pulse lasers [235].

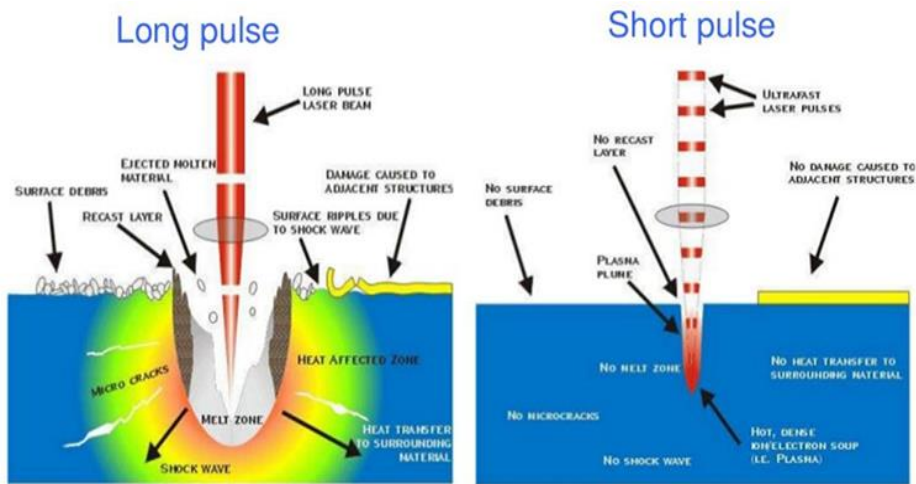


Fig. 2.4: The interaction of long-pulse and short-pulse laser with target material [236].

On the other hand, the ns and μ s pulse lasers have the following disadvantages. Their heating and melting processes can cause damage. When using in ablation and thermal decomposition processes, they generate a considerable high-temperature gradient in bulk materials with a laser-induced shock [237]. Excimer and YAG lasers are examples of ns and ms pulse lasers. The heating problem affects the quality of the thin film, particularly in complex materials as the size of the particle that is generated

broadens and becomes clustered. These disadvantages can be overcome by the use of ps and fs PLD with short and ultrashort ablation that causes very minimal a heat-affected zone and does not damage the targeted surface [234], as can see in Fig. 2.6. When the short and ultrashort lasers' energy interacts with the target material, their energies are absorbed by free electrons on the target surface, which consists of partially ionised vapour and a plume of hot nanoparticles via fragmentation and phase explosion, and homogeneous nucleation and decomposition [237, 238].

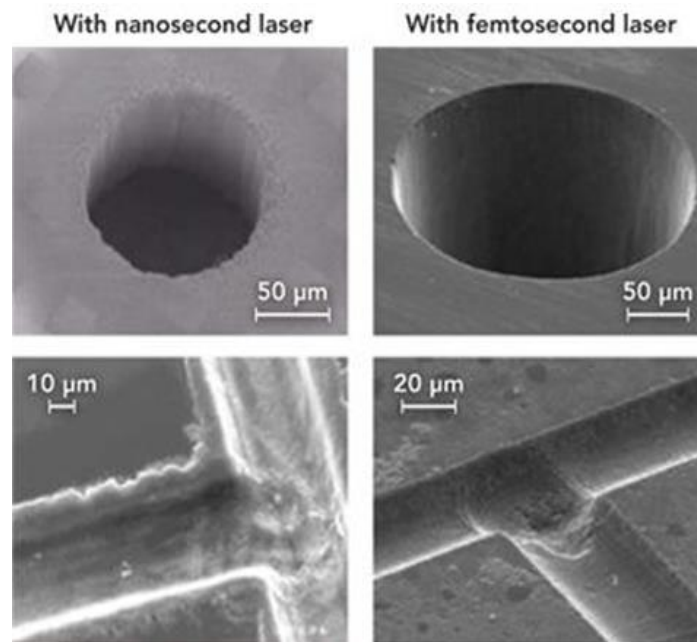


Fig. 2.5: Laser material processing of a glass target by ablation of nanosecond laser (left) and femtosecond laser (right) [239].

Fs-PLD can be done at any pressure either high or ultra-high as well as in an atmosphere that can be either inert or reactive. Additionally, fs-PLD shows flexibility to various types of targets in the growth processes of single films. It is also easy to focus the fs-PLD laser beam to two or more types of targets, and therefore sequential ablation can be performed. Sequential ablation is referred to as alternate PLD and is very suitable for the production of complex structure including nanostructured films or multilayers.

Additionally PLD drawback, it is possible to display droplets on the PLD deposited films. Light scattering sites result from these particulates, thereby

decreasing the films' optical quality. Besides, a significant number of electrical applications do not appropriate the particulate rough (uneven) surfaces, for instance among phase-change non-volatile memories [119]. However, this can be reduced by changing the deposition parameters, such as decreasing the laser power density or using femtosecond pulses [240, 241]. Increment in pulses frequency and decrement in the laser pulse energy, for the ultra-fast PLD process, contributes to the lessening of the particulates present in deposited films [68, 71, 75].

In the research work reported in this thesis, the deposition of high-quality chalcogenide thin films was carried out using fs-PLD onto a silicon substrate. The research reports the structure as well as the optical properties of the as-deposited thin films under different parameters for potential applications in NIR optical waveguides.

2.4 Ion implantation and diffusion processes

Research for the implantation of ions into silicon and other semiconductors can be traced back to the days of photocell and transistor development by Russell Ohl [242] and other researchers [243] at Bell Labs. However, the commercialisation of the same only first appeared in the late 1960s [244]. Advancement in the ion implantation technology has enabled the growth in the performance of semiconductors and their continuous reduction in size. Ion implantation can be defined as the process of accelerating ions to a target at energy so high that they can get buried below the target surface. A discovery was made in the 1970s that the implantation of ions on some materials could improve their thermal, optical, electric, and mechanical features.

Conventional ion implantation can be described as a 'line of sight' process in that the extraction of the ions occurs from a plasma source, then the acceleration of ions occurs to the desired energy before the ions are framed across a target where they arrange themselves uniformly (Fig. 2.7). Due to the line of sight process performed during implantation, a manipulator stage is necessary to ensure that the target is rotated in the beam for the ions to

get implanted on all sides. The handling of the target increases the complexity and leads to the reduction of the size of the target being implanted. This target manipulation issue in normal ion implantation worsens due to the need of providing enough heat sinks at the target to prevent the rise of temperature during the process [245, 246].

Moreover, the plasma source ion implantation (PSII) process [246-249] shows a drift from normal implantation technology, given that it avoids the line-of-sight limitation. During the PSII process, the targets needed for implantation are put directly in a plasma source, then pulse biased to a high negative potential (Fig. 2.7). The acceleration of the ions is normal to the surface of the target across the sheath of the plasma [246, 247] leading to the elimination of the line-of-sight issue as well as the ‘retained dose’ problem [249]. The first experiments showed that PSII was efficient in the implantation of ions to the right concentrations and depths needed for surface readjustment thus producing a material having improved wear and microhardness characteristics as evaluated in lab experiments and leads to the improvement of life of the manufacturing tools when applied in an industrial setup.

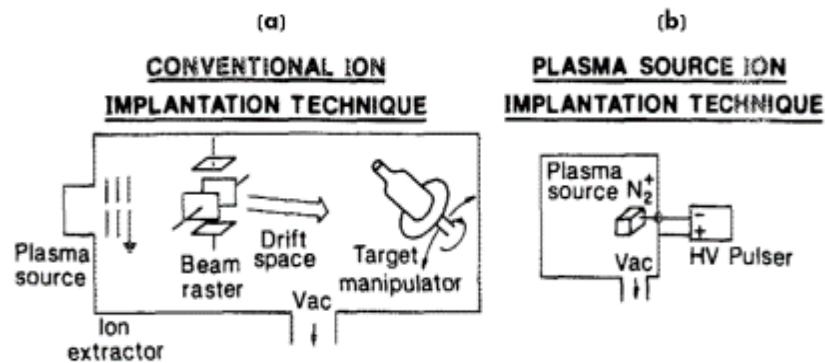


Fig. 2.7: The comparison of (a) conventional ion implantation technique with (b) plasma source ion implantation (PSII) [246].

As noted by Ahmad et al. [250], the increase in ion energy occurs as a result of the damage caused by the ions that have been induced on the AL surfaces. Consequently, after the Al ions have been implanted, there is a noticeable reduction in the hardness of the substrate due to the thermal sputtering. Latif et al. [251] noted that the variation that occurs in the

crystallite size is caused by the recovery and the annihilation process when a silver surface is exposed by the induced Cu ions from the laser. Moreover, Conrad et al. [246] pointed out that, after the implantation of ions, the wear resistance, as well as the hardness of steel, exhibited better performance. On the other hand, Giuffrida et al. [252] and Cutroneo et al. [253] stipulated that the implantation of ion plays a significant role in modifying certain properties such as; chemical resistance, wear, electrical conductivity and material hardness. Subsequently, further published studies indicate that implantation ions on the solid's surface has the capability of changing the chemical properties and the state of defect of a given material [254, 255].

Plasma has been observed to deliver ions with kinetic energy and a charge state both dependent on the crystallised target material and the characteristics of the laser in use (mostly the laser pulse duration and the laser pulse energy). The hot and very thick plasma that contains ions that have high charge states can be obtained by crystallising solid targets with laser pulses of high energy. Ions that are released have charge state of up to 50^+ for heavy material and can reach kinetic energy greater than a couple of MeV and densities of tens of mA/cm^2 within a distance of 1m of the target [256-259]. Additionally, they have a leaner angular distribution which is pointed along the normal of the target surface. These differences are crucial for ion implantation technology.

One of the areas that has intrigued researchers in the industry due to its efficiency in the preparation of nanostructured components is controlled laser plasma. A dependable method for customising growth of semiconductor nanocrystals is gotten by using high ion current balanced with high ion energy/charge state through the adjustment of laser power density. Take an example of a nanosecond Nd: YAG laser that has a power density of $10^{10}\text{W}/\text{cm}^2$ and which leads in the formation of hot plasma, which has densities and temperatures of 10^{17} electrons/ cm^3 and tens of eV, respectively. The key takeaway of the laser ion implantation technique is that it makes it possible to use a huge variety of a solid component.

Given the many applications of ion beams in research laboratories, the industrial fields of medicine, and engineering, there has been a new interest in how new ion sources can be developed based on innovational methods. One of these methods that looks promising is one that has the likelihood of taking advantage of high energy pulsed laser beams with a given component. Pulsed laser crystallisation is a method that has been used for several years now for several purposes including the ablation of targets, decomposing thin films, and producing plasma to the high-energy ion acceleration.

The plasma that is the output of the ultrashort laser pulse of a very powerful light field at the top of the solid-state target is a distinct origin of the high-energy ion as well as electron beams. In the case that femtosecond laser radiation that has a high contrast ratio with an intensity of 10^{15} - 10^{16} W cm⁻² comes into contact with a solid target, then a high-energy ion material (over 10 keV) is created within the laser-plasma. The degree of ionisation, the elemental composition of the expanding plasma, and the directivity pattern are dependent on two characteristics namely the components of the laser radiation (energy contrast ratio, wavelength, intensity, duration pulse) and the state of the surface of the said target. The plasma components can be controlled by modifying the surface layer of the target [260, 261]. The fast ion beams developed during very vigorous laser radiation matter interaction can be used in developing a new ion implantation method. The conventional method of ion implantation of ion beams that are already accelerated provides a chance to introduce a controlled number of impurity atoms inside the surface layer of the target and can lead to the alteration of the physical and chemical components of the surface layer in various materials. A combined method exists where ionisation material is got by a nanosecond laser pulse, and the following ion acceleration to high energies was got by an electric field.

A new technique was used by Belloni F. et al. [262] whereby, the implantation was done using a laser to generate the ion. The technique was done by subjecting the high voltage on the gap that is accelerating. The device that was compact demonstrated the ability to accelerate in the

direction of the substrate ions that originated from the plasma that had been ablated. The ablation of the plasma that comes from the solid target emanated from the KrF laser that was pulsating on a nanosecond. From the setup, a pulse duration of 20 ns and a radiation wavelength of 248 nm were achieved. Moreover, an irradiance value of approximately 3.5×10^8 W/cm² was obtained when a 70mJ per pulse laser beam from a lens of 15 cm focal length focussed on various targets covering an area of approximately 1mm². From this experiment, the implantation effects of Ge and Al on substrates made of Si occurred up to a depth of approximately 80nm, with the accelerating voltage of about 40 kV. The estimated ion dose by faraday diagnostic cup was ranging in the order of 10^{10} ions/cm² in a given pulse. In other studies, The Ge crystals prepared by Rosinski M. et al. [263] using the implantation of induced laser ion. In this experiment, the pulsated laser of Nd: YAG nanosecond with a pulse duration of 3.5 ns, a frequency of 10 Hz and the pulse energy of approximately 0.5 J were utilised. In addition, they used a vacuum chamber that had pressures of approximately 10^{-6} mbars and a system that generated an electrostatic acceleration and deflection. A laser beam of 10^{10} W/cm² power density was used to irradiate the Ge target. From this setup, it was evident that the variation in the implantation of ion, and by annealing treatment of the post preparation aspect. Moreover, it was possible to attain the Ge crystalline micrometer size with a likelihood of obtaining an amorphous one. Consequentially, these yields to the implantation process with high-quality results and maybe find its use in the nanotechnology and the microelectronics.

With a view to generate high-energy ions, Implanting ions direct from a plasma produced from laser where the accelerating potential was not implemented were got by using the third harmonic of iodine Prague Asterix Laser (PALS) laser radiation ($\lambda = 1315 \mu\text{m}$) at a pulse duration of 400 ps in a vacuum chamber (10^{-5} Torr) and an intensity of up to 10^{16} W cm⁻² [264]. On different conditions where the PALS laser-based iodine system is used, Rosiński J. M et al [265] described that the direct implantation utilising the lasers that converted the Ge ions into SiO₂ films is a more effective method.

Back to femtosecond the potent field continuously pulsed laser systems allows the production of directional higher-energy ion beams and the implantation promises the alternation of the target surface layer and can also be used. Ion implantation can also as a diagnostic tool in that it gets used in experiments in generating the thermonuclear neutrons from solid-state targets with a concurrent determination of ion energy distribution averaging over several shots. This method is advantageous since it works in low temperatures and avoids diffusion of the implanted ions. Volkov R.V. et al [266] elucidated that, it is possible to implant the Ge ion into a Si substrate by the aid of femtosecond pulses of a laser. The considered criteria involved a time duration t of 200 fs, the intensity of 10^{15} Wcm^{-2} , the energy of between 200 to 300 μJ and a λ of 616 nm, which were put in an evacuated vacuum chamber that had a residual pressure of 10^{-5} Torr. In this experiment, the Ge ions occupied a substrate material depth of about 400nm. The density profile from the implanted ions gives the average energy of the ions emanating from the produced laser plasma.

Since all the energy for implantation is higher than the threshold for the displacement of the lattice atoms, the implantation of ions certainly causes damage to the lattice structure of silicon through the collision of the dopant ions with the silicon atoms and the accommodation of the implanted ions within the matrix [267]. The range of implant energies that has attracted much interest is between 1 and 5 keV. During implant, this energy is transferred through the interaction of the nuclear or elastic collision from energetic ions to initially stationary atoms. With the collision, the ions are scattered with energy loss occurring, causing the projectile to slow down. After several collisions with the various target atoms, the ion will rest at a range within the Si once it has lost its energy. A shorter range is obtained for lower implant energy for a given implant species. Statistically, the nature of the process of slowing down of the ions produces a distribution of the implanted ion within the Si at about some mean depth.

The collision between Si atoms with the incoming dopant ions also generates energetic recoil Si atoms that also collide with other Si atoms. If

this collision causes the transfer of sufficient energy, these atoms will also be displaced. This process keeps occurring, forming a collision cascade. For heavy implanted ions such as Sb, As, and Xe, their collision cascade also produces small amorphous zones. A spatial overlapping of these zones occurs when a certain level of the concentration of the implant occurs, leading to the formation of a continuous amorphous layer.

Si lattice may undergo less damage when light ions such as B are implanted. However, there may be a build-up of these small damages until specific critical defect concentration is achieved, leading to the collapse of that particular crystal structure into an amorphous structure [268]. Producing an amorphous layer with light ions is difficult as it requires a higher number of light ions in comparison to that of heavy ions. With the binding energy of silicon (4.6 eV) being lower than the energy of the implantation of ions, crystal defects occur and these include interstitials, vacancies, and amorphous layer.

In silicon, diffusion primarily takes place at native point defects as well as at impurity related point defects. Typically, a perfect crystal lattice contains some form of native defects, such as line defects, point defects, and surface defects. Point defect concentration at room temperature is low, and no diffusion occurs. However, diffusion will increase with an increase in point defects. Heating or irradiating a crystal with ions increases the concentration of point defects. During the fabrication of devices, both these situations are likely to occur. In addition, the introduction of a group- III elements or group-V elements into the silicon lattice is associated with impurity related defects [269].

This work has been investigated the direct implantation/diffusion of ChGs ions produced in fs-PLD.

Chapter 3: Instrumentation and Methodology

This chapter describes the various experimental procedures that were employed for both materials fabrication and characterisation. Details of procedures adopted during the experiment are also discussed along with a discussion of the fundamental principles of some of the analytical techniques used for materials characterisation.

The chapter begins with discussions on fs-PLD. It is followed by explanation focused on the instruments used in characterising the samples produced. Analysis can be divided into two parts, namely: structural and optical characterisation. The structural characterisation of the materials begins with an X-ray diffraction (XRD), followed by a brief description of Raman spectroscopy. An overview of the transmission electron microscope (TEM) with energy-dispersive X-ray spectroscopy (EDX) is presented, which includes the relevant operation modes, working principles along with focused ion beam (FIB) sample preparation. Characterisation concludes with a scanning electron microscope (SEM). On the other hand, the optical characterisation of materials starts with a photoluminescence (PL) spectroscopy, followed by an ultraviolet-visible-near-infrared (UV-Vis-NIR) spectroscopy.

3.1 Sample fabrication

Two main procedures were used for sample fabrication. Starting with the preparation of target materials, referred to as fabrication of glass, which is then used as a “target” in the process of fs- PLD.

3.1.1 Target materials

In this work, four types of target materials were prepared. The details and figures of each target will describe at the beginning of each results chapter: Gallium lanthanum sulphide (Ga-La-S) in chapter 4, erbium-doped gallium lanthanum sulphide (Er³⁺-doped Ga-La-S) in chapter 5, germanium selenide (GeSe₄) in chapter 6, and germanium antimony selenide (Ge₂₀Sb₁₅Se₆₅) in chapter 7.

3.1.2 Femtosecond pulsed laser deposition (fs-PLD)

There has been an extensive study of a pulsed laser deposition (PLD) more so to make novel devices and materials, which has enthused scientific interest in chemistry and physics. When it comes to PLD, the target material surface gets vaporised by the ultraviolet (UV) laser radiation, leading in the maximum particles atomisation in the ablation plume, which then causes the composition reconstruction. As shown in Figure 3.1, a classic fs-PLD system comprises of femtosecond (fs) laser, several optical mechanisms, like polarise, mirrors, beam expander, and focusing lens that aids in focussing the laser beam onto the target glass as well as a vacuum chamber, substrate and a target situated opposite, and close to one another. There is also a heater that aids in heating the substrate.

In this study, a commercial Coherent titanium-sapphire LIBRA laser (Ti: Sapphire laser) with pulse duration 100 fs, pulse repetition rate = 1 kHz, and wavelength centred at 800 nm was employed to fabricate chalcogenide films. By using 800 nm wavelength laser, we can introduce signal photon absorption in ChGs and subsequence ablation. Laser energies were precisely controlled by adjusting the polariser, and the laser energy was measured using a Coherent LabMax-Top laser power and energy meter. The fs laser pulses of chosen energy was focused onto the target material at an angle of 60° through a transparent window of the vacuum chamber to generate plasma plume directed perpendicular to the substrate surface (Figure 3.1).

Initially, the target and the commercially available silicon substrate of dimensions 20 mm (L) × 12 mm (W) × 675 μm (T) were mounted in their respective holders inside the chamber. A programmable heating element heated the substrate at the rate of 50°C per minute. On top of the substrate, is a thermocouple having a digital output that displays the temperature and beneath the substrate was a shutter to control the deposition process.

The chamber lid was closed and the pressure inside evacuated till 9×10^{-5} Torr immediately after completion of the set-up above. As the substrate was

being heated at the rate of 50°C per minute, the temperatures increased towards the set-point, which lead to release the background gas inside the chamber at a set pressure. Subsequently, the plasma plume should be first checked by turning on the target raster and rotator and opening the laser shutter for about 5 minutes.

The poor focus would result in reduced visibility of the plasma plume; as a result, adjusting the focus to the desired point led to good visibility of the plasma plume. A non-stationary plasma plume would result from an irregular target surface. Therefore, the plasma plume was assessed for flickering, however, if the presence of flickering would imply the misalignment of the laser regarding the target, as well as, the laser striking at unintended places such as the target holder. Conversely, allowing the laser strikes the target would serve a great ordeal in eradicating contamination form the target surface.

After successfully attaining target surface cleanliness and plume dynamics, the laser shutter, target rotator, and target raster were closed, respectively. Before refilling the chamber to its standard pressure, it was pumped down to base pressures of roughly 9×10^{-5} Torr so as to eliminate traces of vapour phase contamination. Both target and substrate holders were allowed to rotate continuously at a constant speed of 40 rpm and 20 rpm, respectively, while the target-to-substance distance was kept at 70 mm. This rotation was to ensure that the laser could ablate the target surface uniformly.

Regular checks during the experiment entailed: fs-laser energy, plume dynamics, gas pressure, and substrate temperature, and they were assessed every 30 minutes. After completion of the ablation process, the substrate shutter and laser were closed as the sample cooled to room temperature (25°C). The chamber was then vented by the use of nitrogen gas (N₂).

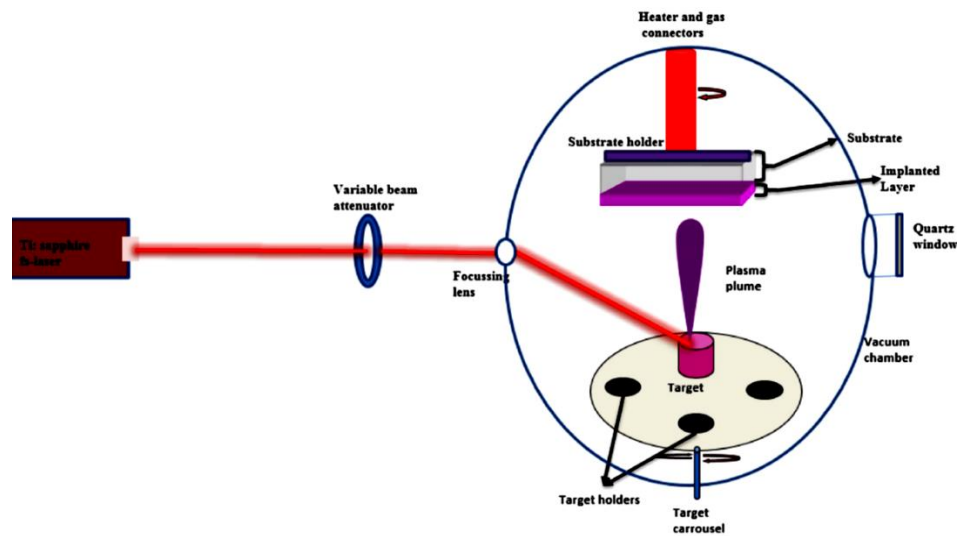


Fig. 3.1: Schematic setup of the fs-PLD system.

3.2 Thin film characterisations

3.2.1 Structural characterisations

3.2.1.1 X-ray diffraction (XRD)

The study of nanomaterials with dimensions ranging from 1-100 nm has been made effective, a technique known as X-ray diffraction (XRD). X-rays are a type of electromagnetic radiation comparable to light, but with a much shorter wavelength. X-rays are created as a result of particles that have been charged with electricity to a high enough level that they are decelerated. As shown in Fig. 3.2, the process involves maintaining a high voltage in an X-ray tube, which attracts electrons toward an anode. X-rays are created from the collision. As a result, they are radiated at many angles. The X-ray tubes employ copper targets, which typically produce the highest level of radiation (K1) at a wavelength of about 1.5 angstroms. This is often used in applications associated with geology. When the X-ray beam hits a crystal lattice, it will be scattered. Most of this scattering is diminished as a result; this is known as *destructive interference*. However, diffraction takes place if the scattering is in phase with rays that have been scattered from other atomic planes. As a result, the joining creates new enhanced wave fronts. These can reinforce each other; this effect is known as *constructive interference* [270].

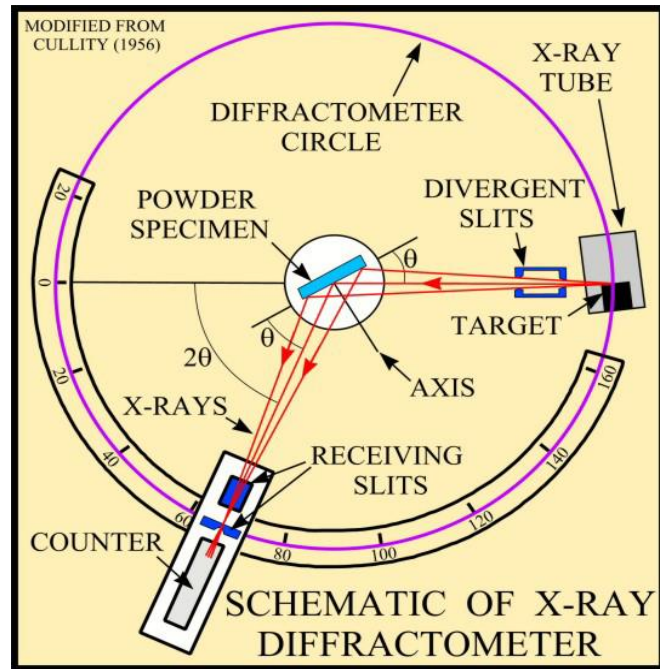


Fig. 3.2: Basic features of an X-ray diffractometer [271].

XRD is an ideal technique for in-situ studies; this is because of their non-destructive and non-contact nature. X-ray diffractograms offer vast information ranging from lattice strain to crystallographic orientation, and from phase composition to crystalline size [270].

Figure 3.3 is the schematic of Bragg's law, which diffraction angle 2θ lies between the diffracted and incident rays. The nature of the diffraction effect is stipulated by Bragg law (or equation):

$$n\lambda = 2d \sin\theta \quad (3.1)$$

Where the rays' wavelength is represented by (λ), the angle between the incident rays and the crystal surface is represented by (θ), and the spacing between atoms' layers is represented by (d) [270].

In the first diffraction order of $n=1$, evaluation of the interplanar spacing d -value of a specific plane is possible.

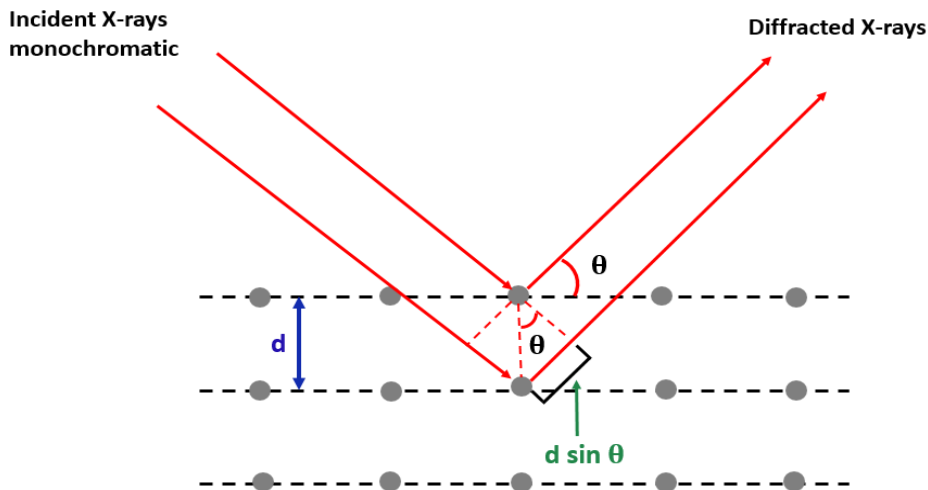


Fig. 3.3: Diagram of Bragg's law.

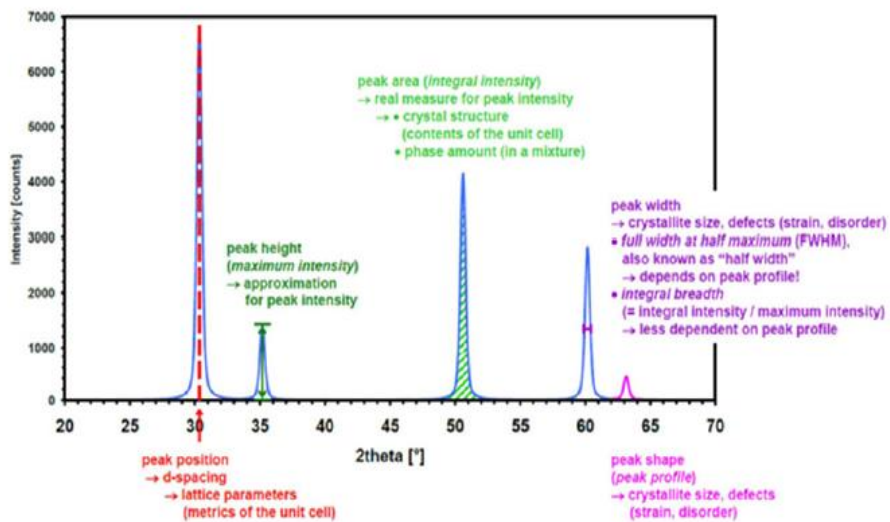


Fig. 3.4: Information content of an idealised diffraction pattern [270].

Figure 3.4 illustrates the data that can be derived from an ideal diffraction pattern. To begin, an XRD pattern entails XRD peaks indexing; this implies that respective peaks of diffraction patterns are assigned correct Miller indices(hkl). There are three key strategies in indexing a diffraction pattern, first, is by equating already measured XRD patterns to a standard database (international centre for diffraction data ICDD-cards), followed by analytical techniques and lastly, graphical techniques. However, in the graphical representation of diffraction signal intensity against diffraction angle 2θ ,

alternatives such as d [nm] or $1/d$ [nm^{-1}] can be used. Conversely, a wavelength of 1.54Å (Cu $K\alpha$) is commonly used.

Crystalline size, d , from the peak width in XRD pattern can be asessed using Debye-Scherrer's formula as below [272]:

$$d = \frac{K\lambda}{\beta \cos \theta} \quad (3.2)$$

where: λ = X-ray wavelength (0.15418 nm with Cu $K\alpha$ radiation).

β = full width at half maximum (FWHM) of a diffraction peak.

θ = diffraction angle.

K = Scherrer constant of the order of unity for usual crystal and thin films.

The fore-mentioned Scherrer constant (K) is reliable for particle's shape and is presumed to have the value 0.9 [273]. The derived size from the formula gives an average size of a particle in a material.

Debye-Scherrer's equation has significant drawbacks. The constant value used in the equation fluctuates with the particle's shapes. However, it does not consider the essence of distribution sizes and defects present in the crystalline lattice. As a result, calculations involving grain diameter from FWHM of the peak can miscalculate the ideal values since strong inputs to the intensity emanating from the larger grains, while smaller grains are at the base of the peak. However, defects in a considerable amount lead to further enlargement of the diffraction line. These drawbacks can be solved by using TEM and SEM in measuring particle size.

Treatment by heat results in annealing of particles hence larger grains, as a result, the degree of crystallinity in the sample is increased. In the diffraction data, the effect is perceived as elevated peak intensity. Exposing samples to heat treatment creates a plethora of opportunities to differentiate diffraction patterns of bulk materials and nanoparticle, this has enabled one see how the intensity and shape of peaks fluctuate between samples of different particle sizes [274].

There are key differences between diffraction patterns of bulk materials and nanomaterials. The former has sharp, narrow and high peaks, while the latter, has small particle sizes resulting in broadening of their respective diffraction peak, which is due to an insignificant number of crystal planes.

Diffracted rays in crystalline substances are in a specific direction and relay a high-intensity narrow peak, whereas, in amorphous materials, diffracted rays are in a random direction as a result of the random configuration of atoms giving it a large hump or peak as shown in Fig. 3.5 [275, 276].

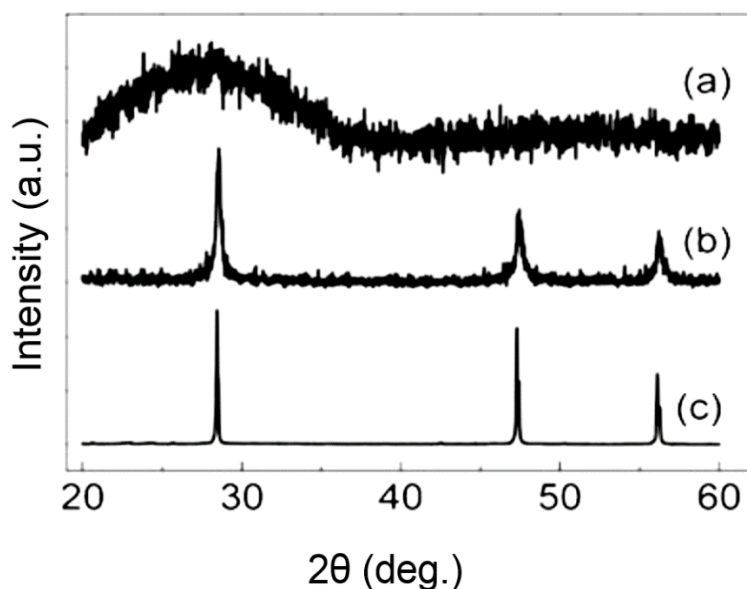


Fig. 3.5: XRD spectra corresponds to (a) an amorphous, (b) polycrystalline silicon colloids, and (c) a single crystal silicon sample [275].

In this study, the grazing incidence angle was opted, which applies the GIRXD technique, instead of conventional $\theta/2\theta$ scanning techniques. Using the latter on “thin” films (1-1000nm) XRD measurements, leads to weak signals from the film relative to the substrate, whereas, the former can be used to avert dominating signals from the substrate and further enhance the signals by implementing the $2\theta_0$ scan. The selection of the fixed angle is usually positioned slightly above the critical angle for the complete reflection of the film material. It is evident in Fig. 3.6 that the 2° fixed angle is between the sample’s source and plane, while an angle of 10° - 80° (swept) lies between the sample’s detector and plane with a $2\theta - 1$ variable. The entire angle between the detector and the source is 2θ .

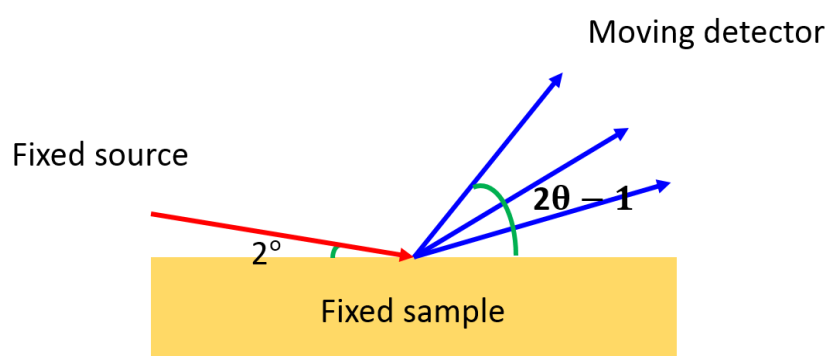


Fig. 3.6: Grazing incidence XRD.

In this work, XRD was utilised to investigate and understand the structural characteristics of the deposited film. The XRD patterns of Si substrate, target bulk ChGs, and thin films were determined using a Philips X'Pert with Cu K α radiation ($\lambda = 1.54056 \text{ \AA}$), at 40 kV and 40 mA. Each sample was scanned using grazing angle in which omega (incidence angle) was kept in 2 degrees for 60 min with a diffractometer angle range from 10° to 60° in a step size of 0.033° /s at room temperature in air.

3.2.1.2 Raman spectroscopy

Raman spectroscopy (RS) is an all-around method of analysing a broad range of material. RS is capable of being utilised for qualitative and quantitative purposes. It is possible to perform qualitative analysis through measurement of the scattered radiations' frequency, while quantitative analysis is based on the measurement of the scattered radiations' intensity [277].

A monochromatic laser beam is used by Raman spectroscopy. The sample is lighted up, thereby establishing contact with the sample molecules. Molecules are capable of absorbing or emitting photons-electromagnetic radiation using precise energy and, in doing so, alter their energy [278]. The energy of a photon E , based on the quantum theory, is given by the equation:

$$E = h\nu \quad (3.3)$$

or

$$E = \frac{hc}{\lambda} \quad (3.4)$$

Where Planck's constant (6.626×10^{-34} Js) is represented by h , its frequency is represented by ν . The velocity of light is represented by c , and the wavelength is represented by λ . Mentioned specific energy ΔE has to achieve the succeeding quantum condition.

$$\Delta E = E_p - E_q = h\nu = \frac{hc}{\lambda} \quad (3.5)$$

The energies of different quantum states where a molecule is capable of existing are represented by E_p and E_q .

Raman scattering phenomenon:

Figure 3.7 is an illustration of the energy level diagram. When an intense monochromatic light irradiates a material, there is a scattering of light beam that is typically from close to infrared, noticeable or close to ultraviolet range with no changes made in frequency, no gain or loss of energy, in other words, Rayleigh (elastic) scattering, partly absorbed and a tiny fraction left, is essential for the spectra origin and scattered non-elastically. After the photon has interacted with the molecule, specifically with the electron cloud and the molecule bonds, the photon induces molecule excitation from the ground state to a practical energy state. Upon the relaxation of the molecule, a photon is emitted and transformed into another vibrational or rotational state. The difference in energy between the ground state and its last state leads to a shift in the emitted wavelength of the photon.

If the energy absorbed by the molecule; in other words, there is more energy in the final state compared to the initial state, then a Stokes line is generated by the emitted lower frequency photon. An anti-Stokes line is generated by a higher frequency emitted a photon in the event that the molecule loses energy. Analytical information with regards to differences between the individual levels of quantum is carried by shifts in Wavenumber (Raman) plays a major role in in the identification of the substance. These Raman shifts are dependent on the material's precise molecular geometry and are

autonomous on the incident wavelength photon, that is, on the laser's excitation wavelength [278-283]. Several characteristic shifts can exist for a specific material originating from the Raman spectrum.

Frequently, measurement focuses on Stokes section of the spectrum. Anti-Stokes and Stokes are roughly proportioned near the nil shift of the wavelength that matches up with the incident laser streak wavelength. Data concerning the kind of bonds in the particle is acquired from the dispersal of the streaks in the spectrum. Each matter has its special Raman spectrum feature, precisely only to the particular matter [278].

Raman spectrum signifies a dependency of the strength of the dispersed light (in random units) on the wavelength (calculated in cm^{-1}). The strength of the Raman dispersion depends on numerous causes as the excitation wavelength of the applied laser, variations in polarizability, applied excitation energy, the quantity of Raman active particles the laser beam and temperature irradiates. George Placzek hypothetically describes the strength of a Raman ensemble [284].

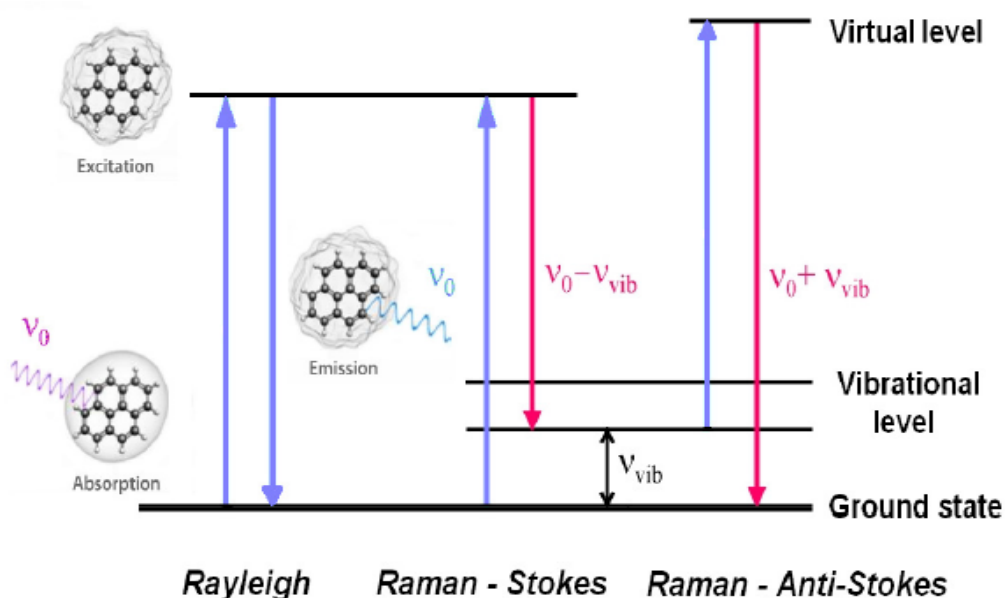


Fig. 3.7: Energy level diagram of Rayleigh and Raman scattering [278].

A source of the laser, a monochromator, microscope and filter, plus as a detector and information processing part, build up the device. The technique

comprises using a microscope in aiming the concentration of light on to the sample. The scattered signal that comes from the sample reflects in a filter. Subsequently, the Rayleigh scattering is eliminated. The filters gatherer the Raman scattering. Afterword, collecting these scattering by a detector. This tactic makes it probable for the surveillance and identification of the wavelength and intensity signal for the Raman spectra to be generated. The Raman spectroscopy structure's graphic diagram is shown in Fig. 3.8. In this work, to investigate and understand the structural characteristics of the deposited film, a Renishaw inVia Raman spectrometer was used, for the measurement of Raman scattering spectra of samples. The spectrometer uses an Ar⁺ laser (514 nm) excitation source and a 25 milliwatt (mW) power.

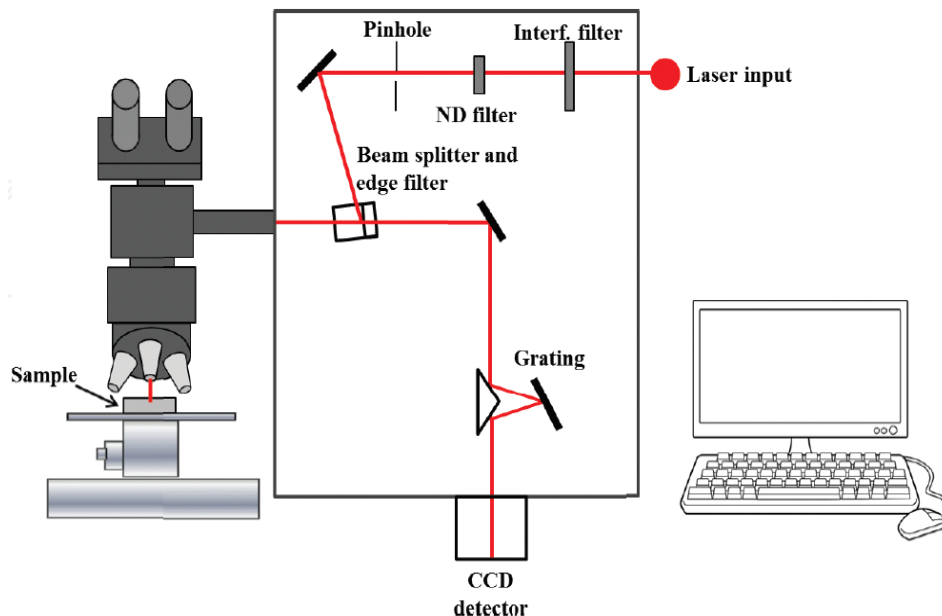


Fig. 3.8: Schematic structure of a Raman spectroscopy system [285].

3.2.1.3 Transmission electron microscopy (TEM)

Among the material science tools, a transmission electron microscopy (TEM) is having great power. A high energy electrons beam is radiated by means of a very thin specimen, and the resulting interaction between the atoms and electrons is useful in observing special properties like crystal structures. Also, the performance of chemical analysis can be undertaken. TEM is applicable in studying layers growth, the composition of this growth,

and semiconductors deficiencies. Also, high resolution is useful in the analysis of the size, shape, density, and quality of the wires, dots, as well as quantum wells. [286, 287].

TEM's working principle is very much identical to that of a conventional optical microscope where electrons rather than visible light are used. The highly energetic electrons wavelength (such as 200 kV acceleration voltage results in $\lambda = 2.5$ pm) is significantly shorter, compared to the visible light wavelength (400-750 nm). Such results in a point resolution that is much higher (down to 2 Å), making it possible for sample features to be investigated at the atomic level.

Using the condenser lens, the focus of the electron beam coming from the electron gun is directed into a small and thin clear beam. The condenser aperture beam restricts this beam while excluding high angle electrons. The specimen is then struck by the beam with parts of it transmitted in accordance with the specimen's thickness and electron transparency. The focus of this transmitted portion is directed by the objective lens into an image on a phosphor screen or charge-coupled device (CCD) camera. It is possible to use the optional objective apertures in improving the contrast by having the high-angle diffracted electrons blocked out. Through the intermediate and projector lenses, the image then moves down the column, enlarging down.

A simple sketch of an electrons' beam path in a TEM that is above the specimen and below the column to the phosphor screen is shown in Fig. 3.9. The electrostatic potential which the constituent elements in the specimen set up scatters the electrons as they pass through the sample. Upon passing through the specimen, they move through the electromagnetic objective lens that has all electrons scattered from one point of the sample focused into one point in the image plane. A dotted line where there is collection into a single point, of all the electrons scattered in the same direction by the sample, is also displayed in Fig. 3.9. This is the objective lens back focal plane, and that is where the formation of the diffraction pattern takes place.

Light is generated as the phosphor screen is struck by the image, making it possible for the user to observe the image. Those sample areas where the transmission of fewer electrons take place are represented by the image's darker areas, while those sample areas where more transmission of electrons take place are represented by the image's lighter areas.

The electron gun generates a high energy electron beam in a TEM system. The emitting of electrons is from a cathode, and a TEM system and high voltage (V_0) accelerates these electrons. The electron beam energy will be $E=eV_0$, and the wavelength of electrons will be determined by it. Moreover, as the microscope resolution is mostly determined by the wavelength, the resolution, to a large extent, will be determined by the acceleration voltage [288-291].

Contrast formation in TEM images is dependent on operation modes. Most popularly utilised (and also utilised in this work) are the imaging modes of a bright field and dark field, selected area electron diffraction (SAED), and energy dispersive X-ray analysis (EDX). The formation of image, in the bright field mode case, as the electrons going through the specimen are scattered, is dependent on atomic number or the sample thickness. There will be an appearance of a bright spot in the image in places where electrons go through the sample virtually without scattering, while there will be the appearance of dark patches in places, where there was the scattering of electrons.

The use of an objective diaphragm in intercepting all except the diffraction pattern's selected region is the most direct TEM dark-field analogue. These electrons pass through the TEM detector and make the signal available for the image available.

If a microscope's point resolution is amply high and a suitable crystalline sample oriented along a zone axis, then there is an acquisition of high-resolution TEM (HRTEM) images. In numerous cases, HRTEM can investigate a specimen's atomic structure directly. The highest point resolution obtained these days by TEM is approximately 0.5 Å [288-291].

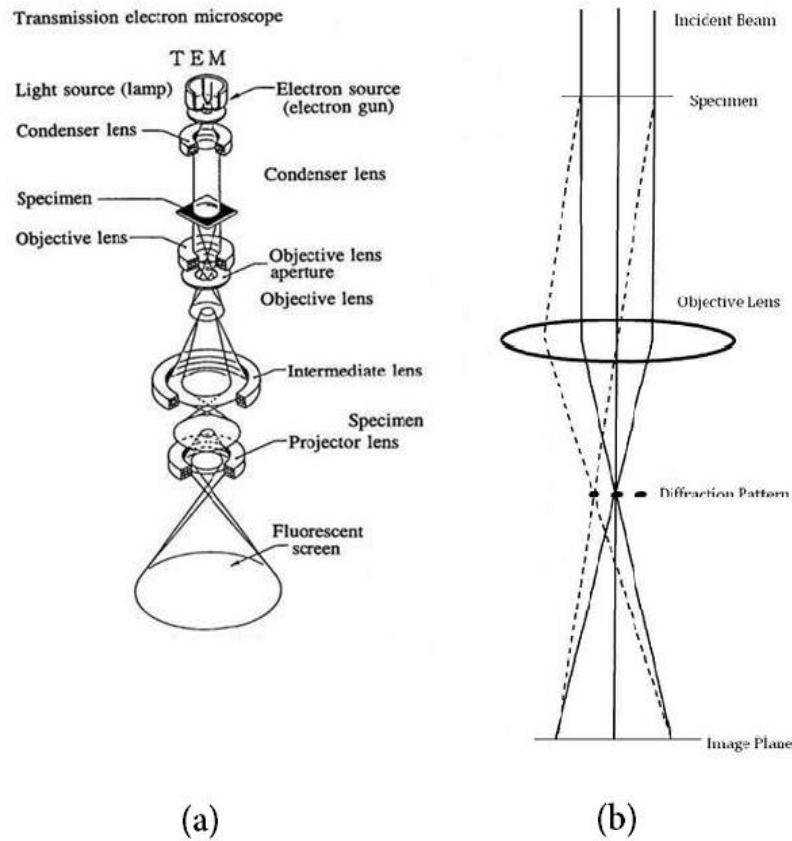


Fig. 3.9: (a) General layout of a TEM describing the path of electron beam in a TEM and (b) a ray diagram for the diffraction mechanism in TEM [292].

3.2.1.3.1 Selected area electron diffraction (SAED)

Selected area electron diffraction (SAED) (also called SAD), is a crystallographic experimental technique capable of being performed using a TEM. This technique can be used in determining any material's crystal structure. It is akin to XRD, although exclusive, in the fact of its ability to examine size areas as small as several hundred nanometres, while XRD characteristically examines sample areas that are several centimetres in size. An aperture is used in the specimen's plane for the selection of the sample region, where one is attempting to obtain diffraction. Because of this, we will obtain reciprocal lattice's sharp diffraction spots. Table 3.1 displays the contrast of the SAED in TEM with XRD. Based on the SAED pattern, we obtained the following vital information. It has the ability of being utilised possible to observe (i) if ones' sample is amorphous (diffuse rings), crystalline (bright spots), polycrystalline (small spots that make up the rings,

every spot stemming from the reflection of Bragg from an individual crystallite) refer to Fig. 3.10.

Table 3.1: Comparison of the SAED in TEM with XRD

	XRD	SAED in TEM
Scattering nature	Scattering by shell electrons	Scattering by atom nucleus
Wave paths	Reflection (XRD) Transmission (Laue)	Transmission
Diffraction angle θ	0~180°	0~2°
Intensity	low	10 ⁶ ~10 ⁷ times higher
Precision	high	Relatively low

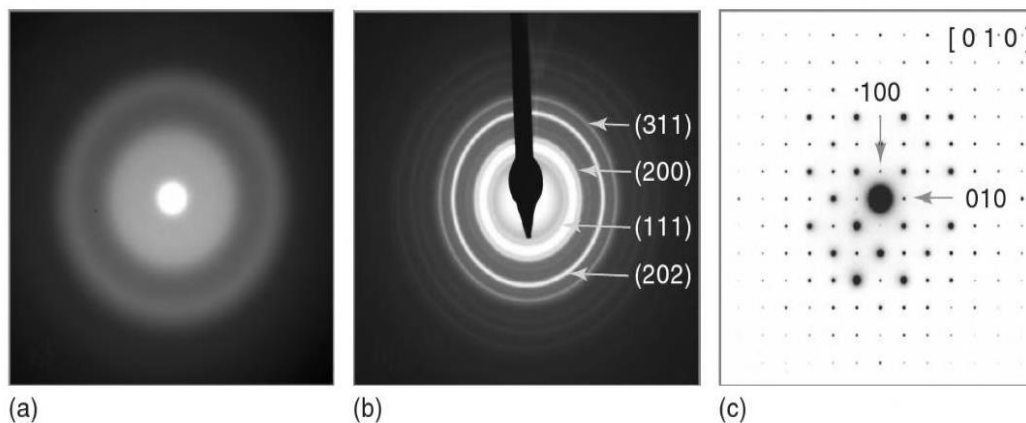


Fig. 3.10: SAED pattern showing; **(a)** an amorphous sample pattern, **(b)** a polycrystalline sample pattern, and **(c)** a single crystal sample pattern [293].

3.2.1.3.2 Focused ion beam (FIB) lithography for the preparation of cross-sections for TEM analysis

TEM measurement is a technique that is said to be non-destructive, as it requires very thin samples (some nanometers in hundreds) to make a pass-through of the electron beam possible. Sample thickness, in ideal cases, should be similar to the electrons standard free path in the sample (one-tenth of nanometres). A diverse number of methods are available for the preparation of TEM samples in order to obtain appropriate thickness. Method selection was dependent on the sample material and on the desired information to be acquired. Sample cutting and grinding, as well as ion beam milling, are needed for the preparation of the conventional thin film sample for TEM analysis for the creation of electron transparent (thickness < 100 nm) regions. On the other hand, it is possible to prepare a TEM sample

through focused ion beam (FIB), which happens to be more costly and time-consuming, but results in less damage to the sample and makes the selection as a precise interest area possible. FIB method was utilised in this work for the preparation of the sample.

Procedure for focused ion beam (FIB)

- Use the electron beam for depositing a thin protective platinum (Pt) layer on the sample surface. Next, have another Pt layer with the ion beam deposited. The ion beam is more capable of cracking the Pt precursor but also can damage the sample surface. Therefore, the first Pt layer has to protect the surface before the second deposition.
- Generally, the source of the ions utilised in the FIB system is gallium (Ga) because of its low melting point, which is close to room temperature. In addition, its ability to focus a highly accurate spot size beam (usually less than 10 nanometres in diameter) [294]. Rough milling is done with Ga ions beam at a 30 keV energy and 6.5 nA currents. Once the membrane becomes 200–300 nm thick, the energy of the ion beam is decreased for the TEM samples flatness to improve and the damage to the surface to reduce. The last polishing energy is 2 keV.
- A micromanipulator with a glass needle is used in plucking the TEM membrane from the sample and placed on a TEM grid. The TEM grid, using the membrane, is now set to be analysed [295, 296].



Fig. 3.11: Schematic diagram showing coating FIB-TEM layers.

3.2.1.3.3 Energy dispersive X-ray (EDX) analysis through TEM

EDX (also called EDS) can be described as an additional analysis technique usually fastened to SEM or TEM. EDX uses a characteristic X-rays which a solid sample emits after bombardment by a focused electron beam to obtain the local structure chemical analysis. It is possible to display the data in the form of peaks conforming to the elements or in the form of a sample image's elemental map. EDX has turned into a powerful tool in multi-technique analysis for characterisation of the sample. This technique is non-destructive, with little or no preparation of samples involved. It is possible to detect, in principle, every element from atomic number 4 (Be) to 92 (U), although not every instrument is fitted out for "light" elements ($Z < 10$).

EDX is the basis for the sample investigation through interactions between electromagnetic radiation and matter and analysing X-rays emitted by the matter in reaction to being struck with the electromagnetic radiation. Its characterisation abilities stems, in large part, from the basic principle of each element having a distinctive atomic structure, thereby making it possible for X-rays characteristic of atomic structure element to be distinctively identified from one another [297, 298].

Stimulating the characteristic X-rays emission from a specimen calls for the focusing of charged particles' high energy beam like electrons or a beam of X-rays. This is focused on the sample under study. An atom within the sample, when at rest, is made up of ground state (or unexcited) electrons in distinct energy levels or electron shells attached to the nucleus. The incident beam can excite an electron in an inner shell, expelling it from the shell while an electron-hole is being created at the former position of the electron. An advanced energy electron coming from an outer shell ultimately takes the place of the relinquished position of an expelled inner shell electron, and it becomes possible for the difference in energy between the greater energy shell and the lesser energy shell to be released in an X-ray form as illustrated in Fig. 3.12. The amount of released energy through the transfer of electron is dependent on the shell being transferred from, and the shell is transferred to. It is possible to use an energy dispersive spectrometer in

measuring the number and energy of the emitted X-rays from a specimen. Considering the fact of the X-ray energy is characteristic of the energy difference between the two shells, and the element's atomic structure that they were emitted from, this makes it possible to have the specimen's elemental composition measured [297, 298].

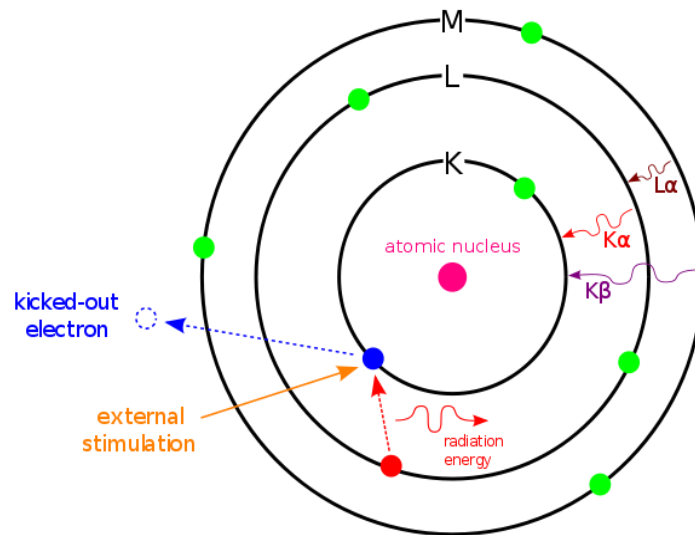


Fig. 3.12: Principle of EDX [297].

In this work, the surface morphology, thin film thickness, elemental maps, elemental concentrations, and SAED pattern were obtained using an FEI Titan Themis Cubed 300 TEM and high-resolution monochromated field emission gun-scanning electron microscope (FEG-SEM) with a precise FIB (FEI Helios G4 CX DualBeam).

3.2.1.4 Scanning electron microscope (SEM)

A focused electron beam is scanned by a scanning electron microscope (SEM) over a surface for the creation of an image. The electrons in the beam communicate with the sample, resulting in the production of different signals capable of being utilised in obtaining information regarding the surface topography and composition [295].

The morphological and compositional characterisation of some of Ge-Se and Ge-Sb-Se thin films in this work are carried out using a Hitachi Tm3030Plus Tabletop microscope, equipped with EDX X-Stream-2

3.2.2 Optical characterisation

3.2.2.1 Photoluminescence (PL) spectroscopy

Photoluminescence (PL) spectroscopy is an optical method of probing the materials' electronic structure that is contactless and versatile, as well as non-destructive and powerful. Light is focused on a sample, where absorption takes place and excess energy imparted into the material in a procedure known as photoexcitation. A possible method of dissipating this excess energy by the sample is through light emission or luminescence. This luminescence, in photoexcitation case, is known as PL. Therefore, the spontaneous light emission from the material under optical excitation is known as PL. It is possible to collect this light and analyse it spectrally and spatially, as well as temporally. A direct measure of different significant material properties is this PL power and spectral content.

Photoexcitation results in the movement of electrons within the material into excited states. Upon the return of these electrons to their stability states, they will release excess energy which possibly includes light emission (a radiative process) or excludes light emission (a non-radiative process), as shown in Fig. 3.13. The emitted light's energy (PL) is associated with the difference in levels of energy between the two-electron states engaged in the transition between the excited state and the stability state, while the amount of light emitted is associated with the radiative process's comparative contribution. Information given by PL spectroscopy is only on the low-lying levels of energy of the investigated system. The most common radiative transition in semiconductor systems is between states in the conduction and valence bands using the energy difference known as the band gap. Excitation during a PL spectroscopy experiment is made available by laser light having energy that is much larger compared the optical band gap consisting of electrons and holes relaxing toward their respective band edges and recombined through the emission of light at the band gap's energy that make up the photo-excited carriers. There is the possibility of radiative transitions in semiconductors involving localised defects or an impurity, thus, the PL spectrum analysis leading to the specific

identification of defects or impurities, and the PL signal magnitude making the determination of their concentration possible. It is possible to estimate the radiative and nonradiative recombination rates respectively from a careful temperature variation analysis of the PL intensity and PL decay time. There is activation of nonradiative recombination channels and the exponential decrease of PL intensity at higher temperatures. Thus, PL is a photon excitation process followed by emission of a photon. This is important in the determination of band gap and purity, as well as semiconducting material's crystalline quality and impurity defect levels. It also assists in comprehending the fundamental physics of the recombination mechanism [299].

There are differences between the PL spectrum and the absorption spectrum. Transitions from the ground state to excited state are measured by absorption spectrum, while transitions from the excited state to the ground state are dealt with PL. There is a characteristically extreme short period between absorption and emission. An excitation spectrum is an emission intensity graph against excitation wavelength much similar to an absorption spectrum. It is possible to make use of the wavelength value at which energy is absorbed by molecules as the excitation wavelength which makes a more intense emission available at a red-shifted wavelength, using a value that is usually double that of the excitation wavelength.

Figure 3.14 displays the PL spectroscopy block diagram setup. An Edinburgh Instruments FLS920 spectrometer was used, in obtaining the PL spectra. This is made up of a light source and excitation, as well as emission monochromator, sample cell, and a cooled photomultiplier tube (PMT) detector for the infrared light. Liquid nitrogen cools near infrared-red PMT while the temperature is made to remain steady at -80°C . The focus of the light beam producing laser diode was on the sample. The 980 nm laser diode excitation wavelength was used in obtaining the emission from excited Er^{3+} ions within the 1400-1700 nm range, which happens to be the Er^{3+} ions (${}^4\text{I}_{13/2}$ - ${}^4\text{I}_{15/2}$) emission bandwidth. The PMT detector collected the

emission signal, and a computer running software tool named F900 was used in recording and plotting the intensity of emission versus wavelength.

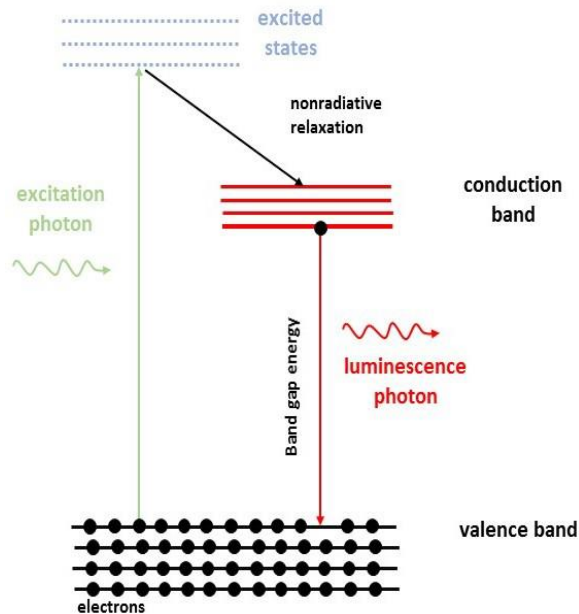


Fig. 3.13: Principle of photoluminescence spectroscopy (PL) [300].

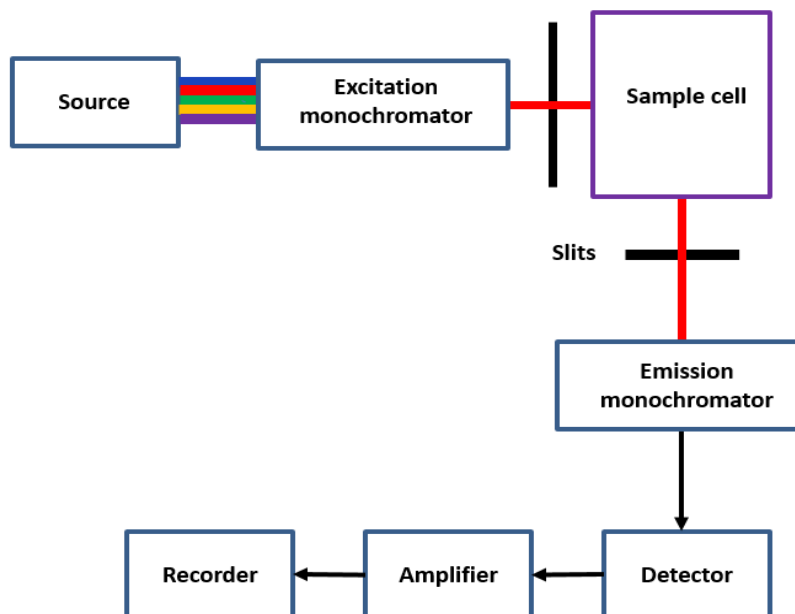


Fig. 3.14: Block diagram of fluorescence spectrometer [301].

3.2.2.1.1 Time-resolved photoluminescence (TRPL)

Time-resolved PL is a standard PL spectroscopy extension where a short laser pulse is used for excitation. There is no immediate ending of the PL

process after pulse excitation, but it rather goes on for a while until a ground state is reached by all the excited electrons. This technique measures the excited electron's lifetime before its relaxing to a ground state. A laser pulse generator was utilised in generating the pulsed signals for these measurements, and an oscilloscope is used in examining the process. The period and a pulse width possessed by the pulsed laser source are 100 ms and 10 μ s, respectively. The recording of the signal intensity was made as a function of time and the lifetime derived through the fitting of the intensity data with an exponential curve.

In this work, NIR emission spectra and lifetime of the Er³⁺-doped Ga-La-S bulk sample and as-deposited thin films were measured using a fluorescence spectrometer (FS920; Edinburgh Instruments, UK) equipped with semiconductor laser diode emitting 980 nm excitation source at room temperature.

3.2.2.2 Ultraviolet–visible (UV-Vis-NIR) spectroscopy

A UV-Vis-NIR spectrophotometer makes provisions for ways of analysing of liquids and gases, together with solids by using radiant energy in the far and near-ultraviolet, as well as invisible and near-infrared electromagnetic spectrum regions. The definitions of the predetermined electromagnetic radiation wavelengths for ultraviolet (UV) and for visible (Vis), as well as near-infrared (NIR) radiation, are as follows:

UV radiation: 100 to 400 nm

Vis radiation: 400 to 765 nm

NIR radiation: 765 to 3200 nm

Two sources of light are used by the UV-Visible spectrophotometer. The first is a deuterium (D2) lamp which produces ultraviolet light. The second is a tungsten (W) lamp which produces visible light. The light beam, upon bouncing off from a mirror (mirror 1, Fig. 3.15), goes through a slit and strikes a diffraction grating. It is possible for the grating to be rotated, thereby making room for the selection of a precise monochromatic wavelength

which goes through a slit successfully. A filter is then used to remove unwanted higher diffraction orders. A second mirror receives by the light beam before getting split by a half mirror (50% of the light is reflected, the other 50% passes through). One of the beams is permitted to go through a reference cuvette (containing the solvent alone), the other goes through the sample cuvette. The measurement of the intensities of the light beams is then taken at the end.

In this work, the transmission property of the thin films was measured by PerkinElmer Lambda 950 High- Performance UV-Vis/NIR spectrometer. The ions concentrations were discovered to be below this system's detection capabilities as a result of the basic nature of this work directed towards the GhGs doped thin films' fabrication. This is aggravated by the strong visible Si absorption, thereby disguising any absorption indication from any such ions.

The characterisation of silicon thin films' absorption properties is, however, possible. Their optical band gap's determination is the primary interest of the fabricated Si thin films' transmission spectra. The optical band gap, in contrast to the electronic band gap, is defined as the least photon energy necessary for the generation of an electron-hole pair (exciton). One has the ability to characterise the material's optical band gap by manipulating the mentioned equation in the "2.2.1.3 optical properties" section [105, 106].

A material's optical band gap can be calculated through the application of a linear slope to the curve's linear region, where the x-intercept is discovered to be the optical band gap, which is highly helpful in comprehending the deposited silicon thin films' material properties as it makes it possible for the particle size's interpretation. A decrease in particle size results in the rise of the band gap, which is apparent through a Tauc plot formation.

Before a transmission scan is performed on a deposited chalcogenide thin film, a clean, blank silicon substrate of matching thickness is used to take a reference scan, so that the following measurement will only be as of the result of thin film contributions.

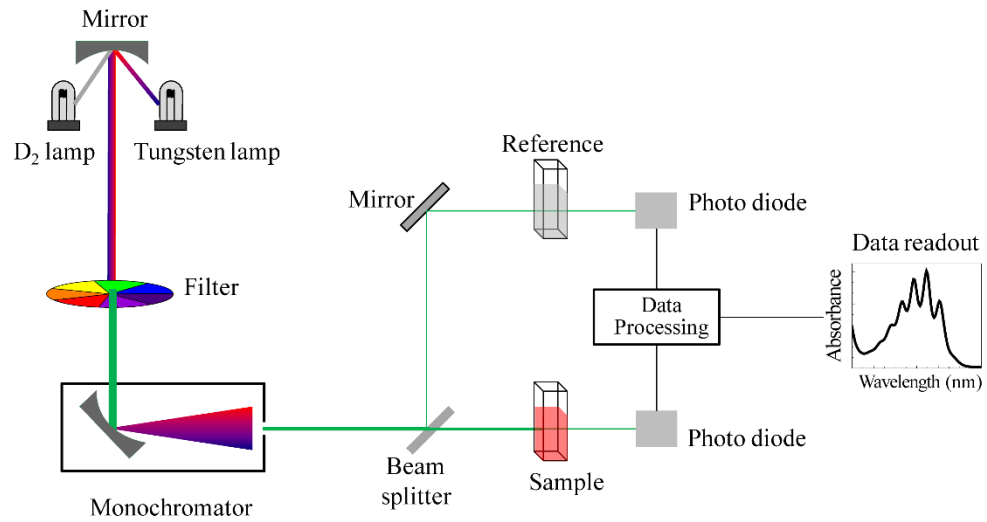


Fig. 3.15: Schematic diagram of UV–Vis–NIR spectrophotometer [302].

This chapter has explained the fs-PLD method used to deposit ChGs thin films followed by description their characterisation techniques utilised in this investigation, including; structural and optical characterisations. Thus, the results and analysis obtained are illustrated and described in the next chapters.

Chapter 4: Gallium lanthanum sulphide (Ga-La-S) deposition on silicon

4.1 introduction

Fs-PLD is a relatively uncomplicated and straightforward method for depositing a thin film, although, in practice, the need for precise control over deposition parameters to achieve good quality films is required. Deposition parameters, such as the rate of deposition, the ablated nanoparticles kinetic energy, and the mobility of the particles forming the thin film can be controlled by changing the deposition parameters, like substrate temperature, the repetition rate of the laser, laser fluence, and processing gas pressure. Optimal process parameters are often unique for different target materials.

This chapter describes the fabrication of gallium lanthanum sulphide Ga-La-S ($65\text{Ga}_2\text{S}_3:35\text{La}_2\text{S}_3$) thin film onto Si substrate by varying fs-PLD process parameters, such as substrate temperature, deposition period, and fs-laser energies to study their structural properties. This chapter aimed to obtain the best possible process parameters in terms of fabricating a good quality Ga-La-S thin film.

4.2 Deposition of gallium lanthanum sulphide (Ga-La-S) glass

The ingot of Ga–La–S glass target material employed in this research work has a composition of $65\text{Ga}_2\text{S}_3:35\text{La}_2\text{S}_3$, and was purchased from ChG Southampton Ltd at the Southampton University, UK. Table 4.1 below exhibits some of the primary optical and thermal properties of the Ga-La-S glass target, while Fig. 4.1 shows images of both the target glass and glass holder.

Table 4.1: Properties of $65\text{Ga}_2\text{S}_3:35\text{La}_2\text{S}_3$ glass [144, 158]

Optical	
Refractive index at $0.589\ \mu\text{m}$	2.493
Approximate transmission range (μm)	0.53-10.5
Thermal	
Glass transition temperature T_g ($^\circ\text{C}$)	580
Melting temperature ($^\circ\text{C}$)	830

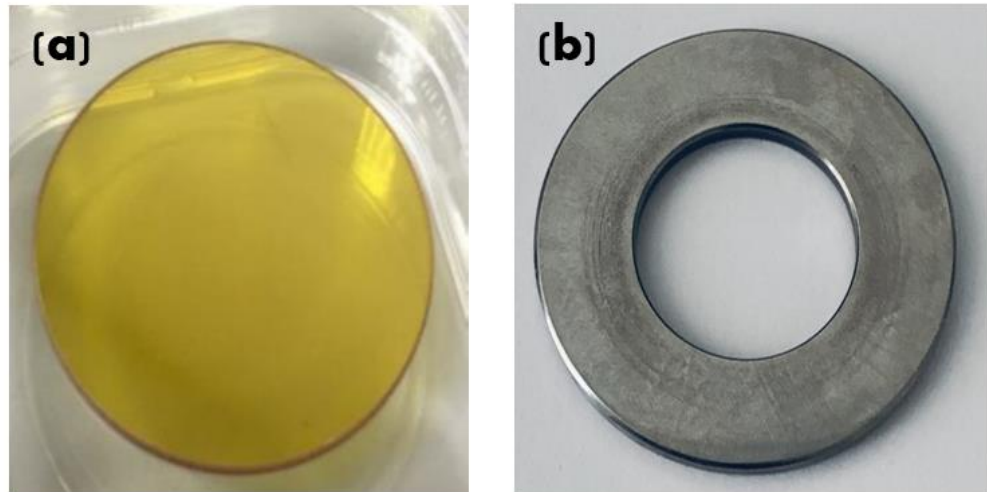


Fig. 4.1: (a) Pure Ga-La-S target glass and (b) target glass holder used to fabricate thin film in the fs-PLD.

4.3 Effect of substrate temperatures on the Ga-La-S thin film deposit on Si (100) substrate

The Ga-La-S thin films were fabricated at four different substrate temperatures, which range from 450, 500, 550, to 600°C, while keeping all other process parameters constant. Table 4.2 below shows the deposition parameters of four samples (G1, G2, G3, and G4) fabricated at each temperature.

Table 4.2: The deposition parameters for G1, G2, G3, and G4 employed in investigating the effect change in substrate temperature of Ga-La-S onto Si substrate

Process parameter	Operating conditions
Substrate	Silicon; dimensions 20 mm Length (L) × 12 mm Width (W) × 675µm Thickness (T)
Target material	65Ga ₂ S ₃ : 35La ₂ S ₃
Target to substrate distance (d_{st})	70 mm
Fs-laser repetition rate	1.0 kHz
Fs-laser energy	30 µJ
Background gas pressure	80 mTorr - Argon gas (Ar)
Substrate temperature (sample ID)	450°C (G1), 500°C (G2), 550°C (G3), and 600°C (G4).
Deposition time	2 hours

4.3.1 TEM analysis of the Ga-La-S thin films

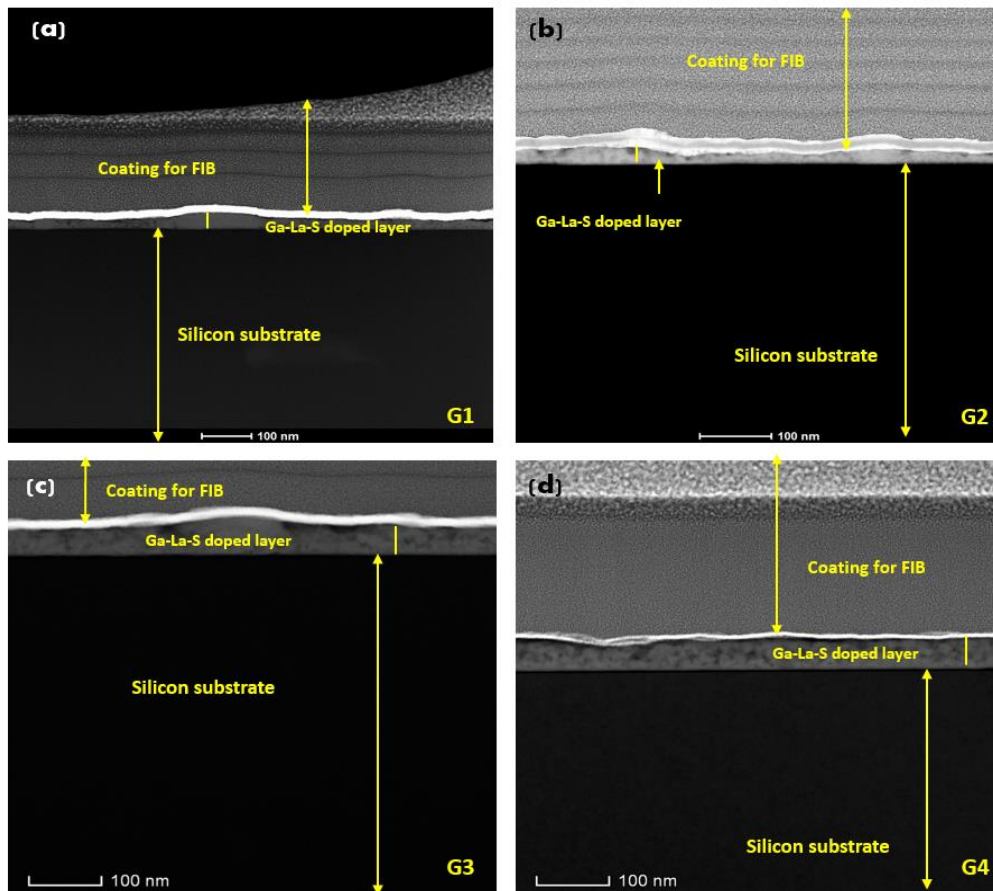


Fig. 4.2: TEM cross-section images of Ga-La-S thin film on silicon glass substrates by fs-PLD at different substrate temperatures; **(a)** 450°C (G1), **(b)** 500°C (G2), **(c)** 550°C (G3), and **(d)** 600°C (G4).

Figure 4.2 (a-d) shows the TEM cross-sectional images of the Ga-La-S thin films deposited at substrate temperatures range between 450 and 600°C. The lower black layer represented a silicon substrate and the bright middle layer on the silicon substrate corresponds to Ga-La-S thin film. The top layer denoted iridium (Ir) used for coating the surface of the Ga-La-S thin film. TEM analysis was also employed to evaluate the thin film thicknesses. The average thickness for deposited Ga-La-S thin films was found to be around 25 nm at 450°C, 38 nm at 500°C, 58 nm at 550°C, and 54 nm at 600°C for samples G1, G2, G3, and G4, respectively. The Ga-La-S film thickness increased with an increase in temperature due to the sintering and coalescence of small grains to form larger grains. Fs-PLD predominantly contains nanoparticles than ions. At higher temperature they coalesce to

form larger particles or crystallites. This confirmed later in XRD result (Fig. 4.7).

4.3.2 STEM-EDX analysis of the Ga-La-S thin film deposited at 600°C

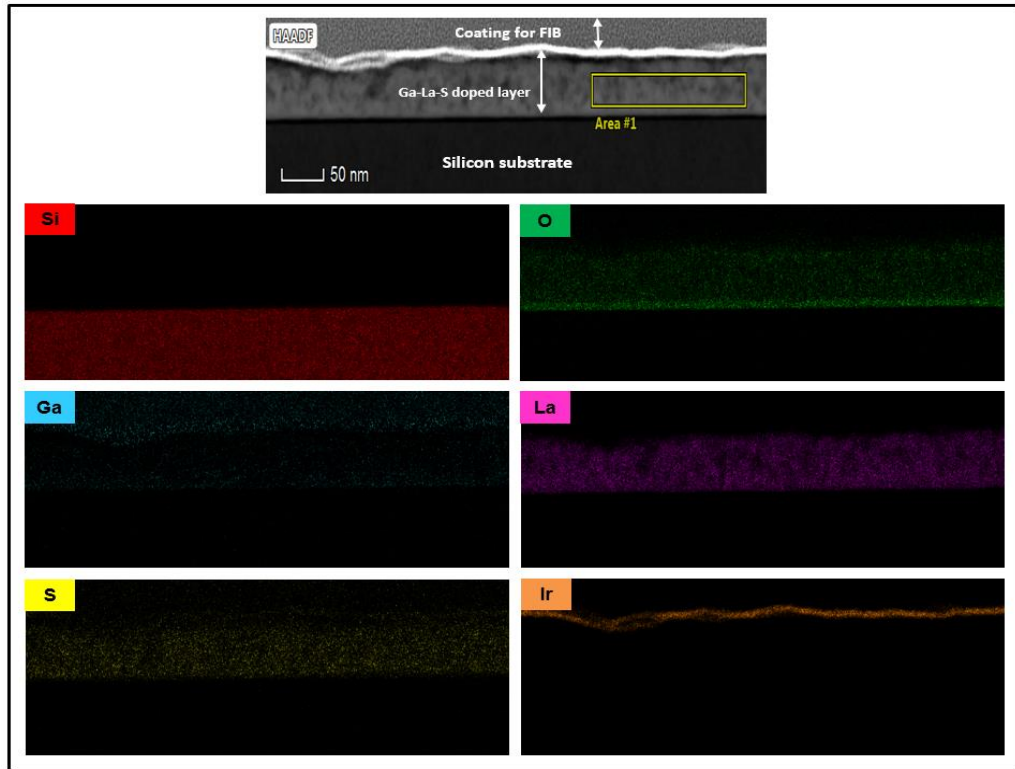


Fig. 4.3: HAADF-STEM image and STEM-EDX elemental mapping image of Ga-La-S thin film deposited on silicon at a substrate temperature of 600°C (sample G4).

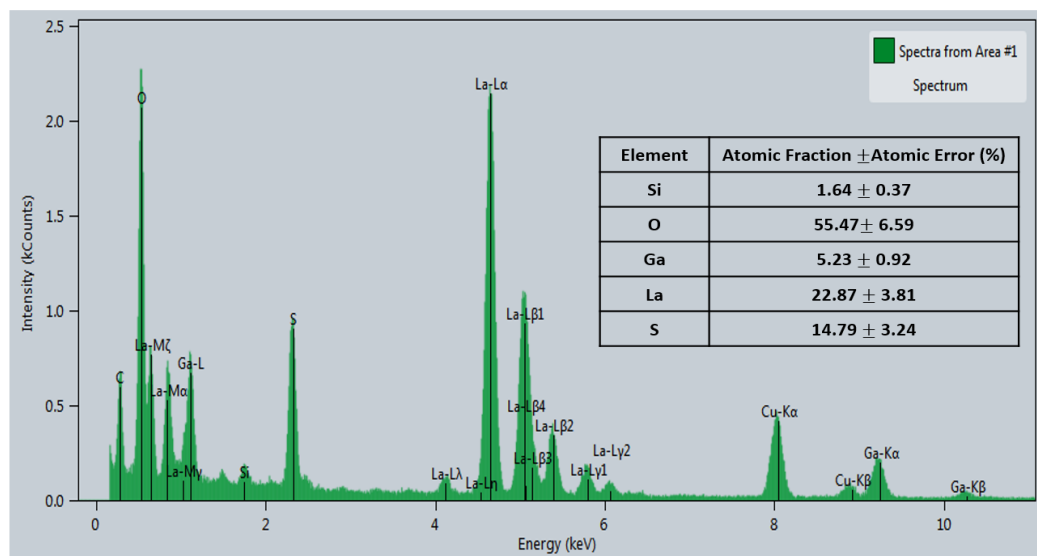


Fig. 4.4: STEM-EDX spectrum of the Area#1 labelled in Fig. 4.3.

Figure 4.3 shows an elemental mapping by a TEM-EDX, which indicated the presence of silicon (Si), oxygen (O), gallium (Ga), lanthanum (La), sulfur (S), and iridium (Ir) elements, respectively. The figure shows a relatively homogeneous distribution of Ga, La, and S in the Ga-La-S film grown at 600°C, while the elements were clearly distributed unevenly.

Figure 4.4 shows the EDX spectrum of the elemental composition of the region indicated area#1 in the high angle annular dark field (HAADF) image depicted in Fig. 4.3. The concentration of Ga (~5 at. %) and S (~15 at. %) in the Ga-La-S layer was low when compared to La concentration, which is found to be ~23 at. %. The EDX map analysis revealed that no silicon was detected in the Ga-La-S film prepared on silicon at a higher substrate temperature (600°C). This is a clear demonstration that there is no intermixing or interdiffusion between the Ga-La-S film and Si substrate.

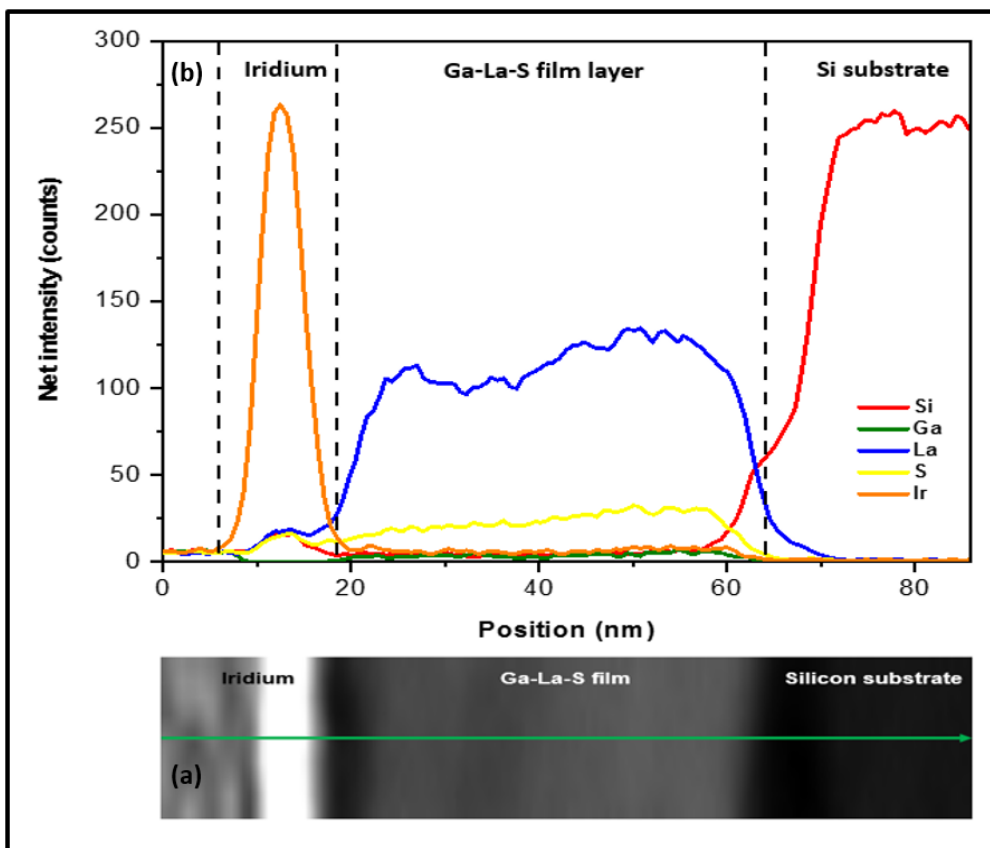


Fig. 4.5: (a) A HAADF-STEM image and (b) a line scan obtained from STEM-EDX showing that no silicon was detected in the Ga-La-S thin film prepared on silicon at a higher substrate temperature (600°C).

To evaluate the elemental distribution of the Ga-La-S thin film grown on Si substrate, an EDX line scan of a sample G4 fabricated at a substrate temperature of 600°C was performed. The result line scan is shown in Fig. 4.5 (b), which exhibited a homogeneous distribution of La, and S in the Ga-La-S thin film grown. Gallium atoms start to evaporate after the deposition at 600°C. This observed distribution agreed well with the elemental mapping by STEM-EDX in Fig. 4.3.

4.3.3 XRD patterns of the Ga-La-S thin film prepared at different substrate temperatures

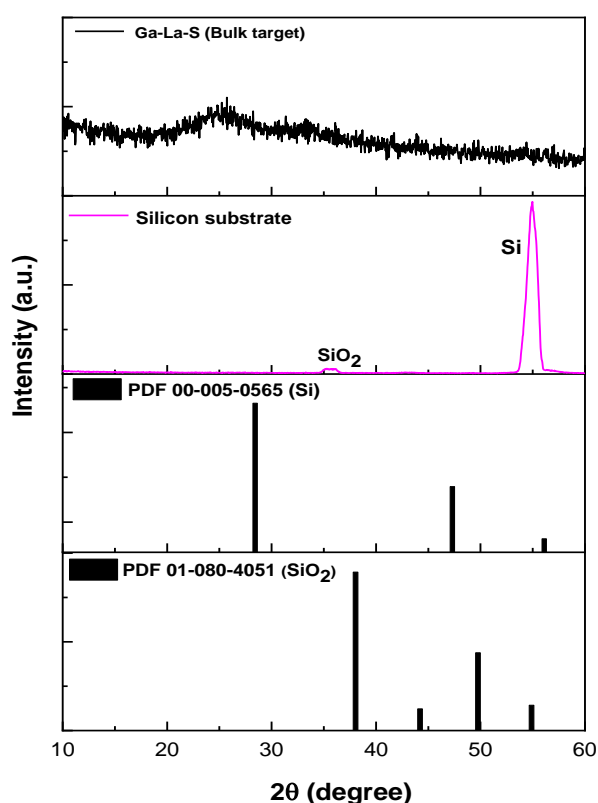


Fig. 4.6: XRD patterns of pure silicon substrate (thickness = 675 μm), Ga-La-S bulk glass, and ICDD reference patterns for silicon and silica.

The crystalline structure of the Ga-La-S thin film deposited at various substrate temperatures was investigated by XRD pattern, in a 2θ-range between 10 and 60°. Figure 4.6 shows the XRD results of the silicon substrate and bulk glass along with ICDD reference patterns for silicon and silica. The silicon substrate revealed two significant peaks centred at 36° (111) and 56° (311), which confirmed that the substrate is crystalline and

consists of Bragg's reflection of cubic silicon [303-305]. The sharp peak occurred at 56° corresponded with the silicon ICDD (International Centre for Diffraction Data) pattern No. 00-005-0565. The other peak located at 36° is indexed to the ICDD diffraction pattern No. 01-080-4051 for silica. No sharp peaks were observed in the XRD pattern of the Ga-La-S target glass, but, rather, a broad halo amorphous structure occurs between $2\theta = 20^\circ$ and $\sim 30^\circ$ [133, 306].

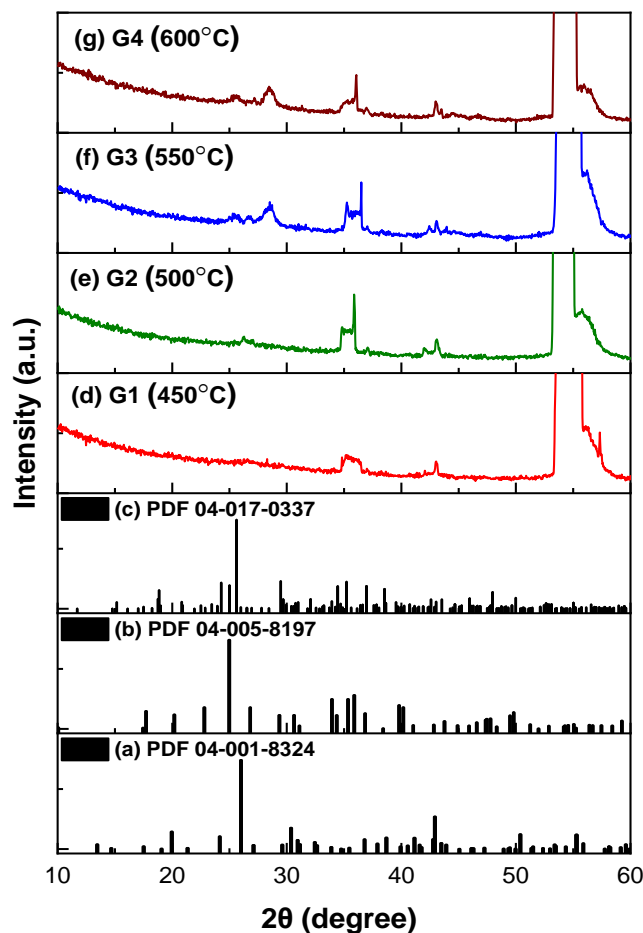


Fig. 4.7: XRD patterns of Ga-La-S thin film deposited on silicon at various substrate temperatures; 450, 500, 550, and 600°C along with ICDD reference patterns for Ga-La-S bulk glass.

The XRD patterns of the Ga-La-S thin films deposited at different substrate temperatures between 450°C and 600°C is also presented in Fig. 4.7 (d-g) above. All the samples fabricated at these temperatures revealed intense peaks of silica and silicon at $2\theta = 37^\circ$ and 56° , respectively, as observed from the Fig. 4.6. The Ga-La-S thin film fabricated at 450°C exhibited the amorphous phase, whereas those synthesised above 450°C are crystalline,

as shown in Fig. 4.7 (d-g). The crystalline peaks of these Ga-La-S thin films occur at $\sim 2\theta = \sim 26^\circ$, 35° , and 43° , which could be assigned to $\text{La}_{1.67}\text{Ga}_3\text{S}_7$ (ICDD No. 04-001-8324), $\text{La}_3\text{Ga}_{1.67}\text{S}_7$ (ICDD No. 04-005-8197), and $\text{La}_{1.67}\text{Ga}_3\text{S}_7$ (ICDD No. 04-001-8324), respectively. Furthermore, an increase in the substrate temperature to 550°C and 600°C resulted in the emergence of two additional new crystalline peaks at $2\theta = \sim 25^\circ$ and 28.5° . These peaks were not found in the previous samples (G1 and G2) and are in good agreement with $\text{LaGaS}_3\text{La}_3$ based on ICDD pattern No. 04-017-0337. These results clearly demonstrated that the substrate temperature had a significant impact on the structural and phase transformation behaviour of the Ga-La-S films. The crystallisation increased with an increase in the substrate temperature from 450 to 600°C according to the XRD results.

4.3.4 Raman spectroscopy of Ga-La-S thin film fabricated at different substrate temperatures

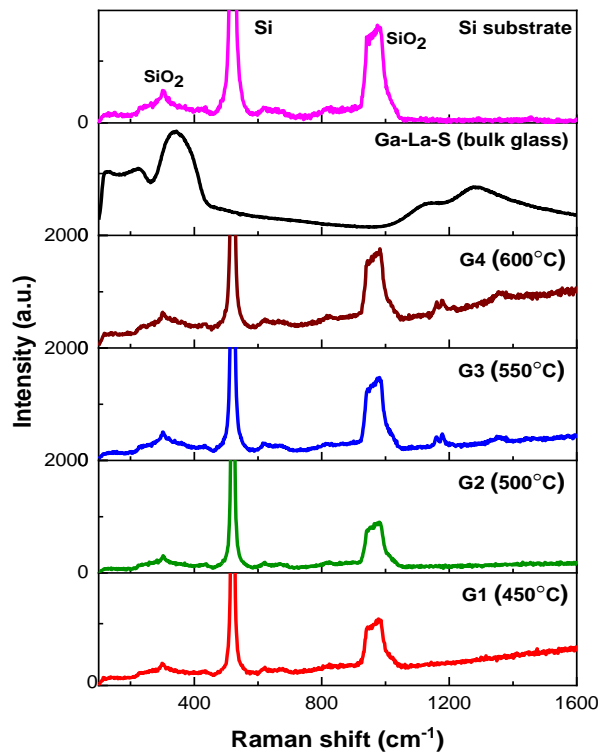


Fig. 4.8: Raman spectra of a pure Si substrate (thickness = $675 \mu\text{m}$), Ga-La-S bulk glass, and thin films deposited on Si at various substrate temperatures; 450 , 500 , 550 , and 600°C .

Figure 4.8 shows the Raman spectra for a pure Si substrate, a bulk Ga-La-S target, and the Ga-La-S thin films deposited on Si substrate, by employing an argon laser excitation source at 514.5 nm. The silicon substrate spectrum revealed a peak at $\sim 520\text{ cm}^{-1}$, which is associated with single crystalline silicon [307, 308]. Two additional broad but weak peaks were also observed at ~ 300 and $\sim 990\text{ cm}^{-1}$, which represented an amorphous fraction of silica [308-310].

The Raman spectrum of the Ga-La-S bulk glass in Fig. 4.8 has four main features, which are centred at 225, 337, 1116, and 1270 cm^{-1} . The vibration band occur at a lower frequency of 225 cm^{-1} is attributed to GaS_4 vibration. Moreover, the vibration band centred around 337 cm^{-1} is connected to GaS_4 tetrahedra vibrations overlapping with LaS_8 vibrations in the Raman spectra of Ga-La-S glass [129, 311-313]. The vibration bands arising at 1116 cm^{-1} and higher frequency are probably attributed to impurities in the Ga-La-S.

In Figure 4.8 above, the Raman spectra of the prepared Ga-La-S thin films can also be seen. Vibration bands around 300, 520, and 990 cm^{-1} were observed for all the Ga-La-S thin film samples; these lines were assigned to Si and SiO_2 . The samples fabricated at 450°C (G1) and 500°C (G2) exhibited the only peaks observed in the Raman spectra of the silicon substrate. However, no Raman vibration band is observed at a higher frequency above 1000 cm^{-1} . By increasing deposition temperature of the substrate to 550°C (G3) and 600°C (G4), the Raman spectra revealed new vibration bands at around 1200 cm^{-1} and 1350 cm^{-1} . These new vibration bands correlated with the Raman spectrum of the bulk glass impurity.

4.4 Effect of fs-laser energy and deposition time of Ga-La-S thin film on Si (100) substrate

This section investigates the impact of using various laser energies and deposition time to obtain optimal parameters for preparing Ga-La-S thin films at a substrate temperature of 450°C . Table 4.3 below exhibits the details of three samples of G1 [already discussed in section 4.3], and two new samples G1B and G1C fabricated at different length of time and laser

energy, while keeping all other process parameters constant [shown in Tables 4.3 and 4.4].

Table 4.3: Experimental variables used for fabricating Ga-La-S samples described in this section

Sample ID	Fs-laser energy (μJ)	Deposition time (h)
G1	30	2
G1B	50	2
G1C	50	4

Table 4.4: Constant parameters utilised in fabricating Ga-La-S thin film samples at different laser energies and duration

Substrate	Silicon; dimensions 20 mm (L) \times 12 mm (W) \times 675 μm (T)
Target material	65Ga ₂ S ₃ :35La ₂ S ₃
Target to substrate distance	70 mm
Fs-laser repetition rate	1.0 kHz
Background gas pressure	80 mTorr – Argon gas (Ar ⁺)
Substrate temperature	450°C

4.4.1 TEM cross-section of Ga-La-S thin film samples fabricated at different deposition times and laser energies

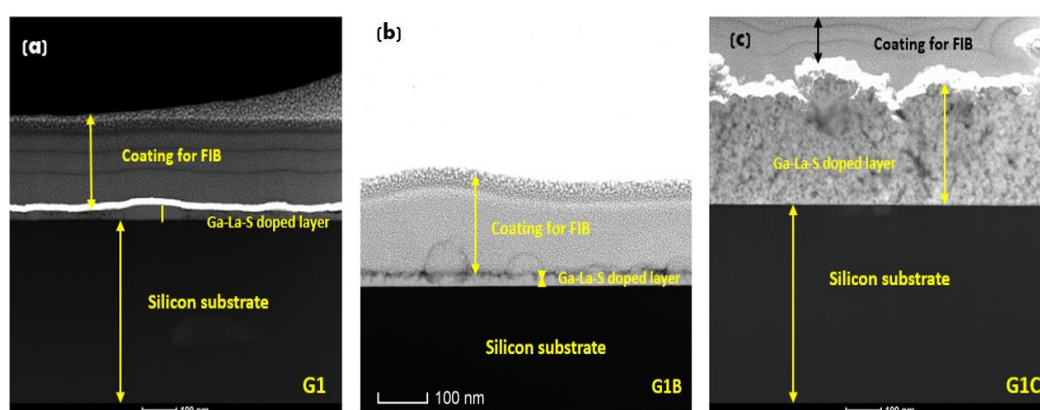


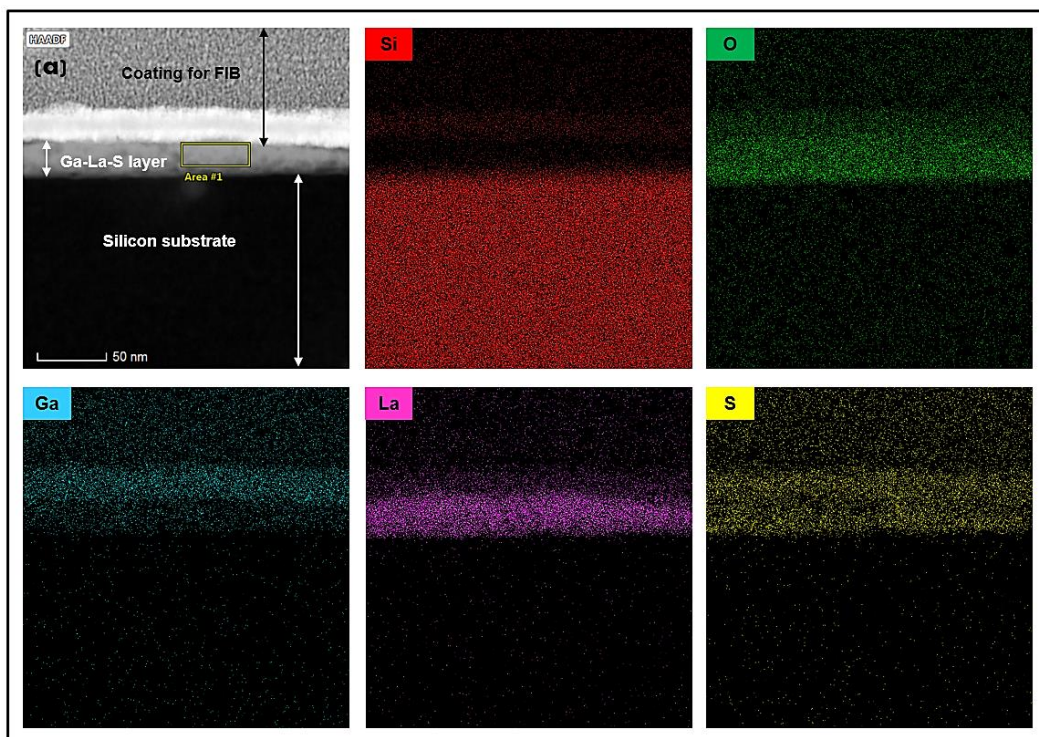
Fig. 4.9: TEM cross-section images of the Ga-La-S thin film deposited on a silicon substrate at different laser energies and depositions times: **(a)** G1 sample prepared with 30 μJ for 2 h, **(b)** G1B sample prepared with 50 μJ for 2 h, and **(c)** G1C sample prepared with 50 μJ for 4 h.

The cross-sectional images of the Ga-La-S thin film prepared at various deposition times and laser energies were investigated by employing TEM,

as shown in Fig. 4.9. It was observed that the cross-section thickness of the samples G1 and G1B varied with increasing the laser energies. Samples G1 and G1B had film thicknesses of ~25 nm and ~50 nm, respectively. Besides, the nanoparticle grain size of Ga-La-S layer increased with increasing laser energy (50 μ J), as shown in Fig. 4.9 (b).

Furthermore, the deposition time also increased from 2 to 4 hours to fabricate another Ga-La-S thin film [Fig. 4.9 (c)]. In contrast to earlier findings [Fig. 4.9 (b)], sample G1C film fabricated for 4 hours with 50 μ J had a thickness of ~200 nm, which is about four times thicker than sample G1B. Besides, the TEM imaging revealed that the nanoparticle size increased with increasing deposition time, and the grain size expanded to the full height of the layer. Hence, this result demonstrated that fabricating Ga-La-S thin film for a longer period has detrimental effects on the film thickness and the quality of the thin film.

4.4.2 STEM-EDX of samples deposited at different length of time and laser energies



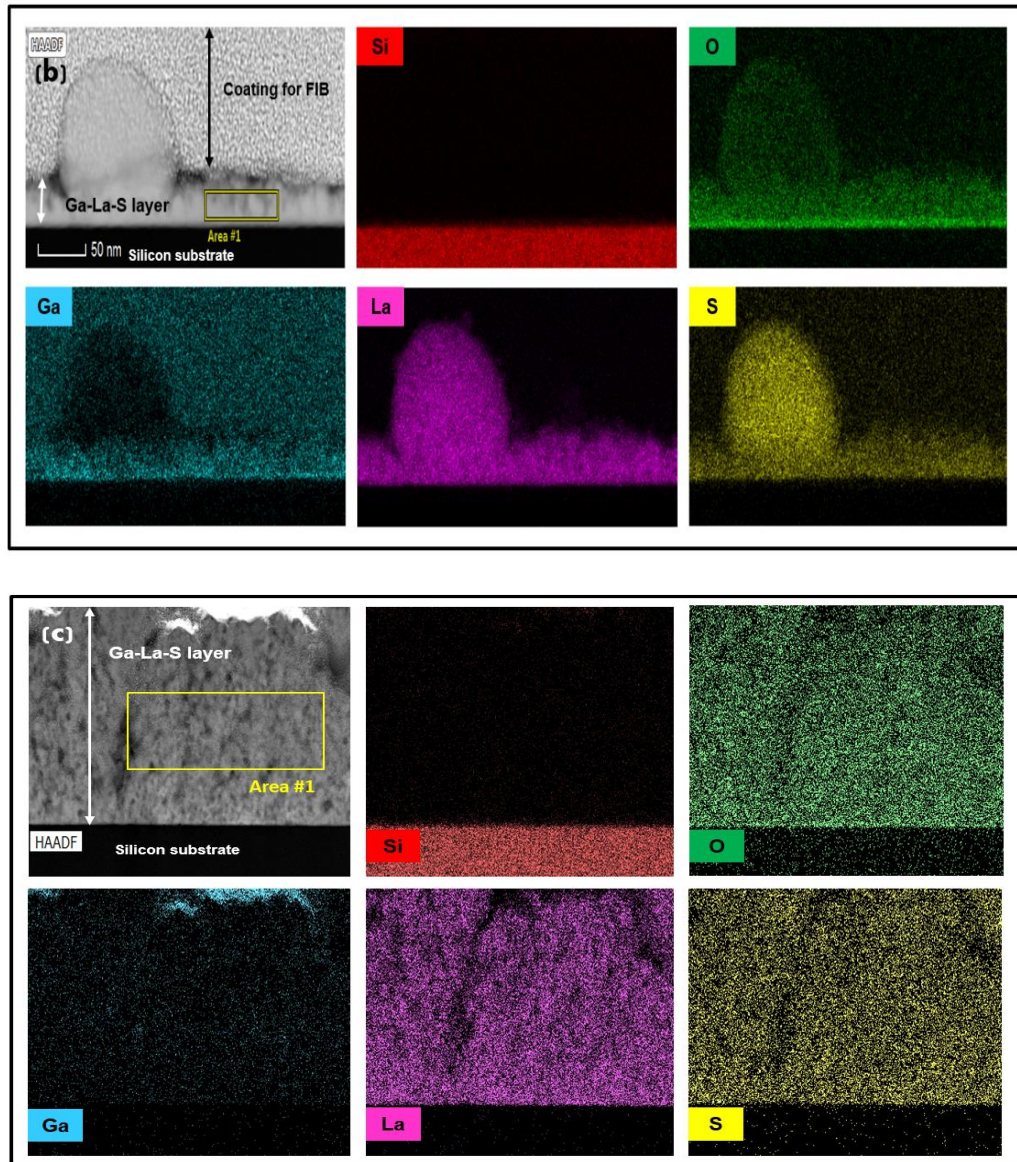


Fig. 4.10: HAADF-STEM images and STEM-EDX elemental mapping obtained during the cross-sectional TEM analysis of; **(a)** G1 sample prepared with 30 μJ for 2 h, **(b)** G1B sample prepared with 50 μJ for 2 h, and **(c)** G1C sample prepared with 50 μJ for 4 h.

EDX analysis of the thin films manufactured at different laser energies and varying deposition times was carried out to provide an insight into the elemental distribution within Ga-La-S thin film. In Fig. 4.10, TEM cross-sectional images and the results EDX-STEM analysis of the Ga-La-S thin films (composed of Si, O, Ga, La, and S) are presented. It shows a homogeneous distribution of Ga, La, and S in the Ga-La-S films. It was found that La and S contents were dense and evenly distributed in the entire films when compared to Ga content, which appeared to have evaporated as

the laser energy and deposition time increased. It has appeared that La content in all thin films is higher than S and Ga [see Table 4.5]. Also, it should be noted that there is no intermixing between the silicon substrate and Ga-La-S film deposited.

Table 4.5: The elemental concentration of different Ga-La-S specimens at measured areas #1 shown in TEM-HAADF images obtained in Fig. 4.10.

Sample	Chemical composition (net. %)				
	Ga	La	S	Si	O
G1 (2h - 30 μ J)	6.65 \pm 1.65	27.09 \pm 8.09	13.57 \pm 3.80	3.27 \pm 0.95	49.43 \pm 10.40
G1B (2h - 50 μ J)	10.74 \pm 1.88	29.78 \pm 4.7	18.50 \pm 4.06	4.25 \pm 0.96	36.74 \pm 4.28
G1C (4h - 50 μ J)	2.83 \pm 0.14	32.04 \pm 7.6	12.76 \pm 0.24	1.16 \pm 0.04	51.20 \pm 0.57

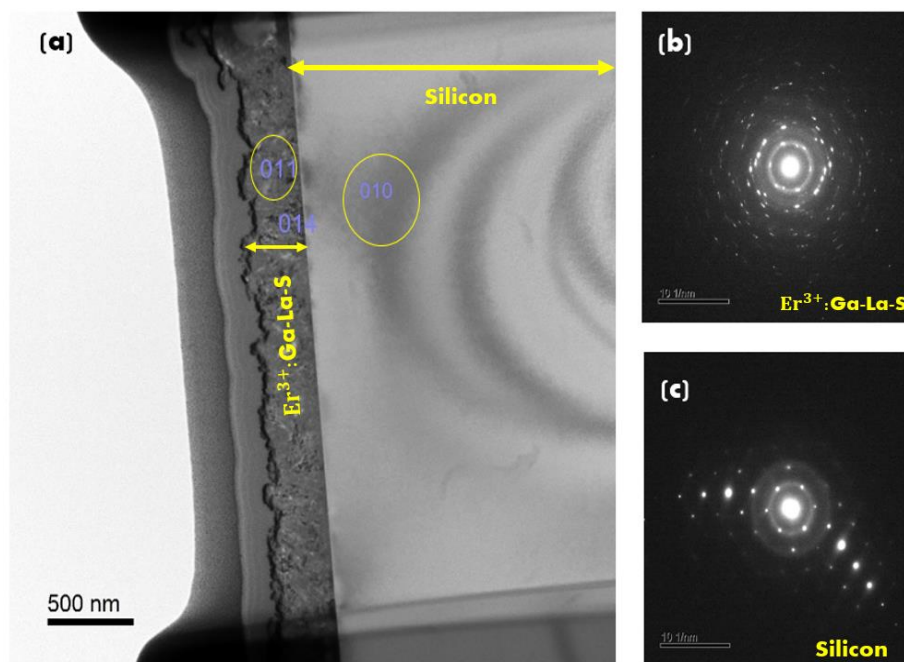


Fig. 4.11: (a) Cross-sectional bright-field BF-TEM image of Ga-La-S film of G1C sample prepared with 50 μ J for 4 hours at 450 $^{\circ}$ C, (b) SAED pattern captured from Ga-La-S layer, and (c) SAED pattern captured from the silicon substrate region.

The morphology of the crystalline Ga-La-S thin film of G1C sample was characterised by using the SAED method and shown in Fig. 4.11. Both distinct zones had visible diffraction spots obtained from characteristic

crystalline planes. As can be seen in Fig. 4.11(a), the FIB preparation processes produced a high density of dislocation in the film matrix; this had an impact on observations in the diffraction pattern. In Figure 4.11(b), the film's diffraction pattern indicated streaks on the spots. These are usually caused by a high amount of accumulation of dislocations. Also, there were a large number of partial rings caused by the orientation. In the pattern the spots transform from their characteristic circular form, becoming elongated and less regular, appearing as a disk-type halo. At a local level, the distortions affected the crystal orientation; the spots of diffraction were extended the length of the diffraction. The SAED pattern in Fig. 4.11 (c) exhibits a spot diffraction pattern from single-crystal silicon.

4.4.3 Influence of deposition time and laser energy on the deposited Ga-La-S thin film (XRD)

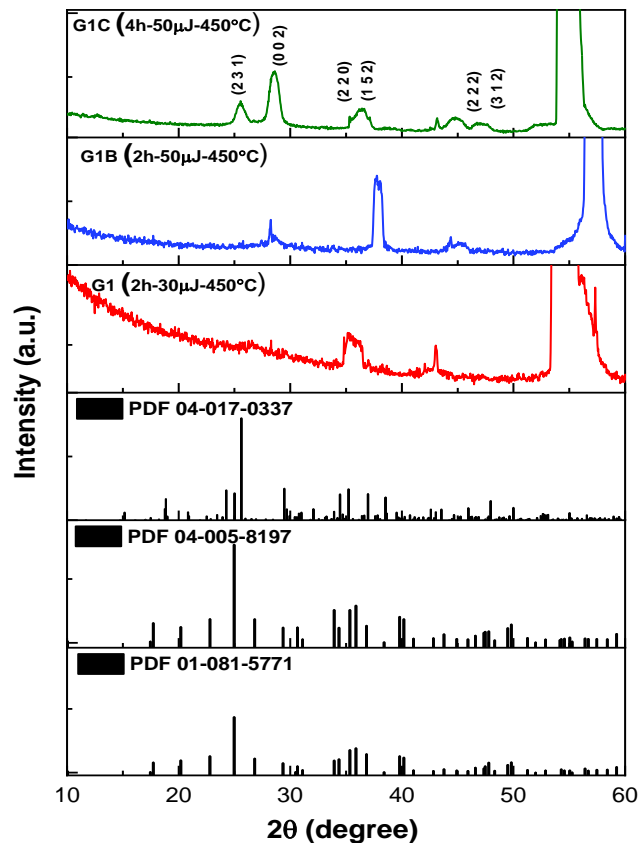


Fig. 4.12: XRD patterns of the Ga-La-S thin films deposited on silicon glass substrates by fs-PLD at various deposition times and laser energies.

Figure 4.12 presents XRD results obtained for samples prepared with 30 μJ (G1), and 50 μJ (G1B) for a period of 2 hours at 450°C. As can be seen from the Figure, the film deposited at 30 μJ was found to be amorphous in structure compared with the film fabricated by using 50 μJ laser energy [which was observed to be polycrystalline]. On the other hand, comparing samples of deposited at different length of time [2 h (G1B) and 4 h (G1C)], it has found that the film exhibited higher crystallisation structure as deposition time increased. It can be seen that the film deposited for 2 hours is relatively polycrystalline, while the film fabricated for 4 hours has diffraction peaks related to planes of bulk Ga-La-S. These diffraction patterns are in good agreement with the SAED pattern [Fig. 4.11(b)]. The XRD pattern peaks are indexed to ICDD pattern Nos: 00-04-017-0337 for Orthorhombic LaGaS₃. Comparing the XRD patterns of samples G1, G1B, and G1C on ICDD database, it is observed that the crystalline phase peaks are in agreement with La₆Ga_{3.3}S₁₄, La₃Ga_{1.67}S₇, and LaGaS₃, respectively, (ICDD reference patterns No. 00-01-081- 5771, 00-04-005-8197, and 00-04-017-0337). A similar observation has been reported previously elsewhere [133, 306].

4.4.4 Influence of laser energies and deposition time on the deposition of Ga-La-S thin film (Raman spectroscopy)

Figure 4.13 shows the Raman spectra of the Ga-La-S film for G1 and G1B samples deposited with laser energies of 30 and 50 μJ , respectively, for 2 hours. Vibration bands around 300, 520, and 990 cm^{-1} were observed for all the Ga-La-S thin film samples; these lines were assigned to Si and SiO₂. It also shows the Raman spectra of the Ga-La-S films for samples G1B and G1C with deposition times of 2 and 4 hours, respectively, when the laser energy was kept constant at 50 μJ . As it has already discussed in the above, peaks assigned to the silicon substrate were also observed in all the prepared films. In the case of Ga-La-S thin films deposited at different laser energies [G1 and G1B samples], no significant difference in the vibrational bands is observed. The presence of Ga-La-S bulk glass was only exclusively observed in sample G1C grown on the silicon substrate with 50

μJ for 4 hours, as shown in Fig. 4.13. The vibration band occur at a lower frequency of 225 cm^{-1} is attributed to GaS_4 vibration. Moreover, the vibration band centred around 337 cm^{-1} is connected to GaS_4 tetrahedra vibrations overlapping with LaS_8 vibrations in the Raman spectra of Ga-La-S glass [129, 311-313]. The vibration bands arising at 1116 cm^{-1} and higher frequency are probably attributed to impurities in the Ga-La-S. This is in good agreement with observations from XRD analysis [Fig. 4.12]. The absence of these peaks in G1 and G1B is due to their lower gallium, lanthanum, as well as sulphur content, compared to that of the G1C sample [see Table 4.5].

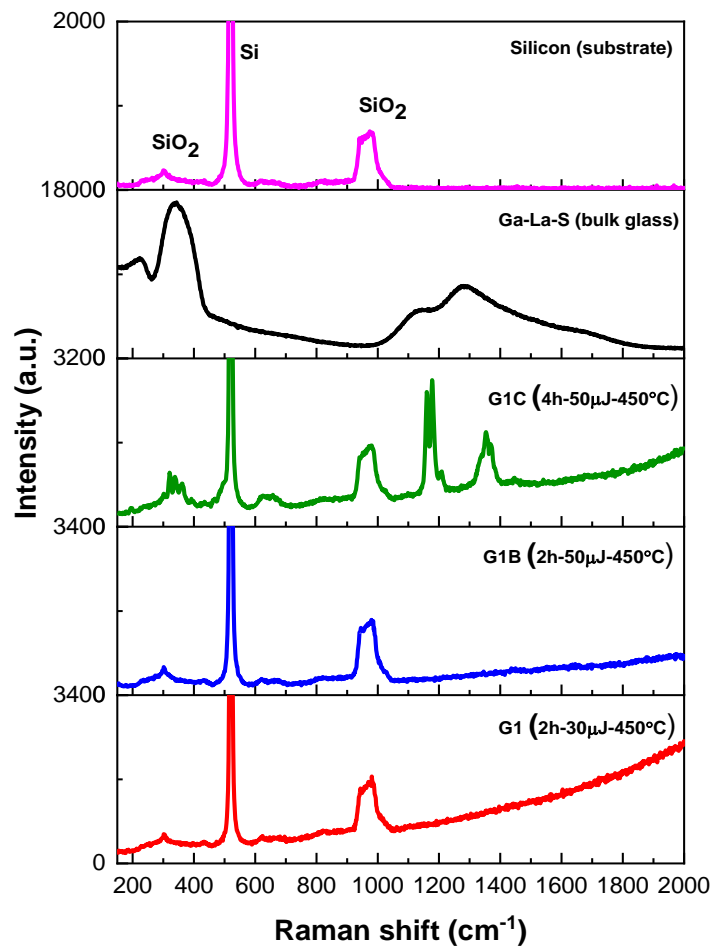


Fig. 4.13: Raman spectra of the Ga-La-S thin films deposited on silicon glass substrates at different time depositions and laser energies.

4.5 Conclusions

In conclusion, the fs-PLD approach influenced the effective deposition of Ga-La-S glass thin layers on unalloyed Si substrate. It was found that the

effectiveness of deposition was dependent on deposition temperature, deposition time, and laser energies. Systematic investigations were carried out to ascertain the consequence of deposition temperatures, laser energies, and deposition time on the limpid structure and thickness of the deposited films. Findings show an upsurge of limpid phases and the thickness of the film coinciding with an escalation in deposition temperature, laser energies, and deposition time. Moreover, the targeted chalcogenide glass changed its structural physiognomies from amorphous to crystalline. However, the observation of the Si substrate and the deposited Ga-La-S layer show no comportment of inter-diffusion and intermixing, which could relate to the chalcocite of the chalcogenide target glass quality.

Chapter 5: Erbium-doped gallium lanthanum sulphide (Er³⁺-doped Ga-La-S) deposition on silicon

5.1 Introduction

This chapter describes the fabrication of Er³⁺-doped gallium lanthanum sulphide (Ga-La-S) thin films with a nominal composition of Ga-La-S 65:34 + 1 mol% Er₂O₃ onto Si substrate. The fs-PLD technique was employed to deposit Er-Ga-La-S target material by varying process parameters, such as substrate temperature and working chamber pressure to study the structural, physical, and optical properties of the thin films. The aims and objective of this chapter are the same as the previous chapter (chapter 4).

5.2 Target material: Er-doped gallium lanthanum sulphide (Er³⁺-doped Ga-La-S) glass

Fig. 5.1 illustrates Er³⁺-doped Ga-La-S glass ingot from ChG Southampton Ltd GLS as well as the stainless-steel target holder for the fs-PLD chamber used to mount the target material inside the chamber during the thin film fabrication. The optical and thermal properties of this target glass such as refractive index, spectral transmission range, glass transition and melting temperatures are depicted in Table 5.1.



Fig. 5.1: Er³⁺-doped Ga-La-S bulk glass (**left**) and Er³⁺-doped Ga-La-S bulk glass holder (**right**) which is used for fs-PLD.

Table 5.1: Properties of Er³⁺-doped Ga-La-S glass [144, 158]

Optical	
Refractive index at 0.589 μm	2.493
Approximate transmission range (μm)	0.53-10.5
Thermal	
Glass transition temperature T _g (°C)	580
Melting temperature (°C)	830

5.3 Influence of substrate temperatures on Ga–La–S 65:34 +1 mol % Er₂O₃ bulk glass deposit on Si (100) substrate

In the previous chapter (chapter 4), it was demonstrated that the fs-PLD processing parameters, such as substrate temperature, fs-laser energy, and the deposition time have significant effects on the surface structural and physical properties of Ga-La-S thin films deposited on the silicon substrates. In this chapter, the Er³⁺-doped Ga–La–S thin films were fabricated by varying substrate temperatures while keeping all other process parameters constant. Table 5.2 below shows the deposition parameters of the three different thin film samples, namely GE1, GE2, and GE3 prepared at substrate temperatures of 25°C, 450°C, and 660°C, respectively. The selection of those temperatures because it has been clear from the previous study that the effect of various substrate temperatures (450-600 °C) on the deposition of Ga-La-S film had no significant difference. Thus, 25 and 450 have been chosen along with 660 °C, which is the highest temperature can our fs-PLD reach to it.

Table 5.2: List of parameters employed to deposit Er³⁺-doped Ga-La-S on Si substrate by using various substrate temperatures

Process parameter	Operating conditions
Substrate	Silicon; dimensions 20 mm (L) × 12 mm (W) × 675 μm (T)
Target material	Gallium lanthanum sulphide (Ga-La-S) 65:34 + 1 mol% Er ₂ O ₃
Target to substrate distance	70 mm
Fs-laser repetition rate	1.0 kHz
Fs-laser energy	50 μJ
Background gas pressure	80 mTorr (Ar ⁺)
Substrate temperature (Sample ID)	25°C (GE1), 450°C (GE2), and 660°C (GE3)
Deposition time	4 hours

5.3.1 STEM-EDX cross-sectional analysis the Er³⁺-doped Ga–La–S thin film at different temperatures

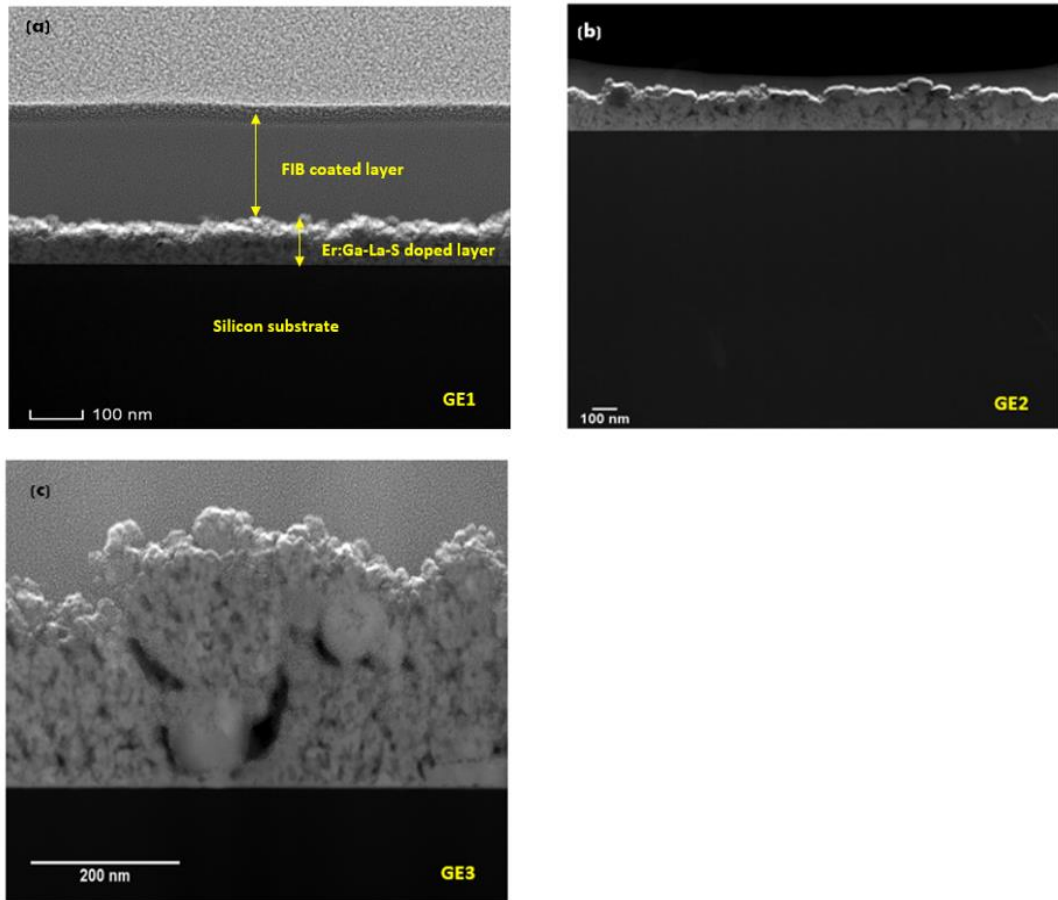


Fig. 5.2: TEM cross-section images of Er³⁺-doped Ga-La-S thin films deposited on Si substrate at different substrate temperatures; **(a)** 25°C (GE1), **(b)** 450°C (GE2), **(c)** 660°C (GE3).

Figure 5.2 (a–c) illustrates the TEM cross-sectional images of the films processed using an Er³⁺-doped Ga–La–S target at different substrate temperatures. The plan view of TEM micrographs reveal an average film thickness of around 45 nm, 95 nm, and 208 nm for samples GE1, GE2, and GE3, respectively. From the TEM results, it can be seen that the thickness of the film increased with deposition temperature from 45 nm at 25°C to 208 nm at 660°C. Therefore, it can be said that an increase in deposition substrate temperature has a significant effect on the film thickness.

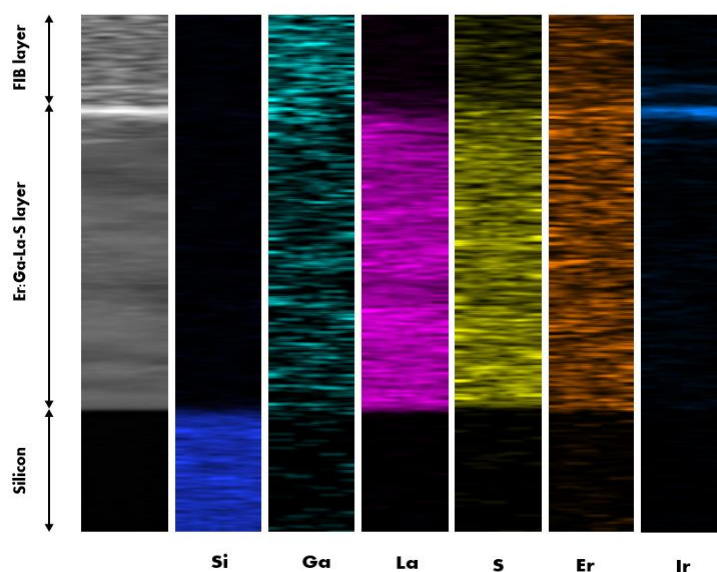


Fig. 5.3: HAADF-STEM image and STEM-EDX elemental mapping obtained during cross-sectional TEM analysis of a GE3 sample prepared at 660°C.

Figure 5.3 shows the cross-sectional elemental mapping images obtained for GE3, which confirmed that the deposited layer consisted of the uniform distribution of the Ga, La, S, and Er elements. However, no intermixing was observed between the Er³⁺-doped Ga–La–S coating and the silicon substrate network.

5.3.2 Influence of substrate temperature on Er³⁺-doped Ga–La–S thin film (XRD)

The silicon substrate shows two distinct peaks at around 36.24° and 55.62°, which indicates that the substrate was crystalline [303-305]. The stronger peak at approximately 55.62° was indexed as silicon-based on ICDD reference pattern No. 00-005-0565 for silicon (not shown here), while the other peak at 36.24° correlated with the ICDD reference pattern No. 00-039-1425 for silica. On the other hand, no peaks were observed in the diffraction pattern of the bulk target glass; instead, the pattern contained wide-stretched halo amorphous structure between $2\theta = 20^\circ$ and 30° [158, 306]. The XRD pattern of the Er³⁺-doped Ga–La–S thin film deposited at room temperature 25°C (GE1) was very similar to that of the silicon substrate, no additional peaks were observed. This indicates that the film formed at this

temperature was amorphous in nature. An examination of the diffraction patterns of sample GE2 prepared at higher temperature displayed two crystalline peaks centred at around $2\theta = 25^\circ$ and 28° . These peaks were not observed in sample GE1. Finally, XRD analysis of the sample obtained when the substrate temperature was increased to 660°C (GE3), revealed similar crystalline peaks observed in sample GE2 and two new peaks at $2\theta = 45^\circ$ and 47° . These peaks were indexed as $\text{La}_6\text{Ga}_{3.3}\text{S}_{14}$, $\text{La}_3\text{Ga}_{1.67}\text{S}_7$, and LaGaS_3 based on ICDD reference pattern No. 00-01-081- 5771, 00-04-005-8197, and 00-04-017-0337. A similar observation had been reported by Frantz et al. [306], where they concluded that such crystal phase's formation could be attributed to quenching and/or heat treatment of Ga–La–S target glass. Crystallite size was calculated from the XRD data for peaks occurring around $2\theta = 25^\circ$ and 29° using the Debye–Scherer formula (3.2) [272] mentioned in the “Instrumentation and Methodology” chapter.

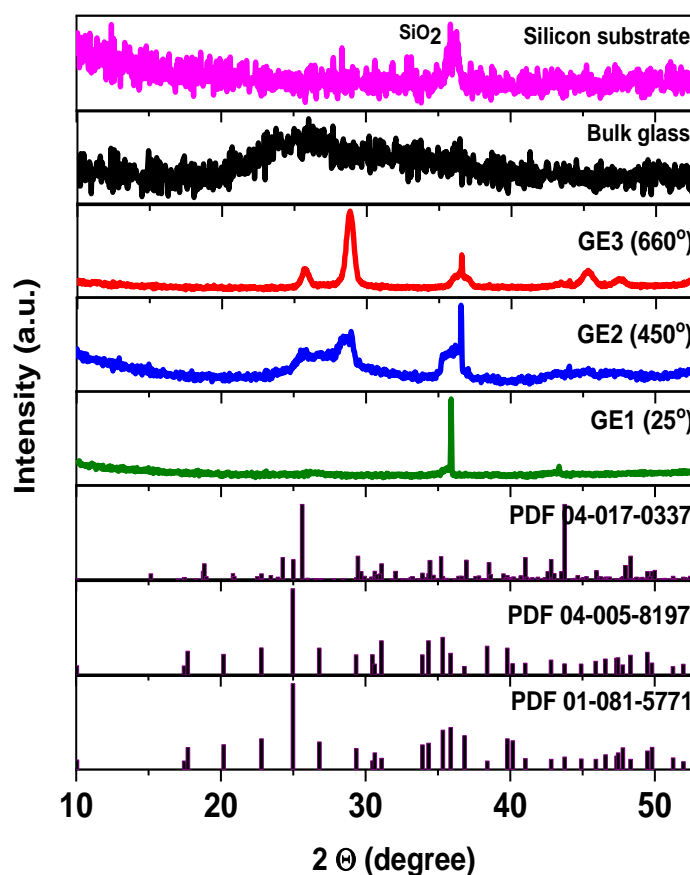


Fig. 5.4: XRD patterns for a pure silicon substrate (thickness = $675\ \mu\text{m}$), Er^{3+} -doped Ga–La–S bulk glass, and thin films deposited on silicon at various substrate temperature.

The average crystallite size for samples GE2 (450°C) and GE3 (660°C) was calculated to be ~5 nm and ~15 nm, respectively. This shows that the crystallite size increased from 5 to 15 nm with increasing deposition temperature from 450 to 660°C.

5.3.3 Influence of substrate temperature on Er³⁺-doped Ga–La–S thin films (Raman Spectroscopy)

Figure 5.5 represents the Raman spectra for a pure silicon substrate, the bulk target, and thin films prepared at various temperatures when excited by a 514.5 nm argon laser. The silicon substrate's spectrum contained a sharp peak with a characteristic band at 520 cm⁻¹, attributed to single crystalline silicon. While the Raman spectrum of Er³⁺-doped bulk Ga–La–S glass consisted of three main group bands between 190–920 cm⁻¹, 920–1200 cm⁻¹, and 1200–1800 cm⁻¹. The broad band centred around 420 cm⁻¹ corresponds to GaS₄ tetrahedron stretching vibration modes or vibration of LaS₈ structural [129] units present in amorphous Ga–La–S. The broad bands at higher frequencies (around 1200 cm⁻¹ and 1300 cm⁻¹, respectively) are from Er³⁺ photoluminescence (PL) corresponding to ²H_{11/2} – ⁴I_{15/2} (547 nm) and ⁴S_{3/2} – ⁴I_{15/2} (553 nm) transitions in a glassy medium [314, 315].

In addition to this, Raman spectra of all the thin film samples prepared by the fs-PLD were also investigated. The sample prepared at 25°C (GE1) reveals no assigned Raman bands of the Er³⁺-doped Ga-La-S glass, only a single crystalline peak in the Raman spectrum of the silicon substrate. Analysis of samples deposited at 450°C (GE2) and 660°C (GE3), the Raman spectra revealed five bands with the maximum peak intensities centred around 335 cm⁻¹, 495 cm⁻¹, 644 cm⁻¹, 1200 cm⁻¹, and 1350 cm⁻¹. The sharper bands at 335 cm⁻¹, 495 cm⁻¹ and 644 cm⁻¹ correlated to vibrations of LaS₈ or GaS₄ tetrahedron stretching vibrations [311]. The clearly split strong Raman bands peaking at 1200 cm⁻¹, and 1350 cm⁻¹ exhibit the characteristic features of Er³⁺-doped crystalline thin films, due to the Er³⁺ ions PL under 514.5 nm laser excitation [314].

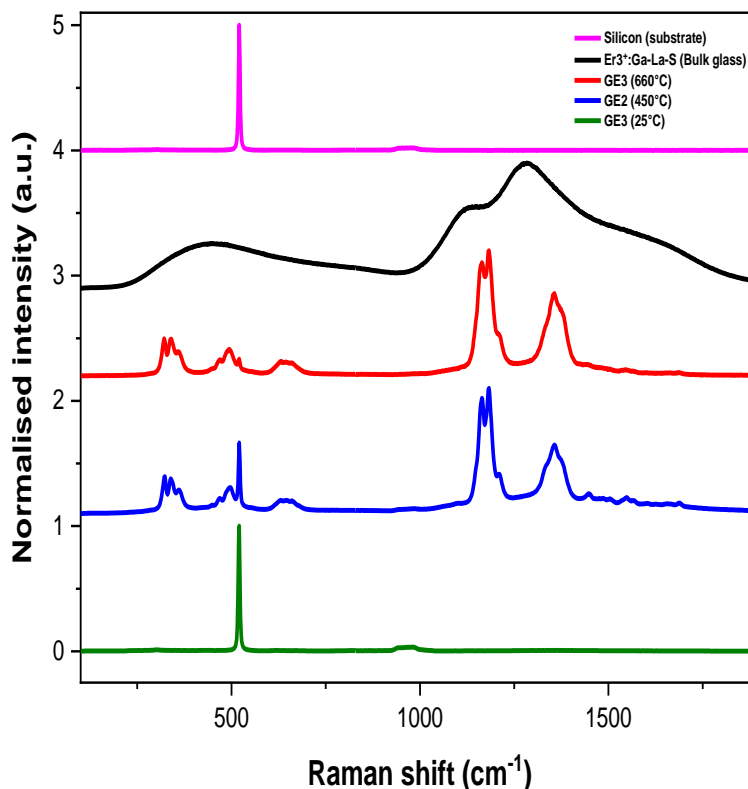


Fig. 5.5: Raman spectra of a pure silicon substrate (thickness = 675 μm), Er^{3+} -doped Ga–La–S bulk glass, and thin films on silicon at various substrate temperatures.

5.3.4 Influence of substrate temperature on Er^{3+} -doped Ga–La–S thin film (PL spectroscopy)

The PL spectra of Er^{3+} -doped Ga–La–S target glass and thin films recorded at room temperature using a 980 nm excitation source is illustrated in Fig. 5.6 (a). This will excite Er^{3+} ions for $^4I_{15/2} - ^4I_{15/2}$ and subsequently, radiation transition from $^4I_{13/2}$. The PL spectra peak around 1.54 μm corresponded to the $^4I_{13/2} - ^4I_{15/2}$ transition of the Er^{3+} ions and the energy diagram is depicted in Fig. 5.6 (b). Figure 5.6 (a) shows a very intense peak for all samples with the full spectral width at half maximum (FWHM) ~ 50 nm, while the target chalcogenide glass (Er^{3+} -doped Ga–La–S) exhibits a much broader FWHM of ~ 75 nm. Also, sample GE3 exhibits five multiples sharp peaks known as Stark levels, which can be attributed to the thermal population of the higher levels of the 1.54 μm manifold. The presence of these transitions from Stark levels confirm the crystalline phases of the doped material present in the thin film.

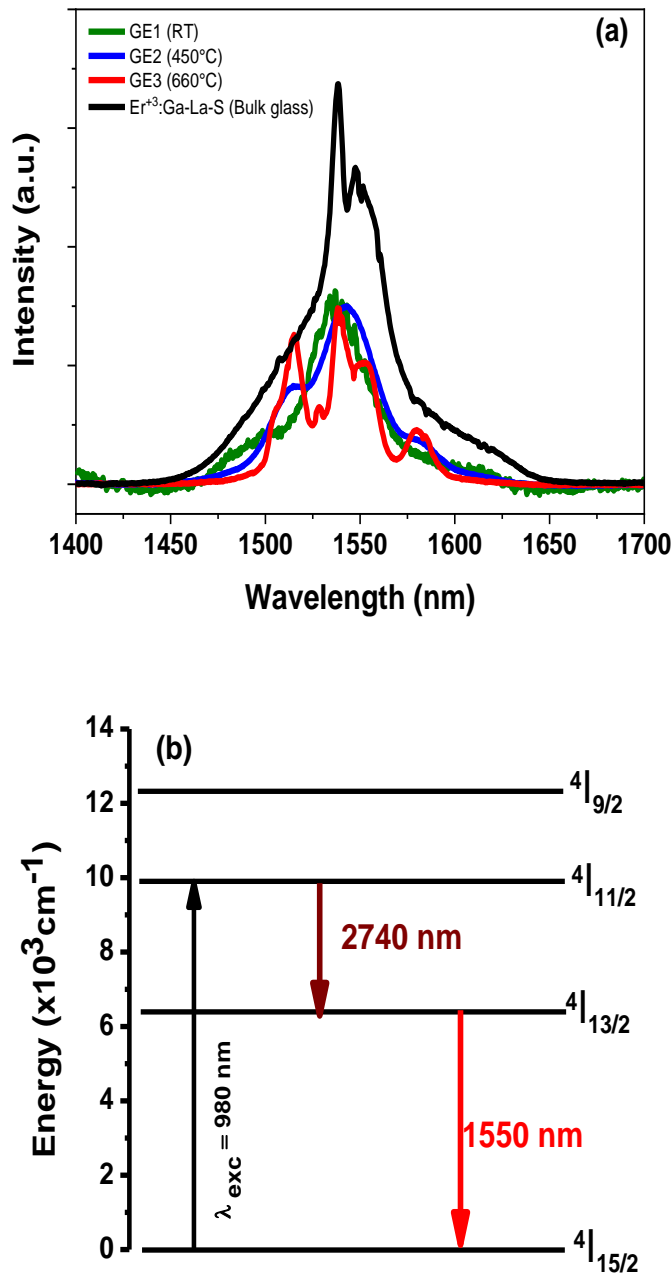


Fig. 5.6: (a) PL spectra of 1 mol% Er³⁺-doped Ga-La-S glass and Er³⁺-doped Ga-La-S thin films deposited at various substrate temperatures, and (b) Energy transfer sketch of Er³⁺-doped glass when pumped at 980 nm.

Table 5.3 shows the PL lifetime (τ) data for Er³⁺-doped Ga-La-S target glass and various thin films prepared. The lifetime of the $4I_{13/2}$ transition for the thin films decreases very rapidly from 1.82 to 0.46 ms with increasing deposition temperature, which confirms the changes in the local crystal field. The drop in measured fluorescence lifetime of the thin film prepared at room temperature to that corresponding to the bulk glass is attributed to the

reduction in reabsorption that results in longer measured lifetimes in bulk glasses [316-318]. In the powders and thin films of Er³⁺-doped chalcogenide glasses, the measured lifetimes are more accurate and comparable to radiative lifetimes [315]. Another attribute of the drop in a lifetime is the higher presence of –OH⁻ radicals in the thin film compared to bulk glasses that result in nonradioactive relaxation of the ⁴I_{13/2} level, leading to a reduction in the measured lifetime. In our studies, as the deposition temperature increased, we also observed that the crystallinity of the films also increased, as shown in Fig. 5.4. This results in more Er³⁺-ions being incorporated into the crystalline phases reported above, leading to Er³⁺ ion-ion interactions and self-quenching of photoluminescence and subsequently lower measured lifetime [319, 320]. The drop in a measured lifetime with film preparation temperature can be understood on this basis.

Table 5.3: Fluorescence lifetimes of Er³⁺-doped Ga-La-S samples at different substrate temperatures

Er³⁺ -doped Ga-La-S samples	Fluorescence lifetime τ (ms)
Bulk glass	4.87
GE1 (25 °C)	1.82
GE2 (450 °C)	0.59
GE3 (660 °C)	0.46

5.3.5 Influence of substrate temperature on Er³⁺-doped Ga–La–S thin film (UV-Vis spectroscopy)

The transmission spectra of the thin films are measured by using the UV-Vis-NIR spectrometer in the wavelength range between 320 and 2000 nm. Thus, the absorption coefficient (α) spectra are determined from transmission through the thin films by the approximate expression [see in equation (2.1)].

Assuming that the reflectance of these thin films is very low in the photon energy range of interest. The optical band gap energy of Er-doped Ga-La-

S thin films prepared is calculated from the UV-Vis absorption edge by using the absorption coefficient obtained from transmission measurements and Tauc optical band gap [see the relation in (2.2)].

The optical band gap was calculated by using $n = 1/2$ for direct allowed from the absorption spectra, which exhibits a perfect fit for all the thin film samples. Figure 5.7 (a) shows the plots of $(\alpha hv)^2$ as a function of hv (eV). Sample GE1 prepared at a low temperature (25°C) has a strong absorption with E_g around ~ 2.15 eV, and then decreases gradually with increase in deposition temperature to E_g values of 1.90 eV and 1.75 eV for sample GE2 and GE3, as depicted in Fig. 5.7 (b). As discussed previously, when the temperature of the film increased from room temperature (25°C) to 660°C, the films were found to be more crystalline. This was confirmed by the average crystallite size estimated from the XRD data for samples GE2 (450°C) and GE3 (660°C). Henceforth, the change in optical band gap is inversely dependent on the diameter of the crystalline size [272, 321, 322], which explains the decrease in the observed band gap E_g with the increase in deposition temperature [321, 322]. Similar results have been reported previously for optical absorption of Ga–La–S thin film [128] samples fabricated by employing different deposited energy densities.

Table 5.4: Optical energy band gap of Er³⁺-doped Ga-La-S prepared at various substrate temperatures

Sample	Substrate temperature T_s (°C)	Thickness d (nm)	Optical energy band gap (eV)
GE1	25	45	~2.15
GE2	450	95	1.90
GE3	660	208	1.75

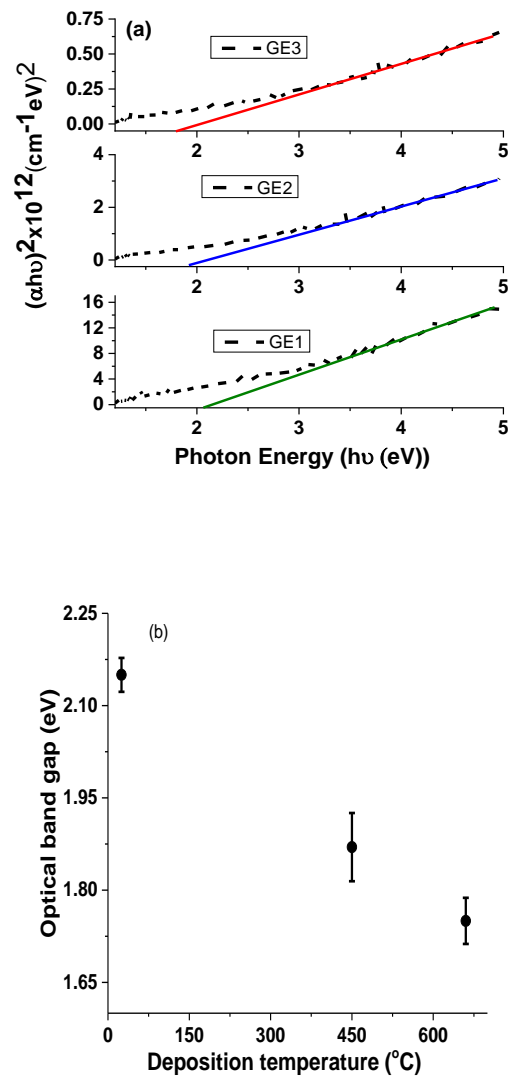


Fig. 5.7: (a) Tauc plot as a function of photon energy, and (b) Optical band gap versus deposition temperature of Er^{3+} -doped Ga-La-S glass thin films on a Si substrate.

5.4 Effect of deposition pressure on the of Er^{3+} doped Ga-La-S thin films on Si (100) substrate at 660°C

The previous study examined the influence of the substrate temperature on the deposited Er^{3+} -Ga-La-S thin films. Further investigation was also conducted to better understand the effect of deposition pressure on the surface morphology and structural quality of the thin films. The substrate temperature was maintained at 660°C based on an optimal value from the previous work on the substrate temperature. As the sample fabricated at this substrate temperature (660°C) demonstrated a thicker thin film based on the TEM cross-section images shown in Fig. 5.2. Moreover, XRD and

Raman spectra [Fig. 5.4 and 5.5] exhibited the strong Er³⁺-doped Ga–La–S crystalline phase peaks. Furthermore, the optical band gap and PL lifetime at ⁴I_{13/2} transition decreased for the thin film prepared at this temperature as compared to the other samples deposited at other substrate temperatures (25°C and 450°C). Table 5.5 below exhibits the details of four samples, GP1, GP2, and GP3 fabricated at 50 μJ of laser energy under vacuum, 40 mTorr, and 200 mTorr, respectively, while keeping all other process parameters constant.

Table 5.5: List of parameters employed to deposit Er³⁺-doped Ga-La-S on Si substrate by using different pressures

Process parameter	Operating conditions
Substrate	Silicon; dimensions 20 mm (L) × 12 mm (W) × 675 μm (T)
Target material	Gallium lanthanum sulphide (Ga-La-S) 65:34 + 1 mol% Er ₂ O ₃
Target to substrate distance (<i>d_{st}</i>)	70 mm
Fs-laser repetition rate	1.0 kHz
Fs-laser energy	50 μJ
Background gas pressure (sample ID)	Under vacuum (GP1), 40 mTorr (GP2), 200 mTorr (GP3)
Substrate temperature (°C)	660°C
Deposition time	4 hours

5.4.1 Influence of pressure on the deposition Er³⁺-doped Ga–La–S thin film (SEM and TEM)

Figure 5.8 (a-c) shows SEM images of the surface morphology of Er³⁺-doped Ga-La-S thin films grown onto the silicon substrate under three different chamber pressure while keeping the substrate temperature fixed at 660°C. The surface morphology of the Er-Ga-La-S deposited films was observed to be homogeneous, although the nanoparticles in the films are not uniformly distributed.

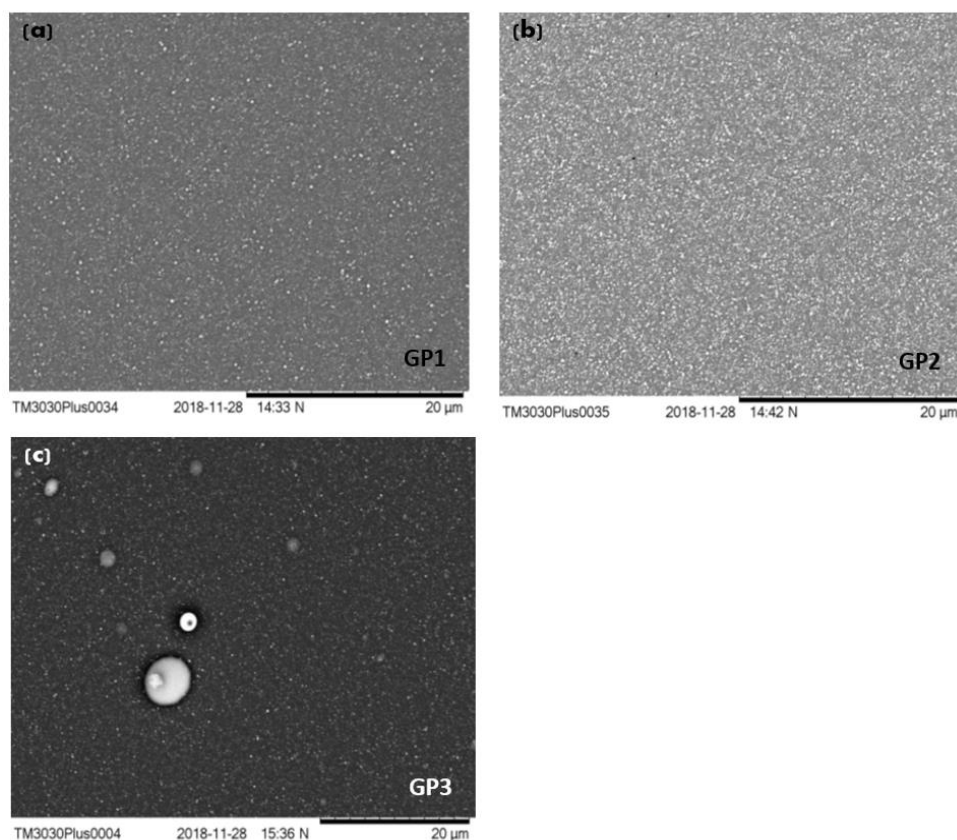


Fig. 5.8: SEM images of the top surface of Er³⁺-doped Ga-La-S thin films deposited on Si substrate with different pressures; **(a)** GP1 (under vacuum), **(b)** GP2 (40 mTorr), and **(c)** GP3 (200 mTorr).

It can be seen in Fig. 5.8 (a) that the sample deposited under vacuum is relatively smooth and less agglomerated. Given the lack of background gas, the particles of which the plume is formed (ions, atoms, and electrons) are probably reflected at the moment when they come to the substrate which affects the film that is developing. The effect is in part produced by the particles that rebounded, which caused the surface to become smooth [323]. However, by increasing the working chamber pressure to 40 and 200 mTorr, various sizes of spherical nanoparticles are deposited on the substrate surface during sample fabrication, as shown in Fig. 5.8 (b) and (c) [324-326]. As a result, the particles that have been deposited are of lower energy when they arrive at the surface of the substrate. This observation explains that the growth rate of the particle grains is quite slow at higher chamber pressure, which leads to an increase in surface roughness of the films. Henceforth, the higher working pressure results in the formation of clusters in a gas phase [323, 327]. Such clusters may condense on the film

surface, which is not desirable for most applications. This reduces the film quality and damages the microstructure, of the Er³⁺-doped Ga-La-S films.

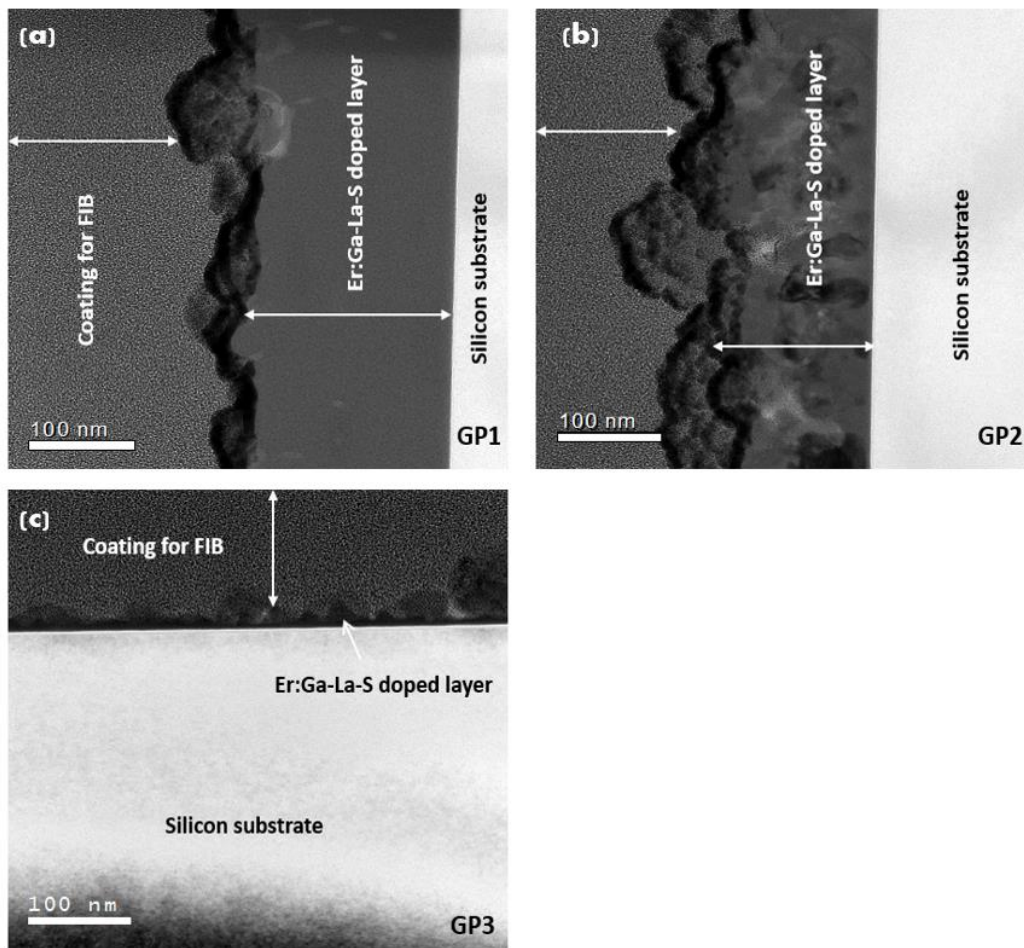
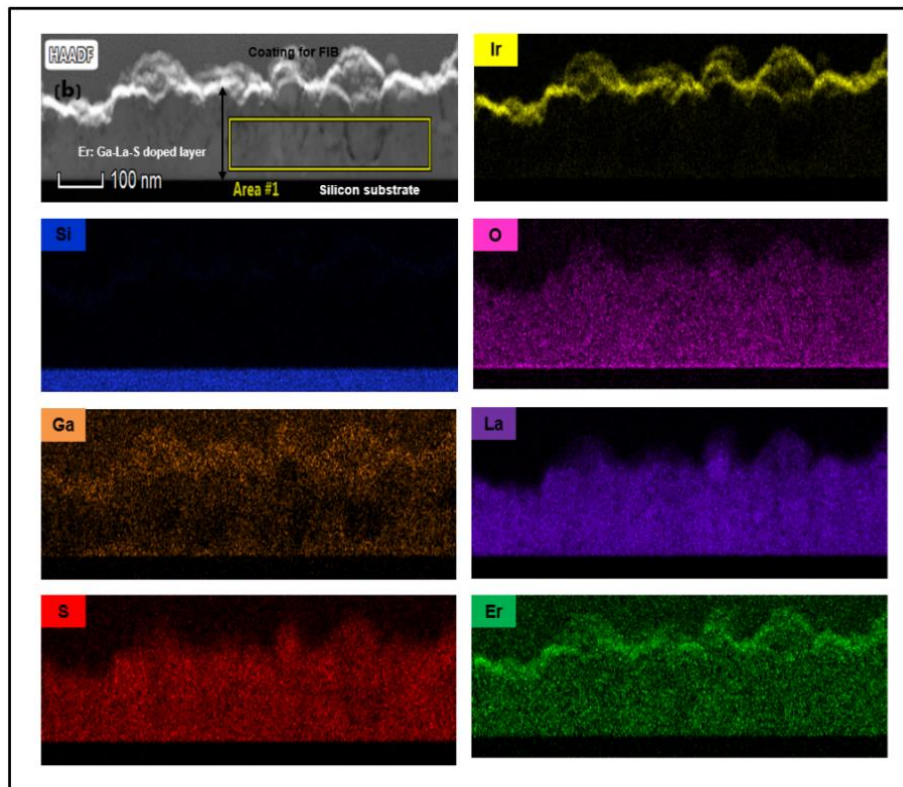
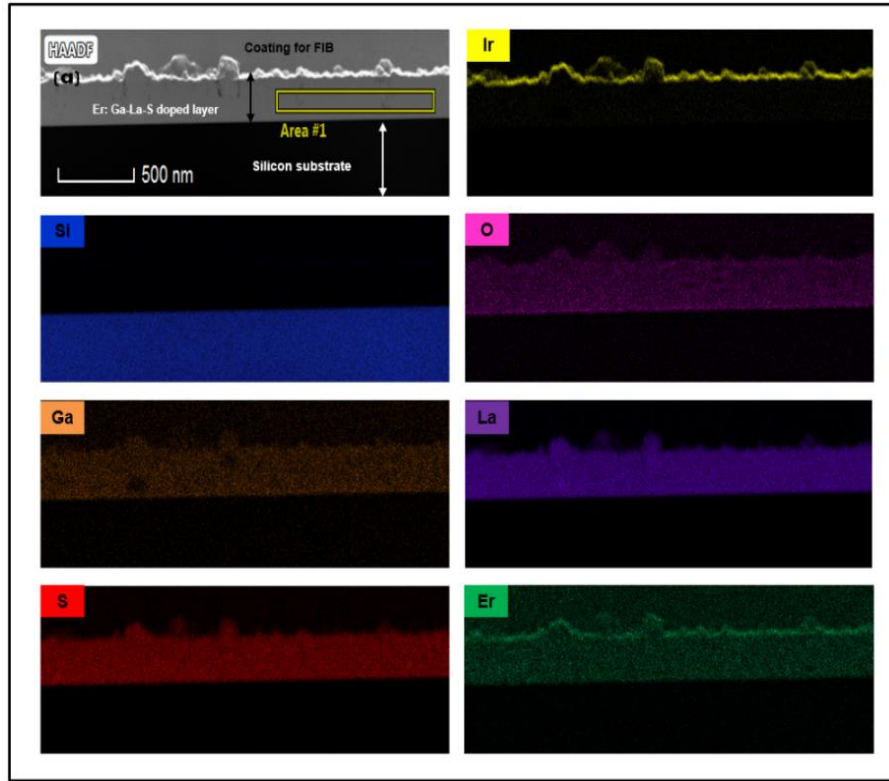


Fig. 5.9: TEM cross-sections of Er³⁺-doped Ga-La-S layer formed on Si substrates by fs-PLD with different pressures; **(a)** under vacuum (GP1), **(b)** 40 mTorr (GP2), and **(c)** 200 mTorr (GP3).

Figure 5.9 (a-c) shows the cross-sections of the Er³⁺-doped Ga-La-S thin films grown on Si substrate under various pressures at a constant substrate temperature (660°C). According to these images, it can be seen that the thin film thicknesses decreased with increasing chamber pressure. The films thickness was estimated to be around 220 nm, 172 nm, and ~ 20 nm for the films deposited under vacuum pressure (10⁻⁶ mTorr), 40 mTorr, and 200 mTorr, respectively. Thus, it can be seen that the chamber environment affected the surface morphology as well as the thickness of films.

5.4.2 Influence of pressure on the deposition Er³⁺-doped Ga-La-S thin film (STEM-EDX)



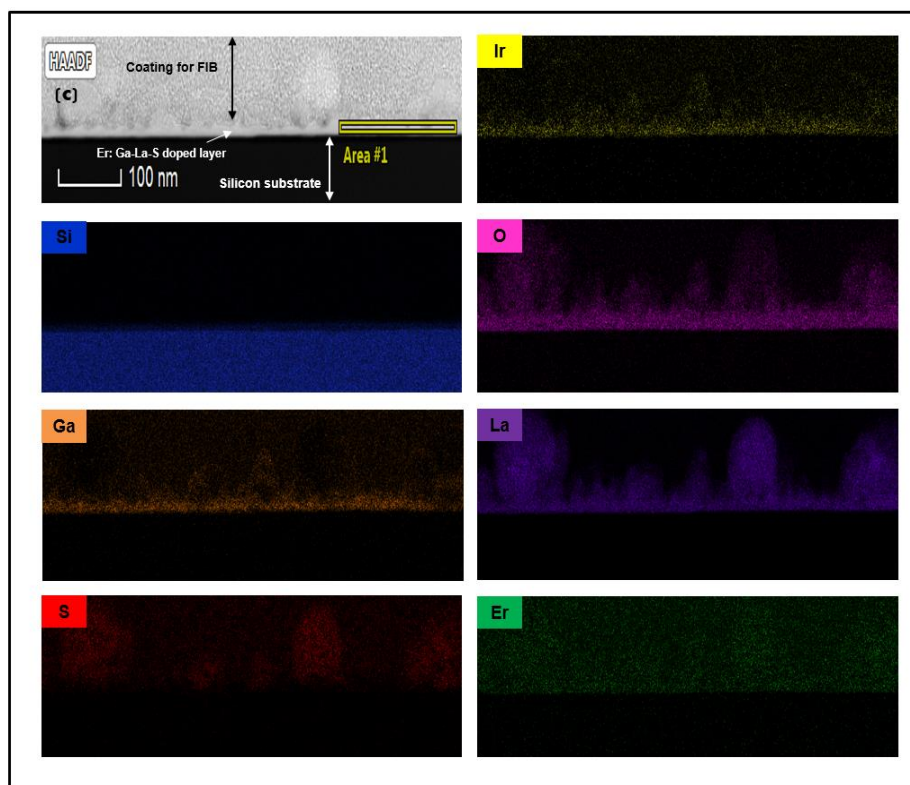


Fig. 5.10: HAADF-STEM images and STEM-EDX elemental maps images of Er^{3+} -doped Ga–La–S thin films prepared on Si with different pressures; **(a)** sample prepared under vacuum (GP1), **(b)** sample prepared at 40 mTorr (GP2), and **(c)** sample prepared at 200 mTorr (GP3).

Figure 5.10 shows the HAADF-STEM images of the deposited films and the results of EDX spectroscopy within STEM analysed for sample GP1, GP2, and GP3 prepared at different pressures. This confirms that the deposited layer consisted of the uniform distribution of Ga, La, S, and Er elements. There is no intermixing between the deposited Er^{3+} -doped Ga–La–S thin film and silicon substrate network. Elements such as Ga, La, S, and Er are apparent on the STEM-EDX maps for sample GP1 prepared under vacuum pressure in Fig. 5.10 (a). The EDX data reveal the generation of a uniform, homogeneous mixture of Ga, La, S, and Er extending to the bottom of the deposited layer. It is apparent that Ga was deposited on the top of the film, which is due to its overlapping with the iridium (Ir) element that comes from FIB coating. Furthermore, EDX mapping scan of sample GP2 prepared at 40 mTorr depicted in Fig. 5.10 (b) shows that the elemental distribution of Ga, La, S, and Er are also homogeneous in the Er^{3+} -doped Ga–La–S thin film grown. Mapping scan of GP3 sample, prepared at higher pressure (200

mTorr) in Fig. 5.10 (c) indicated that the distribution of Ga, La, S, and Er had a disparity in the Er³⁺-doped Ga-La-S thin film grown.

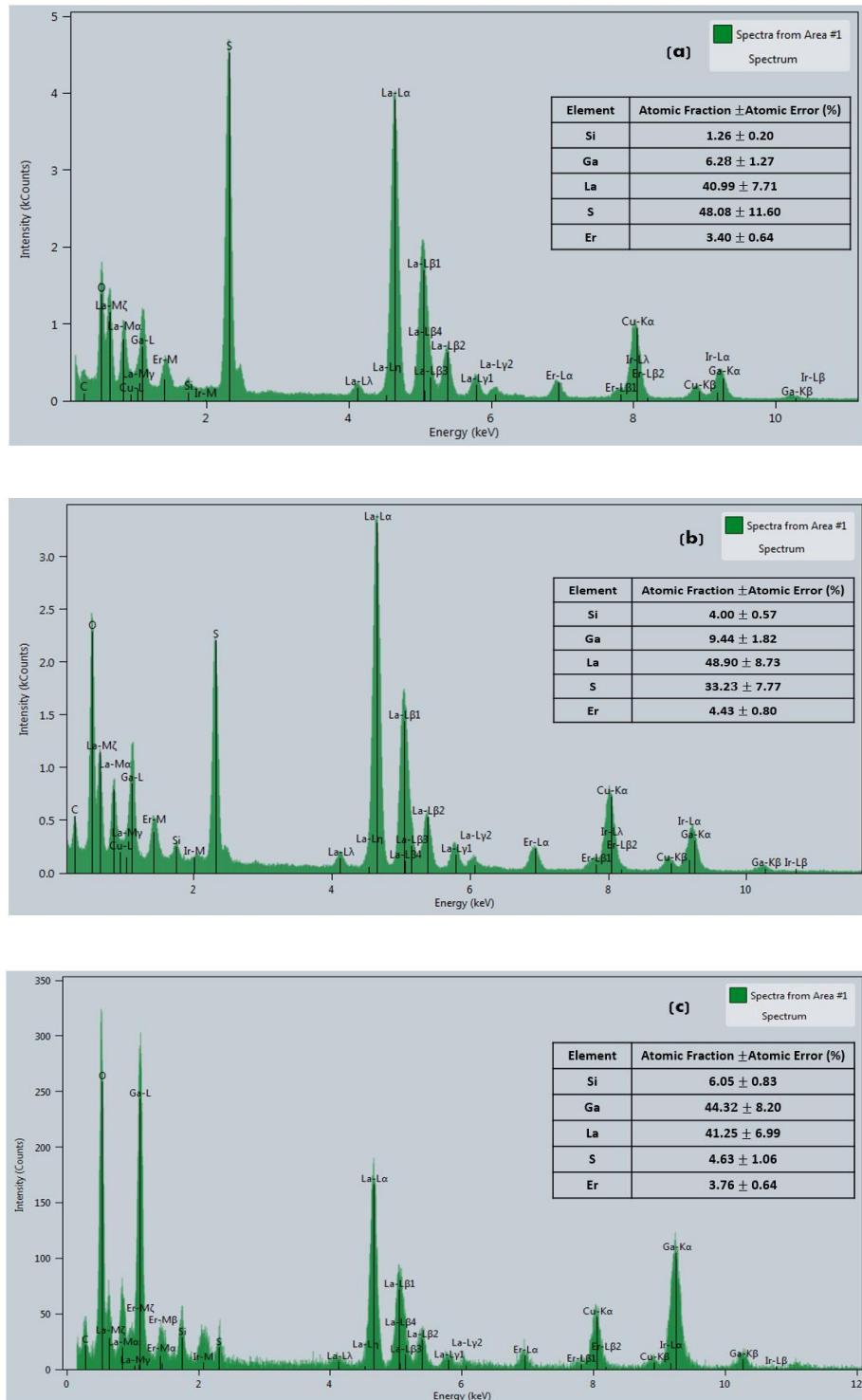


Fig. 5.11: TEM-EDX spectrum of the yellow region labelled (Area#1) in HAADF-STEM Fig. 5.10 of the doped layer on silicon for samples; **(a)** GP1 prepared under vacuum, **(b)** GP2 sample prepared at 40 mTorr, and **(c)** GP3 sample prepared at 200 mTorr.

In Figure 5.11, the elemental composition of the Er^{3+} -doped Ga-La-S thin film areas highlighted in the HAADF image evaluated with TEM-EDX. According to Fig. 5.11 (a), the EDX spectrum revealed atomic percentages of 1.26, 6.28, 40.99, 48.08, and 3.40 at. % for Si, Ga, La, S, and Er in the thin film fabricated under vacuum. This result shows that the thin film had virtually no Si, and was entirely made up of elements from the Er^{3+} -doped Ga-La-S target. On the other hand, the sample prepared at 40 mTorr [Fig. 5.11 (b)] had a higher atomic percentage of Si (4.00 at. %) and Ga (9.44 at. %), however, the atomic percentage of S (33.23 at. %) is quite low as compared to sample prepared under vacuum. With increasing pressure to 200 mTorr [Fig. 5.11 (c)], the atomic percentage of Ga (44.32 at. %) and Si atomic percentage (6.05 at. %) increased dramatically. Besides, the atomic percentage fraction of S in the deposited layer sharply decreased at higher pressure (200 mTorr). The EDX spectrum analysis suggests that the S ions have been evaporated from the plasma plume in the course of the process of deposition. This study shows that the doping concentration of Er and La ions remains substantially nearly the same in all the Er^{3+} -doped Ga-La-S thin films prepared.

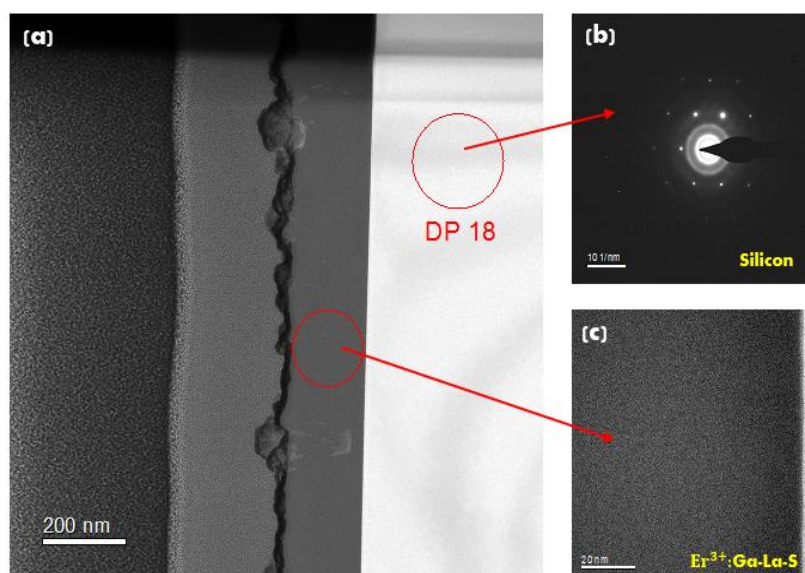


Fig. 5.12: TEM images of Er^{3+} -doped Ga-La-S thin film on silicon from sample GP1 prepared under vacuum; **(a)** cross-sectional BF-TEM image of the Er^{3+} -doped Ga-La-S layer, **(b)** SAED pattern captured from a silicon substrate region, and **(c)** SAED pattern captured from the Er^{3+} -doped Ga-La-S layer region.

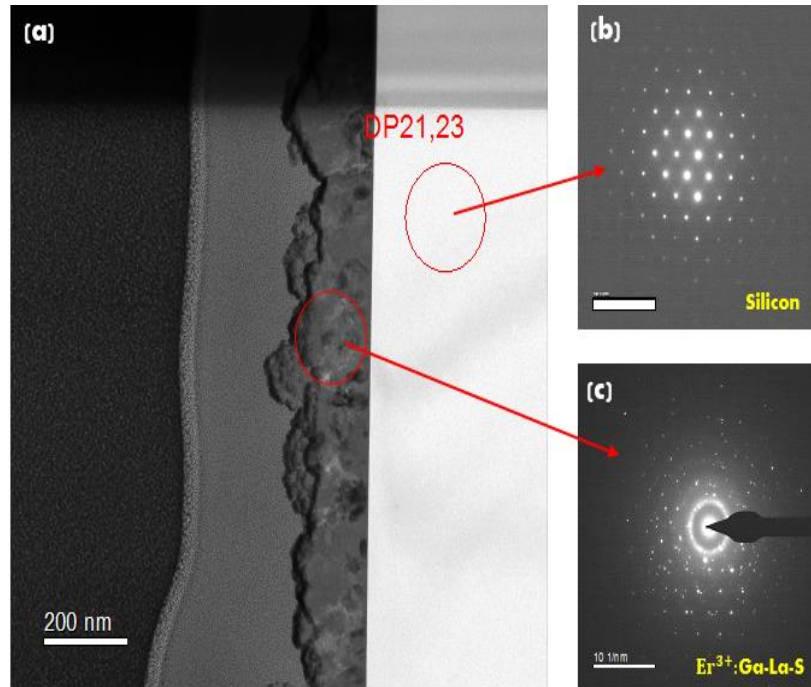


Fig. 5.13: TEM images of the Er^{3+} -doped Ga-La-S thin film on silicon from sample GP1 prepared at 40 mTorr; **(a)** cross-sectional BF-TEM image of Er^{3+} -doped Ga-La-S layer, **(b)** SAED pattern captured from a silicon substrate region, and **(c)** SAED pattern captured from the Er^{3+} -doped Ga-La-S layer region.

Figure 5.12 (a) illustrates a cross-sectional BF-TEM image of a high smooth Er^{3+} -doped Ga-La-S thin film, which does not reveal visible crystalline grains. While Figure 5.12 (b) presents the SAED pattern of the silicon substrate, exhibiting circular shapes around the centre. In Fig. 5.12 (c), the Er^{3+} -doped Ga-La-S thin film layer did not reveal any diffraction pattern for the sample prepared under vacuum.

Figure 5.13 shows the SAED patterns for sample GP2 (40 mTorr). It shows the crystalline nature of the silicon substrate and Er^{3+} -doped Ga-La-S film [Fig. 5.13 (b) and (c), respectively].

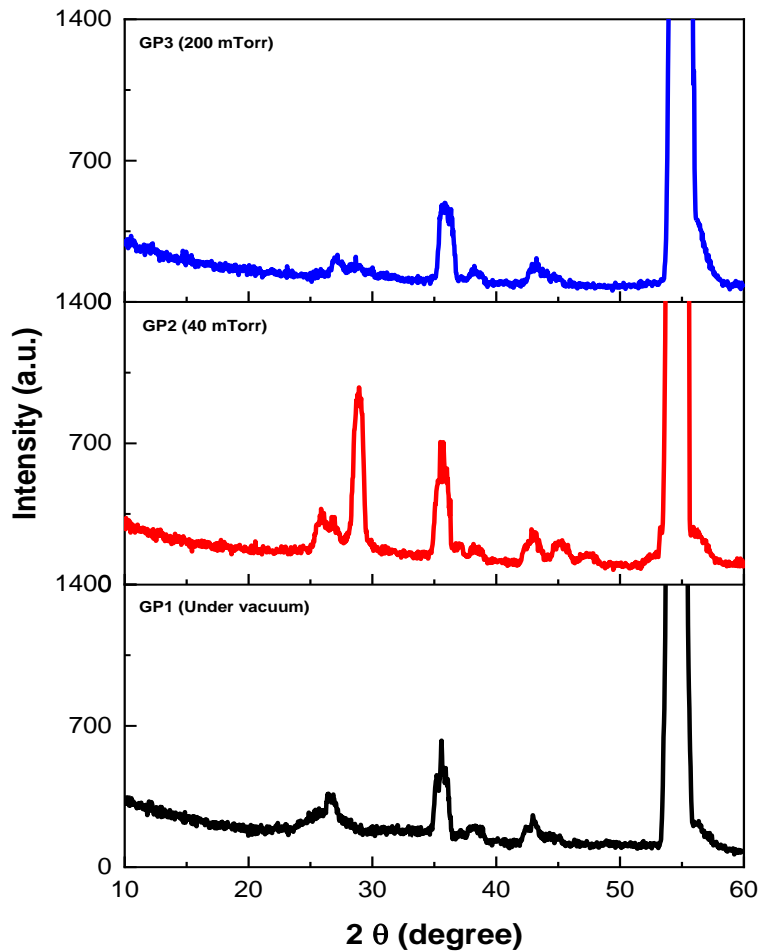
5.4.3 Influence of pressure on Er³⁺-doped Ga–La–S thin film (XRD)

Fig. 5.14: XRD patterns of a pure silicon substrate (thickness = 675 μm), Er³⁺-doped Ga–La–S bulk glass, and thin films deposited on silicon at various working pressure; a vacuum (GP1), 40 mTorr (GP2), and 200 mTorr (GP3).

Figure 5.14 shows the XRD patterns of the silicon substrate, Er³⁺-doped Ga–La–S bulk target glass, and Er³⁺-doped Ga–La–S thin films deposited at different pressures (under vacuum, 40, and 200 mTorr argon pressure). The XRD patterns of the silicon substrate and Er³⁺-doped Ga–La–S target material have been obtained and discussed previously in Fig. 5.4 [section 5.3.2 page 85].

Furthermore, XRD analysis in Fig. 5.14 was performed to investigate the impact of chamber pressure to understand the effect of the crystalline structure of the Er³⁺-doped Ga–La–S thin films. While the substrate

temperature was kept constant at 660°C. The most intense peak at ~37° in all the samples corresponds to SiO₂ (111) while the peak at ~55° is associated with Si (311) [303-305]. This result reveals the crystallisation structure of silicon and silica phases. From the XRD results, it was also found that the crystallinity of Er³⁺-doped Ga-La-S films increased with decreasing argon pressure. At 200 mTorr (Ar) deposition ambience (GP3 sample), the peak at ~27° can hardly be observed, and a minor peak at ~43° became conspicuous. These two peaks are the slowest growing planes in their structures because they are closely packed argon planes; then these surfaces have the lowest surface energy. Hence at lower argon pressure (40 mTorr), the particles that are ablated from the target usually have more energy for rearrangement on the substrate surface. In other words, as the argon pressure is enhanced, the collisions between ablated particles within the plume and argon gas also increase, thus the kinetic energy of particles becomes low, resulting in a higher intensity of the peak at ~27° for deposition of the Er³⁺-doped Ga-La-S films at 40 mTorr (Ar) pressure (GP2 sample) [230, 328].

The crystallised films are made up of hexagonal and tetragonal phases of La₆Ga_{3.3}S₁₄ and La_{1.67}Ga₃S₇, respectively. These crystalline phase peaks matched with ICDD reference pattern No. 01-081-5771 and 04-001-8324. The diffraction peaks centred at 2θ values of 27.00° and 43.41° were relatively intense for Er³⁺-doped Ga-La-S thin film deposited at a pressure of 40 mTorr as compared to those films deposited under vacuum and at 200 mTorr. This shows that the crystalline quality of the film is improved under 40 mTorr chamber pressure at a substrate temperature of 660°C. A comparison of samples GP1, GP2, and GP3 spectra revealed a significant improvement in the crystallinity of the film deposited at 40 mTorr.

5.4.4 Influence of pressure on the deposition Er^{3+} -doped Ga–La–S thin film (Raman spectroscopy)

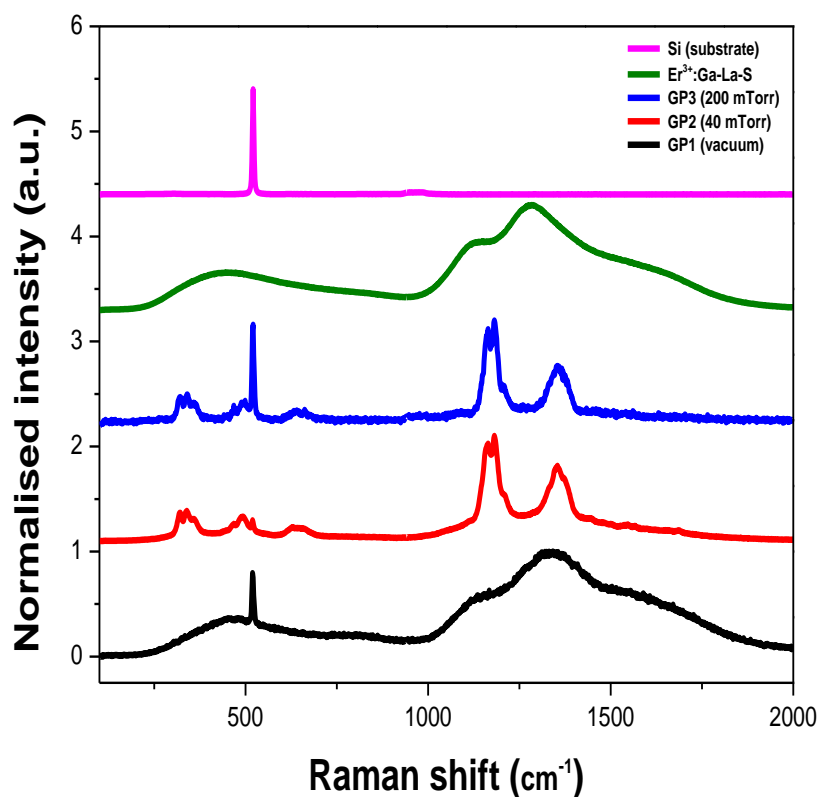


Fig. 5.15: Raman spectra of a pure silicon substrate (thickness = 675 μm), Er^{3+} -doped Ga-La-S bulk glass, and thin films on silicon at different pressures.

Figure 5.15 represents the Raman spectra for a pure silicon substrate, a bulk target, and thin films prepared at three different chamber pressures when excited by a 514.5 nm Argon laser. The silicon substrate spectrum and bulk glass have already been discussed in Fig. 5.5. Raman spectra of all the thin film samples prepared by the fs-PLD were investigated. The sample GP1 deposited under vacuum showed a sharp silicon peak of the substrate at around 520 cm^{-1} and broad amorphous bands identical to the bulk glass, as shown in Fig. 5.15. Contrariwise, by increasing the pressure of argon to 40 mTorr (GP2) and 200 mTorr (GP3), the Raman spectra revealed many bands correlating to the silicon and Er^{3+} -doped Ga-La-S target. The Raman spectra showed five bands. The strongest peak intensities occur at approximately 335 cm^{-1} , 495 cm^{-1} , 644 cm^{-1} , 1200 cm^{-1} , and 1350 cm^{-1} . The Raman sharper bands centred at 335 cm^{-1} , 495 cm^{-1} ,

and 644 cm^{-1} are correlated with the LaS_8 or GaS_4 tetrahedron stretching vibrations [311]. This observation indicates that the Er^{3+} -doped Ga-La-S thin films are crystalline, which are caused by the Er^{3+} ions PL under 514.5 nm laser stimulation [314].

5.4.5 Influence of pressure on the deposition Er^{3+} -doped Ga-La-S thin film (PL spectroscopy)

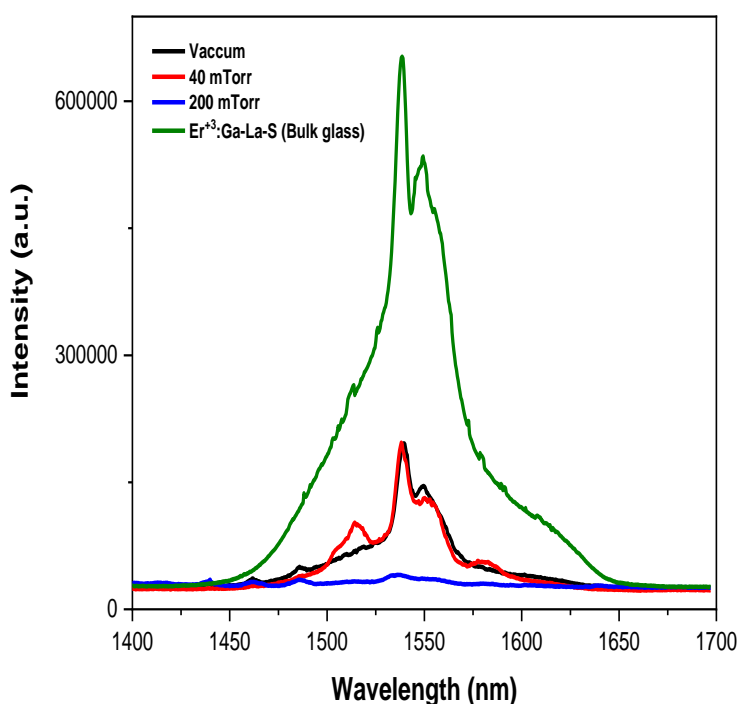


Fig. 5.16: PL spectra of 1 mol% Er^{3+} -doped Ga-La-S glass and Er^{3+} -doped Ga-La-S thin films deposited at different chamber pressures.

The PL spectra of Er^{3+} -doped Ga-La-S target glass and thin films were measured under room temperature by using a 980 nm excitation source. Results are shown in Fig. 5.16. Characteristic PL behaviour of Er^{3+} -doped Ga-La-S was observed in all films, irrespective of the level of argon partial pressure that was applied. In other words, a broadband emission spectrum peaking at $1.54\mu\text{m}$ (approx.) due to $^4\text{I}_{13/2} - ^4\text{I}_{15/2}$ transition of the Er^{3+} ions are observed as shown in Fig. 5.6 (b). The peak intensity increases as the argon partial pressure is decreased. This finding corresponds to a decrease in film thickness trend as the partial chamber pressure increased. The film deposited at 40 mTorr was also found to be the best in terms of the PL intensity of Er^{3+} -doped Ga-La-S emission at $1.54\mu\text{m}$, and after that, the PL

intensity decreased significantly as the argon partial pressure increased to 200 mTorr. Thin film thickness was significant for determining whether the luminescence is active. The research showed that a thicker film with improved crystallinity could be achieved when the argon pressure was low during the deposition process.

Table 5.6 summarises the results of PL lifetime (τ) measurement data for Er³⁺-doped Ga-La-S target glass and different thin films prepared. The lifetime of the ⁴I_{13/2} transition for the thin films was almost the same for all samples ~ 1.2 ms, which shows that the argon pressure does not have a significant impact on the fluorescence lifetimes of Er³⁺-doped Ga-La-S. As a generalisation, it can be observed that decreasing argon pressure can diminish the intensity of the PL.

Table 5.6: Fluorescence lifetimes of Er³⁺-doped Ga-La-S samples at various chamber pressures

Er ³⁺ -doped Ga-La-S samples	Fluorescence lifetime τ (ms)
Bulk glass	5.33
GP1 (vacuum)	1.1
GP2 (40 mTorr)	1.2
GP3 (200 mTorr)	1.1

5.5 Conclusions

In summary, Er³⁺-doped Ga–La–S thin films were successfully deposited on the pure silicon substrate at various substrate temperatures and pressures by utilising the fs-PLD technique. The effects of deposition temperatures and pressures on the thickness and crystalline structure of the deposited films have been systematically investigated. This clearly shows that an increase in deposition temperature leads to increase the film thickness and increase in crystallinity phases. The structural characteristics of the target changed from amorphous to crystalline phase as well. However, no intermixing and interdiffusion behaviour is observed between the silicon substrate and the deposited layer. This could be linked to the composition

of the chalcogenide target glass since fs-PLD-assisted induced intermixing is actually dependent on the target and substrate materials [329]. The PL spectra of as-deposited Er³⁺-doped Ga–La–S chalcogenide thin films at various temperatures exhibited very intense emission signal at 1534 nm under a pump wavelength of 980 nm with FWHM at ~ 50 nm.

On the other hand, the PL lifetime at ⁴I_{13/2} transition decreased with increase in deposition temperature as discussed; clear temperature dependences of the lifetime could be associated with increasing Er³⁺ ion concentration in the thin films and non-radiative decay or change in the local crystal field. Whereas, the lifetime of the ⁴I_{13/2} transition for the thin films was almost the same for all samples fabricated at different pressures. This shows that the argon pressure has no major impact on the fluorescence lifetimes of Er³⁺-doped Ga-La-S.

Finally, a large optical band gap was observed from the film prepared at the low deposition temperature. The decrease in band gap with the increase in deposition temperature is associated with an increase in film thickness, as well as structural modification of the thin films. The structural and optical properties of these films show their promising use in devices such as lasers and optical amplifiers opportunities.

Chapter 6: Germanium selenide (GeSe₄) deposition and doping on silicon

6.1 Introduction

This chapter describes the deposition and doping of Ge and Se from germanium selenide (GeSe₄) glass onto/into Si substrate (100) to fabricate Ge-Se layer or induced intermixing of the target with Si substrate by varying fs-PLD process parameters such as; fs-laser energy and substrate temperature. The surface morphological, structural, and optical properties of the as-deposited thin films were evaluated to ascertain parameters that are needed to deposit a uniform Ge-Se layer on a silicon substrate through the fs-PLD process. Doping of Ge and Se into silicon has been shown to provide a suitable candidate for infrared spectroscopy and telecommunication applications due to its strong transmission in the infrared range, from 0.9 μm to 12 μm [184, 330]. In this chapter, we present results of samples prepared from GeSe₄ target that was prepared and provided by Jiangsu Normal University (School of Physics and Electronic Engineering).

6.2 Target material: germanium selenide glass (GeSe₄) synthesis

The GeSe₄ glass was synthesised by the conventional melt quenching technique use for ChGs [49, 187]. The method of preparation used by Jiangsu researchers is described as follows. 5N 99.999% purity germanium lumps and 6N 99.9999% purity selenium particles were weighed and loaded into a low-OH silica tube in a glove box filled with dry nitrogen. The tube containing the elemental materials was then connected to a vacuum system. Once the pressure was below 10⁻³ Pa, the tube was sealed using H₂-O₂ flame. After that, the tube was put into a rocking furnace, and heated to 850°C. After being homogenised at this temperature for 12 hours, the mixture in the tube was quenched in water. The formed glass was finally annealed at 160°C for 3 hours. Table 6.1 provides some of the optical and thermal properties of bulk GeSe₄ glass material.

Table 6.1: Some properties of GeSe₄ bulk glass [330, 331]

Optical	
Refractive index at 1.55 μm	2.35
Approximate transmission range (μm)	0.9-12
Thermal	
Glass transition temperature T _g (°C)	400
Melting temperature (°C)	675



Fig. 6.1: GeSe₄ bulk glass (**left**) and GeSe₄ bulk glass holder (**right**) which are used for fs-PLD.

6.3 Influence of laser energies on the deposition of GeSe₄ on Si (100) substrate

Four samples (S20, S30, S40, and S50) were fabricated from the same target by varying the laser energies of the fs-PLD. Four different laser energies of; 20, 30, 40, and 50 μJ, were applied respectively, all other process conditions were kept constant. Table 6.2 below provides details of the deposition parameters for the four samples.

Table 6.2: Deposition parameters employed to deposit GeSe₄ onto silicon substrate

Process parameter	Operating conditions
Substrate	Silicon; dimensions 20 mm (L) × 12 mm (W) × 675 μm (T)
Target material	GeSe ₄
Target to substrate distance	70 mm
Fs-laser repetition rate	1.0 kHz
Fs-laser energy (sample ID)	20 μJ (S20), 30 μJ (S30), 40 μJ (S40), and 50 μJ (S50)
Background gas pressure	Under vacuum (10 ⁻⁶ mTorr)
Substrate temperature	400°C
Deposition time	4 hours

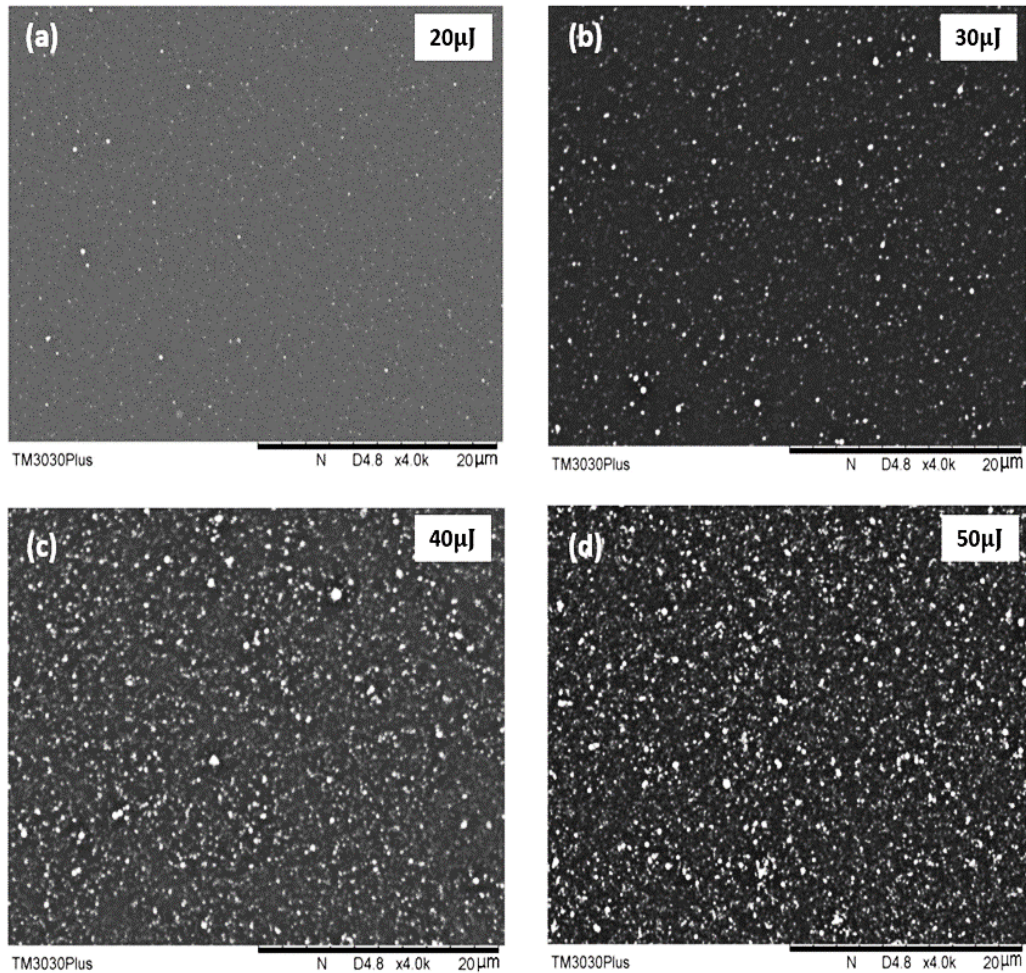


Fig. 6.2: SEM images of Ge-Se thin films deposited on silicon substrates at different laser energies; **(a)** 20 μJ , **(b)** 30 μJ , **(c)** 40 μJ , and **(d)** 50 μJ .

SEM images of the deposited Ge-Se thin films at different laser energies are shown in Fig. 6.2 (a-d). The morphology of the deposited films was observed to be homogeneous, although the cluster sizes are observed to be increasing with energy. The thin film deposited with fs-laser energy of 20 μJ [Fig. 6.2 (a)] showed a relatively thinner particulate surface without apparent porosity or any cracks. However, as the fs-laser energy increased to 30 μJ , 40 μJ , and 50 μJ , the distribution of the grains on the substrate surfaces increased and became more compact [Fig. 6.2 (b-d)].

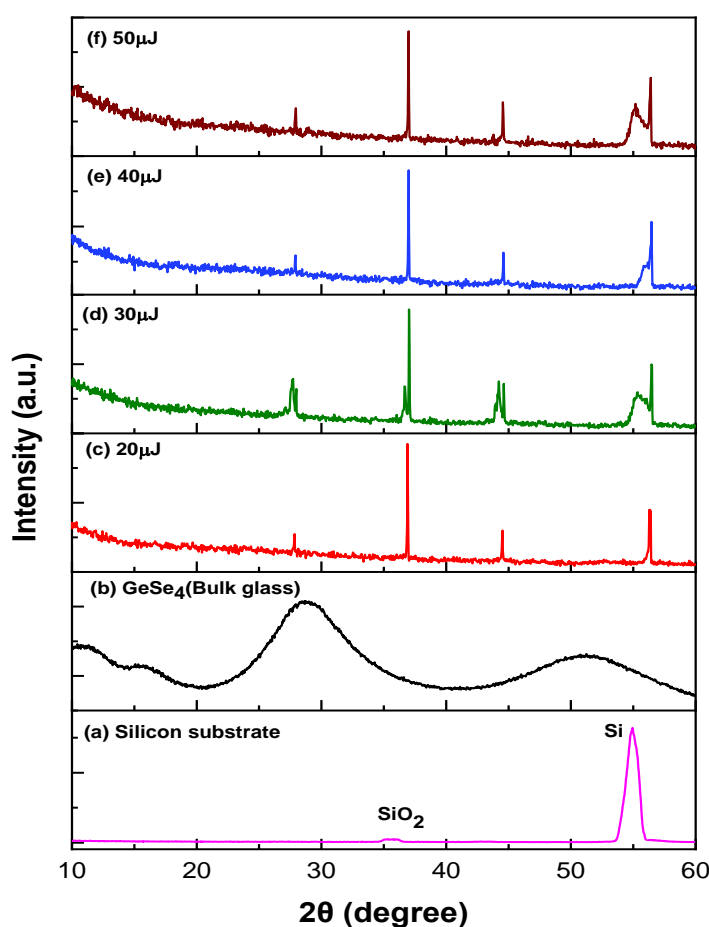
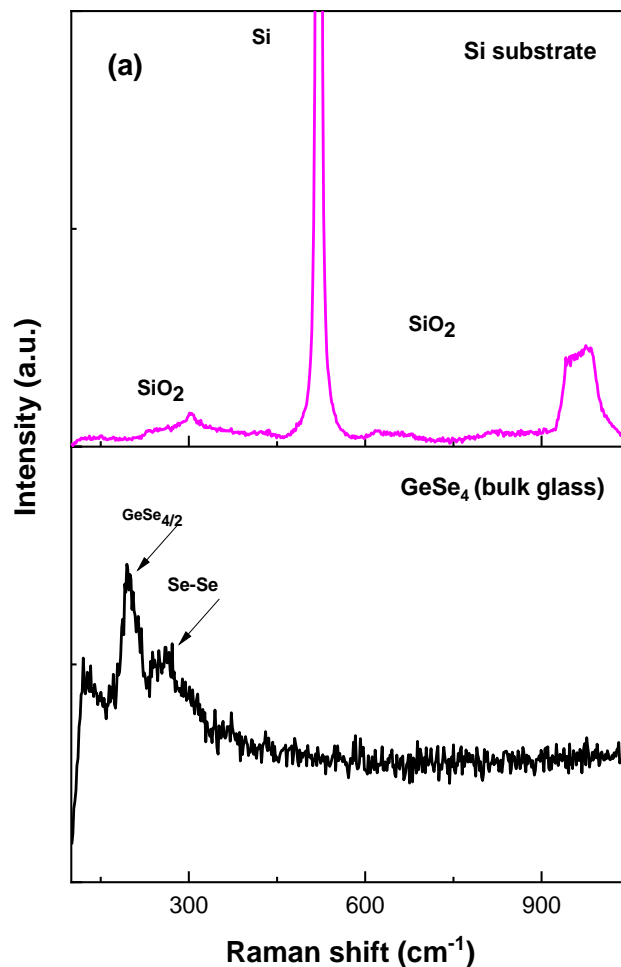


Fig. 6.3: XRD patterns of (a) pure silicon substrate (thickness = 675 μm), (b) GeSe_4 bulk glass, and (c-f) Ge-Se thin films fabricated on silicon glass by fs-PLD at laser energies of; 20 μJ , 30 μJ , 40 μJ , and 50 μJ , respectively.

Figure 6.3 shows the XRD patterns of the silicon substrate, GeSe_4 bulk target glass, and Ge-Se thin films deposited at various laser energies. The XRD pattern obtained from the silicon substrate in Fig. 6.3 (a) exhibited a strong diffraction peak at approximately $2\theta = 56.07^\circ$, which was indexed as the (311) plane and corresponded to Bragg reflection of cubic silicon [303-305] based on the ICDD reference pattern No. 00-005-0565 for cubic silicon. In addition to this, the diffraction peak position at $2\theta = \sim 37^\circ$ (111) was identified as silica, correlating to the ICDD reference pattern No. 00-080-4051. On the other hand, the XRD pattern of the bulk GeSe_4 glass target in Fig. 6.3 (b) revealed four distinct wide-stretched amorphous halo structures centred at around $2\theta = 13^\circ$, 17° , 28° , and 51° without any sharp peak. These wide-stretched bands correspond to amorphous diffraction patterns of GeSe , GeSe_2 and GeSe_4 [49, 176, 186, 187, 332, 333].

Further experiments were conducted to access the effect of laser energy on the Ge-Se thin film deposited using fs-PLD. The XRD patterns of the resulting samples S20, S30, S40, and S50 are also depicted in Fig. 6.3 (c-d). XRD of the Ge-Se thin films deposited on the silicon substrate at different energies indicated the presence of Ge-Se crystallites. A broad band, amorphous structure observed for the target GeSe_4 has been split into distinct diffraction peaks centred at $2\theta = 28^\circ$ and 44.6° . These diffraction peaks were indexed to the ICDD reference pattern numbers 01-071-4730 and 04-007-0120 for crystalline GeSe_4 . Furthermore, the various thin film samples also showed additional crystalline peaks at $2\theta = \sim 36^\circ$ and $\sim 56^\circ$, which are not observed in the diffraction pattern of the silicon substrate. These peaks correspond to GeSe_2 and $\text{Ge}_{0.44}\text{Si}_{0.56}$ as indexed with ICDD reference pattern numbers of 04-007-0120 and 04-006-2528.



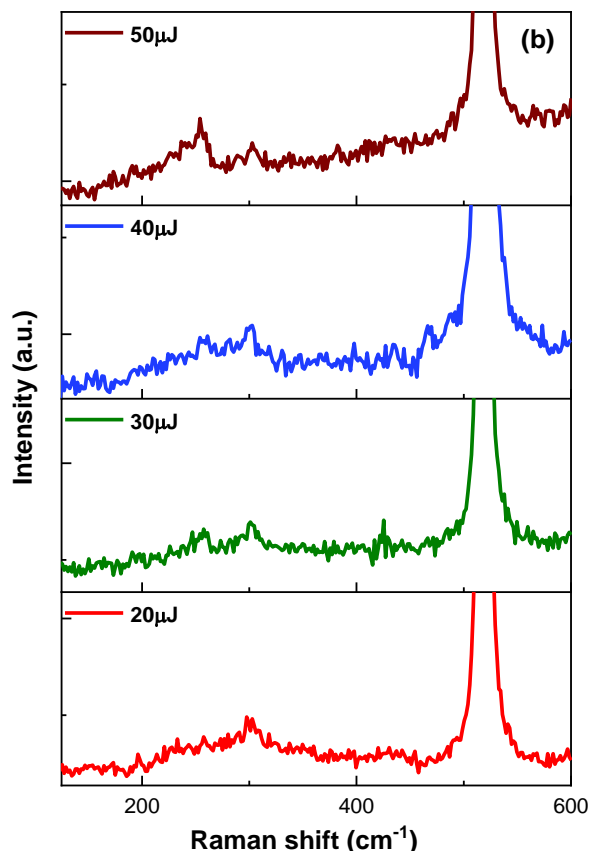


Fig. 6.4: Raman spectra of (a) pure silicon substrate (thickness = 675 μm) and GeSe_4 bulk glass, (b) Ge-Se thin films deposited on silicon substrate at different laser energies; 20 μJ , 30 μJ , 40 μJ , and 50 μJ .

Figure 6.4 represents Raman spectra of the pure Si substrate, GeSe_4 bulk glass, and as-deposited Ge-Se thin films at various fs-laser energies. The Raman spectra of the silicon substrate and GeSe_4 target material is shown in Fig. 6.4 (a). The Raman spectrum of the silicon substrate revealed a sharp Lorentzian peak at $\sim 520 \text{ cm}^{-1}$, which is characteristic of a crystalline silicon peak and in good agreement with observations made by Khorasaninejad et al. [307]. Furthermore, another broad peak was also observed at $\sim 1100 \text{ cm}^{-1}$, which indicates the presence of an amorphous fraction of silica [307-310]. The Raman spectrum of GeSe_4 bulk glass is also illustrated in Fig. 6.4 (a). This consists of four main broad regions, which are distinguishable. The robust and sharp peak at $\sim 195 \text{ cm}^{-1}$ assigned to Ge-Se corner-sharing clusters of GeSe_4 tetrahedral units vibration modes [178, 334]. The vibration shoulder centred at $\sim 215 \text{ cm}^{-1}$ can be attributed to edge-sharing $\text{Ge}_2\text{Se}_{8/2}$ bi-tetrahedra [178, 334]. While the broad band range from

225 to 280 cm^{-1} peaked at 259 cm^{-1} is also consistent with $\text{GeSe}_{4/2}$ network matrix. Additionally, the broad vibration band with the maximum spike at 305 cm^{-1} is associated with the edge-sharing asymmetrical stretching bonds [187]. The Raman bands are in good agreement with previously reported values [49, 176, 177, 186-189, 191, 214, 335].

Fig. 6.4 (b) also shows Raman spectra of all Ge-Se thin film samples deposited on Si substrate. The samples prepared with fs-laser energies of 20 μJ (S20) and 30 μJ (S30) reveal Raman bands for the GeSe_4 target glass, which are centred at $\sim 195 \text{ cm}^{-1}$, $\sim 256 \text{ cm}^{-1}$, and $\sim 300 \text{ cm}^{-1}$ correlate with Ge-Se, Se-Se, and Ge-Se bands, respectively [187, 189, 191]. However, the intensities of these peaks were quite weak in comparison to the target material shown in Fig. 6.4 (a). The single crystalline silicon peak observed from the silicon substrate was also detected at 520 cm^{-1} . As the laser energy increased to 50 μJ (S50), the intensity of GeSe_4 bands identified from the target materials also increased.

6.4 Influence of substrate temperature on GeSe_4 bulk glass doping into Si (100) substrate

Based on the above results; the further investigation was carried out to study the effect on substrate temperature for depositing GeSe_4 target material on the silicon substrate and optimise the process parameters. The fs-laser energy was kept at 40 μJ as the SEM image of the sample fabricated at this energy revealed a relatively small density of droplets, uniformly distributed across the entire substrate [Fig. 6.2] when compared to the other specimens deposited at different fs-laser energies (20 μJ , 30 μJ , and 50 μJ). Moreover, XRD and Raman spectra [Fig. 6.3 and 6.4] exhibited Ge-Se crystalline phase peaks. So, the laser energy of 40 μJ was used to prepare samples reported in this section using varying the substrate temperatures. The substrate temperature at the point of deposition was changed starting from room temperature (25°C), 200°C, 400°C, to 600°C, while other deposition parameters were kept constant. Table 6.3 below provides details of deposition parameters for the four samples fabricated at substrate temperatures ranging from 25°C to 600°C.

Table 6.3: List of parameters employed to deposit GeSe₄ on Si substrate by using different substrate temperatures

Process parameter	Operating conditions
Substrate	Silicon; dimensions 20 mm (L) x 12 mm (W) x 675 μm (T)
Target material	GeSe ₄
Target to substrate distance	70 mm
Fs-laser repetition rate	1.0 kHz
Fs-laser energy	40 μJ
Background gas pressure	Under vacuum (10 ⁻⁶ mTorr)
Substrate temperature (sample ID)	25°C (S25), 200°C (S200), 400°C (S400), and 600°C (S600)
Deposition time	4 hours

6.4.1 Influence of substrate temperature on Ge-Se thin film (SEM)

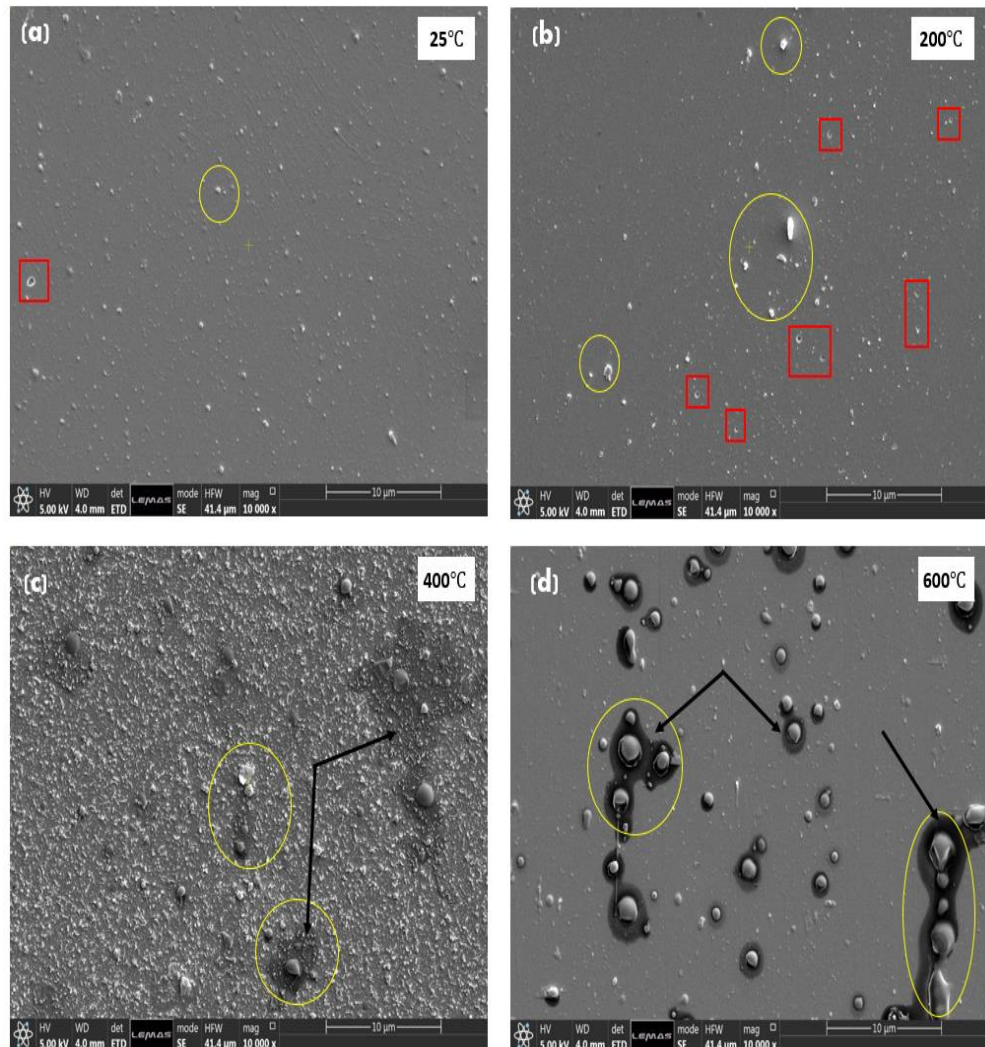


Fig. 6.5: FIB-SEM images of Ge-Se thin films deposited on silicon substrate at various temperatures; (a) 25°C, (b) 200°C, (c) 400°C, and (d) 600°C.

Samples produced at different substrate temperatures during fs-PLD were examined on the SEM to observe changes to surface morphology and other characteristics of the as-deposited thin films. Figure 6.5 shows SEM images of each sample obtained at the same magnification (10,000 x).

The sample fabricated at 25°C exhibited the presence of nanoparticles some with a spherical droplet-like morphology (circled) while another set had a pinhole-shaped morphology (squared) on the surface of the Ge-Se thin film. In addition, there appeared to be some level of homogeneity of the film with a relatively smooth surface profile and little or no particle agglomeration observed (Fig. 6.5 (a) and (b)) at 25°C and 200°C, respectively. However, as the substrate temperature was increased to 400°C, the number of droplet-like nanoparticles on the thin film surface increased with the significant variations in particle size as depicted in Fig. 6.5 (c) [with some of the large particles shown in yellowish circles]. Thus, it leads to an increase in surface roughness of the film. Furthermore, the sample deposited at a substrate temperature of 600°C exhibited larger droplets of particles in smaller quantity on the top surface of the thin film (in yellowish circles) [as depicted in Fig. 6.5 (d)] as compared to sample deposited at 400°C. This shows that as the substrate temperature increased from 400°C to 600°C, the surface roughness of the thin film decreased due to the evaporation of particles during deposition. Henceforth, such changes in surface roughness of the films via increased in substrate temperature can be related to the structural and chemical transformations of the deposited layer (disorder).

Cross-sectional lamina of the Ge-Se thin films was obtained from the samples via FIB lithography and examined on the TEM. Fig. 6.6 (a-d) shows TEM images of the cross-sections of the investigated Ge-Se thin films obtained by using FIB lithography.

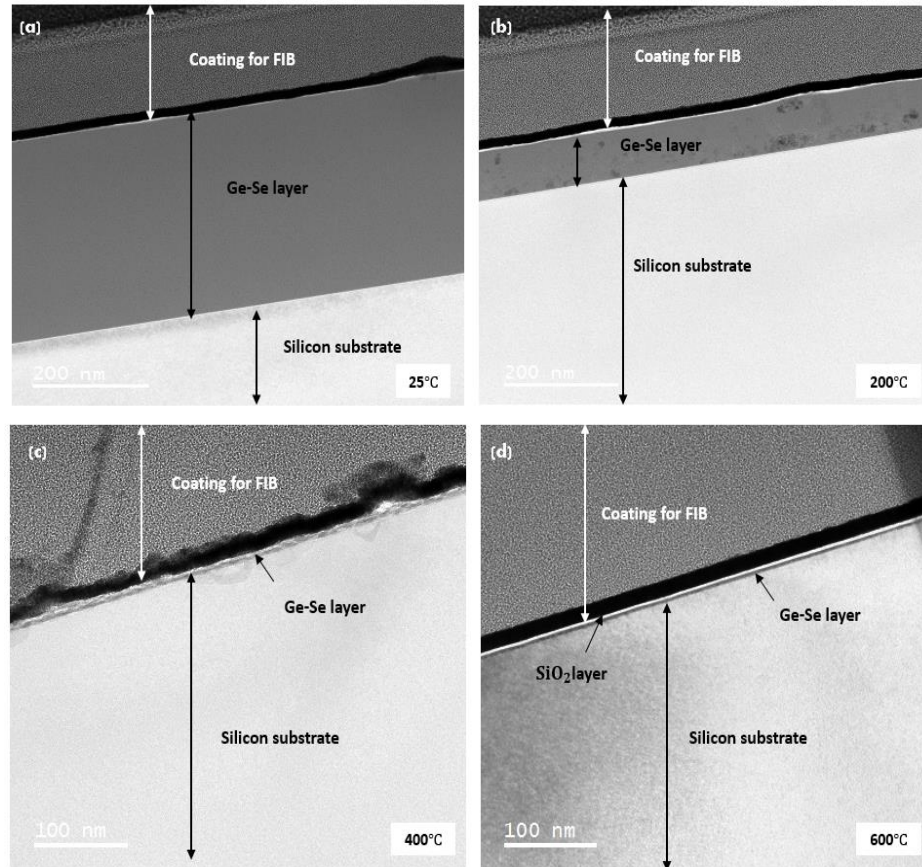


Fig. 6.6: TEM cross-section images of Ge-Se layer formed on silicon substrates by fs-PLD at various substrate temperatures; **(a)** 25°C (S25), **(b)** 200°C (S200), **(c)** 400°C (S400), and **(d)** 600°C (S600).

Figure 6.6 (a) shows a closer view of the TEM image of the Ge-Se thin film deposited at room temperature (25°C), which displayed a uniform cross-section of Ge-Se layer sandwich between the coated FIB layer on top and pristine silicon. The cross-section of Ge-Se thin film looked darker than the silicon layer, as Ge and Se are heavier elements than the silicon. It is important to mention that the deposited Ge-Se layer was smooth without the presence of nanoparticle clusters or defects. Nevertheless, as the substrate temperature increased from 25°C to 200°C, the TEM image shows occasionally defects within the Ge-Se thin film layer. These defects may compose of a different phase of Ge-Se. The TEM cross-section of samples deposited at 400°C and 600°C clearly indicated that the substrate temperature has significant effects on the thin film thickness and quality, as shown in Fig. 6.6 [(c) and (d)]. The plan view of TEM images revealed an

average Ge-Se thin film thickness of about ~400 nm for at 25°C, ~150 nm for at 200°C, and ~7nm for at 400°C and 600°C.

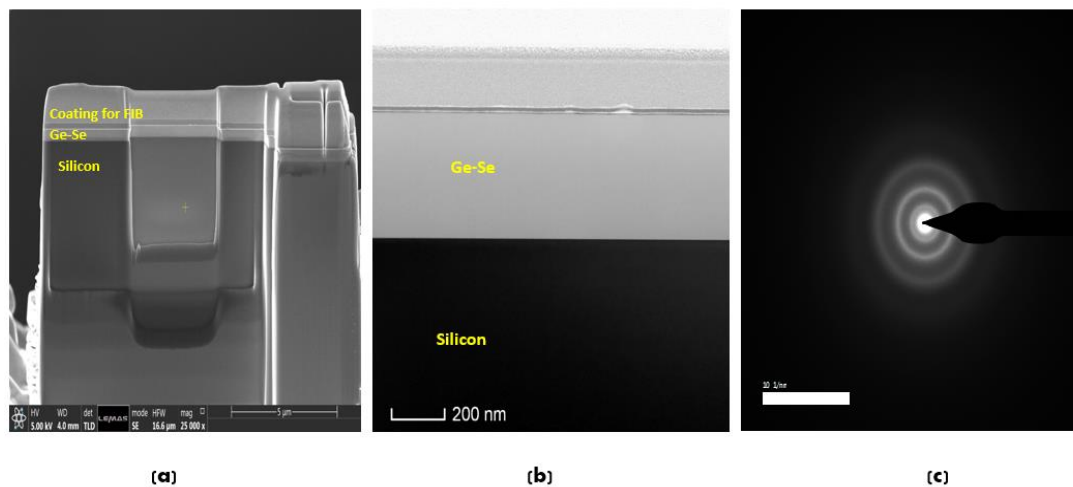
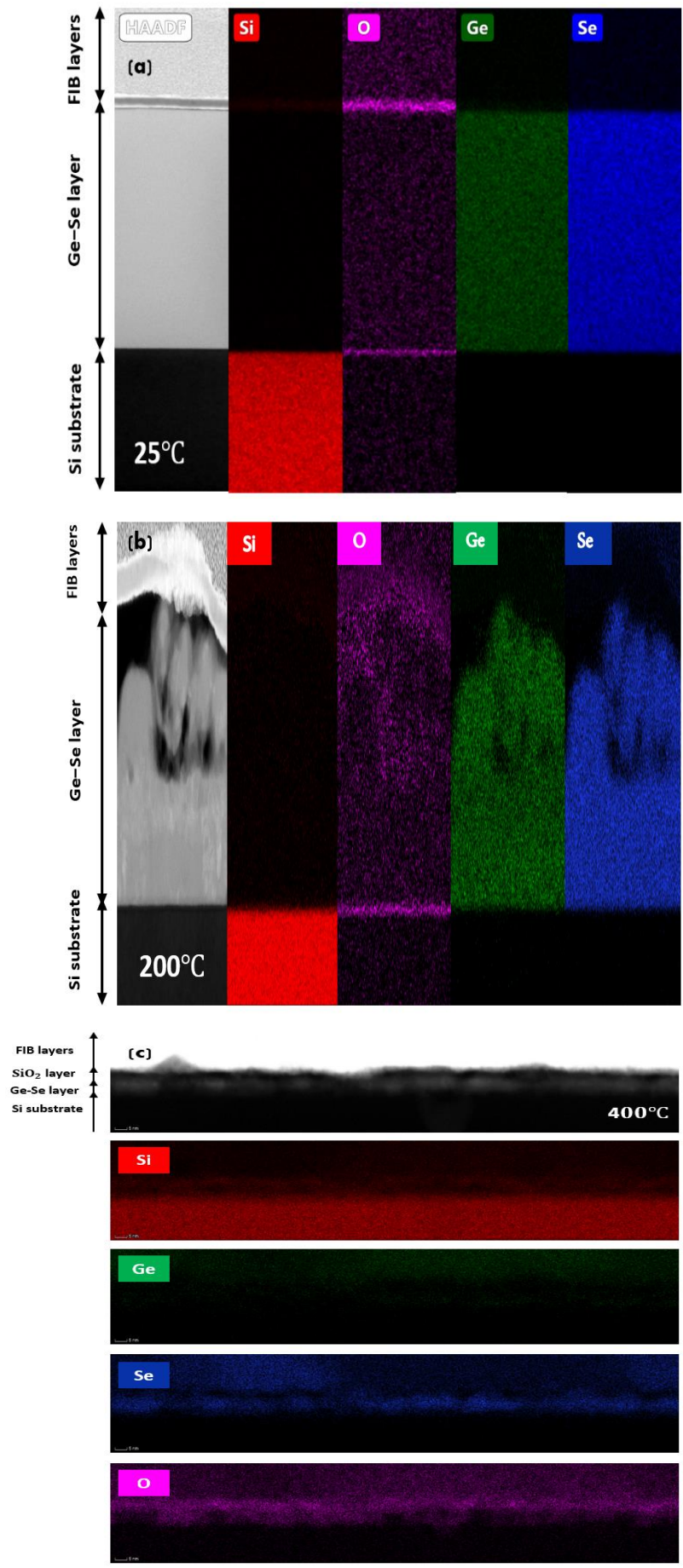


Fig. 6.7: Images of Ge-Se layer on silicon from sample S25 prepared at room temperature (25°C); **(a)** FIB-SEM image of the Ge-Se layer cross-section, **(b)** cross-sectional BF-TEM image of Ge-Se layer, and **(c)** SAED pattern captured from the Ge-Se layer region confirming the amorphous state.

Figure 6.7 (a) illustrates the cross-section of Ge-Se thin film layer fabricated at 25°C using FIB lithography. A clear distinction is observable between the Ge-Se layer and the underlying Si substrate layer. Fig. 6.7 (b) shows a cross-sectional TEM image of a high-quality Ge-Se film without crystalline grains. SAED pattern from the Ge-Se thin film layer reveals circular rings around the central spot, as illustrated in Fig. 6.7 (c), confirming the presence of amorphous structure in the Ge-Se thin film prepared at 25°C.

6.4.2 Influence of substrate temperature on Ge-Se thin film (EDX spectroscopy)

EDX analysis of the four TEM cross-sections of the thin films fabricated at various temperatures (25, 200, 400, and 600°C) was performed using STEM mode on the TEM to understand the elemental distribution within the thin film layer. EDX spectroscopy was also performed. The TEM cross-sectional images of the deposited films and the results of EDX-STEM analysis of the films are presented in Figure 6.8 for each temperature variable.



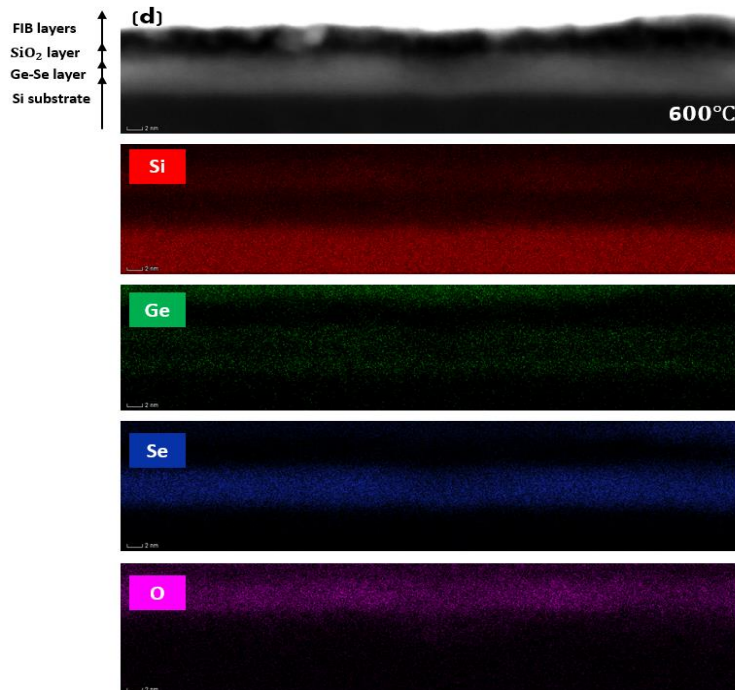


Fig. 6.8: HAADF-STEM images and STEM-EDX elemental mapping images of Ge-Se thin film prepared on silicon at different temperatures; **(a)** 25°C, **(b)** 200°C, **(c)** 400°C, and **(d)** 600°C.

Elemental EDX-STEM maps of Si, Ge, Se, and O of the samples prepared at 25°C and 200°C are shown in Fig. 6.8 (a) and (b) without any intermixing of the deposited Ge-Se thin film with the silicon substrate and the thin silica layer on it. This shows evidence that Ge, Se, and O elements are uniformly distributed relatively only in the thin film area. However, as substrate temperature increased to 400°C, it was observed that deposited Ge-Se layer started to mix with the silicon substrate at the interface. At 600°C, the STEM-EDX map showed that the deposited Ge-Se layer is entirely absent; however, Ge and Se are seen embedded within the silicon. Nanoparticles and ions are present in the plasma produced by fs-PLD. However, at higher temperatures the nanoparticles got evaporated from the substrate owing to their lower melting point/sublimation temperature. The ions that are present in the plasma therefore do not experience any hindrance and subsequently they implanted into the silicon substrate penetrating through the thin silica layer. They are however not seen within the thin silica layer on silicon through. It is believed that this is attributable to the implantation of Ge/Se ions produced in the fs-laser plasma into the silicon substrate. The

accumulation of Ge/Se ions within silicon crossing the silica layer of $\sim 2\text{-}3$ nm is aided by the instantaneous evaporation of GeSe_4 nanoparticles at this temperature on arrival at the substrate. The concentration of ions within the plasma compared to nanoparticles will be significantly lower based previous studies fs-laser plasma. The ions implanted within silicon can introduce strong intrinsic point defects and act as impurities [336, 337].

However, at a higher deposition temperature (600°C), the Se concentration dominates in the Ge-Se thin film layer in comparison to Ge. This may have resulted from the loss of Ge during the deposition process at elevated temperatures because of its volatility leading to preferential inclusion of Se in the thin films fabricated at higher temperatures. It has been previously reported that the depth of ion distribution and implantation depends on the ion kinetic energy, the target material, and the substrate temperature or surrounding the target [338].

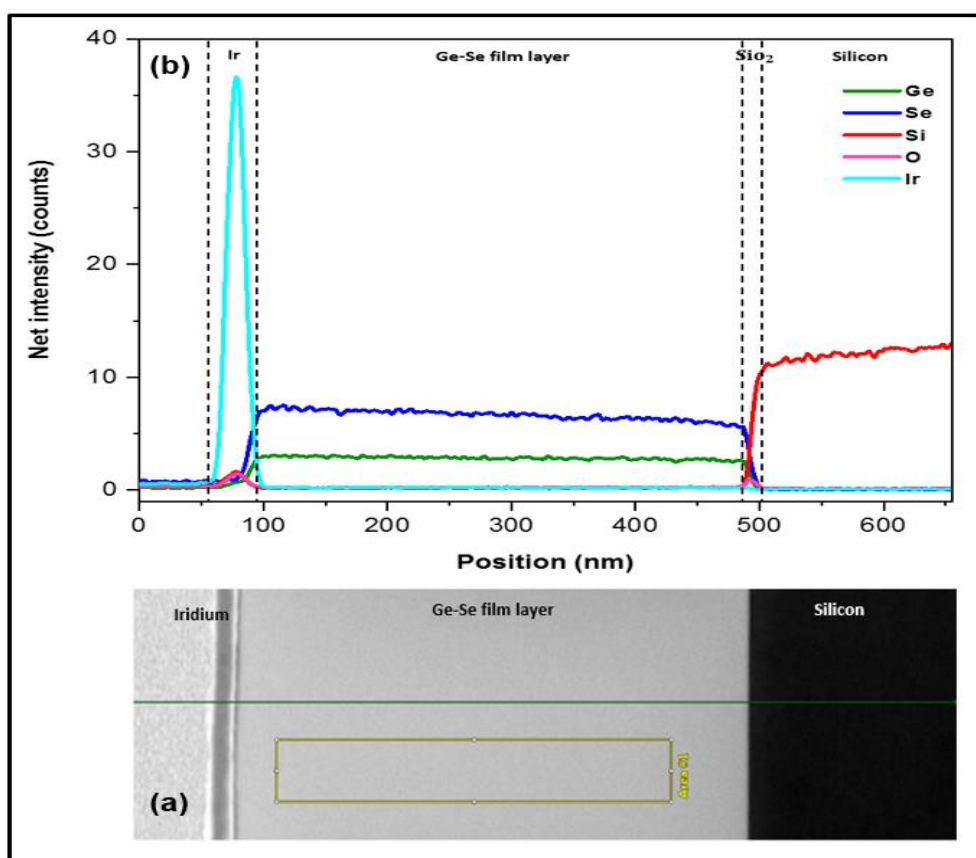


Fig. 6.9: (a) A HAADF-STEM image, and (b) a line scan obtained from STEM-EDX showing that no silicon was detected at the Ge-Se film prepared on silicon at a lower substrate temperature (25°C).

Figure 6.9 shows the HAADF-STEM image and the line-scan EDX analysis of Ge, Se, Si, and O elements over the Ge-Se film fabricated at 25°C. A line scan of the HAADF-STEM image obtained from the sample deposited at a substrate temperature of 25°C is depicted in Fig. 6.9 (b). The elemental composition analyses of the Ge-Se thin film evidenced the presence of Ge and Se in the line-scanning and are well distributed within the Ge-Se thin film layer.

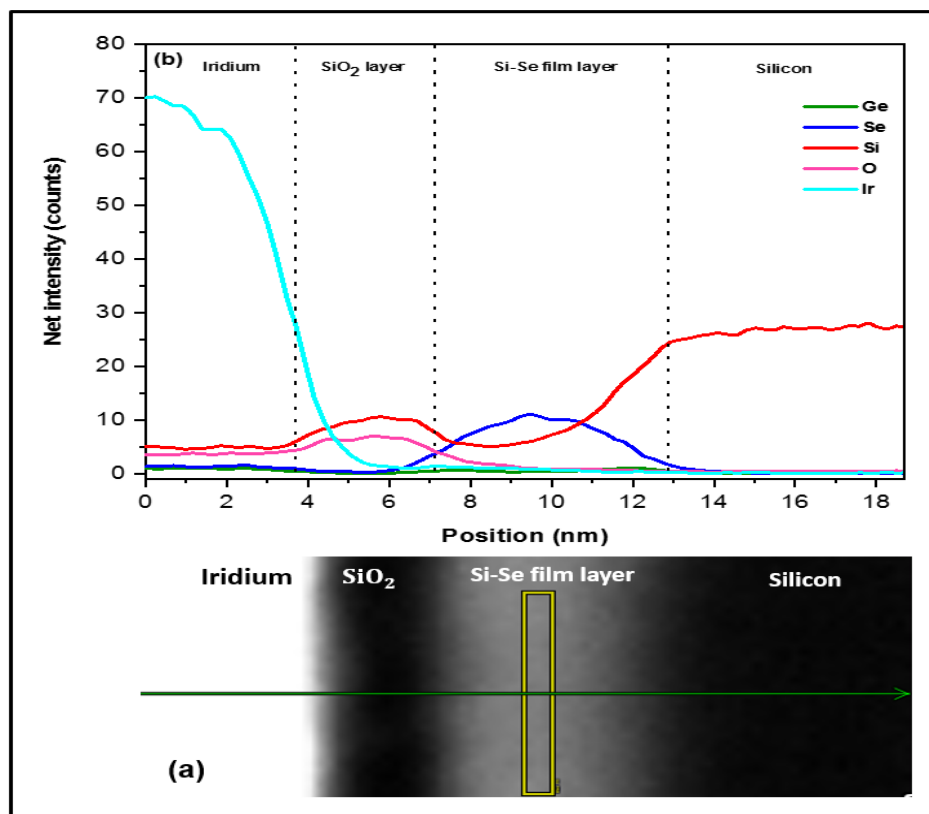


Fig. 6.10: (a) A HAADF-STEM image, and (b) a line scan gained from STEM-EDX showing that silicon was detected at the Ge-Se film prepared on silicon at a higher substrate temperature (600°C).

Figure 6.10 displays the HAADF-STEM image and the line-scan EDX analysis of Ge, Se, Si, and O elements over the Ge-Se film implanted at 600°C. The line-scan of sample grown at 600°C is shown in Fig. 6.10 (b). It confirmed the presence of Se and Ge elements in the doped Si layer. Despite this, the line-scan intensity of elemental Ge is relatively low as compared to the sample fabricated at 25°C. The low intensity of Ge could be attributed to the loss or volatility of Ge ions in the plasma plume during the deposition, which affected the bond structure of the film.

In addition to this, the elemental composition of the Ge-Se thin film areas highlighted in Fig. 6.9 (a) and Fig. 6.10 (a) was evaluated. Figure 6.11 (a) is the TEM-EDX spectrum of a sample prepared at 25°C. It showed an atomic percentage of 0.4, 0.59, 25.41, and 73.6 at. % obtained for Si, O, Ge, and Se, respectively. This result confirmed that the thin film fabricated at 25°C had barely any Si and O and is wholly made up of elements from the GeSe₄ target. On the other hand, the TEM-EDX spectrum of the sample prepared at a higher substrate temperature (600°C) [Fig. 6.11 (b)] had a higher atomic percentage of Se (63.4 at. %) and Si (29.4 at. %) when compared to O (6.3 at. %) and Ge (1.0 at. %).

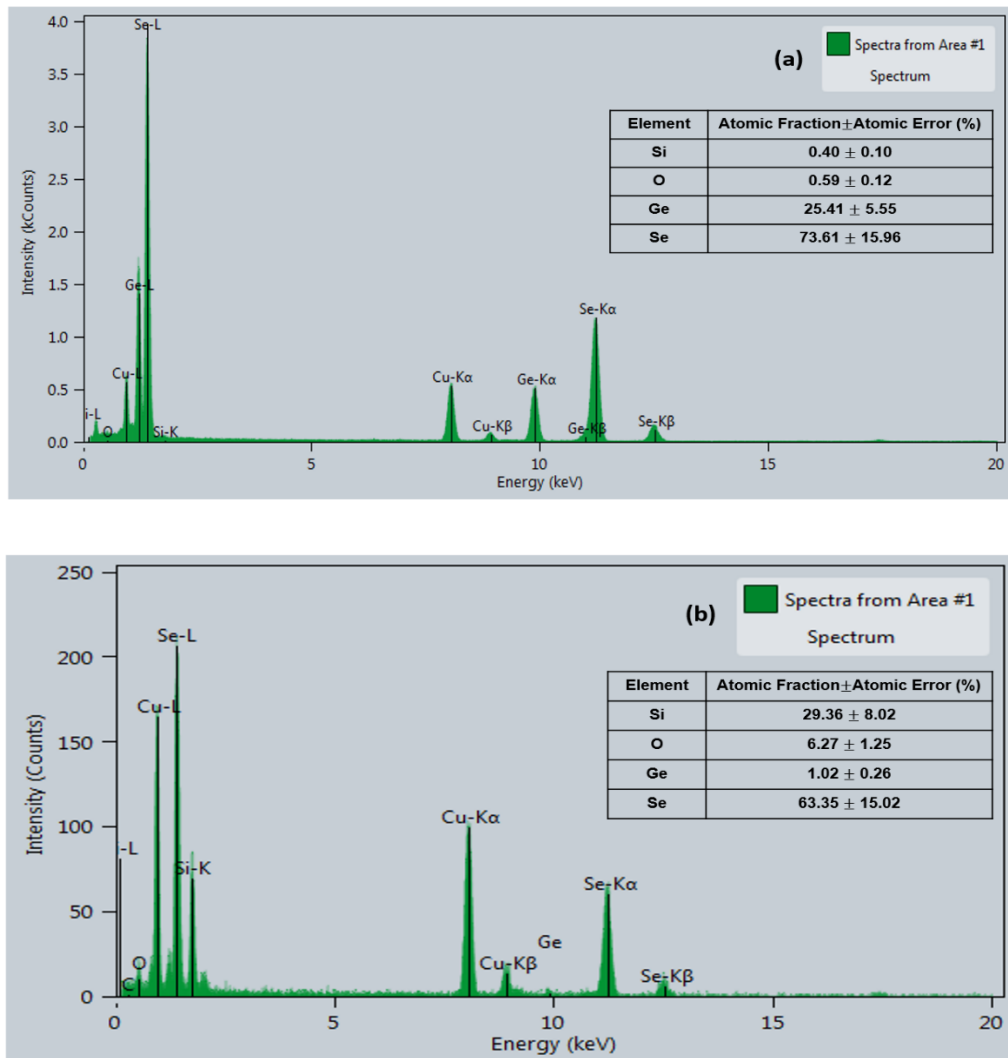


Fig. 6.11: TEM-EDX spectrum of the yellow region labelled in Fig. 6.9 (a) and 6.10 (a) of the doped layer on silicon for samples; **(a)** S25 prepared at room temperature (25°C) and **(b)** S600 prepared at 600°C.

6.4.3 Influence of different substrate temperatures on Ge-Se thin film (XRD spectroscopy)

The phase composition of the Ge-Se thin films obtained at various substrate temperatures was also analysed using XRD and is shown in Fig. 6.12. XRD phase composition analysis enables us to have a better understanding of the temperature stability of the Ge-Se thin films deposited.

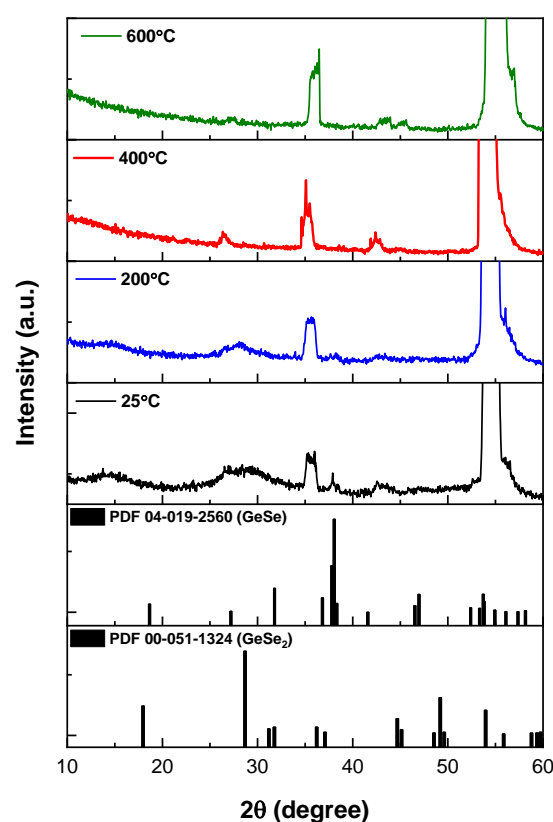


Fig. 6.12: XRD patterns of thin films fabricated on Si substrate by fs-PLD at various substrate temperatures; 25, 200, 400, and 600°C along with ICDD reference patterns for Ge-Se bulk glass.

Figure 6.12 displays the XRD patterns of the Ge-Se thin films deposited at various substrate temperatures. The XRD patterns of the silicon substrate and GeSe₄ target material are shown and discussed in Fig. 6.3.

A further experiment was conducted to study the influence of substrate temperature on the Ge-Se thin film deposited with fs-PLD. The more intense diffraction peak at $2\theta = 56^\circ$ can be attributed to Ge-Se and silicon overlap diffraction pattern identified in all the thin film samples. The XRD patterns of samples fabricated at a substrate temperature of 25°C and 200°C exhibited

similar diffraction patterns with the peaks centred at $2\theta = 15^\circ$, 29.5° , and 43° , which are identical to the GeSe_4 target. Furthermore, the two broad band features range from $2\theta = 10^\circ$ to 20° and 25° to 36° correlated with the amorphous structures identified from the target material. This correlated with the TEM-SAED pattern shown in Fig. 6.7 (c). The XRD pattern of sample S25 revealed additional peaks at $2\theta = \sim 27^\circ$, 38° , and 53° , which are indexed as the crystalline structure of the Ge-Se, as shown in Fig. 6.12. These diffraction peaks match with Ge-Se orthorhombic phase (ICDD reference code: 04-019-2560). However, as the substrate temperature increased to 400°C , the intensity of these broad amorphous diffraction bands diminished and disappeared completely. For instance, the GeSe_4 amorphous structures observed from the samples deposited at 25°C and 200°C disappeared completely in the deposited sample at 600°C . The absence of GeSe_4 amorphous diffraction patterns with a substrate temperature of 400°C and 600°C could be attributed to the Ge-Se thin film thickness (~ 7 nm) implanted in the silicon substrate, which may not be sensitive enough for the XRD instrument to detect [187].

6.4.4 Influence of various substrate temperatures on the Ge-Se thin film (Raman spectroscopy)

Figure 6.13 represents Raman spectra of the as-deposited Ge-Se thin films at various substrate temperatures of 25°C , 200°C , 400°C , and 600°C . The Raman spectra of the silicon substrate and GeSe_4 target material are shown and discussed in Fig. 6.4 (a).

The Raman spectra of the four samples deposited at various substrate temperatures are shown in Fig. 6.13 with distinctive features. For instance, samples deposited at 25 and 200°C had a sharp high-intensity band at 195 cm^{-1} . This corresponded to the corner-sharing (CS) tetrahedral structures $\text{GeSe}_{4/2}$ along with the edge-sharing (ES) tetrahedral structures peaked at 214 cm^{-1} . In addition to these structures, a shallow intensity shoulder centred at 170 cm^{-1} can be assigned to Ge-Se vibrational. A weaker vibration band of Ge-Se is also observed at 308 cm^{-1} . The Raman bands

agree with the previously reported results [308, 335, 339]. However, the Raman vibration bands of the GeSe₄ target disappeared completely at higher substrate temperatures (400 and 600°C), whereas the silicon band occurs at 520 cm⁻¹ dominated. This is attributed to a lower level of Ge-Se material deposition on the silicon substrate. The Raman spectra of these thin films is in good agreement with the XRD results already discussed above.

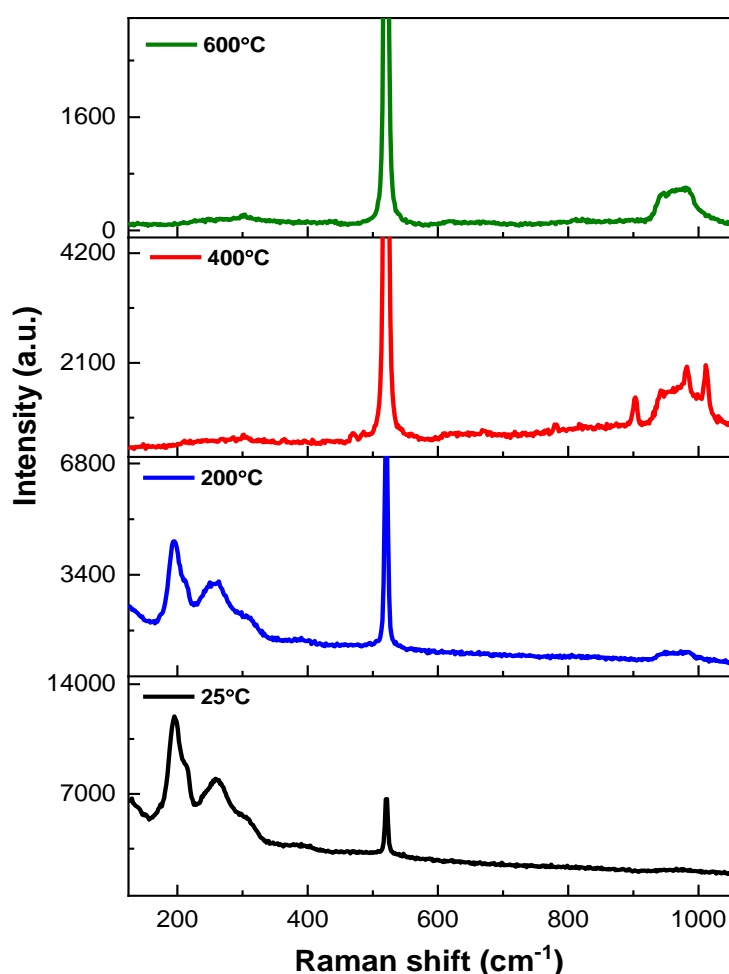


Fig. 6.13: Raman spectra of Ge-Se thin films fabricated on Si substrate by fs-PLD at various substrate temperatures; 25, 200, 400, and 600°C.

6.4.5 Influence of substrate temperatures on the Ge-Se thin film (UV-Vis spectroscopy)

Optical properties of Ge-Se films grown by fs-PLD at different substrate temperatures were measured at room temperature by using the UV-Vis-NIR spectrophotometers in the 250-2000 nm wavelength range. The

absorption coefficient (α) of the film has been obtained from the transmission via Lambert formula in [see equation 2.1]. Besides, the optical band gap of Ge-Se thin film is determined by using Tauc's relationship, which is illustrated in equation [2.2].

In this study, $n = 1/2$ corresponds to direct transition, which was utilised to estimate the optical band gap of all the thin films. The optical band gap (E_g) was obtained by extrapolating the linear portion of the curve to $\alpha h\nu = 0$, as illustrated in Fig. 6.14 and the values are shown in Table 6.4. The optical band gap of the Ge-Se films is in the range of 2.0-2.4 eV. According to Table 6.4, the optical band gap slightly decreased as the substrate temperature increased, and the thin film thicknesses decreased. Similar results have been reported elsewhere for GeSe_2 , GeSe_3 , and $\text{Ge}_{0.28}\text{Se}_{0.72}$, [176, 177, 179, 181, 188].

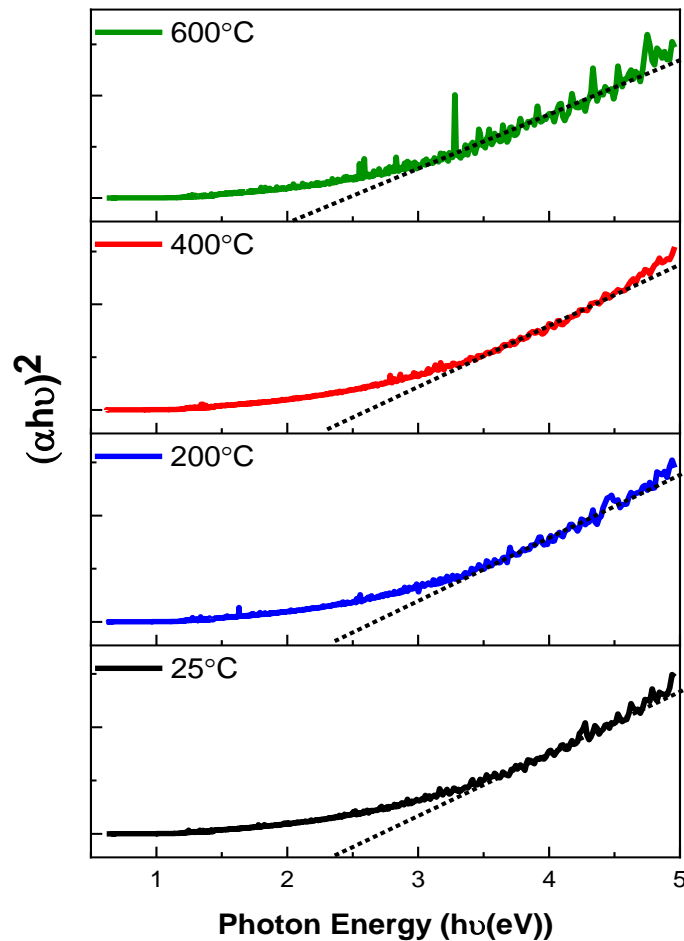


Fig. 6.14: Absorption coefficient as a function of photon energy for different Ge-Se thin films.

Table 6.4: Optical energy band gap of Ge-Se films prepared at various substrate temperatures

Sample	Substrate temperature T_s (°C)	Thickness d (nm)	Optical energy band gap (eV)
S25	25	400	2.4
S200	200	15	2.4
S400	400	~7	2.3
S600	600	~7	2.0

6.5 Conclusion

In the present study, fs-PLD was employed to deposit and dope Ge-Se thin films on/in silicon (100) substrate at various laser energies and substrate temperatures. The effect of them on the structural and optical properties of Ge-Se thin films was investigated. The structural characterisation showed that laser energy and substrate temperature significantly impacted on the surface roughness and quality of Ge-Se film thickness deposited on the silicon substrate. For instance, as the substrate temperature increased the grain size of the nanoparticles on the film surface also increased. Cross-sectional analysis of the Ge-Se thin film revealed that an increase in substrate temperature leads to a decrease in film thickness. The high substrate temperature also exhibits fs-PLD-assisted induced intermixing and ion implantation on the silicon. Optical properties of the Ge-Se thin films were also analysed by measuring the transmission spectra in wavelength ranging from 250 to 2000 nm. The associated interband transition of the Tauc relationship was found to be allowed and then used to estimate the optical band gap at various substrate temperature. It was observed that the optical energy band gap of the Ge-Se films decreased with increasing substrate temperature with estimated values ranging from 2.4 to 2.0 eV.

Chapter 7: Germanium antimony selenide ($\text{Ge}_{20}\text{Sb}_{15}\text{Se}_{65}$) deposition and diffusion on silicon

7.1 Introduction

In this chapter, results from the fabrication and characterisation of a Ge-Sb-Se layer on/in Si substrate using fs-PLD is presented. Details of deposition and diffusion of Ge, Sb, and Se from ($\text{Ge}_{20}\text{Sb}_{15}\text{Se}_{65}$) chalcogenide glass target onto/into Si substrate (100) to fabricate the Ge-Sb-Se layer or induced intermixing of the target with Si substrate are discussed. Fs-PLD process parameters such as; fs-laser energy and substrate temperature were varied. Surface morphological, structural, and optical properties of the as-deposited thin films were evaluated to understand better the relationship between deposition parameters and the properties of the thin film with the aim of pinpointing optimal conditions needed to fabricate a uniform Ge-Sb-Se layer on the Si substrate. Understanding structure and optical properties in the thin films is essential for the effective usage of the film in devices.

7.2 Target material: germanium antimony selenide ($\text{Ge}_{20}\text{Sb}_{15}\text{Se}_{65}$) glass

The $\text{Ge}_{20}\text{Sb}_{15}\text{Se}_{65}$ glass was synthesised by the conventional melt quenching technique use for ChGs [46, 340]. The ingot of $\text{Ge}_{20}\text{Sb}_{15}\text{Se}_{65}$ glass target material employed in this research work was prepared and provided by Jiangsu Normal University-China (School of Physics and Electronic Engineering). Table 7.1 provides some of the optical and thermal properties of bulk $\text{Ge}_{20}\text{Sb}_{15}\text{Se}_{65}$ glass material.

Table 7.1: Some properties of $\text{Ge}_{20}\text{Sb}_{15}\text{Se}_{65}$ bulk glass [341, 342]

Optical	
Refractive index at 1.55 μm	2.6
Approximate transmission range (μm)	1-14
Thermal	
Glass transition temperature T_g ($^{\circ}\text{C}$)	~296
Melting temperature ($^{\circ}\text{C}$)	~850

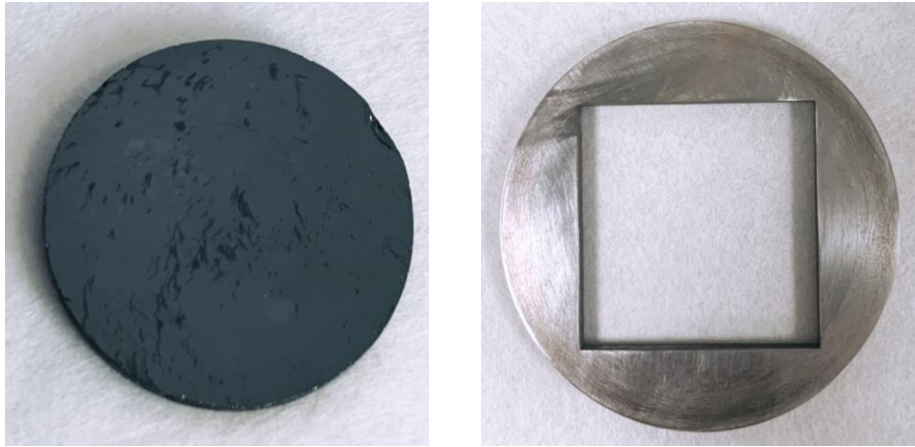


Fig. 7.1: $\text{Ge}_{20}\text{Sb}_{15}\text{Se}_{65}$ bulk glass (left) and $\text{Ge}_{20}\text{Sb}_{15}\text{Se}_{65}$ target glass holder (right) used to fabricate Ge-Sb-Se thin film.

7.3 Influence of laser energies on deposition of $\text{Ge}_{20}\text{Sb}_{15}\text{Se}_{65}$ on Si (100) substrate

Four different fs-laser pulse energies (20, 30, 40, and 50 μJ , respectively) were used in the deposition of the $\text{Ge}_{20}\text{Sb}_{15}\text{Se}_{65}$ onto Si substrate. Table 7.2 below lists the details of the four samples; Sb20, Sb30, Sb40, and Sb50, that were fabricated from the same target by varying fs-laser energies while maintaining all other process parameters fixed.

Table 7.2: Fs-PLD parameters employed in deposition of $\text{Ge}_{20}\text{Sb}_{15}\text{Se}_{65}$ thin film on Si substrate by using various fs-laser energies

Process parameter	Operating conditions
Substrate	Silicon; dimensions 20 mm (L) \times 12 mm (W) \times 675 μm (T)
Target material	$\text{Ge}_{20}\text{Sb}_{15}\text{Se}_{65}$
Target to substrate distance (d_{st})	70 mm
Fs-laser repetition rate	1.0 kHz
Fs-laser pulse energy (sample ID)	20 μm (Sb20), 30 μm (Sb30), 40 μm (Sb40), and 50 μm (Sb50)
Background gas pressure	Under vacuum (10^{-6} mTorr)
Substrate temperature	400 $^{\circ}\text{C}$
Deposition time	4 hours

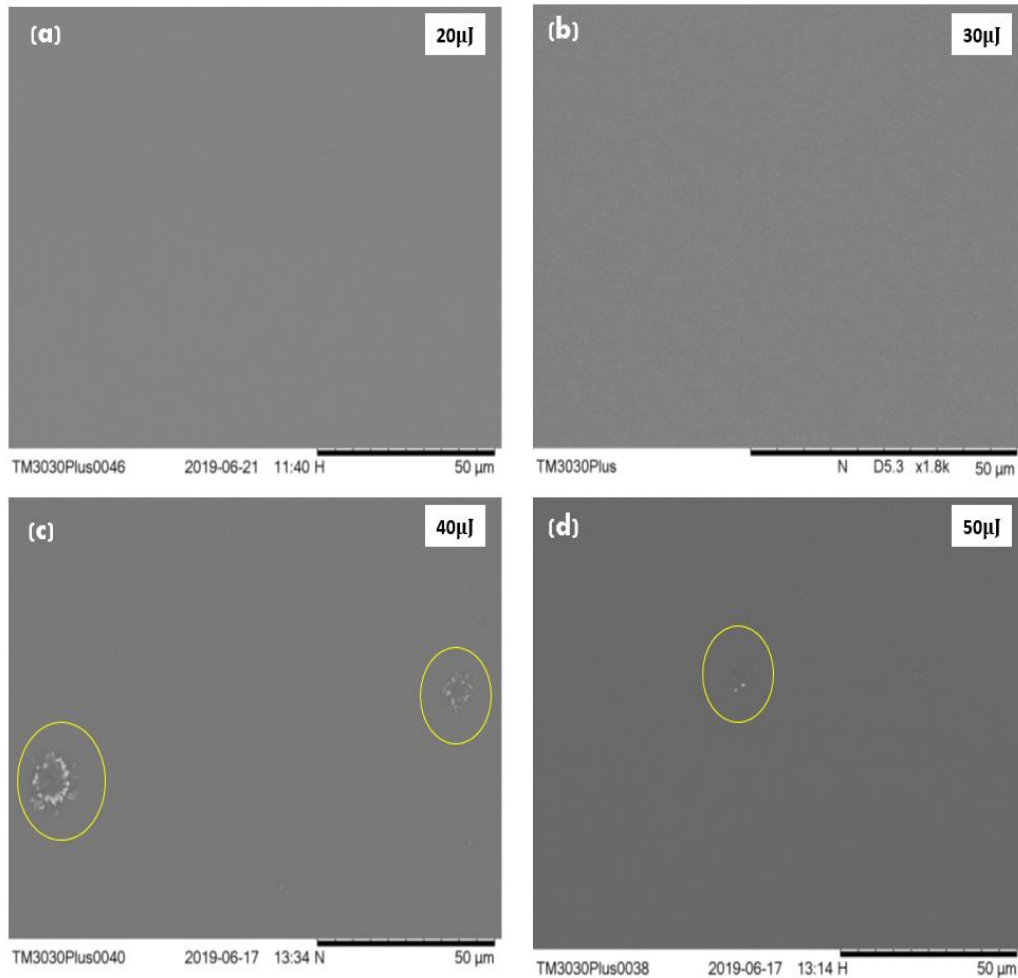


Fig. 7.2: SEM images of Ge-Sb-Se thin films deposited on silicon substrate at different laser energies; **(a)** 20 μJ , **(b)** 30 μJ , **(c)** 40 μJ , and **(d)** 50 μJ .

The morphology of Ge-Sb-Se thin films prepared by fs-PLD using different laser energies was examined on an SEM [Fig. 7.2]. The samples fabricated using 20 and 30 μJ laser energies [Fig. 7.2 (a) and (b)] showed a relatively uniform thin films surface with no apparent porosity or cracked observed. However, the sample produced with laser energy 40 μJ contained a few particles on the substrate surface [as shown in yellow circles in Fig. 7.2 (c)]. Furthermore, the sample fabricated by laser energy of 50 μJ [Fig. 7.2 (d)] also showed the presence of a minor quantity of the particle droplets as compared to Fig. 7.2 (c).

The crystalline properties of the as-deposited Ge-Sb-Se thin films were investigated using XRD.

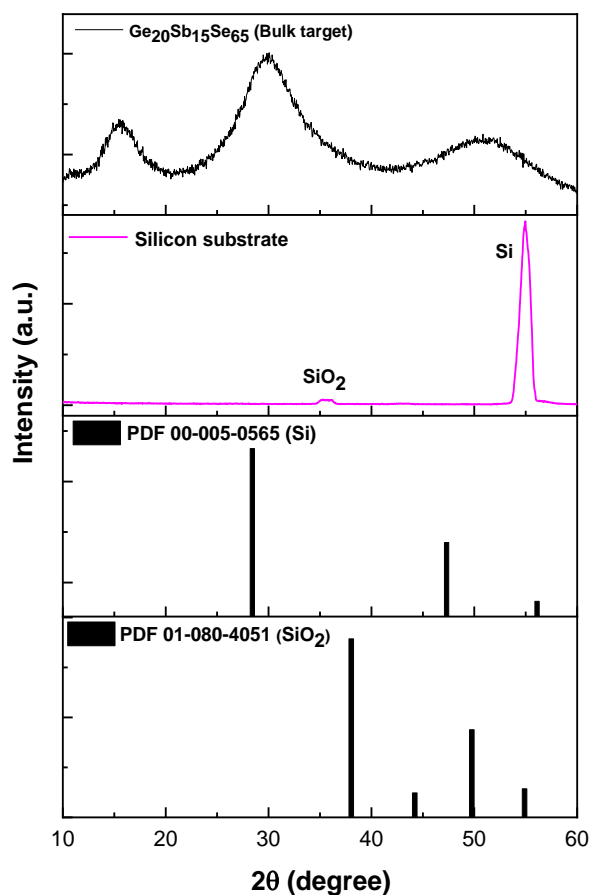


Fig. 7.3: XRD patterns of a pure silicon substrate (thickness = 675 μm) and $\text{Ge}_{20}\text{Sb}_{15}\text{Se}_{65}$ bulk glass.

Figure 7.3 shows the XRD patterns of the silicon substrate, $\text{Ge}_{20}\text{Sb}_{15}\text{Se}_{65}$ bulk target glass, along with ICDD reference patterns for silicon and silica. The XRD pattern obtained from the silicon substrate glass shows a predominant diffraction peak centred at $2\theta = 56^\circ$ (311) [303-305]. The silicon peak is in good agreement with ICDD reference code: 00-005-0565 for cubic silicon. In addition to this, the XRD peak positioned at $\sim 38^\circ$ (111) matches with the formation of silicon oxide cubic phase as indexed by ICDD reference code: 01-080-4051. On the other hand, the XRD pattern of the bulk $\text{Ge}_{20}\text{Sb}_{15}\text{Se}_{65}$ glass target reveals three distinctive wide-stretched halos amorphous structures centred at $2\theta = 13^\circ$, 17° , 28° , and 51° without any sharp peak observed. These broad humps correspond to the amorphous diffraction patterns of $\text{Ge}_{20}\text{Sb}_{15}\text{Se}_{65}$ [207, 343, 344].

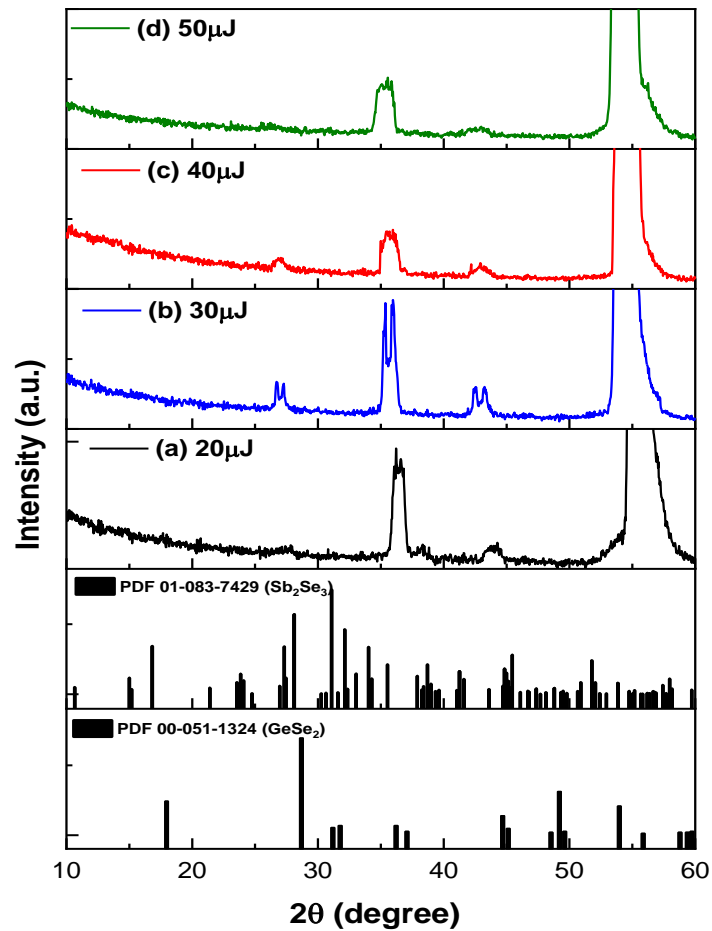
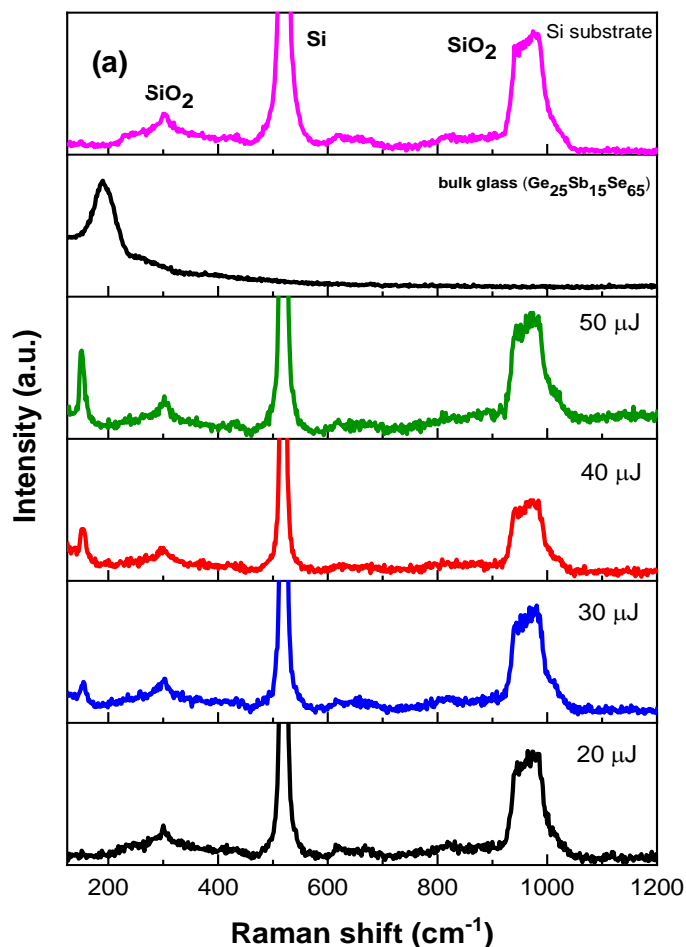


Fig. 7.4: XRD patterns of Ge-Sb-Se thin films fabricated on Si glass substrates by fs-PLD at various laser pulse energies; **(a)** 20 μJ , **(b)** 30 μJ , **(c)** 40 μJ , and **(d)** 50 μJ along with ICDD reference patterns for Ge-Sb-Se bulk glass.

Figure 7.4 shows the XRD patterns of each of the Ge-Sb-Se thin films deposited on the silicon substrate using laser pulse energies of 20, 30, 40, and 50 μJ , respectively. From the XRD patterns of these thin films, it can be deduced that the (311) silicon and (111) silica planes had relatively higher intensities. Further analysis of the XRD pattern of sample Sb20 deposited using 20 μJ laser energy [Fig. 7.4 (a)] reveals two broad weak peaks centred at $2\theta = \sim 28^\circ$ and 43° , which demonstrate antimony selenide orthorhombic phase (Sb_2Se_3) [345, 346] and germanium selenide tetragonal phase (GeSe_2) grown in the thin film [347, 348]. This observation implies that the Ge-Sb-Se thin film deposited using 20 μJ laser energy is an amorphous nature. In addition to this, the XRD pattern of sample Sb30 (sample deposited by utilising laser pulse energy of 30 μJ [Fig. 7.4 (b)]) shows the

appearance of several diffraction peaks of $2\theta = 26^\circ$, 27° , 42° , and 43° . The diffraction peaks at 27° and 35° correspond to the formation of Sb_2Se_3 with the ICDD reference code: 01-083-7429, while the diffraction peak at $2\theta = \sim 53^\circ$ is assigned to the GeSe_2 crystalline structure with ICDD reference code: 00-051-1324. On the other hand, XRD patterns of the samples Sb40 and Sb50 [Fig. 7.4 (c) and (d)] are identical to the sample Sb20 with relatively low intensities of the diffraction patterns. The reduction in intensities of these two samples could be associated with a decrease in crystallinity as compared to sample Sb30. According to XRD data, the deposited Ge-Sb-Se thin film samples could either be amorphous or crystalline depending on the process of laser energy or fluence. For example, the phase of samples Sb20, Sb30, Sb40, and Sb50 correspond to amorphous ($20 \mu\text{J}$), crystalline ($30 \mu\text{J}$), amorphous ($40 \mu\text{J}$), and then amorphous ($50 \mu\text{J}$) as a result of the cooling rate of the nanoparticles of the thin film.



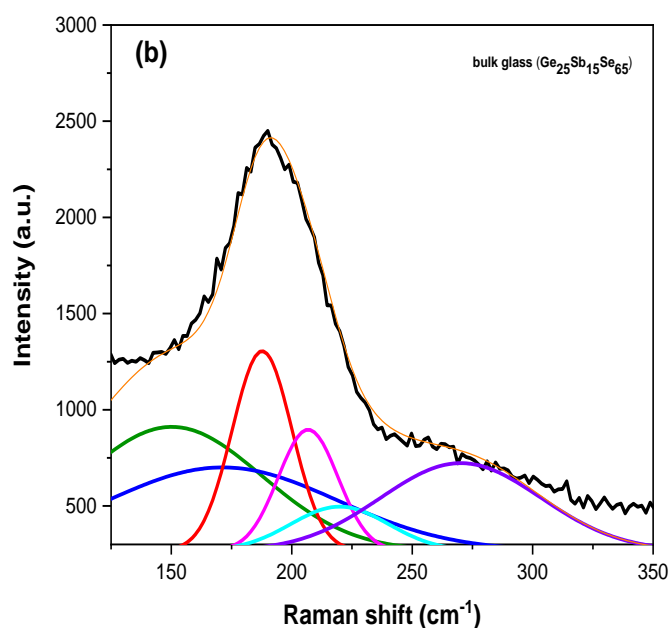


Fig. 7.5: (a) Raman spectra of a pure Si substrate (thickness = 675 μm), $\text{Ge}_{20}\text{Sb}_{15}\text{Se}_{65}$ bulk glass, and Ge-Sb-Se thin films deposited on Si substrate at different laser pulse energies; 20 μJ , 30 μJ , 40 μJ , and 50 μJ , (b) The Gaussian decomposition of the vibration Raman spectra of $\text{Ge}_{20}\text{Sb}_{15}\text{Se}_{65}$ bulk glass.

Figure 7.5 (a) represents the Raman spectra of Si substrate, $\text{Ge}_{20}\text{Sb}_{15}\text{Se}_{65}$ bulk glass, and as-deposited Ge-Sb-Se thin films at various fs-laser pulse energies. The Raman spectrum of Si substrate reveals a sharp Lorentzian peak at $\sim 520\text{ cm}^{-1}$, which corresponds to a crystalline silicon peak and is in good agreement with observations made by Khorasaninejad et al. [307, 308]. A second broad weak peak is also observed at $\sim 1100\text{ cm}^{-1}$, which can be attributed to the presence of an amorphous fraction of silica [308-310].

The Gaussian decomposition of the vibration Raman spectra of the $\text{Ge}_{20}\text{Sb}_{15}\text{Se}_{65}$ target glass is also shown in Fig. 7.5 (b). The general features of this spectrum include: (a) a prominent peak at $\sim 152\text{ cm}^{-1}$, which has been ascribed to heteropolar of Sb-Sb bond vibrations [204, 214, 349-351]; (b) the shoulder at 170 cm^{-1} is ascribed to the vibration of Ge-Ge bonds structure by cross-linked Ge atoms in the $\text{Ge}_2\text{Se}_{6/2}$ chains ($\text{Se}_3\text{Ge-GeSe}_3$ units) [204, 207, 210, 343, 344, 351-354]. This shoulder decreases with the addition of Sb [351]. Furthermore, the shoulder at 190 cm^{-1} is attributed to heteropolar Sb-Sb bond vibrations in the $\text{SbSe}_{3/2}$ pyramids [51, 204, 208, 215, 343, 344, 349-351]. The band at 200 cm^{-1} with a shoulder at 215 cm^{-1}

is assigned to the corner-sharing (CS) and edge-sharing (ES) $\text{GeSe}_{4/2}$ tetrahedral, respectively [51, 200, 215, 354-359]. However, this peak appears to be unclear in the Raman spectra because of its overlapping with the Ge-Se vibrational bands and a low Sb concentration in the investigated glass. The broad, low-intensity Raman band at 256 cm^{-1} and 266 cm^{-1} with a shoulder at 300 cm^{-1} is due to the vibration of Se_n rings and Se-Se chains, respectively [51, 210, 343, 353-358].

Figure 7.5 (a) also shows the Raman spectra of the Ge-Sb-Se thin films deposited at various fs-laser pulse energies. The sample prepared with laser energy of $20\mu\text{J}$ (Sb20) reveals no assigned Raman bands of the Ge-Sb-Se glass, but crystalline peaks of silicon and silica of the silicon substrate as already discussed above. By increasing the laser energies from $20\mu\text{J}$ to $30\mu\text{J}$ (Sb30), $40\mu\text{J}$ (Sb40), and $50\mu\text{J}$ (Sb50), the Raman spectra reveal a band with the maximum peak intensity centred at around 152 cm^{-1} . This correlates with the vibrations of Sb-Sb.

7.4 Influence of substrate temperature on $\text{Ge}_{20}\text{Sb}_{15}\text{Se}_{65}$ bulk glass doping into Si (100) substrate

Based on the results and analysis presented in section 7.3, further experimental investigations were conducted on the Ge-Sb-Se thin film deposited using $40\mu\text{J}$ fs-pulsed laser energy. The effect of varying the temperature of the silicon substrate after the deposition of the $\text{Ge}_{20}\text{Sb}_{15}\text{Se}_{65}$ target bulk glass on the silicon substrate was explored in a bid to optimise the process parameters. The fs-pulsed laser energy of $40\mu\text{J}$ was selected based on the surface morphological studies of the SEM images shown in Fig. 7.2. As the sample fabricated at this energy exhibited smaller droplets of uniform nanoparticles distributed across the entire surface of the substrate. In this section, $40\mu\text{J}$ laser energy was focused on the rotational target with the substrate temperatures of 25, 100, 200, 300, 400, and 600°C , while keeping the other deposition parameters constant. Details of the six fabricated samples at different substrate temperatures ranging from 25 to 600°C are presented in Table 7.3 below. The surface morphology, thickness, and chemical composition of all Ge-Sb-Se thin film samples

fabricated at various substrate temperatures were characterised using SEM, FIB-TEM, EDX analyser, XRD, and Raman spectroscopy, while the optical band gap energy of the Ge-Sb-Se thin films was determined from the UV–Vis/NIR spectrometer transmission measurement.

Table 7.3: List of parameters employed to fabricate Ge₂₀Sb₁₅Se₆₅ bulk glass into Si substrate by using different substrate temperatures

Process parameters	Operating conditions
Substrate	Silicon; dimensions 20 mm (L) × 12 mm (W) × 675 μm (T)
Target material	Ge ₂₀ Sb ₁₅ Se ₆₅
Target to substrate distance <i>d_{st}</i>	70 mm
Fs-laser repetition rate	1.0 kHz
Fs-laser energy	40 μJ
Background gas pressure	Under vacuum (10 ⁻⁶ mTorr)
Substrate temperature (sample ID)	25°C (Sb25), 100°C (Sb100), 200°C (Sb200), 300°C (Sb300), 400°C (Sb400), and 600°C (Sb600).
Deposition time	4 hours

7.4.1 Surface morphology and EDX-mapping of Ge-Sb-Se thin films deposited at various substrate temperatures

Figure 7.6 shows the surface morphology of Ge-Sb-Se thin films deposited at substrate temperatures of 25, 200, 400, and 600°C. The SEM images clearly show that the substrate temperature has a significant effect on the surface morphology quality of the Ge-Sb-Se thin films.

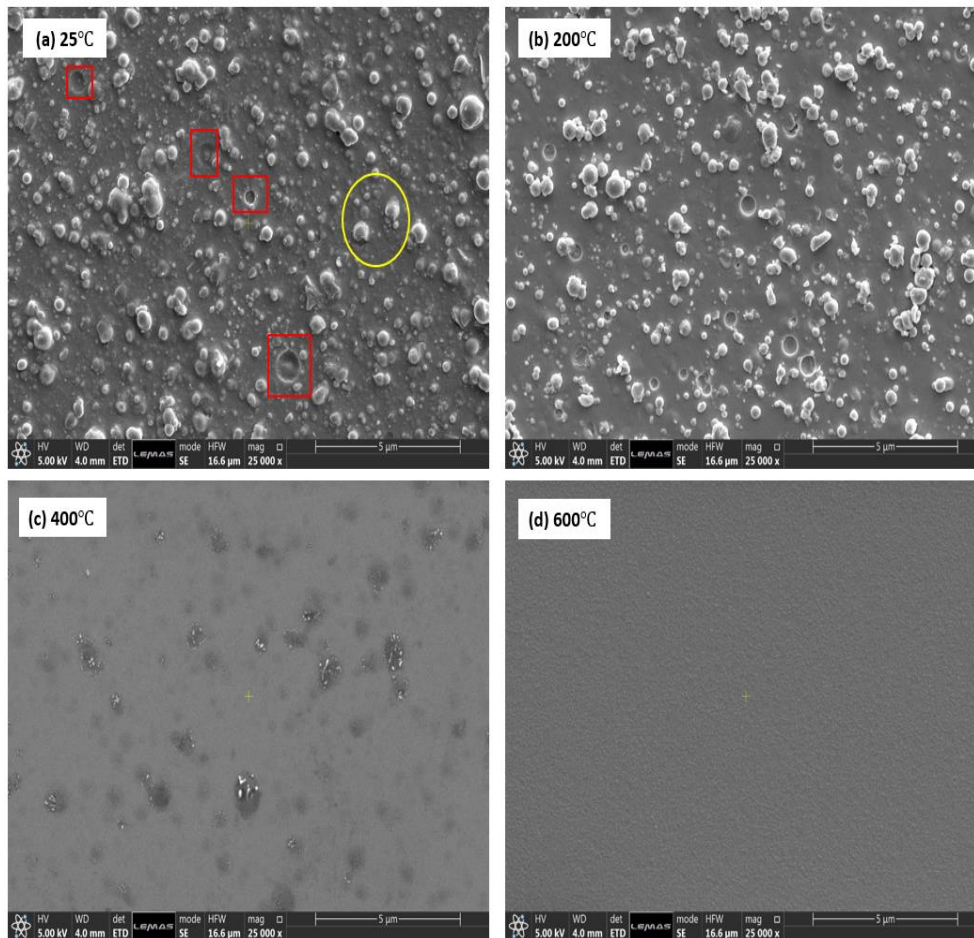


Fig. 7.6: FIB-SEM images showing the surface morphology of Ge.Sb.Se thin film grown at different substrate temperatures; **(a)** 25°C, **(b)** 200°C, **(c)** 400°C, and **(d)** 600°C.

It can be observed that the surface morphology varied with particles size or surface roughness as substrate temperature increases. The thin film samples prepared at 25°C and 200°C clearly are quite rough with large particles size on the surface, as shown in Fig. 7.6 (a) and (b), respectively. They also exhibited distinctively spherical particles with well-defined boundaries. However, as the substrate temperature increased from 25°C to 200°C, the particle droplets on the substrate surface slightly decreased, it can be seen that the surface roughness improved significantly on increasing substrate temperature. For instance, at the substrate temperature of 400°C, smaller nanoparticle droplets are produced with different sizes on the Ge-Sb-Se thin film surface, as depicted in Fig. 7.6 (c). Moreover, when the substrate temperature increased to 600°C, the Ge-Sb-Se's thin film surface looked relatively smoother without any distinct structures being observed.

Further investigation was conducted to identify the elemental composition of thin films using SEM-EDX mapping. Figure 7.7 (a) and (b) shows the SEM-EDX spectra of sample surfaces grown at higher temperatures 400°C and 600°C, respectively. As presented in Fig. 7.7 (a), the SEM-EDX spectrum of Ge-Sb-Se thin film prepared at 400°C detected elemental concentrations of Si (74.90 at. %), O (24.42 at. %), and Sb (0.68 at. %). The SEM-EDX spectrum of sample surface prepared at 600°C (Fig. 7.7 (b)) only indicates a high concentration of Si (96.96 at. %). The result shows that the concentration of Si dominates as compared with the individual elemental component of the Ge-Sb-Se target material.

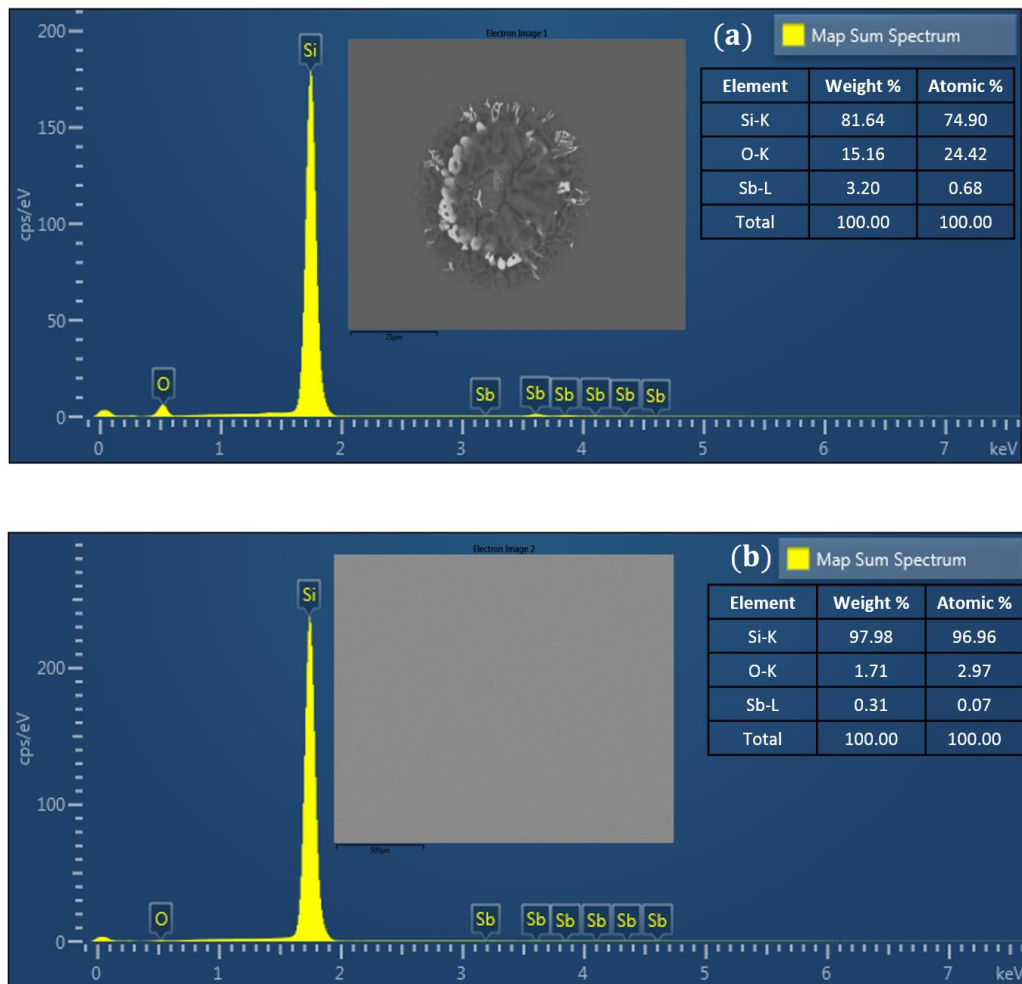


Fig. 7.7: SEM-EDX spectrum and the elemental quantitative data of the Ge-Sb-Se surface prepared at; **(a)** 400°C (sample Sb400) and **(b)** 600°C (sample Sb600).

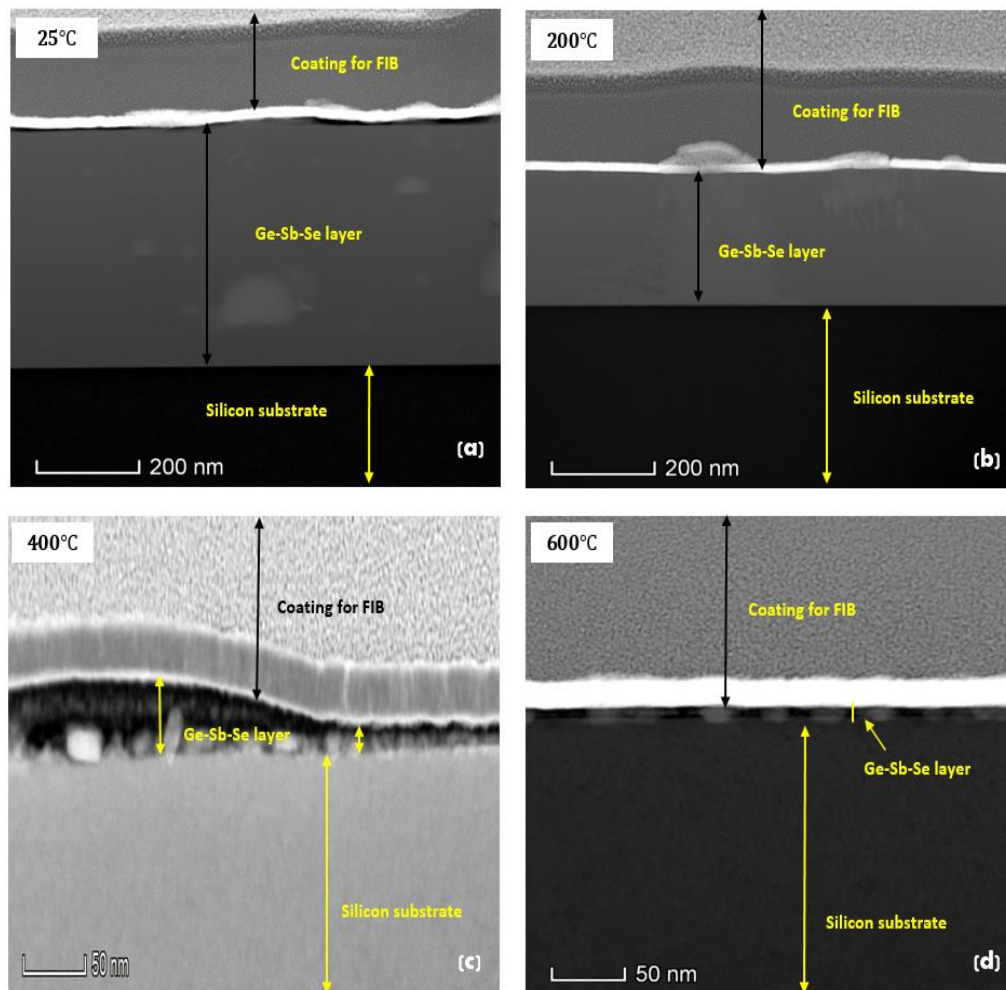


Fig. 7.8: TEM cross-section images of the Ge-Sb-Se thin film fabricated on Si substrate by fs-PLD at various substrate temperatures; **(a)** 25°C (Sb25), **(b)** 200°C (Sb200), **(c)** 400°C (Sb400), and **(d)** 600°C (Sb600).

The FIB technique was employed to prepare cross-sections of the Ge-Sb-Se thin films deposited at various substrate temperatures on Si substrate for TEM analysis. TEM images of the Ge-Sb-Se thin film cross-sections at different substrate temperatures are shown in Fig. 7.8. The images depicted variation in the film thickness as the substrate temperature increased. It was observed that the thickness of the Ge-Sb-Se thin films reduced significantly with increasing substrate temperature. Such observation could probably be due to the low coefficient of adhesion of several elements and increased density by crystallisation at high temperature. Film thicknesses of 480 nm, 275 nm, 30 nm, and ~18 nm correspond to samples deposited at the substrate temperature of 25, 200, 400, and 600°C, respectively. It was also observed that the cross-section samples prepared at 25 and 200°C were

smooth without defects and pores. On the contrary, thin films grown at 400 and 600°C, showed defects on their cross-sections.

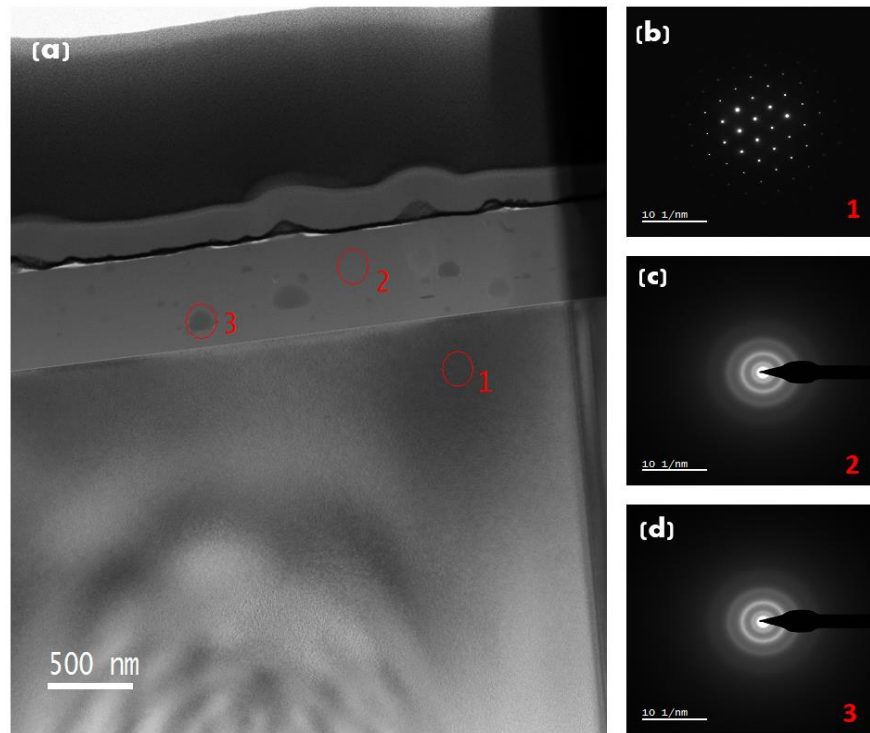


Fig. 7.9: (a) Cross-sectional BF-TEM image of the Ge-Sb-Se layer on silicon from sample Sb25 prepared at 25°C, (b) SAED pattern captured from silicon substrate region, (c and d) SAED pattern captured from different areas of Ge-Sb-Se layer.

Figure 7.9 (a) contains a cross-sectional BF-TEM image of the Ge-Sb-Se thin film layer prepared on a silicon substrate at room temperature (25°C). It exhibited a high-quality Ge-Sb-Se film without any crystalline grains. The SAED patterns in Fig. 7.9 (b-d) show a clear distinction between the Ge-Sb-Se thin film layer and the underlying substrate silicon. The SAED pattern of the silicon substrate region depicted in Fig. 7.9 (b). The SAED patterns from different Ge-Sb-Se film regions are shown in Fig. 7.9 (c) and (d), which revealed circular rings around the central spot confirming the presence of an amorphous structure in the Ge-Sb-Se thin film grown at room temperature (25°C).

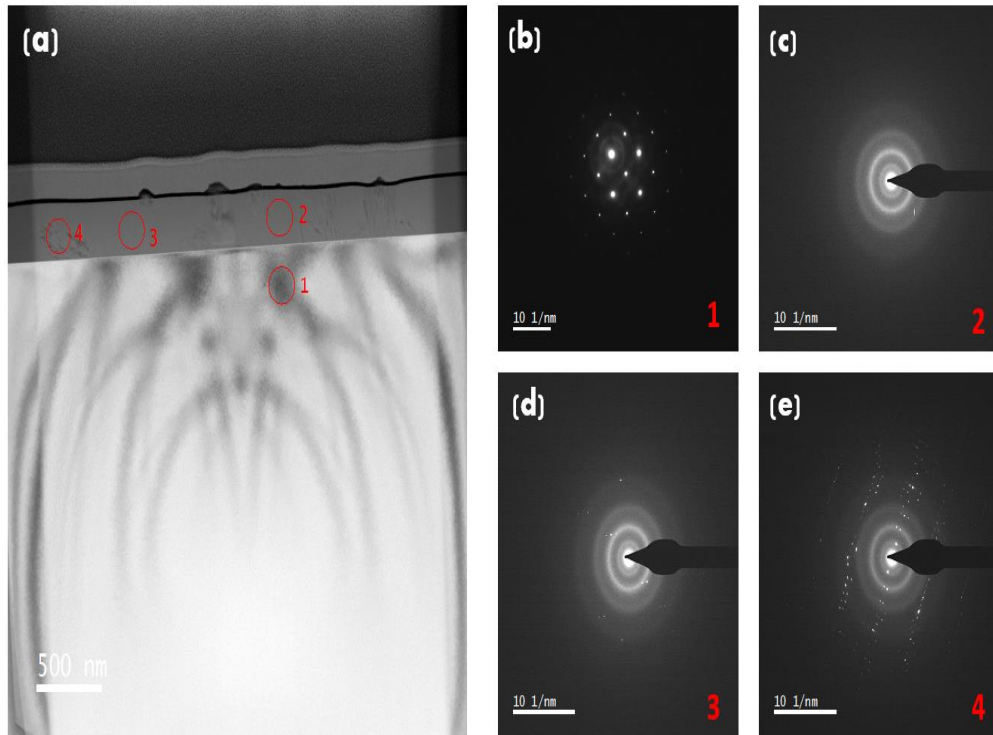
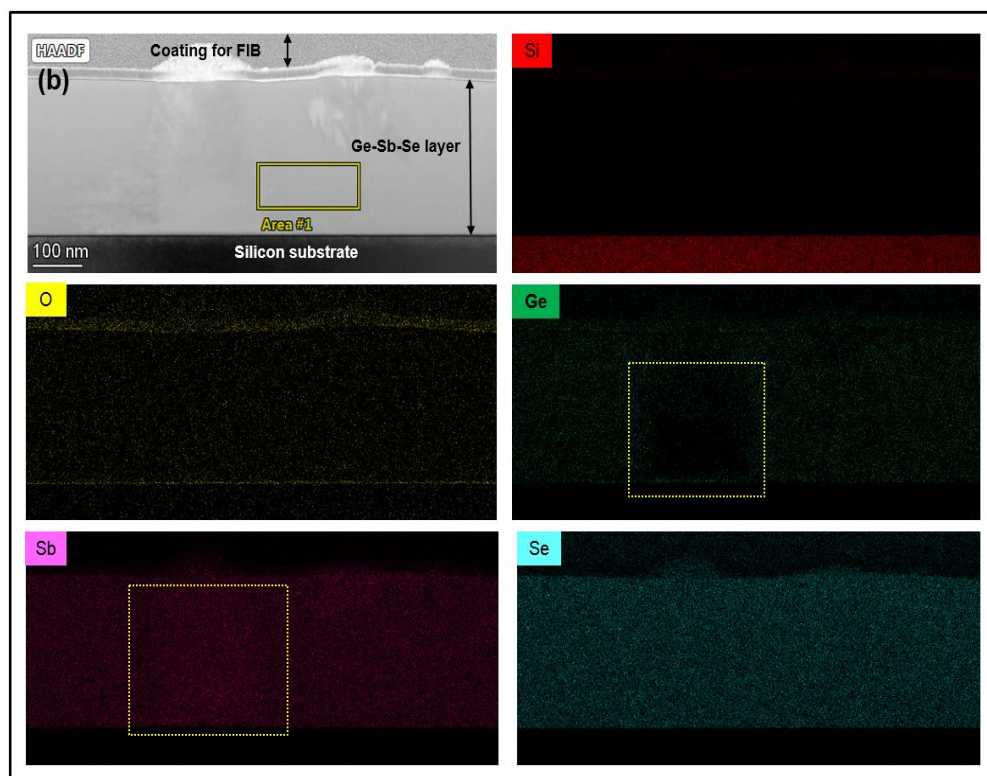
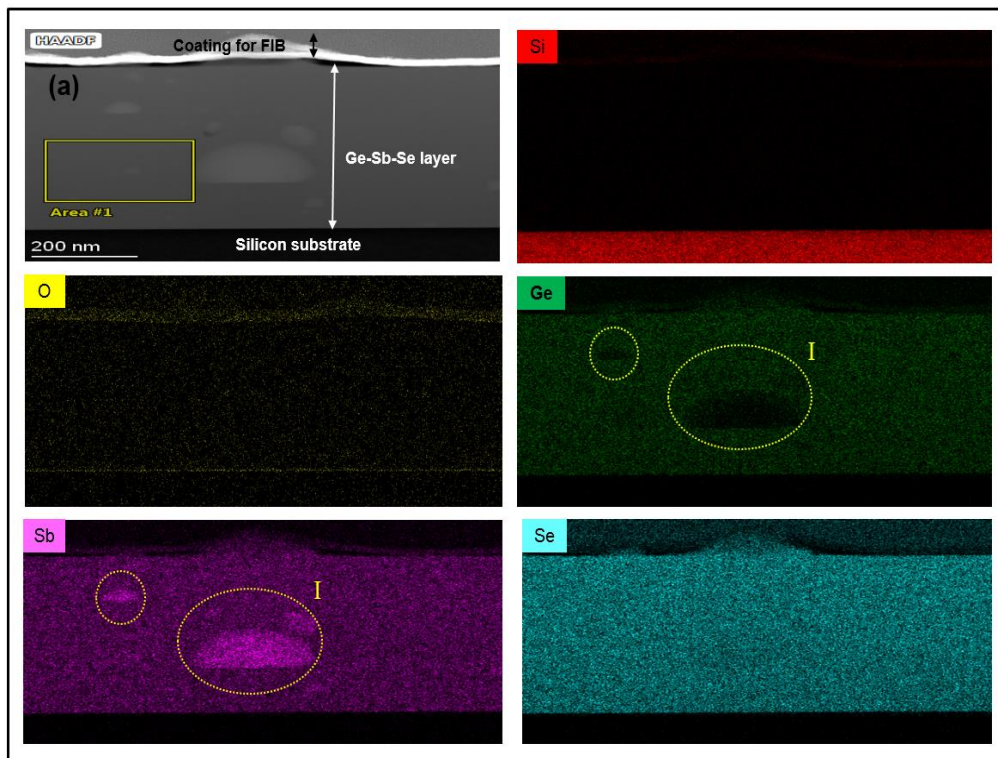


Fig. 7.10: (a) Cross-sectional BF-TEM image of the Ge-Sb-Se layer on silicon from sample Sb200 prepared at 200°C, (b) SAED pattern captured from silicon substrate region, (c-e) SAED pattern captured from different areas of Ge-Sb-Se layer.

Figure 7.10 (a-e) shows a BF-TEM image of the Ge-Sb-Se thin film layer deposited on a silicon substrate at 200°C and corresponding SAED patterns of the regions marked 1, 2, 3, and 4 on the silicon and the Ge-Sb-Se film [Fig. 7.10 (a)]. Figure 7.10 (b) represents SAED patterns taken from the cross-section of the silicon layer, which exhibits a single crystal structure. In contrast, Fig. 7.10 (c-e) corresponds to the SAED image captured from different areas of the Ge-Sb-Se thin film layer. The SAED patterns shown in Fig. 7.10 (c) and (d) consist of a circular ring around the centre spots, which confirm the presence of poly-crystallisation structure. On the other hand, the SAED pattern in Fig. 7.10 (e) also exhibited broad diffuse [marked 4] confirms the presence of nanocrystallites of $\text{Ge}_{20}\text{Sb}_{15}\text{Se}_{65}$ crystals.

7.4.2 TEM-cross-sectional analysis of the Ge-Sb-Se thin film deposited at various substrate temperatures



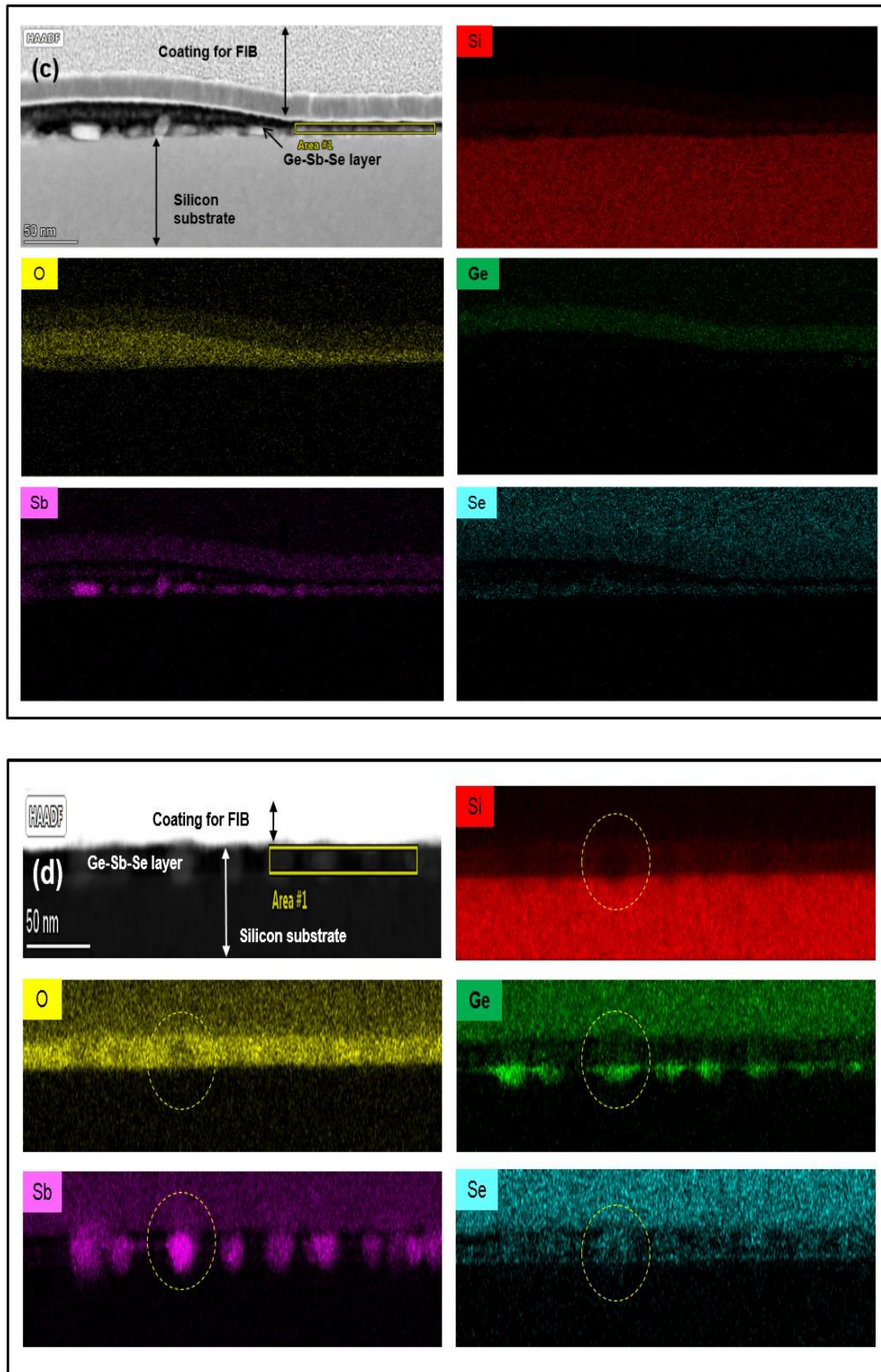


Fig. 7.11: HAADF-STEM images and STEM-EDX elemental mapping images of Ge-Sb-Se thin films prepared on silicon at **(a)** 25°C, **(b)** 200°C, **(c)** 400°C, and **(d)** 600°C.

EDX analysis of fabricated thin films at different temperatures (25, 200, 400, and 600°C) is also performed to identify the elemental distribution within the

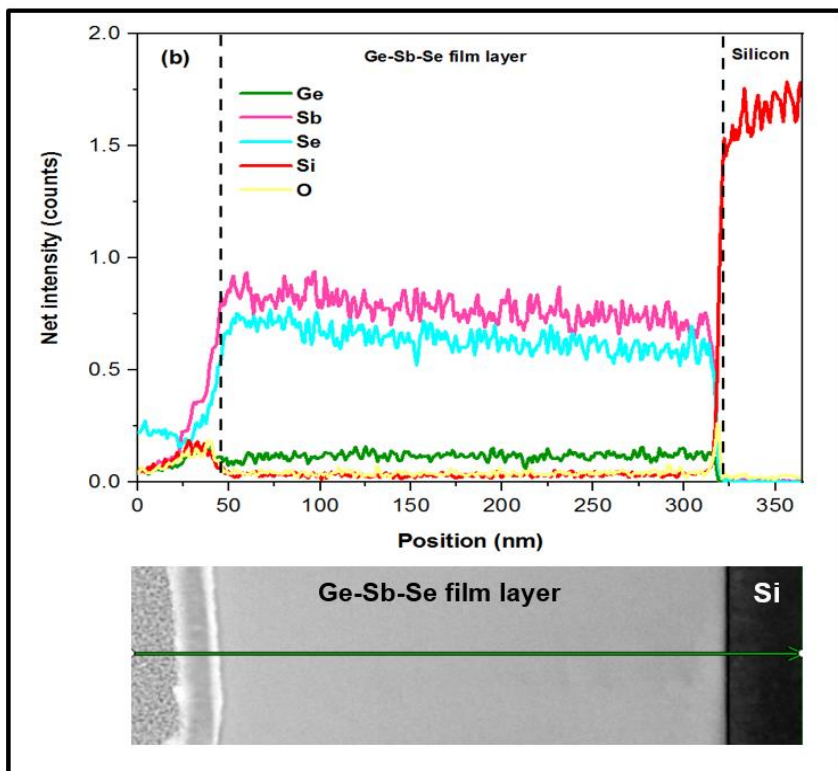
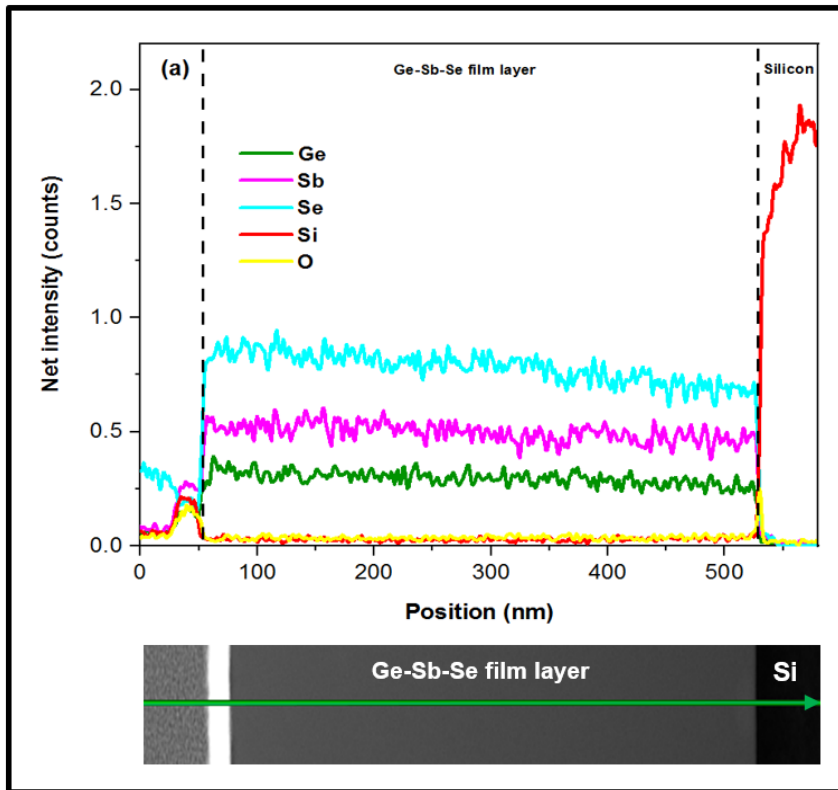
thin film layers. The elemental mapping of the thin film samples clearly shows the presence of Si, O, Ge, Sb, and Se in the thin films as depicted in Fig. 7.11 (a-d). The sample fabricated at room temperature (25°C) exhibited a homogenous thin film without defects [Fig. 7.11 (a)]. Moreover, a uniform distribution of the elemental composition consists of; Ge, Sb, and Se can be seen on the top of the Si layer without any evidence of the intermixing. Surprisingly, the EDX mapping measurement revealed Sb cluster of particles within Ge-Sb-Se layer, which are circled in Fig. 7.11 (a). The presence of oxygen can be observed at the interface between the silicon substrate and Ge-Sb-Se thin film layer.

As the substrate temperature increased to 200°C, elements such as Ge, Sb, and Se became uniformly distributed across the entire thin film without any cluster of nanoparticles as in the case of Fig. 7.11 (a). However, no intermixing between the Ge-Sb-Se film deposited and the silicon substrate network is observed.

The Ge-Sb-Se thin film fabricated at the substrate temperature of 400°C is considerably different from the previous films [Fig. 7.11 (a) and (b)]. From Fig. 7.11 (c), it is observed that the Ge-Sb-Se deposited has diffused slightly into the top surface of the silicon substrate to form a single layer. However, no germanium atom is observed in this thin film according to the EDX elemental mapping [shown in Fig. 7.11 (c)].

At a substrate temperature of 600°C [Fig. 7.11 (d)], the diffusion length of Ge-Sb-Se into the silica-on-silicon substrate increased as compared to thin-film shown in Fig. 7.11 (c). The difference between Figure 7.11 (c) and (d) can be attributed to an increase in the surface diffusion constant as the substrate temperature increases. Ge and Sb ions initially diffused within the grain boundaries of the SiO₂ and then intercalated in the Si layer, as shown in Fig. 7.11 (d). Notably, Ge atoms can be separated from the SiO₂ layer to interact with Si when deposited at 600°C. Selenium also intercalated diffused to the SiO₂ layer, as illustrated in Fig. 7.11 (d). These findings reveal that Ge, Sb, and Se ions can easily be made to mix and inter-diffuse with silicon substrate by adjusting the fs-PLD processing parameters, such

as substrate temperature, laser fluence, substrate -to- target distance, and chamber pressure.



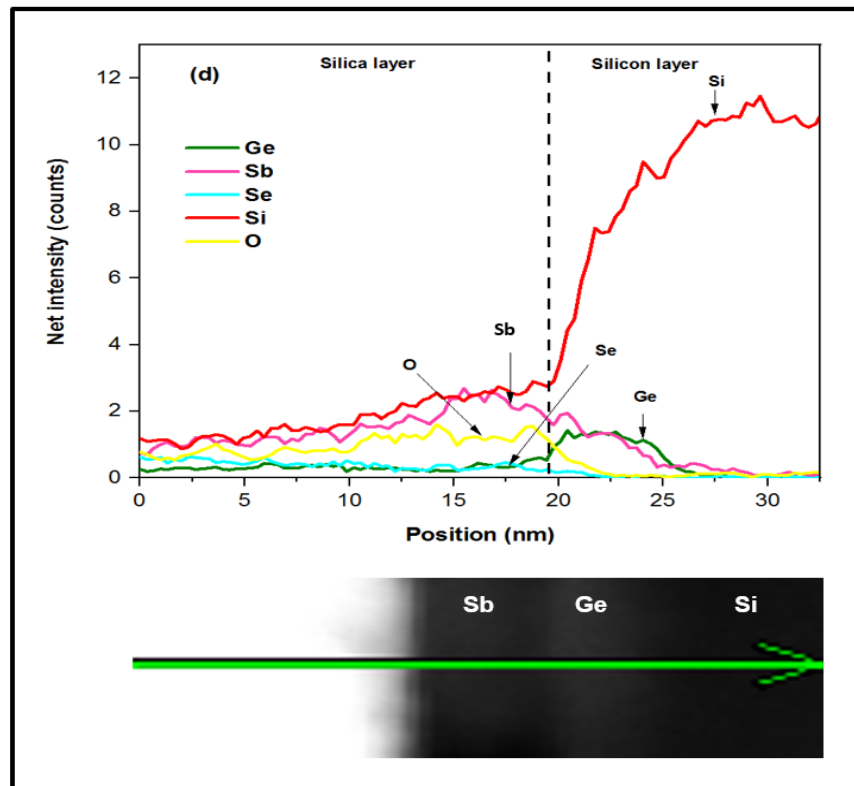
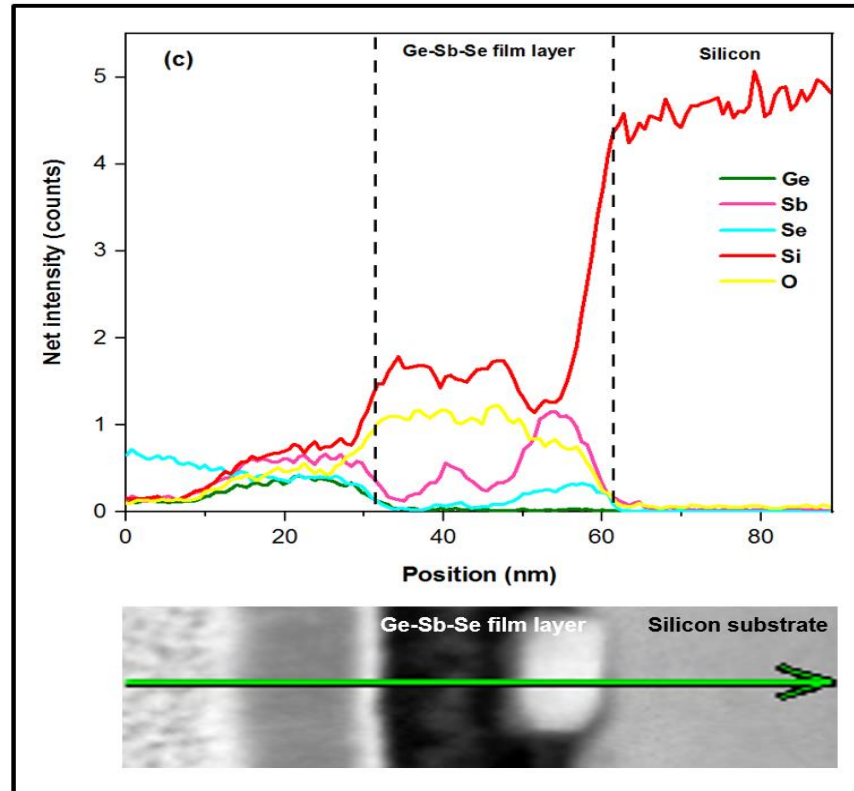
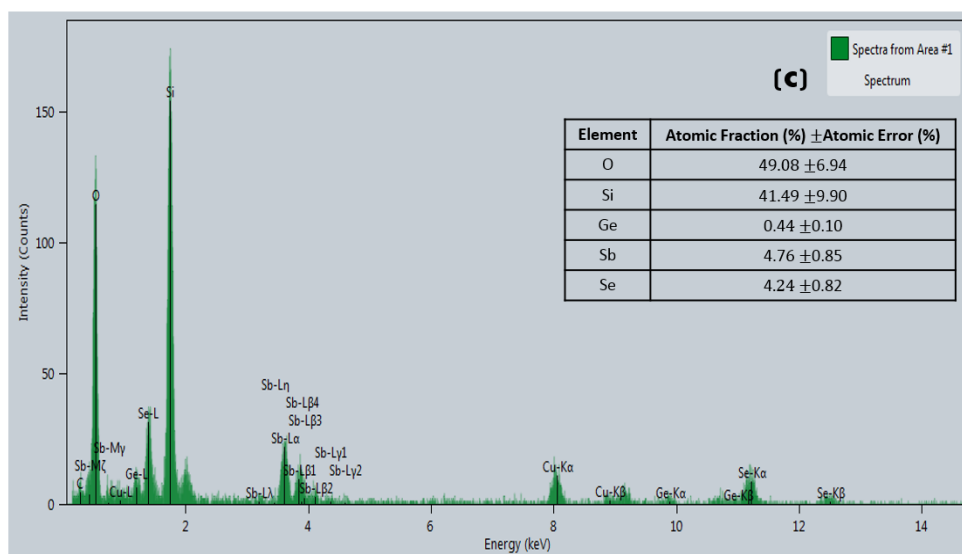
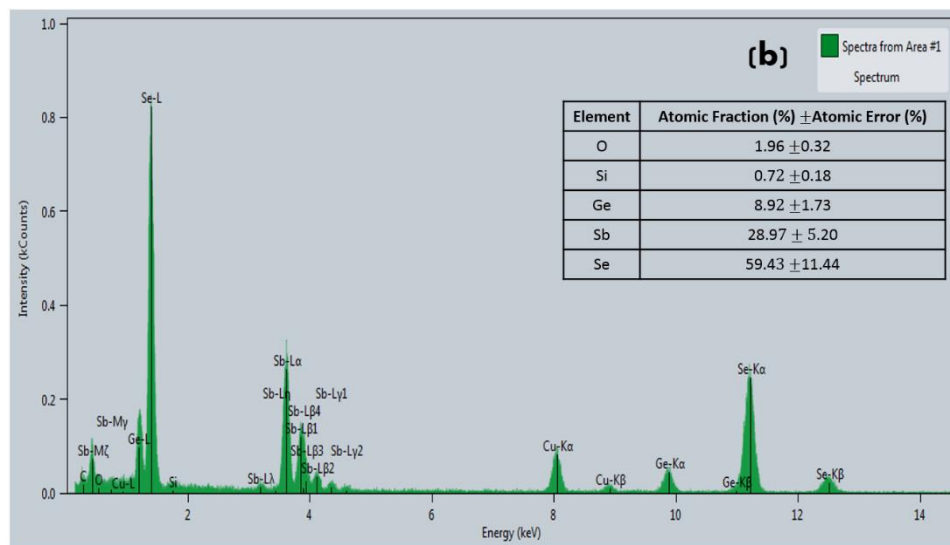
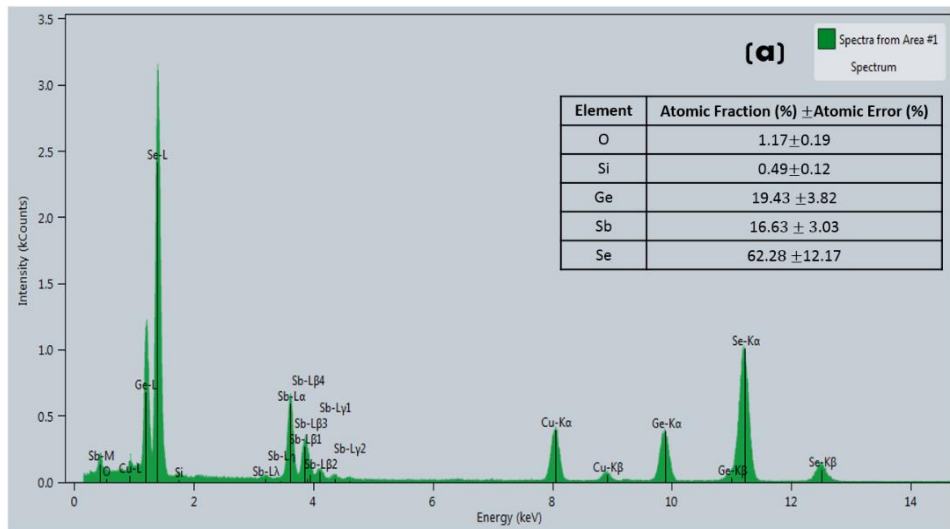


Fig. 7.12: HAADF-STEM images and STEM-EDX line scans were detected Ge-Sb-Se thin film prepared on silicon at different substrate temperatures; (a) 25°C, (b) 200°C, (c) 400°C, and (d) 600°C.

Figure 7.12 shows HAADF-STEM images and STEM-EDX line scans analysis employed to investigate the uniformity of elemental signals, such as Ge, Sb, Se, Si, and O on Ge-Sb-Se thin films prepared at various substrate temperatures. The dashed lines indicate the boundaries between the coated surface-thin film-silica-on silicon substrate. As shown in Fig. 7.12 (a) and (b), the line scans indicate that there is no inter-diffusion between the Ge-Sb-Se thin films with the silica-on-silicon substrate. The elemental profiles of Ge, Sb, Se, Si, and O are uniform across the entire thin film thickness with the intensities been an exact representation of the stoichiometry ratio. It is essential to mention that Si signal was relatively lower at both the top surface and within the thin film thickness, however, relatively higher at the bottom (silicon substrate), respectively.

Figure 7.12 (c) shows the STEM-EDX line scan acquired along the line shown in the HAADF-STEM image of Ge-Sb-Se thin film prepared at 400°C. It is observed that the Sb and Se have diffused into silica layer to form a uniform layer comprises of antimony-selenide-silica (abbreviated as Sb-Se-Si-O). However, Ge signal is not detected in this film. The STEM-EDX line scan signals for the elemental profile of Ge, Sb, Se, Si, and O across the thin film exhibited similar lateral non-uniformities, which indicate inter-diffusion of the Ge-Sb-Se with the top surface of silica-on-silicon substrate.

Figure 7.12 (d) shows another HAADF-STEM image and the corresponding STEM-EDX line scan captured from the Ge-Sb-Se thin film prepared at 600°C. The compositional distribution of Ge, Sb, Se, Si, and O elements in an individual nanoparticle was detected by an EDX line scanning analysis (marked by an arrow). Once again, Sb is diffused into silica and silicon layers while Se is diffused into silica, forming a uniform layer of Si-O-Sb-Se identical to Fig. 7.12 (c). It is also observed that the Ge distribution can be found only in the range of 6 nm of the silicon layer, which indicates that this particular thin film prepared has elemental compositions dominated by Si, O, and Sb from those prepared as discussed before. This observation is in good agreement with the results of corresponding STEM-EDX elemental mapping shown above in Fig. 7.11.



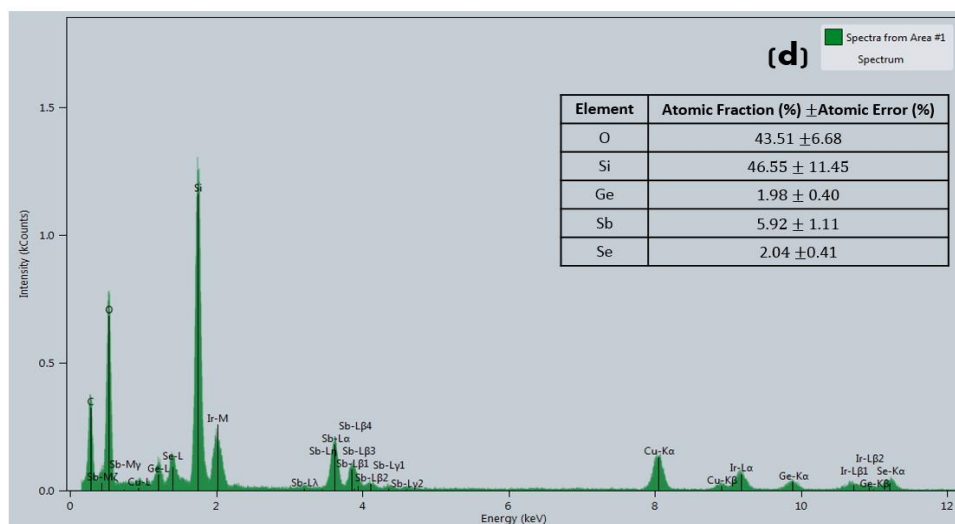


Fig. 7.13: TEM-EDX spectrum of the yellow regions labelled in Fig. 7.11 (a-d) of HAADF-STEM images for the doped layer prepared on silicon at different temperatures; **(a)** 25°C (sample Sb25), **(b)** 200°C (sample Sb200), **(c)** 400°C (sample Sb400), and **(d)** 600°C (sample Sb600).

In addition, the TEM-EDX spectra are depicted in Fig. 7.13 for the yellow marked regions in Fig. 7.13 (a-d) of HAADF-STEM images. The EDX spectra shown in Fig. 7.13 (a) and (b) have higher Se-L peak intensity in comparison to the Ge-K+L and Sb-M+L intensities for the thin film samples prepared at 25°C and 200°C, respectively. The Ge, Sb, and Se elements were found to be uniformly and homogeneously distributed across the whole plane-view of the thin film on silica-on-silicon substrate with no other impurities detected. On the other hand, the EDX spectra in Fig. 7.13 (c) and (d) are for the films prepared at 400°C and 600°C, respectively. These figures show Si and O peak intensities are higher than those of Ge, Sb, and Se, which could be due to the target elements intermixing with the silica-on-silicon substrate at higher temperatures as reported in TEM-EDX line scan results in Fig. 7.12.

Further investigation was conducted to determine the chemical composition of Ge-Sb-Se thin films deposited at different substrate temperatures. The tables summarised in Fig. 7.13 (a-d) indicate elemental composition in each sample prepared. The Ge-Sb-Se thin film on a silica-on-silicon substrate at room temperature (25°C) had chemical compositions closely resembling that of the bulk $\text{Ge}_{20}\text{Sb}_{15}\text{Se}_{65}$ target glass. For instance, the chemical compositions of the sample deposited at 25°C are as follows: Ge (19.43 at.

%), Sb (16.63 at. %), and Se (62.28 at. %). Similar results have been previously reported for Ge–Sb–Se thin film fabricated using conventional radio frequency (13.56 MHz) magnetron co-sputtering method [215] at room temperature. However, sample deposited at higher substrate temperatures, such as 200°C, 400°C, and 600°C has lower concentrations of Ge, Sb, and Se with slight variations in their ratios.

7.4.3 XRD characterisation of the Ge-Sb-Se thin film deposited at different substrate temperatures

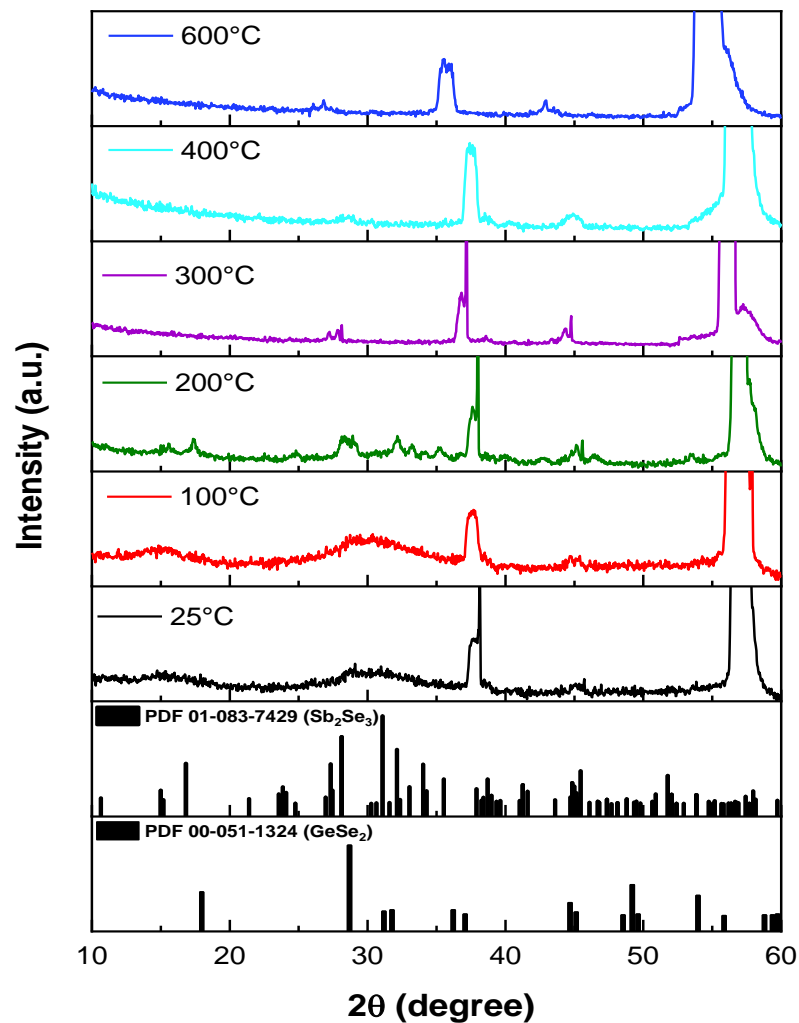


Fig. 7.14: XRD patterns of thin films fabricated on Si glass substrates by fs-PLD at various substrate temperatures; 25, 100, 200, 300, 400, and 600°C.

Figure 7.14 shows the XRD patterns of the Ge-Sb-Se thin films deposited at substrate temperatures of 25, 100, 200, 300, 400, and 600°C under vacuum (10^{-6} mTorr) along with ICDD reference patterns for Sb₂Se₃ and

GeSe₂. The XRD patterns were recorded with a 2θ range from 10° to 60° in a step size of 0.033°. The XRD patterns of all the samples shown predominant diffraction peaks at 2θ = 56° (311), which correspond silicon cubic phase (ICDD reference code: 00-005-0565). In addition, the diffraction peak position at 2θ = 38° (111) correlates with the formation of silicon oxide cubic phase (ICDD reference code: 01-080-4051). Besides, the XRD pattern of the Ge-Sb-Se thin films prepared at the substrate temperatures of 25°C and 100°C consist of two broad band peaks, which range from 2θ = 10 to ~20° and 25 to ~47°. The presence of these two broad peaks indicates that the thin films as-fabricated at these substrate temperatures (25 and 100°C) are made up of an amorphous structure. This observation corroborates with the information obtained from SAED patterns of the same samples, as shown in Fig. 7.9. The amorphous structure may be attributed to the lack of crystallisation of Ge-Sb-Se thin film at a low temperature of ≤ 200°C. The amorphous nature of Ge-Sb-Se films is characterised by three broad diffuse scattering halos confirming a long-range structural disorder characteristic of the amorphous network of chalcogenide glasses. When the substrate temperature increases above 100°C, the Ge-Sb-Se thin film starts to lose its amorphous structure. By increasing the temperature to 200°C, the diffraction peaks appear, which indicate that the Ge-Sb-Se amorphous structure has been crystallised. The diffraction peaks centred at 2θ = 17°, 28°, and 53° match those for germanium selenide tetragonal phase (GeSe₂ (101), (112), and (312); ICDD reference code: 00-051-1324). The diffraction peaks at ~15°, 32°, 35°, and 45° correlated with antimony selenide orthorhombic phase (Sb₂Se₃ (200), (013), (312), and (020); ICDD reference code: 01-083-7429). A similar observation has been reported elsewhere by Shaaban et al. [360]. Moreover, the diffraction pattern of thin film deposited at 300°C shows an increase in the intensity of SiO₂ and Si peaks, while diminishing the intensities of the GeSe₂ and Sb₂Se₃ crystalline structures. The absence of Ge₂₀Sb₁₅Se₆₅ peaks at the substrate temperatures of 400°C and 600°C is attributed to smaller Ge-Sb-Se thin films, as well as the lower concentrations of the Ge₂₀Sb₁₅Se₆₅ target elements, which is confirmed by TEM-EDX spectrum depicted in Fig. 7.13.

7.4.4 Influence of substrate temperature on the Ge-Sb-Se thin film (Raman spectroscopy)

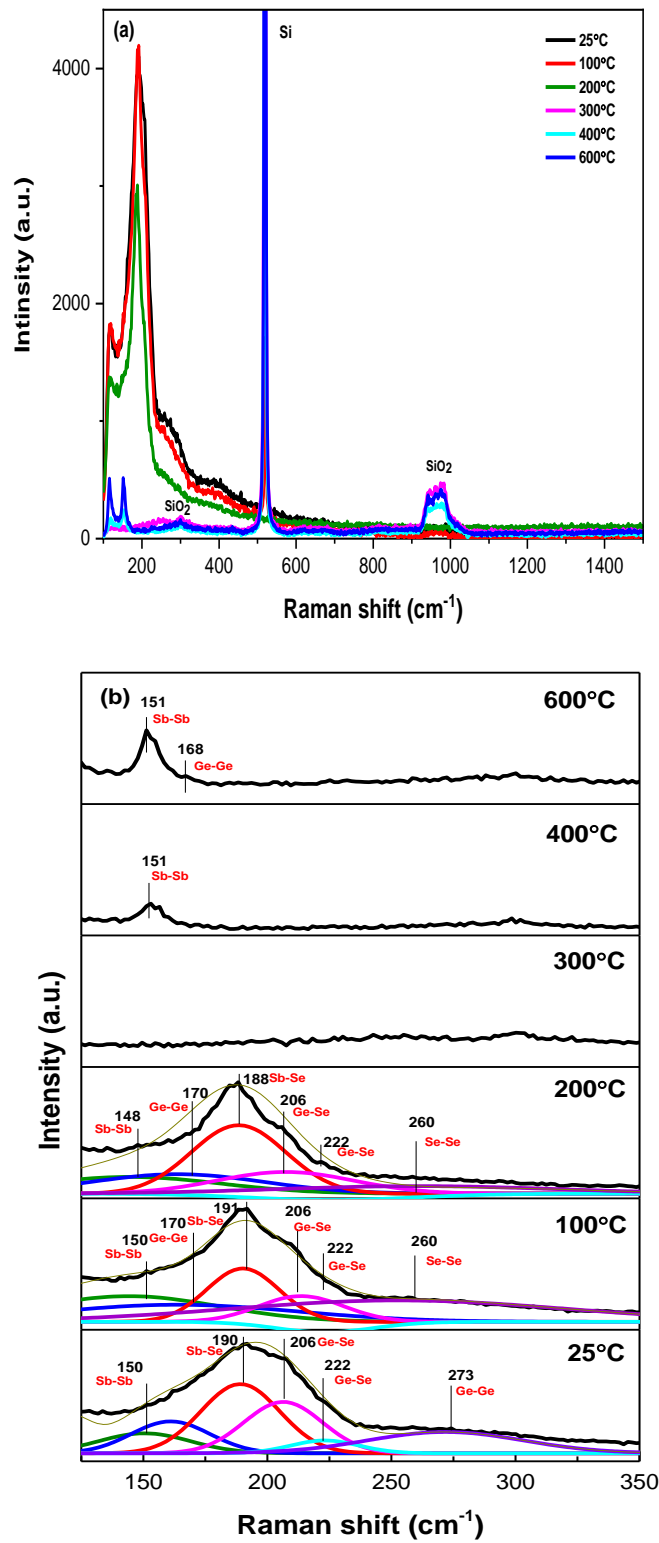


Fig. 7.15: Raman spectra of (a) Ge-Sb-Se thin films prepared on silicon at different substrate temperatures, and (b) comparison of the main peaks for all samples.

The vibration structure of bulk and corresponding thin films was examined using Raman scattering spectroscopy. The Raman spectra of the silicon substrate and $\text{Ge}_{20}\text{Sb}_{15}\text{Se}_{65}$ target material are shown and discussed in Fig. 7.5. The Raman spectra of the Ge-Sb-Se thin film at various substrate temperatures are given in Fig. 7.15 (b) with their Gaussian decomposition peaks.

As shown in Fig. 7.15, the Raman spectra of the Ge-Sb-Se thin films grown at low temperatures $\leq 200^\circ\text{C}$ demonstrate broad bands, which are identical to the bulk glass indicating the presence of an amorphous material. This result is supported by XRD and SAED patterns of the Ge-Sb-Se thin film samples. At a substrate temperature of 300°C , the broad band peaks of the $\text{Ge}_{20}\text{Sb}_{15}\text{Se}_{65}$ bulk glass disappeared completely, while the silicon and silica predominate with increasing intensities [Fig. 7.15 (a)]. It is worthy of note, that though the respective locations of Si peak at $\sim 520\text{ cm}^{-1}$ are similar for all deposited films except the thin film fabricated at 200°C , the peak intensity varied with an increase in substrate temperature. With the Ge-Sb-Se thin films prepared at 25°C and 100°C , the Si peak has a low intensity. At 200°C , the peak disappeared. Whereas, increasing the substrate temperatures to 300 , 400 , and 600°C , the intensity of Si characteristic peaks became enhanced. Similar behaviour was also seen with the SiO_2 peak in Raman spectra shown in Fig. 7.15 (a).

The Raman spectra of the $\text{Ge}_{20}\text{Sb}_{15}\text{Se}_{65}$ glassy target [Fig. 7.5 (b)] and corresponding fs-PLD Ge-Sb-Se thin films present several bands in the range between 150 and 325 cm^{-1} [Fig. 7.15 (b)]. According to previously reported, Raman vibration peak values for Ge-Sb-Se: (i) the peak at $\sim 151\text{ cm}^{-1}$ in the films grown can be described to vibrations of Sb-Sb [204, 214, 349-351]. However, this peak has a weak intensity in Raman spectrum for the thin film sample prepared at a temperature below 400°C . The reason for this vibration band being weak could be related to the overlap of Ge-Ge and Ge-Se vibrational modes of corner linked $[\text{GeSe}_{4/2}]$ tetrahedra. However, as the substrate temperature increase, the vibration band centred at 151 cm^{-1} reappear with increasing intensity as shown by samples fabricated at 400°C

and 600°C. (ii) The distinct broad vibration band at around 170 cm^{-1} can be attributed to the presence of Ge–Ge vibrations [204, 210, 351-354]. (iii) The vibration mode at 190 cm^{-1} is attributed to Sb–Se bond in $\text{SbSe}_{3/2}$ [51, 204, 208, 214, 215, 349-351]. The $\text{SbSe}_{3/2}$ vibrational pyramid band disappear as the substrate temperature increase, which is due to the decreased in Se concentration during the fabrication process. (iv) The vibration band peaked at 206 cm^{-1} and its shoulder at 222 cm^{-1} can be attributed to the heteropolar Ge–Se bonds in the corner-sharing and the edge-sharing $\text{GeSe}_{4/2}$ tetrahedral, respectively [51, 200, 215, 355-359]. (v) The broad Raman band observed at $\sim 265\text{ cm}^{-1}$ is attributed to the vibration mode of Se–Se bond [210, 353, 354, 360]. The broad nature of the band at $\sim 265\text{ cm}^{-1}$ stems from a distribution widening of Se–Se vibration modes related to bond angle/lengths distortions in the amorphous state. This broad band was considered for Ge–Ge bonds vibration modes (in $\text{Ge–Ge}_m\text{Se}_{4-m}$, $m=1, 2, 3, 4$ structural units) already observed in amorphous GeSe_4 , which exhibits a wide band centred at $\sim 270\text{ cm}^{-1}$ with a shoulder at $\sim 170\text{ cm}^{-1}$ [204].

7.4.5 Determining optical band gap of the Ge-Sb-Se thin film (UV-Vis spectroscopy)

The optical transmission spectra of the Ge-Sb-Se thin films prepared at different substrate temperatures were measured using the UV–Vis–NIR spectrometer in the wavelength range of 300 to 2000 nm. The absorption edge of the Ge-Sb-Se thin films is compatible with the electron transitions from valance band to conduction band. Fig. 7.16 shows the band gap energies of the Ge-Sb-Se thin films, which was estimated by employing empirical [see equation 2.1].

In this study, $n = 2$ (which corresponds to the indirect electron transition), was used to estimate the optical band gaps of various thin films. The absorption coefficient α was also obtained from the transmittance data using the relation (2.2) mentioned in chapter 2. The optical band gap energies (E_g) obtain from of the Ge-Sb-Se thin films with different substrate temperatures are listed in Table 7.4.

It can be seen that the calculated optical band gap energy increase from 1.4 to 1.9 eV for films as the substrate temperature increase. The minimum optical band gap (1.4 eV) could be found in the Ge-Sb-Se thin film, prepared at 25°C. However, the energy band gap values of all the films are very close to the optical band gap of the bulk glass Ge₂₀Sb₅Se₇₅ and Ge₂₀Sb₁₀Se₇₀ at ~1.6 eV [198, 361]. Similar results have been reported previously [207] for sputtered Ge-Sb-Se films with ~1.9 eV (Tauc relation) and ~1.65 eV by Balan et al. [362] for sputtered Ge-Sb-Se films. In addition, these values are in agreement with data reported by Halenkovič et al. [215] on Ge₂₈Sb₁₂Se₆₀ thin film with an optical band gap of 1.74 ± 0.02 eV. The increase in the optical energy band gap of Ge-Sb-Se films can be attributed to the decreased in thin films thickness as the substrate temperature increase, which can be explained on the based on the chemical-bond approach proposed by Bicerano and Ovshinsky [363]. For instance, the energies between various bond structures involve namely the heteropolar Ge-Se (206.77 kJ/mol), Sb-Se (183.89 kJ/mol) bonds, and the homopolar Ge-Ge (157.32 kJ/ mol), respectively [207].

Table 7.4: Optical energy band gap of the Ge-Sb-Se thin film prepared at various substrate temperatures

sample	Substrate temperature T _s (°C)	Thickness d (nm)	Optical energy band gap (eV)
Sb25	25	480	1.4
Sb200	200	275	1.5
Sb400	400	~30	1.7
Sb600	600	~18	1.9

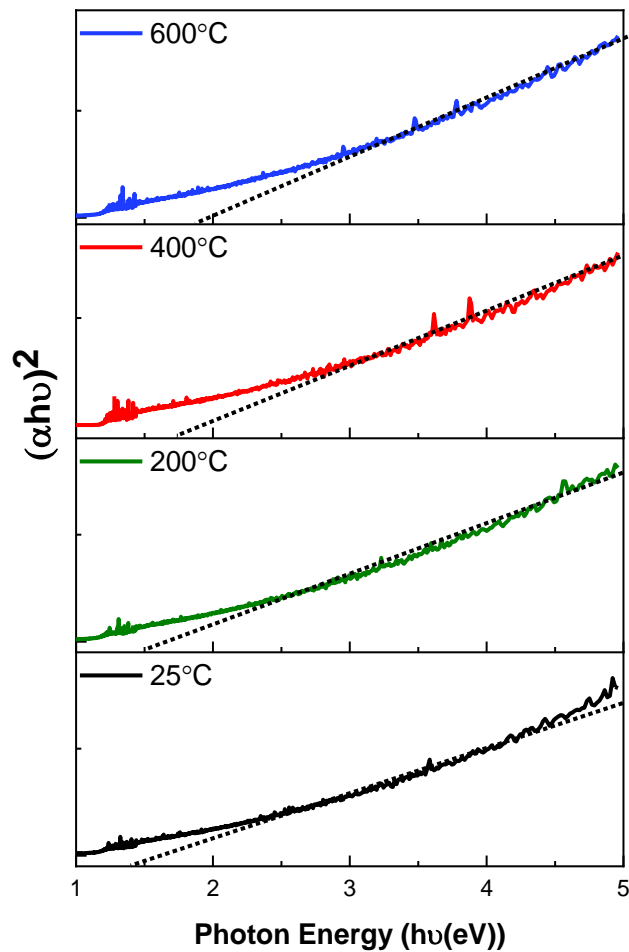


Fig. 7.16: α^2 vs. $h\nu$ plots for Ge-Sb-Se thin films prepared at various substrate temperatures.

7.5 Conclusion

Thin films of Ge-Sb-Se have been successfully prepared on Si substrate by using the fs-PLD technique. The resulting thin films have been characterised by various characteristics XRD, Raman, SEM, TEM, and UV-VIS techniques.

Firstly, XRD and Raman spectroscopy were used to study the influence of laser pulse energy on the structure of the fs-PLD prepared Ge-Sb-Se thin films to optimise the fs-laser energy for studying the effect of temperature on the structures and properties of the fabricated thin films. All the films looked smooth and homogeneously distributed due to the high substrate temperature used in this deposition (400°C). By increasing the fs-laser energy to 30 μ J (Sb30), 40 μ J (Sb40), and 50 μ J (Sb50), the Raman spectra

reveal a band with higher intensities centred at around 152 cm^{-1} are correlated to the vibrations of Sb–Sb.

Secondly, the effect of various substrate temperatures (25, 200, 400, and 600°C) on the fabricated Ge-Sb-Se thin films is investigated when keeping the fs-laser pulse energies in $40\mu\text{J}$. The morphological and compositional characteristics of the films have been studied, which revealed the presence of nano/sub-micro structures and their agglomeration in low temperatures, while the surface converts to be smoother without detecting any particles with increasing the substrate temperature. The structural properties of the target chalcogenide glass change from amorphous to crystalline phase as well. However, there is inter-diffusion behaviour observed between the silicon substrate and deposited layer, which could link to the diffusion of the ion chalcogenide target in the silicon substrate. Besides, amorphous chalcogenide Ge–Sb–Se films with a composition close to the glassy target were successfully deposited at room temperature. The composition in this case (i.e. $\text{Ge}_{19}\text{Sb}_{16}\text{Se}_{62}$), with a thickness of 480 nm and optical energy band gap of 1.4 eV. It was found that the values of deposited thin film's thickness decreased with increasing substrate temperatures, while the values of the band gap criteria increased as a result of the diffusion and decreasing in the thickness of the thin films. The crystalline phases were determined by recording the XRD pattern of the converted material. The XRD results indicated that the crystallinity degree of the deposited thin films sharply changes with increasing substrate temperature. Finally, Raman analysis demonstrated that thin film network is closer to the $\text{Ge}_{20}\text{Sb}_{15}\text{Se}_{65}$ target structure for substrate temperatures lower than 300°C . The study of Raman scattering spectra has revealed a structural organisation varying from bulk to PLD films in which homopolar bonds like Ge(Sb)–Ge(Sb) disappeared and with a lower proportion, in the case of thin films prepared under high temperatures.

Chapter 8: Conclusions and Future Work

8.1 Conclusions

Objectively, the research study proposition was to deposit and implant the host of ChGs material on/in a silicon substrate. The deposition of the ChGs materials onto/into the Si substrate was achieved through effective utilisation of fs-PLD approach. Tentatively, to ascertain the preeminent material parameters, different fs-PLD considerations, including substrate temperature, deposition time, fs-laser pulse energy, and pressure, were utilised. Therefore, this chapter provides a conclusive recap of the results with consideration to the objectives above.

The fabrication of these films on/in the Si substrate resulted from four types of bulk glass, namely Ga-La-S, Er³⁺-doped Ga-La-S, GeSe₄, and Ge₂₀Sb₁₅Se₆₅. However, the success of deposited and implanted ChGs thin films onto/into the unalloyed Si substrate inspired this work. Notably, important characteristics, including higher conductivity, environmental sustainability, higher sensitivity, greater hardness, higher crystallisation temperature, higher stability, sizeable optical transmission range extending in the mid-infrared, and glass-forming ability make those ChGs attractive materials. Also, they can potentially find applications in memory and switching devices.

The characterisation results show that where the substrate temperature has the most noteworthy impact on the quality and surface roughness of ChGs thin films thickness that were fabricated on the Si substrate as ascertained by the structural classification. For example, there is a change from amorphous to the crystalline phase structural properties of the target chalcogenide glass. Also, on the film surface morphology, there is an increase in nanoparticle grain size as the substrate temperature rises.

The thin film thickness changed due to an increase in the substrate temperature according to the thin film's cross-sectional analysis. For the Ga-La-S and Er³⁺-doped Ga-La-S films, it was found that film thicknesses

increased. Besides, their thin films were successfully deposited on the Si substrate without integrating with it, which could bond to the chalcogenide target glasses quality. Conversely, Ge-Se and Ge-Sb-Se films thickness decreased with increasing the substrate temperature. Moreover, the characteristic of fs-PLD assisted induced intermixing, and ion implantation in the silicon for Ge-Se film was exhibited at high substrate temperatures. Similarly, the behavioural characteristic of inter-diffusion among Si substrate and Ge-Sb-Se deposited layer, which could associate ion chalcogenide target in the Si substrate diffusion was revealed at a high substrate temperature (600°C).

It was also seen that, with an increasing substrate temperature of the prepared Er-Ga-La-S and Ge-Se films, the optical energy band gap decreases. Based on the theorisation and constructs of chemical bonds (Ge-Se, Sb-Se, and Ge-Ge), it showed that with increasing substrate temperature, there was an increase in the band gap values of the fabricated Ge-Sb-Se thin films. The observation is attributed to the diffusion and the decrease in the thin films thickness and as the substrate temperature increased.

8.2 Suggestions for future work

For effective utilisation of the fs-PLD approach in depositing and implanting ChGs onto/into Si substrate, there is a need for some improvements in future research investigations. Also, to develop the scope of study further, some recommendations are addressed and presented below:

- 1. study the electrical and optical properties of the prepared ChGs thin films*

For our prepared ChGs thin films, several other important physical properties, including hardness and thermal conductivity, could be studied afterwards. The electrical properties of these materials are interesting due to their phase change characteristics.

It is imperative to perceive the temperature dependency of the dc electrical conductivity of Ga-La-S, Er-doped Ga-La-S, Ge-Se, and Ge-Sb-Se thin films. The electrical property can be achieved if the current (I) and voltage (V) measurements are carried out at their various temperatures. Also, a reliable equation having the dependency of dc electrical conductivity on temperature should be further used to evaluate the activation energy of conduction as follows:

$$\sigma_{dc} = \sigma_0 \exp \left[\frac{-\Delta E}{kT} \right]$$

Where, σ_0 and ΔE represent the pre-exponential factor and activation energy, respectively, and k is the Boltzmann constant.

Tentatively, the Ge-Se and Ge-Sb-Se thin films optical properties are important in effective utilisation of fs-PLD approach in blending ChGs into Si substrate. Therefore, the thin film characteristic should be determined by an extensive transmission spectrum study. The absorption coefficient in absorption regions and values of refractive index optical constants should be computed. Also, the photoluminescence (PL) spectra of the Ge-Se and Ge-Sb-Se films could be recorded by measuring the emitted radiation intensity as a function of the emission wavelength or the excitation wavelength. Besides, measuring the refractive index could be possible to identify the compounds that do not have much absorption band for UV-light.

2. Different range of process parameters

To achieve a thicker thin film layer with a uniform mixture of ChGs and Si means that a wider range of process parameters is required, particularly for higher temperatures. Also, the extenuation of this issue is possible since the fs-PLD new system offers a wider range of process parameters. Also, further dependencies would undoubtedly yield when other parameters, including laser energy, elevated temperatures, and pressure, are investigated. However, to possibly fabricate the mixture's structure to a higher degree, the parameters should be precise and cautiously controlled.

3. Explore different target compositions

Imperatively, apart from selenide and sulfide glasses used in the research project, other materials can be used. Mostly, host materials with low phonon energy, higher melting temperatures, higher optical refractive index, higher thermal stability, and wider transmission windows can be adapted. Such interesting target materials include; $\text{Ge}_{21}\text{Te}_{76}\text{Se}_3$ and $\text{Ge}_{15}\text{Ga}_{10}\text{Te}_{75}$.

Glass	Transmission range*, (μm)	T_g ($^{\circ}\text{C}$)	$T_c - T_g$ ($^{\circ}\text{C}$)	n (λ , μm)	$n_2 \times 10^{-18}$ (m^2/W)
As_2S_3	0.62–11.53	185	–	2.42 (3)	4–6
As_2Se_3	0.85–17.5	178	147	2.83 (3)	14–30
$\text{As}_{40}\text{S}_{30}\text{Se}_{30}$	0.75–12.5	180	–	2.61 (3)	14.5
$\text{As}_{40}\text{Se}_{40}\text{Te}_{20}$	1.23–18.52	140	–	2.9 (5)	>20
GeSe_4	0.75	163	–	2.48 (1.55)	13
$\text{Ge}_{25}\text{Sb}_{10}\text{S}_{65}$	0.65–11.0	315	>200	2.25 (1.55)	2–5
$\text{Ge}_{30}\text{As}_{10}\text{Se}_{30}\text{Te}_{30}$	1.2–17.0	260	225	2.8 (10.6)	>20
$\text{Ge}_{21}\text{Te}_{76}\text{Se}_3$	2–20	160	123		
$\text{Ge}_{15}\text{Ga}_{10}\text{Te}_{75}$	2–25	172	≥ 113	3.415	

* At 1 cm^{-1} absorption coefficient.

References

1. Streshinsky, M., et al., *The road to affordable, large-scale silicon photonics*. Optics and Photonics News, 2013. **24**(9): p. 32-39.
2. Soref, R., *The past, present, and future of silicon photonics*. IEEE Journal of selected topics in quantum electronics, 2006. **12**(6): p. 1678-1687.
3. Arakawa, Y., et al., *Silicon photonics for next generation system integration platform*. IEEE Communications Magazine, 2013. **51**(3): p. 72-77.
4. Tsybeskov, L., D.J. Lockwood, and M. Ichikawa, *Silicon photonics: CMOS going optical [scanning the issue]*. Proceedings of the IEEE, 2009. **97**(7): p. 1161-1165.
5. Sun, C., et al., *Single-chip microprocessor that communicates directly using light*. Nature, 2015. **528**(7583): p. 534.
6. Witzens, J., *High-speed silicon photonics modulators*. Proceedings of the IEEE, 2018. **106**(12): p. 2158-2182.
7. Vivien, L., et al., *42 GHz pin Germanium photodetector integrated in a silicon-on-insulator waveguide*. Optics express, 2009. **17**(8): p. 6252-6257.
8. Duan, G.-H., et al., *Hybrid III--V on Silicon Lasers for Photonic Integrated Circuits on Silicon*. IEEE Journal of selected topics in quantum electronics, 2014. **20**(4): p. 158-170.
9. Jalali, B. and S. Fathpour, *Silicon photonics*. Journal of lightwave technology, 2006. **24**(12): p. 4600-4615.
10. Priem, G., et al., *Impact of absorption mechanisms on Kerr-nonlinear resonator behavior*. Journal of applied physics, 2006. **99**(6): p. 063103.
11. Eggleton, B.J., B. Luther-Davies, and K. Richardson, *Chalcogenide photonics*. Nature photonics, 2011. **5**(3): p. 141.
12. Mairaj, A.K., et al., *Development of channel waveguide lasers in Nd³⁺-doped chalcogenide (Ga: La: S) glass through photoinduced material modification*. Applied physics letters, 2002. **81**(20): p. 3708-3710.
13. Moizan, V., et al., *Er³⁺-doped GeGaSbS glasses for mid-IR fibre laser application: Synthesis and rare earth spectroscopy*. Optical Materials, 2008. **31**(1): p. 39-46.
14. Zakery, A. and S. Elliott, *Optical properties and applications of chalcogenide glasses: a review*. Journal of Non-Crystalline Solids, 2003. **330**(1-3): p. 1-12.
15. Shen, W., et al., *Light trimming of a narrow bandpass filter based on a photosensitive chalcogenide spacer*. Optics express, 2008. **16**(1): p. 373-383.

16. Vigreux-Bercovici, C., et al., *Waveguides based on Te₂As₃Se₅ thick films for spatial interferometry*. Journal of non-crystalline solids, 2006. **352**(23-25): p. 2416-2419.
17. Sanghera, J. and I. Aggarwal, *Active and passive chalcogenide glass optical fibers for IR applications: a review*. Journal of Non-Crystalline Solids, 1999. **256**: p. 6-16.
18. Chauvet, M., et al., *Kerr spatial solitons in chalcogenide waveguides*. Optics letters, 2009. **34**(12): p. 1804-1806.
19. Sulițanu, N., *Thermoelectrical properties and memory switch phenomenon in amorphous Ge₄₆S₅₄ films*. Materials Science and Engineering: B, 2001. **83**(1-3): p. 84-88.
20. Boolchand, P., et al., *129I and 119Sn Mössbauer spectroscopy, reversibility window and nanoscale phase separation in binary Ge_xSe_{1-x} glasses*. Physica B: Condensed Matter, 2007. **389**(1): p. 18-28.
21. Pandey, V., S. Tripathi, and A. Kumar, *Effect of In incorporation on optical properties of amorphous Se-Ge thin films*. Physica B: Condensed Matter, 2007. **388**(1-2): p. 200-205.
22. Borisova, Z., *Glassy semiconductors*. 2013: Springer Science & Business Media.
23. Chen, G., et al., *Study of structural changes in amorphous As₂Se₃ by EXAFS under in situ laser irradiation*. Solid state communications, 2001. **120**(4): p. 149-153.
24. Onari, S., K. Matsuishi, and T. Arai, *Two phonon vibration spectra of amorphous Ge-S and Ge-Se systems*. Journal of Non-Crystalline Solids, 1985. **77**: p. 1121-1124.
25. Wang, Y., et al., *Effect of nanophase separation on crystallization process in Ge-Se glasses studied by Raman scattering*. Physica B: Condensed Matter, 2002. **316**: p. 568-571.
26. Ta'eed, V.G., et al., *Ultrafast all-optical chalcogenide glass photonic circuits*. Optics Express, 2007. **15**(15): p. 9205-9221.
27. Gai, X., et al., *Progress in optical waveguides fabricated from chalcogenide glasses*. Optics express, 2010. **18**(25): p. 26635-26646.
28. Suzuki, K., Y. Hamachi, and T. Baba, *Fabrication and characterization of chalcogenide glass photonic crystal waveguides*. Optics Express, 2009. **17**(25): p. 22393-22400.
29. Thielen, P., et al., *Small-core As-Se fiber for Raman amplification*. Optics Letters, 2003. **28**(16): p. 1406-1408.
30. Marchese, D., et al., *Highly nonlinear GeS₂-based chalcogenide glass for all-optical twin-core-fiber switching*. JOSA B, 1998. **15**(9): p. 2361-2370.

31. Lankhorst, M.H., B.W. Ketelaars, and R.A. Wolters, *Low-cost and nanoscale non-volatile memory concept for future silicon chips*. *Nature materials*, 2005. **4**(4): p. 347.
32. Vogel, E., M. Weber, and D. Krol, *Nonlinear optical phenomena in glass*. *Physics and chemistry of glasses*, 1991. **32**(6): p. 231-254.
33. Mori, A., et al., *Optical amplification with neodymium-doped chalcogenide glass fiber*. *Applied physics letters*, 1997. **70**(10): p. 1230-1232.
34. Masselin, P., et al., *CsCl effect on the optical properties of the 80GeS₂-20Ga₂S₃ base glass*. *Applied Physics A*, 2012. **106**(3): p. 697-702.
35. Masselin, P., E. Bychkov, and D. Le Coq, *Direct laser writing of a low-loss waveguide with independent control over the transverse dimension and the refractive index contrast between the core and the cladding*. *Optics letters*, 2016. **41**(15): p. 3507-3510.
36. Hewak, D.W., et al., *Chalcogenide glasses for photonics device applications*. *Photonic glasses and glass-ceramics*, 2010: p. 29-102.
37. Hughes, M., W. Yang, and D. Hewak, *Fabrication and characterization of femtosecond laser written waveguides in chalcogenide glass*. *Applied Physics Letters*, 2007. **90**(13): p. 131113.
38. McCarthy, J.E., et al., *Mid-infrared spectral broadening in an ultrafast laser inscribed gallium lanthanum sulphide waveguide*. *Optics express*, 2012. **20**(2): p. 1545-1551.
39. McMillen, B., et al., *Ultrafast laser fabrication of low-loss waveguides in chalcogenide glass with 0.65 dB/cm loss*. *Optics letters*, 2012. **37**(9): p. 1418-1420.
40. Arriola, A., et al., *Ultrafast laser inscription of mid-IR directional couplers for stellar interferometry*. *Optics Letters*, 2014. **39**(16): p. 4820-4822.
41. Liu, X., et al., *Expanded-core waveguides written by femtosecond laser irradiation in bulk optical glasses*. *Optics express*, 2014. **22**(23): p. 28771-28782.
42. Demetriou, G., et al., *Refractive index and dispersion control of ultrafast laser inscribed waveguides in gallium lanthanum sulphide for near and mid-infrared applications*. *Optics express*, 2016. **24**(6): p. 6350-6358.
43. Schweizer, T., et al., *Spectroscopy of potential mid-infrared laser transitions in gallium lanthanum sulphide glass*. *Journal of luminescence*, 1997. **72**: p. 419-421.
44. Ganjoo, A., et al., *Planar chalcogenide glass waveguides for IR evanescent wave sensors*. *Journal of Non-crystalline solids*, 2006. **352**(6-7): p. 584-588.

45. Miniscalco, W., *Rare-Earth Doped Fiber Lasers and Amplifiers* ed MJF Diggonet. 1993, New York: Dekker.
46. Zhang, B., et al., *High brightness 2.2–12 μm mid-infrared supercontinuum generation in a nontoxic chalcogenide step-index fiber*. Journal of the American Ceramic Society, 2016. **99**(8): p. 2565-2568.
47. Zhao, H., et al., *The kinetics of the glass transition and physical aging in germanium selenide glasses*. Journal of Non-Crystalline Solids, 2013. **368**: p. 63-70.
48. Li, Z., et al., *The electronic structure of GeSe monolayer with light nonmetallic elements decoration*. Superlattices and Microstructures, 2017. **109**: p. 829-840.
49. Li, P., et al., *Relaxation dynamics in the strong chalcogenide glass-former of Ge₂₂Se₇₈*. Scientific reports, 2017. **7**: p. 40547.
50. Lee, J.H., et al., *Crystallization behavior of Ge-Sb-Se glasses in the compositional range for use as molded lenses*. Journal of Non-Crystalline Solids, 2018. **481**: p. 21-26.
51. Petit, L., et al., *Compositional dependence of the nonlinear refractive index of new germanium-based chalcogenide glasses*. Journal of Solid State Chemistry, 2009. **182**(10): p. 2756-2761.
52. Esquerre, M., et al., *Crystallization of amorphous (bulk and thin films) Ge_xSe_{1-x} (0 < x < 0.20) alloys*. Journal of Materials Science, 1978. **13**(6): p. 1217-1223.
53. Gokhale, A. and R. Abbaschian, *The Ge-Se (Germanium-Selenium) system*. Journal of Phase Equilibria, 1990. **11**(3): p. 257-263.
54. Lyubin, V., M. Klebanov, and V. Tikhomirov, *Photoinduced anisotropy of photoconductivity in chalcogenide amorphous films*. Journal of non-crystalline solids, 2002. **299**: p. 945-948.
55. Fritzsche, H., *Insulating and Semiconducting Glasses* ed P Boolchand. 2000, Singapore: World Scientific.
56. Gan, F., *Structure, properties and applications of chalcogenide glasses: a review*. Journal of non-crystalline solids, 1992. **140**: p. 184-193.
57. Ma, H., et al., *Ga-Ge-Sb-Se based glasses and influence of alkaline halide addition*. Journal of non-crystalline solids, 1999. **256**: p. 165-169.
58. Canham, L.T., *Silicon quantum wire array fabrication by electrochemical and chemical dissolution of wafers*. Applied Physics Letters, 1990. **57**(10): p. 1046-1048.
59. Cullis, A., L. Canham, and P. Calcott, *The structural and luminescence properties of porous silicon*. Journal of applied physics, 1997. **82**(3): p. 909-965.

60. Cullis, A. and L. Canham, *Visible light emission due to quantum size effects in highly porous crystalline silicon*. Nature, 1991. **353**(6342): p. 335.
61. Prokes, S., *Surface and optical properties of porous silicon*. Journal of materials research, 1996. **11**(2): p. 305-320.
62. Chang, I. and Y. Chen, *Light emitting mechanism of porous silicon*. Journal of applied physics, 1997. **82**(7): p. 3514-3518.
63. Ozanam, F., J.-N. Chazalviel, and R. Wehrspohn, *In-situ photoluminescence studies of porous silicon in liquids*. Thin Solid Films, 1997. **297**(1-2): p. 53-60.
64. Rosso-Vasic, M., *Synthesis and photophysics of functionalized silicon nanoparticles*. 2008.
65. Cui, Y. and C.M. Lieber, *Functional nanoscale electronic devices assembled using silicon nanowire building blocks*. science, 2001. **291**(5505): p. 851-853.
66. Liu, A., et al., *A high-speed silicon optical modulator based on a metal-oxide-semiconductor capacitor*. Nature, 2004. **427**(6975): p. 615.
67. Henderson, E.J., et al., *Colloidally Stable Silicon Nanocrystals with Near-Infrared Photoluminescence for Biological Fluorescence Imaging*. Small, 2011. **7**(17): p. 2507-2516.
68. Baratto, C., et al., *Front-side micromachined porous silicon nitrogen dioxide gas sensor*. Thin Solid Films, 2001. **391**(2): p. 261-264.
69. Li, Y.Y., et al., *Polymer replicas of photonic porous silicon for sensing and drug delivery applications*. Science, 2003. **299**(5615): p. 2045-2047.
70. Cui, L.-F., et al., *Crystalline-amorphous core-shell silicon nanowires for high capacity and high current battery electrodes*. Nano letters, 2008. **9**(1): p. 491-495.
71. Chan, C.K., et al., *High-performance lithium battery anodes using silicon nanowires*. Nature nanotechnology, 2008. **3**(1): p. 31.
72. Chen, D., et al., *Reversible Lithium-Ion Storage in Silver-Treated Nanoscale Hollow Porous Silicon Particles*. Angewandte Chemie International Edition, 2012. **51**(10): p. 2409-2413.
73. Jalali, B., et al., *Prospects for silicon mid-IR Raman lasers*. IEEE Journal of selected topics in quantum electronics, 2006. **12**(6): p. 1618-1627.
74. Worldwide, E.O. *The Correct Material for Infrared (IR) Applications*. Available from: <https://www.edmundoptics.com/resources/application-notes/optics/the-correct-material-for-infrared-applications/>.
75. Paniccia, M., R. Rao, and W.M. Yee, *Optical probing of flip chip packaged microprocessors*. Journal of Vacuum Science & Technology B: Microelectronics and Nanometer Structures

- Processing, Measurement, and Phenomena, 1998. **16**(6): p. 3625-3630.
76. Jensen, W.B., *A note on the term "chalcogen"*. Journal of chemical education, 1997. **74**(9): p. 1063.
77. Sanghera, J., J. Heo, and J. Mackenzie, *Chalcohalide glasses*. Journal of non-crystalline solids, 1988. **103**(2-3): p. 155-178.
78. Sanghera, J., et al., *Fabrication of long lengths of low-loss IR transmitting As/sub 40/S/sub (60-x)/Se/sub x/glass fibers*. Journal of lightwave technology, 1996. **14**(5): p. 743-748.
79. Frerichs, R., *New optical glasses with good transparency in the infrared*. JOSA, 1953. **43**(12): p. 1153-1157.
80. Hilton, A.R. and S. Kemp, *Chalcogenide glasses for infrared optics*. 2010: McGraw-Hill New York.
81. Tver'yanovich, Y. and A. Tverjanovich, *Rare earth doped chalcogenide glass in semiconducting chalcogenide glass III—Applications of chalcogenide glasses (eds Fairman, R. & Ushkov, B.)* 160–207. 2004, Elsevier.
82. Sanghera, J.S., L.B. Shaw, and I.D. Aggarwal, *Chalcogenide glass-fiber-based mid-IR sources and applications*. IEEE Journal of selected topics in quantum electronics, 2009. **15**(1): p. 114-119.
83. Lin, H., et al. *Mid-infrared As₂ Se₃ chalcogenide glass-on-silicon waveguides*. in *The 9th International Conference on Group IV Photonics (GFP)*. 2012. IEEE.
84. Cui, S., et al., *From selenium-to tellurium-based glass optical fibers for infrared spectroscopies*. Molecules, 2013. **18**(5): p. 5373-5388.
85. Dwivedi, D., et al., *Structural and optical investigations of amorphous Se_{75-x}Te₂₅Sb_x thin films*. American Journal of Materials Science and Engineering, 2013. **1**(3): p. 46-49.
86. Dwivedi, D., et al., *Effect of Thermal Annealing on Structure and Optical Band Gap of Amorphous Se₆₆Te₂₅Sb₉ Thin Film*. Advanced Science Letters, 2014. **20**(5-6): p. 1081-1084.
87. Dwivedi, D., et al., *Effect of thermal annealing on structure and optical band gap of amorphous Se 75– x Te 25 Sb x thin films by vacuum evaporation technique*. J. Ovonic. Res, 2014. **10**: p. 15.
88. Mairaj, A.K., et al. *Advances in gallium lanthanum sulphide glass for optical fiber and devices*. in *Fiber Optic Sensor Technology II*. 2001. International Society for Optics and Photonics.
89. Goldstein, M., *Viscous liquids and the glass transition: a potential energy barrier picture*. The Journal of Chemical Physics, 1969. **51**(9): p. 3728-3739.
90. Anderson, D.L., *Through the glass lightly*. Science, 1995. **267**(5204): p. 1618-1618.

91. Debenedetti, P.G. and F.H. Stillinger, *Supercooled liquids and the glass transition*. Nature, 2001. **410**(6825): p. 259.
92. McKenna, G.B., *Glass dynamics: Diverging views on glass transition*. Nature Physics, 2008. **4**(9): p. 673.
93. Kerner, R. and M. Micoulaut, *On the glass transition temperature in covalent glasses*. Journal of non-crystalline solids, 1997. **210**(2-3): p. 298-305.
94. Kolobov, A.V., et al., *Understanding the phase-change mechanism of rewritable optical media*. Nature materials, 2004. **3**(10): p. 703.
95. Zallen, R., *Models of amorphous solids*. Journal of Non-Crystalline Solids, 1985. **75**(1-3): p. 3-14.
96. Zachariasen, W.H., *The atomic arrangement in glass*. Journal of the American Chemical Society, 1932. **54**(10): p. 3841-3851.
97. Thorpe, M.F., *Continuous deformations in random networks*. Journal of Non-Crystalline Solids, 1983. **57**(3): p. 355-370.
98. Moharram, A., *Short-range order of germanium selenide glass*. Glass Physics and Chemistry, 2015. **41**(5): p. 453-459.
99. Zakery, A. and S. Elliott, *Springer series in optical*. Science, 2007. **135**: p. 202-213.
100. Lucovsky, G. and T. Hayes, *Amorphous Semiconductors ed MH Brodsky*. Springer-Verlag, Berlin, 1979. **19**(79): p. 215.
101. White, R., *Random network model for amorphous alloys*. Journal of Non-Crystalline Solids, 1974. **16**(3): p. 387-398.
102. Phillips, J.C., *The physics of glass*. Physics Today, 1982. **35**(2): p. 27-33.
103. Sanghera, J.S., L.B. Shaw, and I.D. Aggarwal, *Applications of chalcogenide glass optical fibers*. Comptes Rendus Chimie, 2002. **5**(12): p. 873-883.
104. Tauc, J., *Optical properties and electronic structure of amorphous Ge and Si*. Materials Research Bulletin, 1968. **3**(1): p. 37-46.
105. Tauc, J., *Amorphous and liquid semiconductors*. 2012: Springer Science & Business Media.
106. Tauc, J., *Amorphous and Liquid Semiconductors (Plenum Press, New York, 1974)*.
107. Morigaki, K., *Physics of amorphous semiconductors*. 1999: World Scientific.
108. Marquez, E., P. Villares, and R. Jimenez-Garay, *On the growth and composition of conductive filaments on the surface of As–Se–Te bulk glassy semiconductors*. Journal of Materials Research, 1988. **3**(2): p. 314-320.

109. Hilton, A., D. Hayes, and M. Reichtin, *Infrared absorption of some high-purity chalcogenide glasses*. Journal of Non-Crystalline Solids, 1975. **17**(3): p. 319-338.
110. Ovshinsky, S.R., *Reversible electrical switching phenomena in disordered structures*. Physical Review Letters, 1968. **21**(20): p. 1450.
111. Carlson, D.E. and C.R. Wronski, *Amorphous silicon solar cell*. Applied Physics Letters, 1976. **28**(11): p. 671-673.
112. Boag, J., A. Stacey, and R. Davis, *Xerographic recording of mammograms*. The British journal of radiology, 1972. **45**(537): p. 633-640.
113. Jiang, F. and M. Okuda, *The effect of doping on the erasure speed and stability of reversible phase-change optical recording films*. Japanese journal of applied physics, 1991. **30**(1R): p. 97.
114. Popescu, M., *Disordered chalcogenide optoelectronic materials: phenomena and applications*. Journal of Optoelectronics and Advanced Materials, 2005. **7**(4): p. 2189-2210.
115. Popescu, M. and N.-C. Chalcogenides, *Kluwer Academic Publ.* Dordrecht, p-293, 2000.
116. Seddon, A., *Chalcogenide glasses: a review of their preparation, properties and applications*. Journal of Non-Crystalline Solids, 1995. **184**: p. 44-50.
117. Bureau, B., et al., *Chalcogenide optical fibers for mid-infrared sensing*. Optical Engineering, 2014. **53**(2): p. 027101.
118. Carlie, N., et al., *Measurement of the refractive index dispersion of As₂Se₃ bulk glass and thin films prior to and after laser irradiation and annealing using prism coupling in the near-and mid-infrared spectral range*. Review of Scientific Instruments, 2011. **82**(5): p. 053103.
119. Choi, D.-Y., et al., *Thermal annealing of arsenic tri-sulphide thin film and its influence on device performance*. Journal of Applied Physics, 2010. **107**(5): p. 053106.
120. Dussauze, M., et al., *Photosensitivity and second harmonic generation in chalcogenide arsenic sulfide poled glasses*. Optical Materials Express, 2012. **2**(1): p. 45-54.
121. Caulier, O., et al., *Direct laser writing of buried waveguide in As₂S₃ glass using a helical sample translation*. Optics letters, 2013. **38**(20): p. 4212-4215.
122. D'Amico, C., et al., *Large-mode-area infrared guiding in ultrafast laser written waveguides in Sulfur-based chalcogenide glasses*. Optics express, 2014. **22**(11): p. 13091-13101.

123. Psaila, N.D., et al., *Supercontinuum generation in an ultrafast laser inscribed chalcogenide glass waveguide*. *Optics express*, 2007. **15**(24): p. 15776-15781.
124. Ródenas, A., et al., *Three-dimensional mid-infrared photonic circuits in chalcogenide glass*. *Optics Letters*, 2012. **37**(3): p. 392-394.
125. Gretzinger, T., et al., *Ultrafast laser inscription in chalcogenide glass: thermal versus athermal fabrication*. *Optical Materials Express*, 2015. **5**(12): p. 2862-2877.
126. Arriola, A., D. Choudhury, and R.R. Thomson, *Towards efficient mid-infrared integrated photonic-lanterns*. *Journal of Optics*, 2015. **17**(12): p. 125804.
127. Pompilian, O., et al., *Pulsed laser deposition of rare-earth-doped gallium lanthanum sulphide chalcogenide glass thin films*. *Applied Physics A*, 2014. **117**(1): p. 197-205.
128. Asal, R. and H. Rutt, *Optical properties of laser ablated gallium lanthanum sulphide chalcogenide glass thin films prepared at different deposition laser energy densities*. *Optical Materials*, 1997. **8**(4): p. 259-268.
129. Němec, P., et al., *Gallium–lanthanum–sulphide amorphous thin films prepared by pulsed laser deposition*. *Materials Chemistry and Physics*, 2009. **117**(1): p. 23-25.
130. Petrovich, M., et al., *Near-IR absorption of Ga: La: S and Ga: La: S: O glasses by free-electron laser-based laser calorimetry*. *Journal of non-crystalline solids*, 2003. **326**: p. 93-97.
131. Barnier, S., M. Guittard, M. P. Pardo, A. M. Loireau-Lozach, J. Flahaut, P. Porcher, and J. Livage *Glass forms in the Ga₂S₃–La₂S₃ and Ga₂S₃–La₂O₃ systems*. *Materials Research Bulletin* 1983. **3**.
132. Mairaj, A., R. Curry, and D. Hewak, *Inverted deposition and high-velocity spinning to develop buried planar chalcogenide glass waveguides for highly nonlinear integrated optics*. *Applied Physics Letters*, 2005. **86**(9): p. 094102.
133. Frantz, J., et al., *Sputtered films of Er³⁺-doped gallium lanthanum sulfide glass*. *Materials letters*, 2006. **60**(11): p. 1350-1353.
134. Popescu, A., et al., *Properties of rare earth Ga-La-S glasses obtained by RF inductor heating*. *Dig. J. Nanomater. Biostruct*, 2011. **6**(2): p. 341-348.
135. Youden, K., et al., *Pulsed laser deposition of Ga-La-S chalcogenide glass thin film optical waveguides*. *Applied Physics Letters*, 1993. **63**(12): p. 1601-1603.
136. Gill, D.S., et al., *Characterisation of Ga-La-S chalcogenide glass thin-film optical waveguides, fabricated by pulsed laser deposition*. *Journal of non-crystalline solids*, 1995. **191**(3): p. 321-326.

137. Darby, M., et al., *Influence of deposition parameters on composition and refractive index of femtosecond and nanosecond pulsed laser deposited gallium lanthanum oxysulphide*. Journal of Non-Crystalline Solids, 2008. **354**(40-41): p. 4582-4588.
138. Nazabal, V., et al., *Dysprosium doped amorphous chalcogenide films prepared by pulsed laser deposition*. Optical Materials, 2006. **29**(2-3): p. 273-278.
139. Schweizer, T., *Rare-earth-doped gallium lanthanum sulphide glasses for mid-infrared fibre lasers*. 2000, University of Southampton.
140. Brady, D., T. Schweizer, and D. Hewak, *Gallium lanthanum sulphide glasses for mid infrared fibre applications*. 1998.
141. Digonnet, M.J., *Rare-earth-doped fiber lasers and amplifiers, revised and expanded*. 2001: CRC press.
142. Zakery, A. and S.R. Elliott, *Optical nonlinearities in chalcogenide glasses and their applications*. Vol. 135. 2007: Springer.
143. Schimmel, R., et al., *Development of germanium gallium sulphide glass fibres for the 1.31 μm praseodymium-doped fibre amplifier*. Journal of non-crystalline solids, 2001. **284**(1-3): p. 188-192.
144. Mairaj, A., R. Curry, and D. Hewak, *Chalcogenide glass thin films through inverted deposition and high velocity spinning*. Electronics Letters, 2004. **40**(7): p. 421-422.
145. Charpentier, F., et al., *Infrared monitoring of underground CO₂ storage using chalcogenide glass fibers*. Optical Materials, 2009. **31**(3): p. 496-500.
146. Le Person, J., et al., *Surface plasmon resonance in chalcogenide glass-based optical system*. Sensors and Actuators B: Chemical, 2008. **130**(2): p. 771-776.
147. Lenth, W. and R.M. Macfarlane, *Upconversion lasers*. Optics and Photonics News, 1992. **3**(3): p. 8-15.
148. Prudenzano, F., et al., *Simulation of mid-IR amplification in Er³⁺-doped chalcogenide microstructured optical fiber*. Optical Materials, 2009. **31**(9): p. 1292-1295.
149. Prudenzano, F., et al., *Theoretical study of cascade laser in erbium-doped chalcogenide glass fibers*. Optical Materials, 2010. **33**(2): p. 241-245.
150. Prudenzano, F., et al., *Design of Er³⁺-doped chalcogenide glass laser for MID-IR application*. Journal of Non-Crystalline Solids, 2009. **355**(18-21): p. 1145-1148.
151. Rode, A.V., et al., *Laser-deposited As₂S₃ chalcogenide films for waveguide applications*. Applied Surface Science, 2002. **197**: p. 481-485.

152. Boetti, N.G., et al. *Solar pumping of solid state lasers for space mission: A novel approach*. in *International Conference on Space Optics—ICSO 2012*. 2017. International Society for Optics and Photonics.
153. Madden, S., et al., *Long, low loss etched As₂S₃ chalcogenide waveguides for all-optical signal regeneration*. *Optics express*, 2007. **15**(22): p. 14414-14421.
154. Galili, M., et al., *Breakthrough switching speed with an all-optical chalcogenide glass chip: 640 Gbit/s demultiplexing*. *Optics Express*, 2009. **17**(4): p. 2182-2187.
155. Pelusi, M., et al., *Wavelength conversion of high-speed phase and intensity modulated signals using a highly nonlinear chalcogenide glass chip*. *IEEE Photonics Technology Letters*, 2009. **22**(1): p. 3-5.
156. Gai, X., et al., *Dispersion engineered Ge_{11.5}As₂₄Se_{64.5} nanowires with a nonlinear parameter of 136W⁻¹m⁻¹ at 1550nm*. *Optics express*, 2010. **18**(18): p. 18866-18874.
157. Schweizer, B., R. Samson, and D. Moore, *Hewak, and DN Payne*. *Electron. Lett*, 1997. **33**: p. 414.
158. Frantz, J.A., et al., *Waveguide amplifiers in sputtered films of Er³⁺-doped gallium lanthanum sulfide glass*. *Optics express*, 2006. **14**(5): p. 1797-1803.
159. Schweizer, T., et al., *Rare-earth doped chalcogenide glass laser*. *Electronics Letters*, 1996. **32**(7): p. 666-667.
160. Tohge, N., et al., *Preparation of n-type semiconducting Ge₂₀Bi₁₀Se₇₀ glass*. *Applied Physics Letters*, 1979. **34**(10): p. 640-641.
161. Tanaka, K., *Structural phase transitions in chalcogenide glasses*. *Physical Review B*, 1989. **39**(2): p. 1270.
162. Reddy, K.V., A. Bhatnagar, and V. Srivastava, *The influence of antimony impurity on optical and electrical properties of amorphous selenium*. *Journal of Physics: Condensed Matter*, 1992. **4**(23): p. 5273.
163. Othman, A., K. Tahon, and M. Osman, *Glass transition and crystallization kinetic studies in Mg_{0.10}As_{0.34}Se_{0.56} chalcogenide glass by using non-isothermal techniques*. *Physica B: Condensed Matter*, 2002. **311**(3-4): p. 356-365.
164. Mott, N.F. and E.A. Davis, *Electronic processes in non-crystalline materials*. 2012: Oxford university press.
165. Othman, A., *Influence of ultraviolet irradiation on the optical properties of amorphous Sb₁₀Se₉₀ thin films*. *Thin Solid Films*, 2006. **515**(4): p. 1634-1639.

166. Shimakawa, K., *Residual photocurrent decay in amorphous chalcogenides*. Journal of Non-Crystalline Solids, 1985. **77**: p. 1253-1256.
167. Shim, J.Y., S.W. Park, and H.K. Baik, *Silicide formation in cobalt/amorphous silicon, amorphous CoSi and bias-induced CoSi films*. Thin Solid Films, 1997. **292**(1-2): p. 31-39.
168. Saiter, J., et al., *Crystallization of As_xSe_{1-x} from the glassy state (0.005 < x < 0.03)*. Physica B: Condensed Matter, 1998. **245**(3): p. 256-262.
169. Brüggemann, R. and J. Kleider, *Photoconductivity techniques for defect spectroscopy of photovoltaic materials*. Thin Solid Films, 2002. **403**: p. 30-33.
170. Boolchand, P., et al., *Structural origin of broken chemical order in a Ge Se 2 glass*. Physical Review B, 1982. **25**(4): p. 2975.
171. Afify, N., *Structural relaxation of GeSe 2 chalcogenide glass studied with use of the radial distribution function*. Physical Review B, 1993. **48**(22): p. 16304.
172. Zhang, X., et al., *Thermoelectric properties of GeSe*. Journal of Materiomics, 2016. **2**(4): p. 331-337.
173. Abdel-Aziz, M., *Effect of thallium on the crystallization kinetics of the chalcogenide glasses GeSe 2 and GeSe 4*. Journal of thermal analysis and calorimetry, 2005. **79**(3): p. 709-714.
174. Cobb, M., D. Drabold, and R. Cappelletti, *Ab initio molecular-dynamics study of the structural, vibrational, and electronic properties of glassy GeSe 2*. Physical Review B, 1996. **54**(17): p. 12162.
175. Grande, T., et al., *Structural properties of GeSe₂ at high pressures*. Journal of Solid State Chemistry, 1999. **145**(1): p. 167-173.
176. Pan, R., et al., *Annealing effects on the structure and optical properties of GeSe₂ and GeSe₄ films prepared by PLD*. Journal of Alloys and Compounds, 2009. **484**(1-2): p. 645-648.
177. Němec, P., et al., *Amorphous Ge–Se thin films prepared by pulsed-laser deposition*. Philosophical Magazine, 2004. **84**(9): p. 877-885.
178. Huang, C.-C., D. Hewak, and J.V. Badding, *Deposition and characterization of germanium sulphide glass planar waveguides*. Optics Express, 2004. **12**(11): p. 2501-2506.
179. Solieman, A.S., et al., *Dependence of optical properties on the thickness of amorphous Ge₃₀Se₇₀ thin films*. Journal of Taibah University for Science, 2014. **8**(3): p. 282-288.
180. Pan, R., et al., *Structure and optical properties of amorphous Ge–Se films prepared by pulsed laser deposition*. Optik-International Journal for Light and Electron Optics, 2013. **124**(21): p. 4943-4946.

181. Kutálek, P. and L. Tichý, *On the thickness dependence of both the optical band gap and reversible photodarkening in amorphous Ge-Se films*. *Thin Solid Films*, 2016. **619**: p. 336-341.
182. Němec, P., et al., *GeSe/GeS nanomultilayers prepared by pulsed laser deposition*. *Journal of Non-Crystalline Solids*, 2008. **354**(52-54): p. 5421-5424.
183. Edwards, A., K.A. Campbell, and A.C. Pineda, *Self-trapping of single and paired electrons in Ge₂Se₃*. *Journal of Physics: Condensed Matter*, 2012. **24**(19): p. 195801.
184. Troles, J., et al., *GeSe₄ glass fibres with low optical losses in the mid-IR*. *Optical Materials*, 2009. **32**(1): p. 212-215.
185. Sugai, S., *Stochastic random network model in Ge and Si chalcogenide glasses*. *Physical Review B*, 1987. **35**(3): p. 1345.
186. Kumar, R.A., et al., *Influence of thickness on the optical properties of amorphous GeSe₂ thin films: analysis using Raman spectra, Urbach energy and Tauc parameter*. *Philosophical Magazine*, 2012. **92**(11): p. 1422-1434.
187. Petracovschi, E., et al., *Structural study by Raman spectroscopy and ⁷⁷Se NMR of GeSe₄ and 80GeSe₂-20Ga₂Se₃ glasses synthesized by mechanical milling*. *Journal of Non-Crystalline Solids*, 2016. **431**: p. 16-20.
188. Frumar, M., et al., *Thin chalcogenide films prepared by pulsed laser deposition—new amorphous materials applicable in optoelectronics and chemical sensors*. *Journal of Non-Crystalline Solids*, 2006. **352**(6-7): p. 544-561.
189. Wolf, K., et al., *Electron beam effects in Ge–Se thin films and resistance change memory devices*. *Emerging Materials Research*, 2016.
190. Sakai, K., et al., *Annealing time and temperature dependence for photo-induced crystallization in amorphous GeSe₂*. *Journal of Non-Crystalline Solids*, 2000. **266**: p. 933-937.
191. Santos, L.F., et al., *Optical and spectroscopic characterization of germanium selenide glass films*. *Journal of Non-Crystalline Solids*, 2009. **355**(37-42): p. 1984-1988.
192. Němec, P., et al., *Pulsed laser deposition of pure and praseodymium-doped Ge–Ga–Se amorphous chalcogenide films*. *Optical Materials*, 2000. **15**(3): p. 191-197.
193. Almeida, R.M., et al., *Structural heterogeneity in chalcogenide glass films prepared by thermal evaporation*. *Journal of non-crystalline solids*, 2007. **353**(18-21): p. 2066-2068.
194. Makinistian, L. and E. Albanesi, *Ab initio calculations of the electronic and optical properties of germanium selenide*. *Journal of Physics: Condensed Matter*, 2007. **19**(18): p. 186211.

195. Thakur, A., et al., *Optical properties of amorphous Ge₂₀Se₈₀ and Ag₆ (Ge_{0.20}Se_{0.80})₉₄ thin films*. *Optical Materials*, 2007. **30**(4): p. 565-570.
196. Eagleton, B., B. Davies, and K. Richardson. *Chalcogenide Photonics Nat.* 2011. Photon.
197. Němec, P., et al., *Optical properties of (GeSe₂)_{100-x} (Sb₂Se₃)_x glasses in near-and middle-infrared spectral regions*. *Materials Research Bulletin*, 2014. **51**: p. 176-179.
198. Chen, L., et al., *Third-order nonlinearity in Ge–Sb–Se glasses at mid-infrared wavelengths*. *Materials Research Bulletin*, 2015. **70**: p. 204-208.
199. Olivier, M., et al., *Structure, nonlinear properties, and photosensitivity of (GeSe₂)_{100-x} (Sb₂Se₃)_x glasses*. *Optical Materials Express*, 2014. **4**(3): p. 525-540.
200. Wei, W.-H., et al., *Correlation between structural and physical properties in Ge–Sb–Se glasses*. *The Journal of Physical Chemistry C*, 2013. **117**(32): p. 16571-16576.
201. Ganjoo, A., et al., *Structural modification of Ge–Se amorphous films with the addition of Sb*. *Philosophical magazine letters*, 2005. **85**(10): p. 503-512.
202. Sharda, S., et al., *Finger prints of chemical bonds in Sb–Se–Ge and Sb–Se–Ge–In glasses: a far-IR study*. *Journal of Non-Crystalline Solids*, 2013. **362**: p. 136-139.
203. Li, J., et al., *Fabrication and characterization of Ge₂₀Sb₁₅Se₆₅ chalcogenide glass rib waveguides for telecommunication wavelengths*. *Thin Solid Films*, 2013. **545**: p. 462-465.
204. Ivanova, Z., V. Pamukchieva, and M. Vlček, *On the structural phase transformations in Ge_xSb_{40-x}Se₆₀ glasses*. *Journal of non-crystalline solids*, 2001. **293**: p. 580-585.
205. Sharma, N., et al., *Far-infrared investigation of ternary Ge–Se–Sb and quaternary Ge–Se–Sb–Te chalcogenide glasses*. *Journal of Non-Crystalline Solids*, 2013. **375**: p. 114-118.
206. Shin, S.-Y., et al., *The effect of doping Sb on the electronic structure and the device characteristics of Ovonic Threshold Switches based on Ge-Se*. *Scientific reports*, 2014. **4**: p. 7099.
207. Chen, Y., et al., *Optical and structure properties of amorphous Ge–Sb–Se films for ultrafast all-optical signal processing*. *Journal of Alloys and Compounds*, 2013. **580**: p. 578-583.
208. Lee, J.H., et al., *Broken chemical order in Ge-Sb-Se glasses for use as infrared-transmitting lenses*. *Journal of Non-Crystalline Solids*, 2017. **456**: p. 27-32.
209. Wei, W.-H., et al., *Transition threshold in Ge_xSb₁₀Se_{90-x} glasses*. *Journal of Applied Physics*, 2014. **115**(11): p. 113510.

210. Baudet, E., et al., *Structural analysis of RF sputtered Ge-Sb-Se thin films by Raman and X-ray photoelectron spectroscopies*. Journal of Non-Crystalline Solids, 2016. **444**: p. 64-72.
211. Verger, F., et al., *RF sputtered amorphous chalcogenide thin films for surface enhanced infrared absorption spectroscopy*. Optical Materials Express, 2013. **3**(12): p. 2112-2131.
212. Nazabal, V., et al., *Sputtering and pulsed laser deposition for near- and mid-infrared applications: a comparative study of Ge₂₅Sb₁₀Se₆₅ and Ge₂₅Sb₁₀Se₆₅ amorphous thin films*. International Journal of Applied Ceramic Technology, 2011. **8**(5): p. 990-1000.
213. Chen, Y., et al., *Optical and structural properties of Ge–Sb–Se thin films fabricated by sputtering and thermal evaporation*. Journal of alloys and compounds, 2013. **548**: p. 155-160.
214. Olivier, M., et al., *Photosensitivity of pulsed laser deposited Ge-Sb-Se thin films*. Optical Materials Express, 2015. **5**(4): p. 781-793.
215. Halenkovič, T., et al., *Amorphous Ge-Sb-Se thin films fabricated by co-sputtering: Properties and photosensitivity*. Journal of the American Ceramic Society, 2018. **101**(7): p. 2877-2887.
216. Wasa, K. and S. Hayakawa, *Handbook of Sputter Deposition Technology: Principles, Technology and Applications (Materials Science and Process Technology Series)*. 1993: New York: William Andrew.
217. Birkholz, M., *Thin film analysis by X-ray scattering*. 2006: John Wiley & Sons.
218. Ohring, M., *Materials science of thin films*. 2001: Elsevier.
219. Seshan, K., *Handbook of Thin Film Deposition Techniques Principles, Methods, Equipment and Applications, Second Edition*. 2002.
220. Chopra, K.L., *Thin film phenomena*. 1969.
221. Etzkorn, J., et al., *Metal–Organic Chemical Vapor Deposition Synthesis of Hollow Inorganic-Fullerene-Type MoS₂ and MoSe₂ Nanoparticles*. Advanced materials, 2005. **17**(19): p. 2372-2375.
222. Lauritsen, J.V., et al., *Size-dependent structure of MoS₂ nanocrystals*. Nature nanotechnology, 2007. **2**(1): p. 53.
223. Lazell, M., et al., *Single source molecular precursors for the deposition of III/VI chalcogenide semiconductors by MOCVD and related techniques*. Journal of the Chemical Society, Dalton Transactions, 2000(24): p. 4479-4486.
224. Ouyang, T., et al., *A surface chemistry route to molybdenum sulfide and germanide films using the single-source precursor tetrakis (diethylaminodithiocarbomato) molybdate (IV)*. The Journal of Physical Chemistry B, 2004. **108**(45): p. 17537-17545.

225. Harwood, D.W., et al., *Fabrication of fluoride glass planar waveguides by hot dip spin coating*. Journal of non-crystalline solids, 2003. **332**(1-3): p. 190-198.
226. Macleod, A., *Optical thin films*, in *Handbook of Thin Film Deposition*. 2018, Elsevier. p. 379-416.
227. Jameel, D.A., *Thin film deposition processes*. Thin film deposition processes. International Journal of Modern Physics and Applications, 2015. **1**(4): p. 193-199.
228. Freund, L. and S. Suresh, *Stress, Defect Formation and Surface Evolution*. Thin Film Materials. Cambridge University Press, Cambridge, United Kingdom, 2003.
229. Wasa, K., M. Kitabatake, and H. Adachi, *Thin film materials technology: sputtering of control compound materials*. 2004: Springer Science & Business Media.
230. Eason, R., *Pulsed laser deposition of thin films: applications-led growth of functional materials*. 2007: John Wiley & Sons.
231. Jilani, A., M.S. Abdel-Wahab, and A.H. Hammad, *Advance deposition techniques for thin film and coating*. Modern Technologies for Creating the Thin-film Systems and Coatings, 2017. **2**: p. 137-149.
232. Halada, G.P. and C.R. Clayton, *The intersection of design, manufacturing, and surface engineering*, in *Handbook of Environmental Degradation of Materials*. 2005, Elsevier. p. 321-344.
233. Teghil, R., et al., *Picosecond and femtosecond pulsed laser ablation and deposition of quasicrystals*. Applied Surface Science, 2003. **210**(3-4): p. 307-317.
234. Momma, C., et al., *Short-pulse laser ablation of solid targets*. Optics communications, 1996. **129**(1-2): p. 134-142.
235. Pietroy, D., et al., *Femtosecond laser volume ablation rate and threshold measurements by differential weighing*. Optics Express, 2012. **20**(28): p. 29900-29908.
236. Hamad, A.H., *Effects of different laser pulse regimes (nanosecond, picosecond and femtosecond) on the ablation of materials for production of nanoparticles in liquid solution*. High Energy and Short Pulse Lasers, 2016: p. 305-325.
237. Semerok, A., et al., *Femtosecond, picosecond, and nanosecond laser microablation: Laser plasma and crater investigation*. Laser and Particle Beams, 2002. **20**(1): p. 67-72.
238. Garrelie, F., et al. *New trends in femtosecond Pulsed Laser Deposition and femtosecond produced plasma diagnostics*. in *High-Power Laser Ablation VI*. 2006. International Society for Optics and Photonics.

239. Lucas, L. and J. Zhang, *Femtosecond laser micromachining: a back-to-basics primer*. Industrial laser solutions, 2012.
240. Popovici, N., *Oxide thin films for spintronics application growth and characterization*. 2009.
241. Nemeč, P. and M. Frumar, *Chalcogenide-based amorphous thin films prepared by pulsed laser deposition*. J. Optoelectron. Adv. Mater., 2003. **5**(5): p. 1047-1058.
242. Ohl, R.S., *Properties of ionic bombarded silicon*. The Bell System Technical Journal, 1952. **31**(1): p. 104-121.
243. Shockley, W., *Forming semiconductive devices by ionic bombardment, US patent 2787564 A*. 1957.
244. Currenta, M.I., L. Rubinb, and F. Sinclairc, *Commercial Ion Implantation Systems*.
245. Conrad, J., et al., *Plasma source ion implantation: A new, cost-effective, non-line-of-sight technique for ion implantation of materials*. Surface and Coatings Technology, 1988. **36**(3-4): p. 927-937.
246. Conrad, J.R., et al., *Plasma source ion-implantation technique for surface modification of materials*. Journal of Applied Physics, 1987. **62**(11): p. 4591-4596.
247. Conrad, J., *Sheath thickness and potential profiles of ion-matrix sheaths for cylindrical and spherical electrodes*. Journal of applied physics, 1987. **62**(3): p. 777-779.
248. Conrad, J. and C. Forest. *Plasma source ion implantation*. in *Conference record of the 1986 IEEE international conference on plasma science*. 1986.
249. Smidt, F., B. Sartwell, and S. Bunker, *US Navy manufacturing technology program on ion implantation*. Materials Science and Engineering, 1987. **90**: p. 385-397.
250. Ahmad, R., et al., *Implantation of various energy metallic ions on aluminium substrate using a table top laser driven ion source*. Laser and Particle Beams, 2014. **32**(2): p. 261-270.
251. Latif, A., et al., *IR and UV irradiations on ion bombarded polycrystalline silver*. Physica B: Condensed Matter, 2010. **405**(20): p. 4250-4255.
252. Giuffrida, L., et al., *Surface ion implantation induced by laser-generated plasmas*. Radiation Effects & Defects in Solids: Incorporating Plasma Science & Plasma Technology, 2010. **165**(6-10): p. 534-542.
253. Cutroneo, M., et al., *High-intensity laser for Ta and Ag implantation into different substrates for plasma diagnostics*. Nuclear Instruments and Methods in Physics Research Section B: Beam Interactions with Materials and Atoms, 2015. **354**: p. 56-59.

254. Meunier, C., et al., *Effect on microstructure and hardness of 1 MeV carbon ion implantation in Al, Co and W*. Surface and Coatings Technology, 2015. **262**: p. 191-199.
255. Foerster, C., et al., *Carbon ion implantation into aluminium: Mechanical and tribological properties*. Surface and Coatings Technology, 2006. **200**(18-19): p. 5210-5219.
256. Láska, L., et al., *Laser induced direct implantation of ions*. Czechoslovak Journal of Physics, 2000. **50**(3): p. 81-90.
257. Wolowski, J., et al., *Fast ion emission from the plasma produced by the PALS laser system*. Plasma physics and controlled fusion, 2002. **44**(7): p. 1277.
258. Peřina, V., et al., *Simple technique for measurement of energy spectra of ions from laser produced plasma*. Czechoslovak journal of physics, 1998. **48**(9): p. 1067-1073.
259. Woryna, E., et al., *Laser-Produced Plasma as an Effective Source of Multicharged Ions*. Journal of Technical Physics, 2000. **41**(1): p. 521-531.
260. Golishnikov, D., et al., *Dense femtosecond plasma at moderate intensities: Hot electrons, fast ions, and thermonuclear processes in modified targets*. Laser physics, 2001. **11**(11): p. 1205-1211.
261. Volkov, R.V., et al., *Generation of hot particles in a femtosecond laser-produced plasma with the use of solid modified targets*. Quantum Electronics, 2001. **31**(3): p. 241.
262. Belloni, F., et al. *Ion Implantation Via Laser Ion Source*. in *Conf. Proc.* 2006.
263. Rosinski, M., et al., *Laser produced streams of Ge ions accelerated and optimized in the electric fields for implantation into SiO₂ substrates*. Review of Scientific Instruments, 2012. **83**(2): p. 02B305.
264. Torrisi, L., et al., *Implantation of ions produced by the use of high power iodine laser*. Applied surface science, 2003. **217**(1-4): p. 319-331.
265. Rosiński, J., et al., *Direct implantation of Ge ions produced by high-energy low-intensity laser pulses into SiO₂ films prepared on Si substrates*. Physica Scripta, 2006. **2006**(T123): p. 148.
266. Volkov, R.V., et al., *Implantation of high-energy ions produced by femtosecond laser pulses*. Quantum Electronics, 2005. **35**(1): p. 33.
267. Carter, G. and W.A. Grant, *Ion implantation of semiconductors*. 1976: Hodder Arnold.
268. Pelaz, L., L.A. Marqués, and J. Barbolla, *Ion-beam-induced amorphization and recrystallization in silicon*. Journal of applied physics, 2004. **96**(11): p. 5947-5976.
269. Fahey, P.M., P. Griffin, and J. Plummer, *Point defects and dopant diffusion in silicon*. Reviews of modern physics, 1989. **61**(2): p. 289.

270. Sharma, R., et al., *X-ray diffraction: a powerful method of characterizing nanomaterials*. Recent research in science and technology, 2012. **4**(8).
271. Poppe, L., et al., *A laboratory manual for X-ray powder diffraction*. US Geological Survey Open-File Report, 2001. **1**(041): p. 1-88.
272. Hone, F.G. and F.K. Ampong, *Effect of deposition temperature on the structural, morphological and optical band gap of lead selenide thin films synthesized by chemical bath deposition method*. Materials Chemistry and Physics, 2016. **183**: p. 320-325.
273. Jensen, H., et al., *Determination of size distributions in nanosized powders by TEM, XRD, and SAXS*. Journal of Experimental Nanoscience, 2006. **1**(3): p. 355-373.
274. Xie, Q. and F. McCourt, *Nanotechnology Engineering NE 320L Lab Manual*. University of Waterloo, Waterloo, 2008. **23**.
275. Guinier, A., *X-ray diffraction in crystals, imperfect crystals, and amorphous bodies*. 1994: Courier Corporation.
276. Shabir, Q., et al., *Medically biodegradable hydrogenated amorphous silicon microspheres*. Silicon, 2011. **3**(4): p. 173-176.
277. Subramanian, A., et al., *Non Invasive Glucose Measurement Using Raman Spectroscopy*. International Research Journal of Engineering and Technology (IRJET), 2017. **4**(03).
278. Vašková, H., *A powerful tool for material identification: Raman spectroscopy*. International journal of mathematical models and methods in applied sciences, 2011. **5**(7): p. 1205-12.
279. Hollas, J.M., *Modern spectroscopy*. 2004: John Wiley & Sons.
280. Kalantri, P.P., R.R. Somani, and D.T. Makhija, *Raman spectroscopy: a potential technique in analysis of pharmaceuticals*. Der Chemica Sinica, 2010. **1**(1): p. 1-12.
281. Loader, J., *Basic laser Raman spectroscopy*. 1970: Heyden.
282. Long, D.A. and D. Long, *Raman spectroscopy*. Vol. 276. 1977: McGraw-Hill New York.
283. Long, D., *Introductory Raman Spectroscopy*. John R. Ferraro, Kazuo Nakamoto and Chris W. Brown. Academic Press, Amsterdam, 2003. *xiii*+ 434. Journal of Raman Spectroscopy: An International Journal for Original Work in all Aspects of Raman Spectroscopy, Including Higher Order Processes, and also Brillouin and Rayleigh Scattering, 2005. **36**(10): p. 1012-1012.
284. Placzek, G., *Rayleigh-streuung und Raman-effekt*. Vol. 2. 1934: Akad. Verlag-Ges.
285. Bonales, L.J., et al., *Raman spectroscopy, a useful tool to study nuclear materials*. Applications of Molecular Spectroscopy to Current Research in the Chemical and Biological Sciences, 2016.

286. Williams, D.B. and C.B. Carter, *Transmission Electron Microscopy: Spectrometry. IV.* 1996: Plenum Press New York.
287. Hirsch, P.B., *Electron microscopy of thin crystals.* 1967: Plenum Press.
288. Williams, D.B. and C. Barry, Carter. *Transmission electron microscopy: a textbook for materials science.* 2009, New York: Springer.
289. Kohl, H. and L. Reimer, *Transmission electron microscopy: physics of image formation.* 2008: Springer.
290. Fultz, B. and J.M. Howe, *Transmission electron microscopy and diffractometry of materials.* 2012: Springer Science & Business Media.
291. Bozzola, J.J. and L.D. Russell, *Electron microscopy: principles and techniques for biologists.* 1999: Jones & Bartlett Learning.
292. Warwick, T.U.o. *Transmission Electron Microscopy (TEM)* 2010, Jan 04; Available from: https://warwick.ac.uk/fac/sci/physics/current/postgraduate/regs/mp_gswarwick/ex5/techniques/structural/tem/.
293. Schäfer, R. and P.C. Schmidt, *Methods in Physical Chemistry, 2 Volume Set.* Vol. 1. 2012: John Wiley & Sons.
294. Van Tendeloo, G., D. Van Dyck, and S.J. Pennycook, *Handbook of nanoscopy.* 2012: John Wiley & Sons.
295. Giannuzzi, L.A., *Introduction to focused ion beams: instrumentation, theory, techniques and practice.* 2004: Springer Science & Business Media.
296. Utke, I., S. Moshkalev, and P. Russell, *Nanofabrication using focused ion and electron beams: principles and applications.* 2012: Oxford University Press.
297. Libretexts, C. *Energy-Dispersive X-ray Spectroscopy (EDS)[online].* 2019, Jun 05; Available from: [https://chem.libretexts.org/Courses/Franklin_and_Marshall_Colleg/Introduction_to_Materials_Characterization_CHM_412_Collaborative_Text/Spectroscopy/Energy_Dispersive_X-ray_Spectroscopy_\(EDS\)](https://chem.libretexts.org/Courses/Franklin_and_Marshall_Colleg/Introduction_to_Materials_Characterization_CHM_412_Collaborative_Text/Spectroscopy/Energy_Dispersive_X-ray_Spectroscopy_(EDS)).
298. Goldstein, J., et al., *Scanning electron microscopy and X-ray microanalysis: a text for biologists.* Materials Scientists, and Geologists, 1992: p. 189-230.
299. Chatwal, G.R. and S.K. Anand, *Instrumental Methods of Chemical Analysis:(for Hons. and Post-graduate Students of Indian and Foreign Universities).* 1979: Himalaya publishing house.
300. Heiman, D., *Photoluminescence spectroscopy.* Northeastern University, 2004.
301. Tusscher, L.t., *Photoluminescence and electronic spectroscopy in metal-oxide thin? films, with the prospect of application in extreme-ultraviolet lithography.* 2017.

302. Valikkodi, M., *Synthesis, growth and characterization of piperzium p-aminobenzoate and piperazinum p-chlorobenzoate nonlinear optical single crystals*. 2018, Alagappa university.
303. Luo, W., et al., *Efficient fabrication of nanoporous Si and Si/Ge enabled by a heat scavenger in magnesiothermic reactions*. Scientific reports, 2013. **3**: p. 2222.
304. Asafa, T., et al., *Thickness effect on the structural and electrical properties of poly-SiGe films*. Materials Research Bulletin, 2014. **49**: p. 102-107.
305. Asafa, T., et al., *Influence of germanium incorporation on the structural and electrical properties of boron-doped ultrathin poly-Si 1- x Ge x films deposited by chemical vapour deposition*. Applied Physics A, 2014. **116**(2): p. 751-757.
306. Li, R., et al., *The decisive role of oxide content in the formation and crystallization of gallium-lanthanum-sulfide glasses*. Journal of materials research, 1999. **14**(6): p. 2621-2627.
307. Khorasaninejad, M., J. Walia, and S. Saini, *Enhanced first-order Raman scattering from arrays of vertical silicon nanowires*. Nanotechnology, 2012. **23**(27): p. 275706.
308. Huang, C., et al., *Germanium antimony sulphide nano-wires fabricated by chemical vapour deposition and e-beam lithography. Nano Science and Technology Institute Conference (NSTI Nanotech 2008). 01 - 05 Jun 2008*. p.4.
309. White, W.B. and D.G. Minser, *Raman spectra and structure of natural glasses*. Journal of Non-Crystalline Solids, 1984. **67**(1-3): p. 45-59.
310. Agnello, S., et al., *Interstitial O₂ distribution in amorphous SiO₂ nanoparticles determined by Raman and photoluminescence spectroscopy*. Journal of Applied Physics, 2013. **114**(10): p. 104305.
311. Lucazeau, G., S. Barnier, and A. Loireau-Lozac'h, *Vibrational spectra, electronic transitions and short order structure of rare earth—gallium sulphide glasses*. Spectrochimica Acta Part A: Molecular Spectroscopy, 1978. **34**(1): p. 21-27.
312. Lucazeau, G. and J. Leroy, *Etude vibrationnelle de α Ga₂S₃*. Spectrochimica Acta Part A: Molecular Spectroscopy, 1978. **34**(1): p. 29-32.
313. Barnier, S. and G. Lucazeau, *Étude vibrationnelle de γ sesquisulfures de terres rares*. Journal de Chimie Physique, 1976. **73**: p. 580-582.
314. Barimah, E.K., et al., *Erbium-doped glass nanoparticle embedded polymer thin films using femtosecond pulsed laser deposition*. Optical Materials Express, 2018. **8**(7): p. 1997-2007.
315. Jinqiu, Y., et al., *Raman spectra of RE₂O₃ (RE= Eu, Gd, Dy, Ho, Er, Tm, Yb, Lu, Sc and Y): laser-excited luminescence and trace impurity analysis*. Journal of rare earths, 2014. **32**(1): p. 1-4.

316. Ravagli, A., et al., *Structural and spectral characterisation of Er³⁺ and Nd³⁺ doped Ga-La-S-Se glasses*. RSC advances, 2018. **8**(48): p. 27556-27564.
317. Koughia, C., et al., *Tailoring the 4I9/2→ 4I13/2 emission in Er³⁺ ions in different hosts media*. Optical Materials, 2015. **41**: p. 116-121.
318. Koughia, C. and S.O. Kasap, *Excitation diffusion in GeGaSe and GeGaS glasses heavily doped with Er 3+*. Optics express, 2008. **16**(11): p. 7709-7714.
319. Faber, A.J., et al. *Photoluminescence quenching by OH in Er-and Pr-doped glasses for 1.5 and 1.3 um optical amplifiers*. in *Fiber Optic Materials and Components*. 1994. International Society for Optics and Photonics.
320. Morea, R., et al. *Pulsed laser deposition of rare-earth-doped glasses: a step toward lightwave circuits*. in *Optical Components and Materials XIII*. 2016. International Society for Optics and Photonics.
321. El-Zahed, H., M. Dongol, and M. Radwan, *Annealing and thickness effect on the optical absorption of Ge 20 Te 80 and Cu 6 Ge 14 Te 80 films*. The European Physical Journal-Applied Physics, 2002. **17**(3): p. 179-186.
322. El-Korashy, A., M. Abdel-Rahim, and H. El-Zahed, *Optical absorption studies on AgInSe₂ and AgInTe₂ thin films*. Thin Solid Films, 1999. **338**(1-2): p. 207-212.
323. Dlamini, S., et al., *The effect of different gas atmospheres on the structure, morphology and photoluminescence properties of pulsed laser deposited Y₃ (Al, Ga) 5O₁₂: Ce³⁺ nano thin films*. Solid State Sciences, 2013. **23**: p. 65-71.
324. Dolo, J., et al., *The effect of oxygen pressure on the structure, morphology and photoluminescence intensity of pulsed laser deposited Gd₂ O₂ S: Tb³⁺ thin film phosphor*. Applied Physics A, 2010. **101**(4): p. 655-659.
325. Debelo, N., et al., *The effect of argon gas pressure on structural, morphological and photoluminescence properties of pulsed laser deposited KY₃ F₁₀: Ho³⁺ thin films*. Applied Physics A, 2016. **122**(6): p. 619.
326. Hillie, K. and H. Swart, *Electron beam induced degradation of a pulsed laser deposited ZnS: Cu, Au, Al thin film on a Si (1 0 0) substrate*. Applied surface science, 2001. **183**(3-4): p. 304-310.
327. Amoruso, S., et al., *Dynamics of laser-ablated MgB₂ plasma expanding in argon probed by optical emission spectroscopy*. Physical Review B, 2003. **67**(22): p. 224503.
328. Irannejad, M., et al., *A parametric study of Er³⁺-ions doped Phospho-tellurite glass thin films by pulsed laser deposition*. Optical Materials, 2010. **33**(2): p. 215-219.

329. Albarkaty, K., et al., *Erbium-doped chalcogenide glass thin film on silicon using femtosecond pulsed laser with different deposition temperatures*. Applied Physics A, 2019. **125**(1): p. 1.
330. Lezal, D., J. Pedlikova, and J. Zavadil, *Chalcogenide glasses for optical and photonics applications*. J. Optoelectron. Adv. Mater, 2004. **6**(1): p. 133-137.
331. Wiedemeier, H. and P. Siemers, *The thermal expansion and high temperature transformation of GeSe*. Zeitschrift für anorganische und allgemeine Chemie, 1975. **411**(1): p. 90-96.
332. Ramasamy, P., et al., *Solution synthesis of GeS and GeSe nanosheets for high-sensitivity photodetectors*. Journal of Materials Chemistry C, 2016. **4**(3): p. 479-485.
333. Muranaka, S., Y. Bando, and T. Takada, *Influence of substrate temperature and film thickness on the structure of reactively evaporated In₂O₃ films*. Thin Solid Films, 1987. **151**(3): p. 355-364.
334. Edwards, T. and S. Sen, *Structure and relaxation in germanium selenide glasses and supercooled liquids: a Raman spectroscopic study*. The Journal of Physical Chemistry B, 2011. **115**(15): p. 4307-4314.
335. Tronc, P., et al., *Raman scattering and local order in Ge_xSe_{1-x} glasses for 1/3 ≤ x ≤ 1/2*. Journal de Physique, 1977. **38**(12): p. 1493-1498.
336. Mishra, K. and B. Sopori, *The Role of Point Defects and Defect Complexes in Silicon Device Processing*. 1993.
337. Fage-Pedersen, J., *Impurity–point defect complexes: Diffusion studies in Si and SiGe, and electrical studies in Ge*. 2001, PhD thesis 2001 (www.dfi.aau.dk/~fage/fage-pedersen-thesis.pdf).
338. Glück, M., *MEMS in der Mikrosystemtechnik*. Teubner, Augsburg, Germany, 2005.
339. Pan, R., et al., *Thermal-induced gradually changes in the optical properties of amorphous GeSe₂ film prepared by PLD*. Physica B: Condensed Matter, 2009. **404**(20): p. 3397-3400.
340. Wang, Y., et al., *Composition dependences of refractive index and thermo-optic coefficient in Ge-As-Se chalcogenide glasses*. Journal of Non-Crystalline Solids, 2017. **459**: p. 88-93.
341. Klocek, P. and L. Colombo, *Index of refraction, dispersion, bandgap and light scattering in GeSe and GeSbSe glasses*. Journal of non-crystalline solids, 1987. **93**(1): p. 1-16.
342. Yi, C., et al., *Fabrication and characterization of Ge₂₀Sb₁₅S₆₅ chalcogenide glass for photonic crystal fibers*. Applied Physics B, 2014. **116**(3): p. 653-658.

343. Jiang, C., et al., *Improvements on the optical properties of Ge–Sb–Se chalcogenide glasses with iodine incorporation*. Infrared Physics & Technology, 2015. **73**: p. 54-61.
344. Jiang, C., et al., *Fabrication and characterization of Ge–Sb–Se–I glasses and fibers*. Applied Physics A, 2015. **120**(1): p. 127-135.
345. Lai, Y., et al., *Preparation and characterization of Sb₂Se₃ thin films by electrodeposition and annealing treatment*. Applied Surface Science, 2012. **261**: p. 510-514.
346. Zhao, C., X. Cao, and X. Lan, *Microwave-enhanced rapid and green synthesis of well crystalline Sb₂Se₃ nanorods with a flat cross section*. Materials Letters, 2007. **61**(29): p. 5083-5086.
347. Fjellvåg, H., K.O. Kongshaug, and S. Stølen, *Crystal structure of Ge₄Se₉: a new germanium selenide with Se₂ pairs breaking the edge-sharing GeSe₄ tetrahedra in GeSe₂*. Journal of the Chemical Society, Dalton Transactions, 2001(7): p. 1043-1045.
348. Adam, J.-L. and X. Zhang, *Chalcogenide glasses: preparation, properties and applications*. 2014: Woodhead publishing.
349. Kostadinova, O. and S. Yannopoulos, *Raman spectroscopic study of SbxSe_{100-x} phase-separated bulk glasses*. Journal of Non-Crystalline Solids, 2009. **355**(37-42): p. 2040-2044.
350. Holubova, J., Z. Cernosek, and E. Cernoskova, *SbxSe_{100-x} system (0 ≤ x ≤ 8) studied by DSC and Raman spectroscopy*. J Optoelectron Adv Mater, 2007. **1**: p. 663-6.
351. Dulgheru, N., et al., *Influence of compositional variation on the optical and morphological properties of GeSbSe films for optoelectronics application*. Infrared Physics & Technology, 2018. **93**: p. 260-270.
352. Matsuda, O., K. Inoue, and K. Murase, *Resonant Raman study on crystalline GeSe₂ in relation to amorphous states*. Solid state communications, 1990. **75**(4): p. 303-308.
353. Jackson, K., et al., *Raman-active modes of a- GeSe₂ and a- GeS₂: A first-principles study*. Physical Review B, 1999. **60**(22): p. R14985.
354. Nazabal, V., et al., *Optical waveguide based on amorphous Er³⁺-doped Ga–Ge–Sb–S (Se) pulsed laser deposited thin films*. Thin Solid Films, 2010. **518**(17): p. 4941-4947.
355. Goyal, D. and A. Maan, *Far-infrared absorption in amorphous Sb₁₅GexSe_{85-x} glasses*. Journal of non-crystalline solids, 1995. **183**(1-2): p. 182-185.
356. Němec, P., B. Frumarová, and M. Frumar, *Structure and properties of the pure and Pr³⁺-doped Ge₂₅Ga₅Se₇₀ and Ge₃₀Ga₅Se₆₅ glasses*. Journal of non-crystalline solids, 2000. **270**(1-3): p. 137-146.

357. El-Sayed, S., *Far-infrared studies of the amorphous $Sb_xGe_{28-x}Se_{72}$ glassy semiconductor*. Semiconductor science and technology, 2003. **18**(4): p. 337.
358. Petit, L., et al., *Effect of the substitution of S for Se on the structure of the glasses in the system $Ge_{0.23}Sb_{0.07}S_{0.70-x}Se_x$* . Journal of Physics and Chemistry of Solids, 2005. **66**(10): p. 1788-1794.
359. Xie, M., et al., *Correlation among Structure, Water Peak Absorption, and Femtosecond Laser Ablation Properties of Ge–Sb–Se Chalcogenide Glasses*. The Journal of Physical Chemistry C, 2018. **122**(3): p. 1681-1687.
360. Shaaban, E. and I. Tomsah, *The effect of Sb content on glass-forming ability, the thermal stability, and crystallization of Ge–Se chalcogenide glass*. Journal of thermal analysis and calorimetry, 2011. **105**(1): p. 191-198.
361. Lenz, G., et al., *Large Kerr effect in bulk Se-based chalcogenide glasses*. Optics Letters, 2000. **25**(4): p. 254-256.
362. Balan, V., C. Vignereux, and A. Pradel, *Chalcogenide thin films deposited by radio-frequency sputtering*. Journal of Optoelectronics and Advanced materials, 2004. **6**: p. 875-882.
363. Bicerano, J. and S.R. Ovshinsky, *Chemical bond approach to the structures of chalcogenide glasses with reversible switching properties*. Journal of Non-Crystalline Solids, 1985. **74**(1): p. 75-84.

Appendices

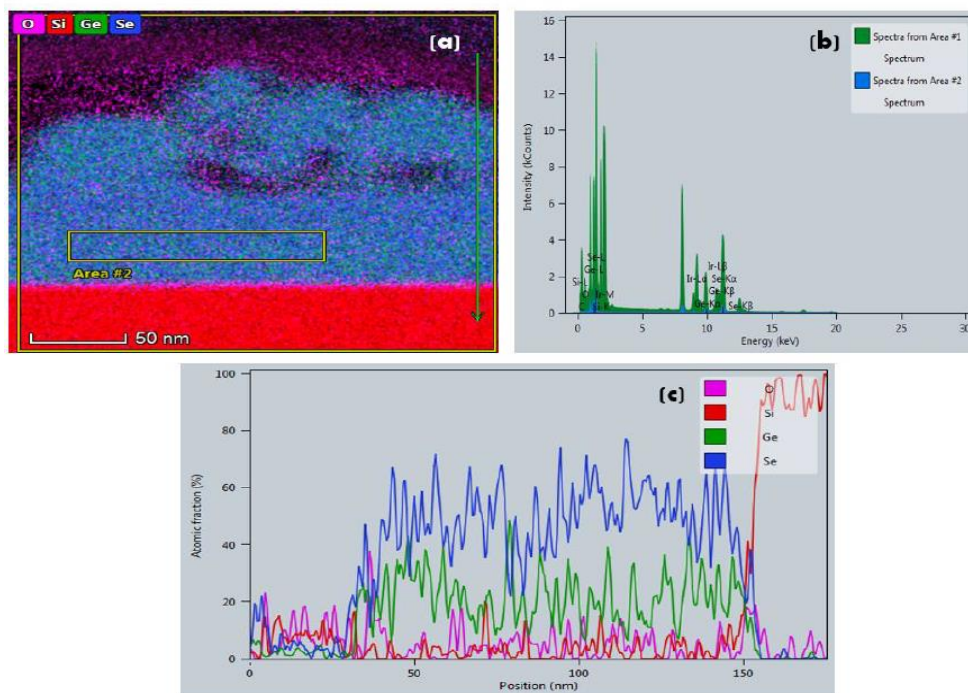


Figure 1: (a) A HAADF-STEM image, (b) TEM-EDX spectrum of the yellow region labelled in (a) of the doped layer, and (c) line scan obtained from STEM-EDX showing that no silicon was detected at the Ge-Se film prepared on silicon at a substrate temperature of 200°C.

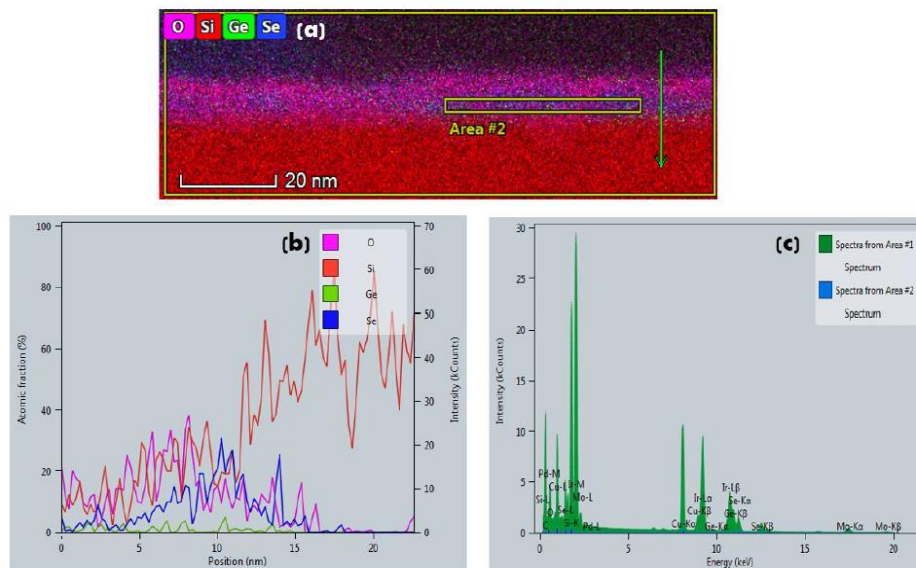


Figure 2: (a) A HAADF-STEM image, (b) TEM-EDX spectrum of the yellow region labelled in (a) of the doped layer, and (c) line scan obtained from STEM-EDX showing that silicon was detected at the Ge-Se film prepared on silicon at a substrate temperature of 400°C.